ROTATION-FREE

MAGNETIC ELECTRON LENSES

A Thesis Submitted for the Degree

of

DOCTOR OF PHILOSOPHY

in

The University of Aston in Birmingham

by

SABAH MAHMOOD JUMA, B.Sc., M.Sc.

December 1975

Department of Physics

Dedicated To My Wife

IN'AM

SUMMARY

The practical realization of rotation-free magnetic electron lenses has been an unsolved problem since the invention of the electron microscope in the 1930's. Preliminary studies showed that new forms of lens construction could conceivably lead to a practical form of rotation-free lens. On the completion of successful tests with an experimental rotation-free lens, it was decided to construct an experimental electron microscope making full use of the advantages of the new lenses. It consisted of a miniature objective lens and two rotation-free projector doublets. A new type of objective lens was designed in which only one polepiece was used instead of the conventional double-polepieces. Each of the projector doublets consisted of two single-pole lenses mounted back to back and mounted outside the vacuum system. The electron-optical properties of the new lenses have been found to be quite different from those of conventional lenses and offer many advantages for electron microscopy. For example, rotation-free selected-area diffraction patterns have been obtained for the first time. In addition, a larger field of view than usual has been achieved, making operation of the microscope more convenient for the operator. The two projector doublets provide a wide range of distortion-free magnification and they are fairly insensitive to lens tilt. The results obtained during this investigation could also find an important application in the design of high voltage electron microscopes.

ACKNOWLEDGMENTS

I wish to express my thanks to my supervisor, Professor T. Mulvey, for suggesting the project, for valuable help, encouragement and stimulating discussions at all stages of the work. I would also like to thank the Head of the Department of Physics, Professor S.E. Hunt, for his permission to use the EM6 electron microscope and other facilities in the Department.

I am also grateful to Mr. F.Z. Marai for his permission to use his computer programs on the properties of the magnetic lenses and his useful discussions on the exponential field model, and to Mr. W. James for his helpful comments on various aspects of the project.

I am indebted to all the technical staff in the University who have kindly given me all the help I needed at various stages during the project. I am particularly grateful to Mr. R. Keen, of the Physics Department, for the valuable assistance in maintaining the experimental microscope in operation, winding coils and photography; to Mr. F. Lane and his colleagues in the Physics Workshop for constructing the components of the new imaging system; to Mr. J. Lloyd and Mr. K. Bate, who were working during the early stages of the project, on a research contract supported by the National Physical Laboratory, for the construction of the early experimental lenses which were later made available to me; to Mr. R. Howes and Mr. R. Banks of the University Communications Media Unit, for photographing the equipment.

S.M.J.

Birmingham

LIST OF SYMBOLS

A	Cross-sectional area of the conductor.
a	Wire diameter of a coil. Half-width of the magnetic field.
B	Magnetic flux density.
B_z	Magnetic flux density along the z axis.
B_m	Maximum axial flux density of a magnetic lens.
B_p	Magnetic flux density in the parallel part of the air gap.
b	Thickness of insulating material.
C_c	Chromatic aberration coefficient.
C_d	Radial distortion coefficient.
C_s	Spherical aberration coefficient.
C_{sp}	Spiral distortion coefficient.
C_Θ	Coefficient of chromatic aberration due to rotation.
D	Diameter of the bore of a magnetic lens.
D_1	Inner diameter of the lens coil.
D_2	Outer diameter of the lens coil.
D_m	Mean diameter of the lens coil.
D_h	Hydraulic diameter of the lens cooling passage.
d	Density of the cooling fluid.
e	Charge of electron (1.60219×10^{-19}C).
f_o	Objective focal length.
f_p	Projector focal length of a single lens.
F_p	Projector focal length of a double lens.
H	Power per unit volume in a coil
h	Heat-transfer coefficient (watts/cm^2.$^\circ$C).
I	Current in a lens coil (amperes).
k	Coefficient of thermal conductivity.

k_c Coefficient of thermal conductivity of the whole lens coil.

k_{in} Coefficient of thermal conductivity of the insulating material of the coil winding.

L Width of the rectangular field distribution. Projection distance. Camera length.

M Magnification.

m Magnification of a lens.

m_o Rest mass of electron (9.1×10^{-28} gram).

n Number of wire-layers along the width of the coil.

N Total number of turns in a coil.

NI Total number of ampere-turns (A-t) in a coil.

NI_o Ampere-turns of the coil at minimum f_p.

Nu Nusselt's number.

P Input power to a coil (watts).

q Power per unit area (watts/cm^2).

Q Rate of flow of the cooling fluid.

R Resistance.

r Radial displacement of the electron beam from the optical axis, z.

R_e Reynold's number.

S Width of the polepiece gap of a lens.

T Temperature (^oC).

T_{av} Average temperature.

T_c Maximum temperature at the centre-line of the coil.

T_s Temperature of the flat water-cooled surface of the coil.

T_w Temperature of the cooling water.

t Thickness of the water channel above the flat surface of the coil.

u Object distance.

v Image distance. Velocity.

V Voltage across a resistor. Accelerating voltage of electrons.

V_r Relativistically corrected accelerating voltage,

$$V_r = V(1 + 0.978 \times 10^{-6}V).$$

w Width of the coil.

z Coordinate of axis of rotational symmetry.

z_o Position of specimen in the field of the objective lens.

β Temperature coefficient of a winding.

ρ_T Resistivity of the coil at T^oC.

σ Current density.

γ Coefficient of viscosity of the cooling fluid.

λ Packing factor of the coil. Electron wavelength.

μ_o Permeability in vacuum ($4\pi \times 10^{-7}$ H/m).

θ Angle of rotation.

ε Angle of tilt of the lens.

SI units are used throughout except where otherwise stated.

CONTENTS

1. INTRODUCTION

Certain electron-optical features and elements are common to all types of electron microscopes, and to many other related instruments such as electron-probe microanalysers and electron-diffraction cameras. One such element is the electron lens. Both the initial conception and the first practical demonstration that a magnetic field can focus an electron beam originated with Busch who published the first paper on this subject in 1926. In modern electron-optical instruments, the electron lenses are magnetic. Magnetic lenses are chiefly used in two ways, to form focused electron beams or "probes", namely a demagnified image of a distant electron source, or to form a highly magnified image of a small object placed near the focal point of the lens. One of the most important electron-optical instruments using magnetic lenses is the transmission electron microscope (TEM).

1.1. Construction of the electron microscope.

A typical transmission electron microscope may be regarded as a close analogy of the optical-projection microscope. It consists mainly of the illuminating system and the imaging system. The illuminating system consists of the electron source and condenser lenses. The electron source, usually a heated tungsten hairpin filament, typically of 125 μm in diameter, emits electrons which are then accelerated through a potential difference, normally of 100 kV. One, two or sometimes three condenser lenses focus the electron beam onto the specimen as shown schematically in Figure 1.1.1. In a double condenser system, the first lens has high refractive power and forms a highly demagnified image of the source; this is then projected onto the specimen plane by the second condenser. The

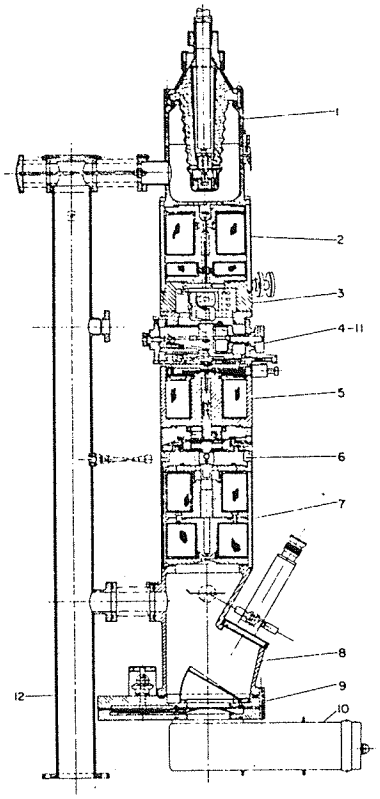

Cross-section through E.M.6 microscope.

1 – 100 kV electron gun
2 – two stage condenser lens system
3 – beam deflector stage
4 – specimen chamber
5 – objective lens
6 – intermediate alignment stage
7 – two-stage projector lens system
8 – viewing chamber and screen
9 – vacuum valve to seal-off the column from the camera
10 – plate camera
11 – specimen manipulator
12 – high vacuum manifold

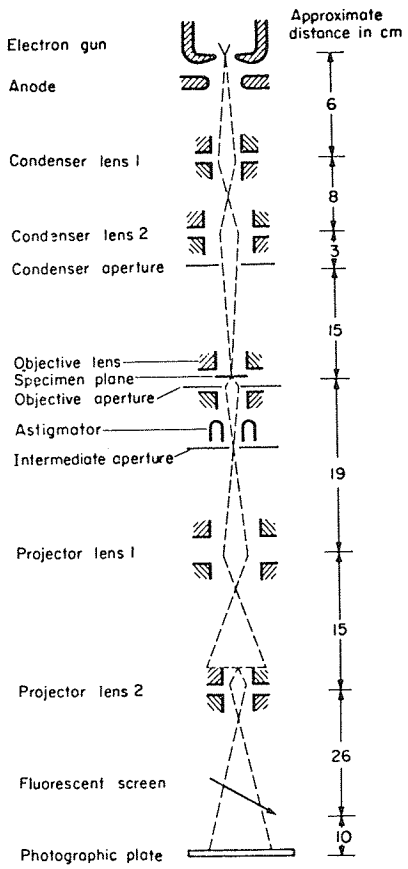

Schematic arrangement of E.M.6 column

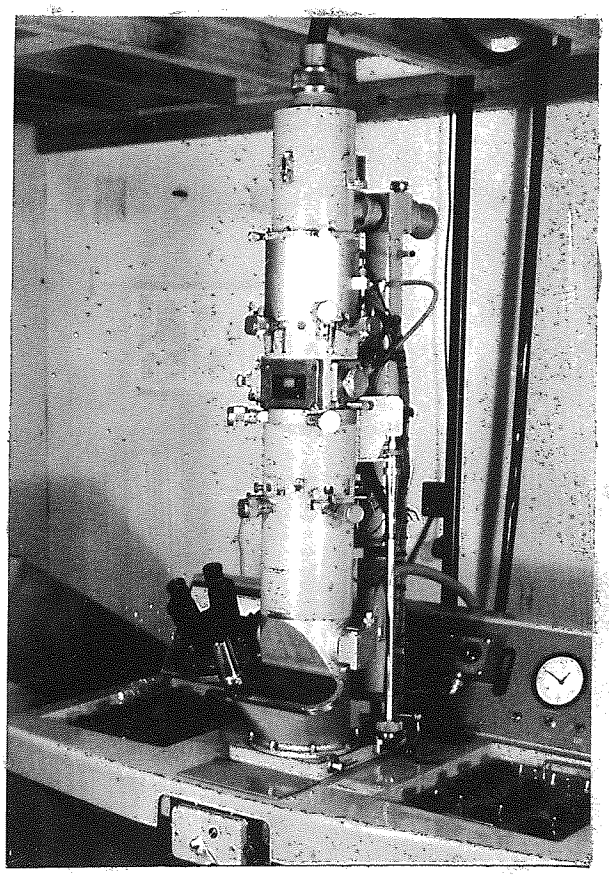

Fig. 1.1.1 The AEI EM6 100kV transmission electron microscope.

specimen is mounted on a copper grid about 3mm in diameter. The specimen is introduced into the column through an airlock in the specimen stage.

The lenses below the specimen constitute the imaging system. There are usually three of these, known as objective, intermediate (projector 1) and projector (P2) lenses respectively. The old instruments usually omitted the intermediate lens, while the new commercial instruments have an additional intermediate lens which gives greater range of magnification especially of electron diffraction patterns. The objective lens produces a focused image of the specimen some distance below the lens where the intermediate aperture (Figure 1.1.1) is situated for selecting a specific area of the specimen. The projector lenses produce the magnified image of the specimen on a fluorescent screen or a photographic plate.

Of the lenses, the objective is by far the most important, as on its perfection and state of cleanliness depends the resolving power of the whole instrument. The other lenses merely serve to magnify the image produced by the objective lens. In general, imperfections in the intermediate and projector lenses do not affect instrumental performance, but may impose restrictions on the field of view over which an acceptable resolution may be obtained.

The microscope shown in Figure 1.1.1. is a typical 100 kV transmission electron microscope. In the work described in the next Chapters, this microscope was used for testing out the new type of magnetic lenses that have been developed. The test was carried out by replacing the original magnetic lenses by the new ones without essentially altering the normal operation of the microscope.

1.2. The magnetic electron lens

The function of a magnetic lens is based upon an important physical principle. A current-carrying winding, symmetrical about the axis Z^1Z (Figure 1.2.1a), creates a field of magnetic induction, B_z. The effect of this field on a beam of charged particles (e.g. electrons) is comparable to that of a centred system on a beam of light rays; the induction field created by the coil constitutes a magnetic lens. In order to obtain a more intensive or better localized field, the coil may be surrounded by a magnetic circuit of ferromagnetic material (Appendix 1), Figure 1.2.1b. This is an electromagnetic lens and it is usually referred to as a magnetic lens.

The magnetic lenses whose field is created by an energised coil are divided into two categories. These are (a) the well known conventional or double-polepiece lens and (b) the recently developed snorkel or single-polepiece lens. A brief review of the properties of these two lenses is given below.

Double-pole magnetic lens

A typical design of a conventional round magnetic lens is shown in Figure 1.2.2. It consists of a large coil usually wound of insulated copper wire, carrying a stabilised current, a yoke and two parallel polepieces of axial symmetry made of soft magnetic material. The product NI of N turns and current I is known as the excitation. The magnetic field is localized in the vicinity of the air gap of width S between the two polepieces. The electrons travel through an axial hole bored in the central core and in the polepieces.

When the bores of the polepieces are of identical diameter D, the lens is considered a symmetrical magnetic lens characterised by its S/D ratio. Since the theory of the symmetrical lens has been used in the development of the new type of magnetic lenses (Chapter Three) the relevant electron-optical properties of this form of lens will be

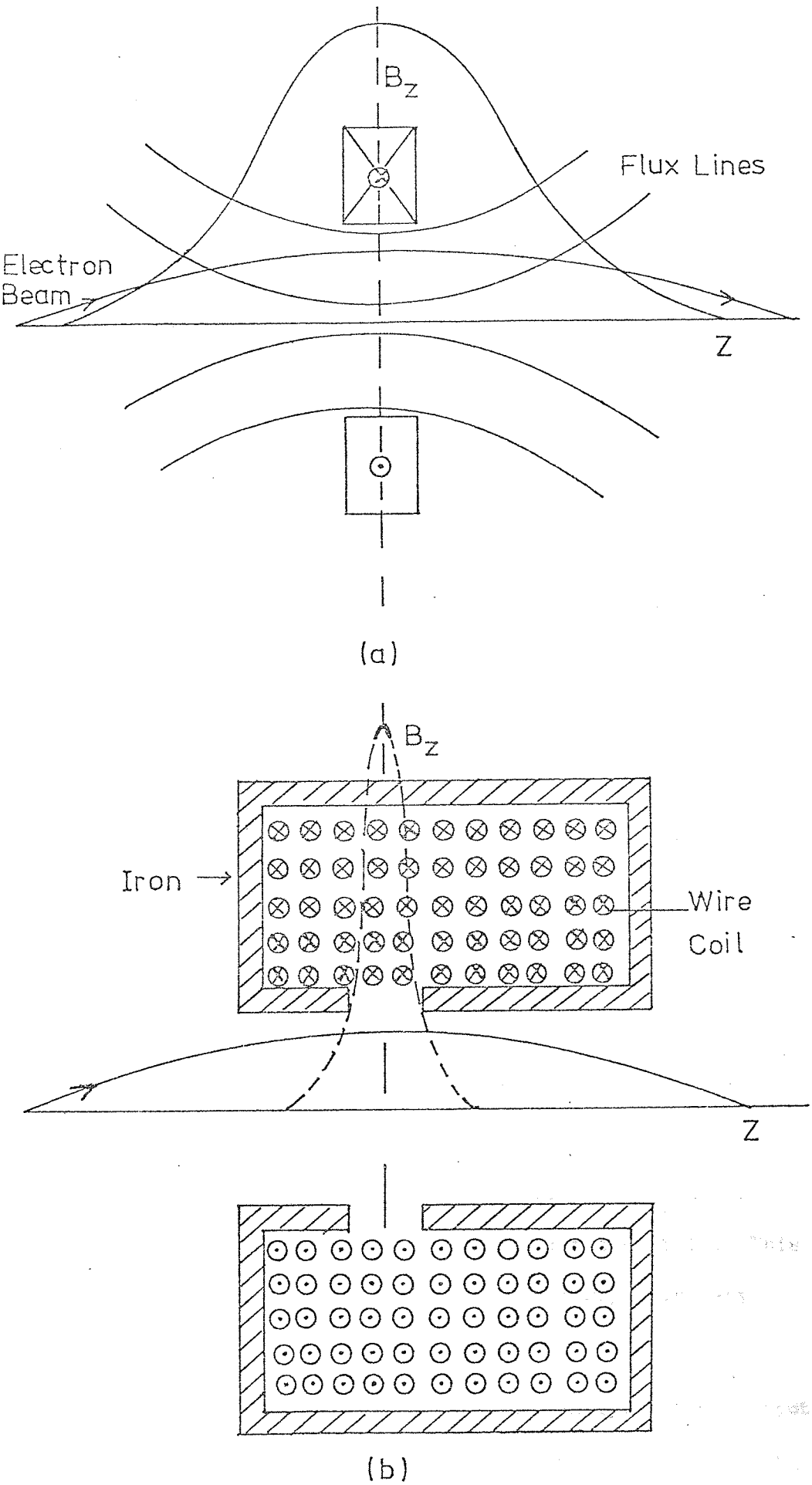

Fig. 1.2.1 The magnetic lens: (a) iron-free lens, (b) iron-shrouded lens.

considered in some detail. The double-pole magnetic lens becomes asymmetrical lens when the bore diameters D_1 and D_2, of the two polepieces are not equal; and it is then defined by its geometrical parameters, S, D_1 and D_2. The asymmetrical form of a magnetic lens is often used for electron microscope objective lenses (Liebmann, 1951) where the enlarged half of the lens accommodates the specimen holder (Yanaka and Watanabe, 1966). Some of the important properties of the asymmetrical double-pole lenses were discussed by Liebmann (1955 A, B).

Symmetrical double-pole magnetic lenses (Figure 1.2.2) have their maximum axial flux density B_m, at the centre of the air gap. In order to deduce the electron-optical properties of the lens, the axial field distribution B_z must be known. At the beginning of the development of electron optics, different mathematical "models" were proposed to represent the function B_z. The most frequently used models are:

(a) the Glaser bell-shaped field (Figure 1.2.3a) which is represented by the equation $B_z = B_m/[1 + (Z/a)^2]$ where 2a is the width of the field between the points at which B_z = Bm/2,

(b) the Grivet-Lenz field which is represented by the equation $B_z = B_m \mathrm{Sech}\ (Z/a)$, (Figure 1.2.3a).

(c) the rectangular field (Figure 1.2.3b) where B_z = Bm between abscissas $Z = \pm L/2$ which limit the field. This is approximately true for a lens whose gap S is very large compared with the bore D.

The rectangular field is simpler mathematically. It constitutes a convenient model and leads to expressions which represent surprisingly well the real properties of double-pole magnetic lenses (Fert and Durandeau, 1967). Thus the properties of any symmetrical magnetic

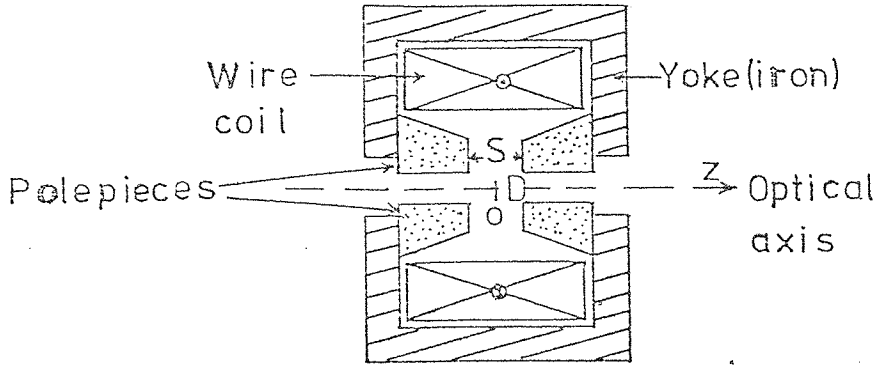

Fig. 1.2.2 Cross-section of a symmetrical double-pole magnetic lens.

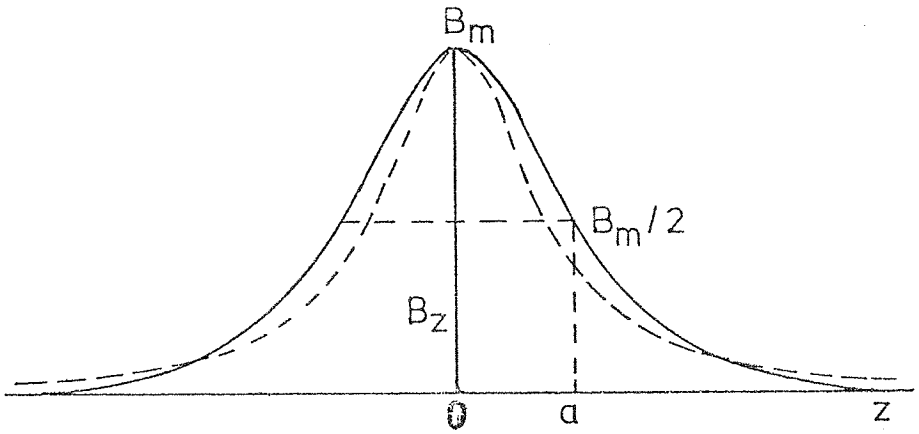

(a) Two analytical field distribution in magnetic lenses: the Glaser bell (broken line), and the Grivet-Lenz model (full line).

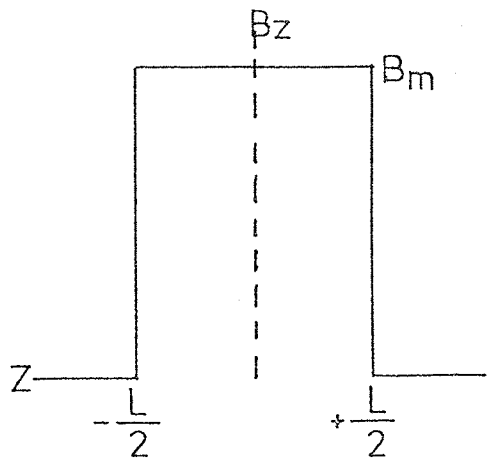

(b) The rectangular field distribution.

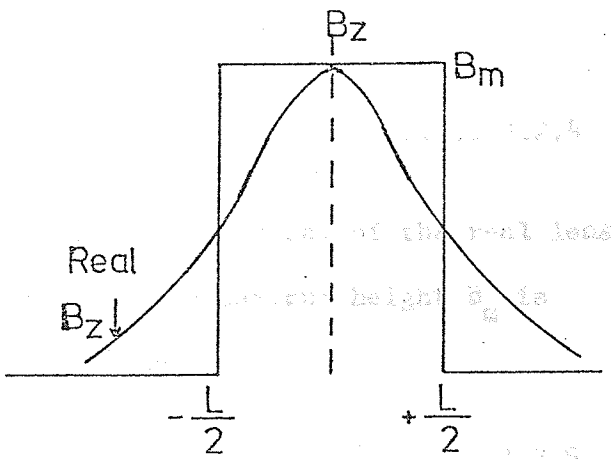

(c) The rectangular field distribution replacing the real field of the lens.

Fig. 1.2.3

lens can be determined once the real lens field is replaced by an ideal rectangular field of length L, (Figure 1.2.3C). Physically this ideal field is that of a solenoid of length S and diameter 2/3D, (Figure 1.2.4a), (Durandeau and Fert, 1957), carrying the same number of ampere-turns, NI, as the lens. Therefore, the diagonal, L, of the solenoid is related to the real lens geometry by

$$L = (S^2 + 0.45D^2)^{\frac{1}{2}} \qquad \ldots\ldots 1.2.1$$

This L is useful for lenses in which D is not small compared to S. For the same number of ampere-turns, NI, the area LB_m, under the rectangular field distribution of the equivalent solenoid is the same as that under the real distribution of the lens, hence,

$$L = \frac{1}{B_m} \int_{-\infty}^{+\infty} B_z \, dz \qquad \ldots\ldots 1.2.2$$

Using Ampere's theorem one may write:

$$\int_{-\infty}^{+\infty} B_z \, dz = \mu_o \, NI \qquad \ldots\ldots 1.2.3$$

where μ_o is the permeability in vacuum ($\mu_o = 4\pi \times 10^{-7}$ H/m). Therefore, from Equations 1.3.2 and 1.3.3,

$$B_m = \mu_o \, NI/L \qquad \ldots\ldots 1.2.4$$

where B_m is in Tesla and L in meters. The width 2a, of the real lens distribution where B_z has fallen to half the maximum height B_m is related to L (Fert and Durandeau, 1967) by

$$2a = 0.97 \, L \qquad \ldots\ldots 1.2.5$$

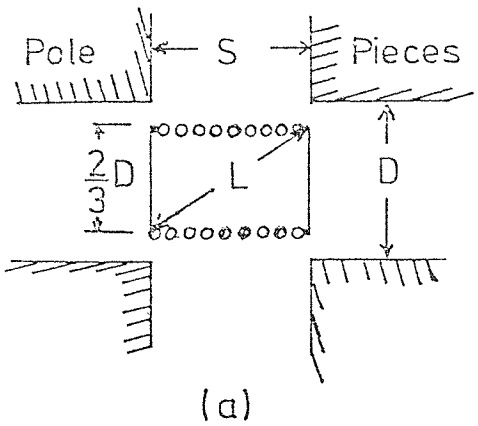

Double-pole lens of bore D and gap S and 'equivalent solenoid' of diameter 2D/3 and length S giving approximately the same field distribution.

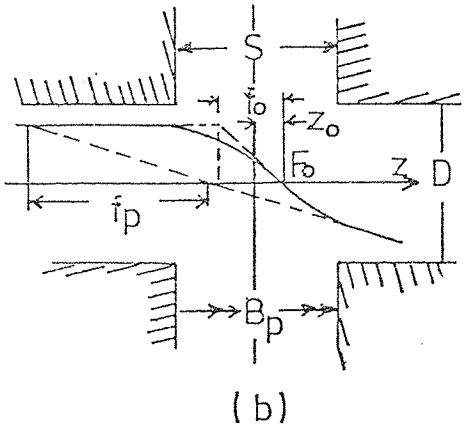

Electron trajectory and definitions of the optical constants of an iron polepiece lens.

Fig. 1.2.4

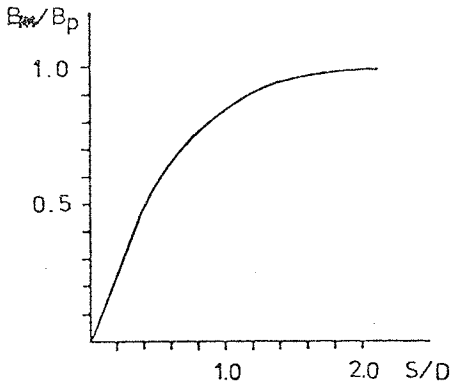

Fig. 1.2.5 Ratio B_m/B_p of maximum axial field strength B_m to field strength B_p in air gap.

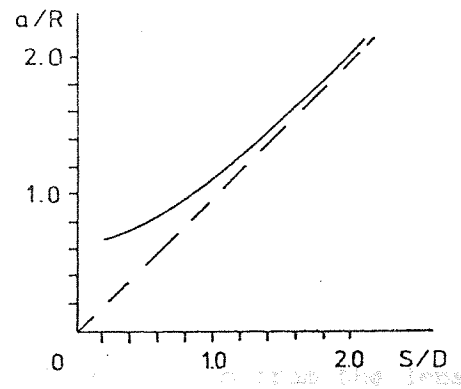

Fig. 1.2.6 Relative 'half width' a/R as function of gap width S/D.

In the gap S between the polepieces at a great distance from the lens axis, the magnetic field Bp is parallel. In the absence of saturation of the magnetic material, Bp is given by

$$Bp = \mu_o NI/S \qquad \ldots\ldots 1.2.6$$

where Bp is in Tesla and S in metres. Liebmann and Grad (1951) calculated the ratio B_m/B_p for different lens geometries, (Figure 1.2.5), which shows that as $S/D \geqslant 3$ the ratio Bm/Bp approaches unity. This is clear from Equations 1.2.4 and 1.2.6 where Bm/Bp = S/L. The ratio of the field half width, a, to the lens bore radius R, given by Liebmann and Grad (1951), as a function of S/D ratio is shown in Figure 1.2.6. It shows that for values of $S/D \geqslant 3$, a/R approaches S/D asymptotically; i.e. 2a = S. This is also clear from Equation 1.2.5. Figures 1.2.5 and 1.2.6 will be used in Chapter Seven to check the accuracy of the measured field distribution of the double-pole objective lens.

The focal properties of a magnetic lens are defined in Figure 1.2.4b. These focal properties can be determined for any lens whose field distribution is known by solving the paraxial ray equation:

$$\frac{d^2r}{dZ^2} + \frac{e}{8m_o V_r} B_z^2 \cdot r = o \qquad \ldots\ldots 1.2.7$$

where r is the radial displacement of the electron beam from the lens axis. A first approximation to the focal properties can be obtained if B_z in Equation 1.2.7 is substituted by the rectangular field distribution given in Equation 1.2.4. However, Durandeau and Fert (1957) have shown that the minimum projector focal length of all symmetrical double-pole magnetic lenses is given by

$$(fp)_{min} = 0.5\,(S^2 + 0.45D^2)^{\frac{1}{2}} \qquad \ldots\ldots 1.2.8$$

this occurs, in general, at an excitation parameter, $NI_o/V_r^{\frac{1}{2}} \simeq 13.5$, where NI_o is the number of ampere-turns required to reach the minimum projector focal length. Thus Figure 1.2.7 represents in a single curve the relative projector focal length of all symmetrical double-pole magnetic lenses; this is extremely useful in estimating f_p for any lens up to $NI = 1.3NI_o$, (Fert and Durandeau, 1967). These universal curves were used throughout the work in studying the projective properties of the newly developed lenses. The rectangular field distribution, is used in Chapter Three for determining the focal properties of a doublet projector lens by solving the paraxial ray equation, (1.2.7).

The apparent simplicity in representing magnetic lenses in universal curves has sometimes been obtained at the price of obscuring some important physical limitations in actual lenses (Mulvey, 1967). For example, the flux density Bp in the parallel part of the air gap is a primary design parameter since the saturation properties of the iron polepieces set a limit to the possible combinations of lens geometry and excitation. The flux density limitation determined the absolute minimum focal length that can be obtained in practice. Mulvey and Wallington (1969) have shown that the absolute minimum focal length $(fp)_{min\ (abs)}$ is quite different from the relative minimum focal length $(fp/L)_{min}$ and occurs at a much lower excitation. They have shown that over a range from $o < S/D < 2$ the choice of a parameter $L = (S^2 + 0.56D^2)^{\frac{1}{2}}$ leads to a simple expression for the absolute minimum projector focal length of any lens, namely

$$(fp)_{min\ (abs)} = 0.55L \qquad \ldots\ldots 1.2.9$$

occurring at an excitation $NI_A/V_r^{\frac{1}{2}} \simeq 10$ where NI_A denotes the ampere-

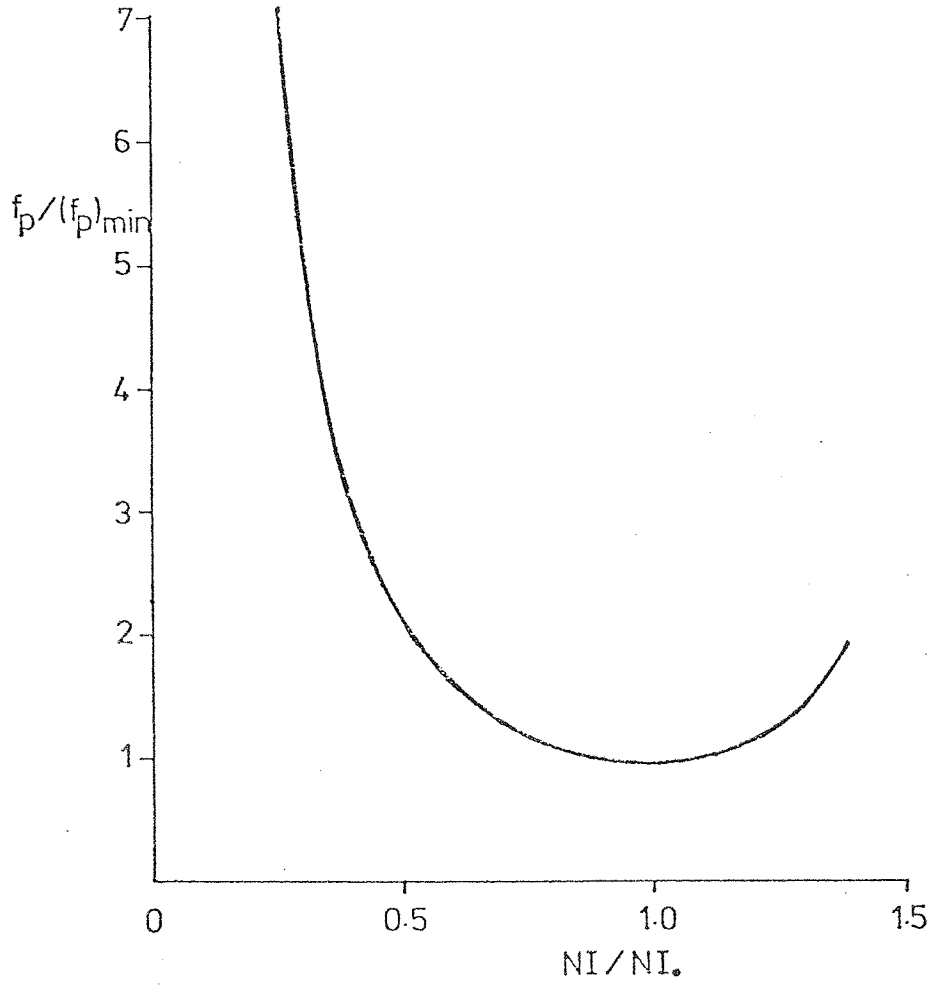

Fig. 1.2.7 Universal curve for all double-pole symmetrical magnetic lenses. The projector focal length is normalized with respect to the minimum projector focal length as a function of excitation normalized in term of the excitation for minimum projector focal length.

turns for absolute minimum projector focal length. The absolute projector focal length falls rapidly as the ratio S/D is increased from 0.2 to 1 then levelling off so that very little gained by making S/D greater than 2.

The single-pole magnetic lens

In the double-pole magnetic lenses, it is necessary to distort the parallel field between the two polepieces by means of the bore in order to produce a lens action. In the single-pole lens, which have been recently suggested by Mulvey, the second polepiece has been dispensed with. Figure 1.2.8 shows the basic features of a single-pole (snorkel) lens whose magnetic field is created by energising a "pancake" type coil. Calculations of Bassett and Mulvey (1969) indicated that the axial field distribution produced by a flat thin helical coil (pancake) with a large ratio outer to inner diameter can have an appreciably lower spherical aberration than that of a double-polepiece lens. The absence of a second polepiece has caused the axial field distribution to be displaced from the coil (Figure 1.2.8a), and may even be located entirely outside the lens structure (Figure 1.2.8b). The iron cylinder which is introduced into the centre of the coil, takes the form of a conical iron snout which protrudes from the main lens structure. If a small hole is bored along the axis of the snout (Figure 1.2.8c) the lens may be used as an objective in the transmission electron microscope (TEM) and scanning transmission electron microscope (STEM), (Mulvey, 1974). A full account of the development of the single-pole lens has been given by Mulvey and Newman (1973).

The advantages of the single-pole magnetic lenses arise from their essentially different axial flux density distribution from those of normal double-polepiece lenses. For this reason their electron-optical properties cannot be predicted from the data of conventional

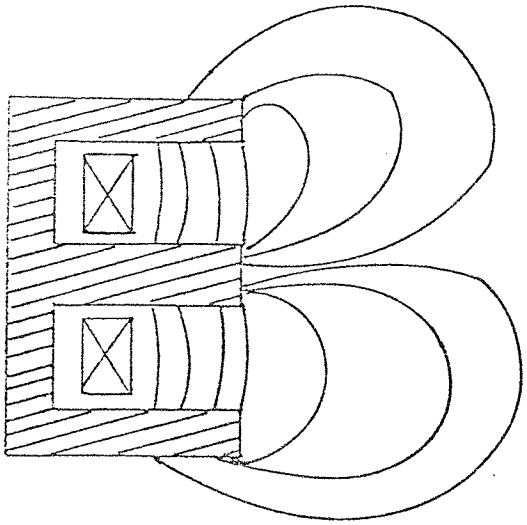

(a)

Magnetic field of a (snorkel) single-pole lens.

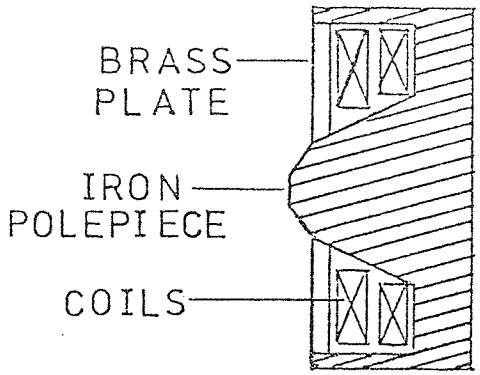

(b)

Snorkel lens for SEM.

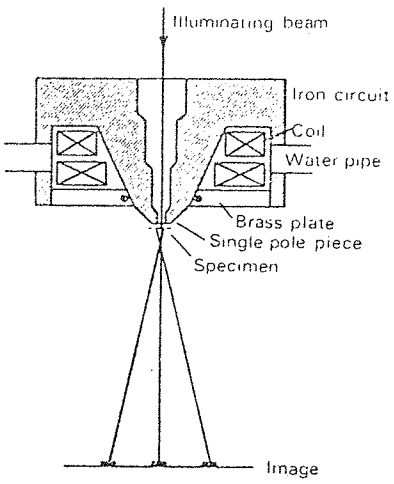

(c)

Snorkel lens for STEM and TEM (Mulvey, 1974).

Fig. 1.2.8 The single-pole lens.

lenses. The fact that the axial field distribution seems to be approximately exponential in shape led to the application of the Glaser's exponential field model to the "half-field" of the single-pole lenses (Marai, 1973). The field distribution B_z, of these lenses along the optical axis, Z can thus be expressed as

$$B_z = Bm \exp - \left[(\ln 2)/a\right] Z \qquad \ldots\ldots 1.2.10$$

where a is the axial distance from the position of the maximum field B_m to where the field has fallen to Bm/2, Figure 1.2.9.

The single-pole lens with no bore is well represented by the exponential field. The presence of the bore will change the lens field distribution slightly; in general there will be a peak few millimetres away from the poleface surface. The field distribution measured from this peak and further away from the lens structure undergoes a gentle decrease and is nearly exponential with a long tail while that from the peak towards the snout undergoes a sudden steep drop.

Using the exponential "half-field", a good approximation of the focal properties of the single-pole lenses has been determined, (Marai and Mulvey, 1974, 1975). Figure 1.3.10 shows the objective focal length f_o, the projector focal length f_p, the objective focal distance Z_o, the chromatic aberration coefficient C_c and spherical aberration coefficient C_s, all normalised in terms of a, as a function of the excitation parameter $NI/V_r^{\frac{1}{2}}$ where NI is the number of ampere-turns and V_r the relativistically corrected accelerating voltage. In the first loop, the minimum projector focal length, $(fp)_{min}$ equals 1.16a and occurs at $NI/V_r^{\frac{1}{2}} = 13$. The minimum objective and projector focal lengths are the same and occur at $Z_o = 0$, $(NI/V_r^{\frac{1}{2}} = 13)$ corresponding the specimen position at the surface of the snout. For greater excitation than this, the objective focal length is constant as is the chromatic and spherical aberrations which have remarkably low

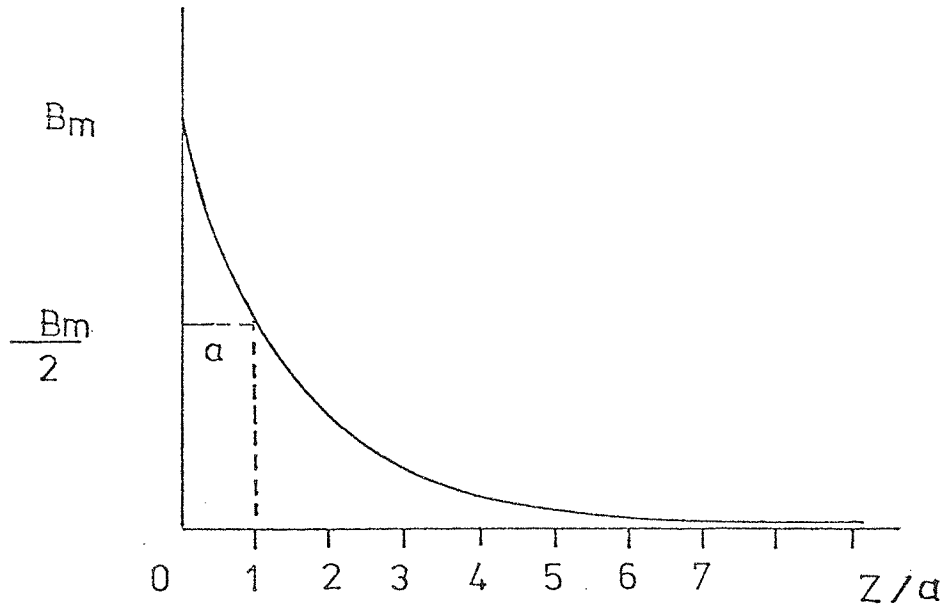

Fig. 1.2.9 The exponential field distribution.

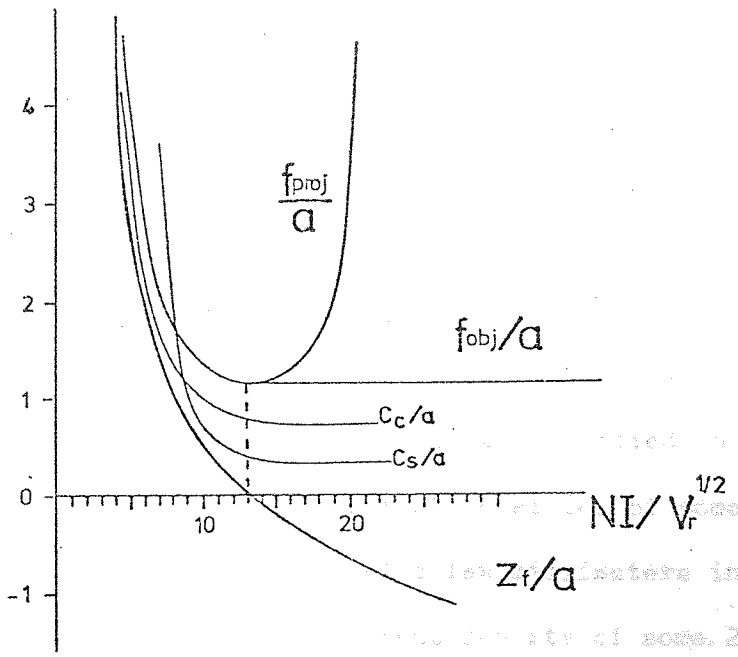

Fig. 1.2.10 Focal properties of the exponential field distribution.

values; C_c (= 0.72a) and C_s (= 0.36a). Other important properties of single-pole lenses will be discussed in Chapter Five.

The important advantages of single-pole lenses have led to their application as objective and projector lenses in a scanning electron microscope (Mulvey and Newman, 1973) and in a transmission electron microscope (Juma and Mulvey, 1975). Single-pole lenses have been used in this work in building an entirely new imaging system for a 100 kV transmission electron microscope.

1.3 Miniature magnetic lenses

A modern 100 kV transmission electron microscope, which contains several lenses is a rather large and heavy piece of equipment. The bulky size of the lenses causes the alignment problems due to any imperfections in the magnetic circuit and other difficulties due to the height of the electron-optical column. Problems are also encountered in probe-forming instruments in the location of detectors for electrons and X-rays.

The main problem in making smaller lenses, is that of removing the heat produced to prevent the coil overheating. The first attempt at producing water-cooled, mini-lenses, which were in the form of an iron-free solenoid on a small-diameter conical former, was made by Le Poole (1964) and have since been successfully applied in electron probe instruments. In such lenses current densities of some 8000 amp/cm^2 have been achieved in lenses of a few millimeters in diamter; while ordinary lenses operate at a current density of some 200 amp/cm^2 (Haine, 1961) and the mean diameter varies from some 8 cm for a 100 kV instrument to 50 cm for a high voltage instrument. The idea has been further developed by Mulvey (1971; Mulvey and Newman, 1972, 1973 A and B) in miniaturising electron magnetic lenses of double-pole and single-pole designs used successfully in 100 kV and high voltage

electron microscopes. These considerable benefits are obtained largely at the cost of increased power input to the lens windings; typically 250 watts compared with about 50 watts in an ordinary lens. Typically, a four-fold increase in total power might well be expected for a fifty-fold reduction in lens volume (Mulvey and Newman, 1973). However, with the advent of stabilised current supplies using solid-state devices, the supplying of high power to a small coil is not such a problem as it would have been ten years ago.

In Chapter Two some work on the miniaturisation of coil windings is described. It was mainly concerned with coil design and heat-transfer. The design of miniature coils needed better understanding because in the present investigation new types of miniature magnetic lenses were needed for a new experimental electron microscope. Recently, for instance, Herrmann et al (1974), published some work on miniaturised coils for electron lenses but it suffered from theoretical and experimental inaccuracies. However, it will be shown in Chapter Two that in a good coil design, current densities comparable with that obtained in super-conductors can be obtained in a copper wire coil, water-cooled at a moderate water flow rate.

1.4 Image rotation and its elimination

A feature which distinguishes magnetic lenses from all other lenses is the rotation of the image plane with respect to the object plane. As is generally known, the angle θ (in radians) through which an electron trajectory is rotated in its passage through a lens field is given by

$$\theta = \left(\frac{e}{8m_o V_r}\right)^{\frac{1}{2}} \int_{-\infty}^{+\infty} B_z \, dz \qquad \ldots\ldots 1.4.1$$

where e/m_o is the charge-to-mass ratio of the electron. Since the integral $\int B_z d_z = \mu_o NI$, it follows that the angle of rotation, θ, is proportional to $NI/V_r^{\frac{1}{2}}$ irrespective of lens geometry, i.e.

$$\theta = \mu_o \left(\frac{e}{8m_o}\right)^{\frac{1}{2}} \frac{NI}{V_r^{\frac{1}{2}}}$$

or $$\theta = 0.1863 \frac{NI}{V_r^{\frac{1}{2}}} \text{ radians} \qquad \ldots\ldots 1.4.2$$

The rotation of the image with respect to the plane of the object is undesirable in electron microscopy. Firstly, it makes it difficult to relate an image detail to its counterpart in the object. This is particularly the case when a diffraction pattern from a crystal is superimposed on its image. Secondly, aberrations associated with this rotation are added to the normal lens aberrations of light optics (Section 1.5).

In principle image rotation can be eliminated by using two or more magnetic lenses designed to have zero overall rotation; the so-called "rotation-free" lens. There is very little published literature on both experimental and theoretical aspects of "rotation-free" magnetic electron lenses. The first attempt to eliminate image rotation was that of Stabenow in 1935. His investigations were based on energising two lenses of different number of turns so that the ampere-turns in both were equal and opposite. Because of field interaction, he used a trial and error method to obtain a zero rotation thereby obtaining an inverted image as in the case of a glass lens in light optics or the analogous electrostatic lens. Stabenow's work, which was limited to very weak excitations and long focal lengths, did not lead to a practical rotation-free lens, but he envisaged that such a lens might be possible.

Later, Becker and Wallraff (1940), investigated the aberrations of a rotation-free magnetic lens which consisted of two iron-free coils. They reported that the spherical aberration of the rotation-free lens was appreciably greater than that for a single lens of the same focal length and they were difficult, if not impossible, to align. On this basis, Becker and Wallraff were pessimistic about the practical feasibility of such lenses.

The simplest form of rotation-free lenses are double lenses. However, double lenses sometimes referred to as "doublets" are not necessarily rotation-free. The two single lenses of the doublet can be energised by one coil or two separately excited coils. Doublets energised by two separate coils can have their coils coupled in cooperation, where the currents pass in the same direction in both coils, or in opposition, where the direction of the current in one coil is opposite to that of the other coil. Double lenses operated in a rotation-free mode, where the two coils are coupled in opposition such that $(NI)_1 = -(NI)_2$, are the most important type of doublets.

The first to report the use of doublets in a microscope was Ruska (1934). His lens consisted to two air gaps excited by two separate coils, separated by a brass plate. In this construction, the two coils were connected in a cooperative mode of operation, energised by one current supply. This lens could be used as a strong objective or as a condenser lens. In his paper, Ruska did not mention the possibility of use of this lens in a rotation-free mode. Indeed, with the brass plate separating the two coils, it certainly could not have been used as a rotation-free lens due to the interaction of the two fields, but with slight modification it could have been converted to a rotation-free doublet. A double projector was first used by Prebus (1942). This doublet and the objective lens constituted the imaging system of the microscope used by Prebus. The doublet was used for the

purpose of increasing the magnification of the microscope. However, no information was published on the properties of this doublet or its mode of operation.

It is desirable in electron microscopy to be able to reduce the magnification to a value comparable with that of the optical microscope in order to obtain a larger field of view. At low magnification, serious distortion and loss of field of view was quite usual. In his investigation on distortion corrections, Hillier (1946) showed that if an auxiliary lens is placed at the focal point of the final projector lens of an electron microscope, image distortion could be eliminated. Thus, he was the first to design a projector doublet consisting of two double-pole gaps in one unit, excited by one coil; the ampere-turns in the gaps are thus in a permanently cooperative mode; this increases spiral distortion (Section 1.5). Hence, correction in this doublet was limited to radial distortion; moreover the correction was valid at one chosen magnification only. An improved result was obtained by the author (Juma, 1972) when a rotation-free lens was operated, at its first maximum magnification, at weak excitation where an image corrected for both radial and spiral distortions was projected.

Theoretical investigations related to double-pole rotation-free lenses have also been reported. Kanaya (1958), Kanaya and Ishikawa (1958), have suggested the use of a rotation-free projector lens in order to eliminate the astigmatism caused by the misalignment of the electron lens elements. They referred to this kind of lens structure as the "anastigmatic lens of three polepieces", but gave no information on the focal properties of such lenses. Later, Der-Schvarts and Rachkov (1965), suggested the use of rotation-free lenses in eliminating the chromatic aberration of rotation (Section 1.5). However, their calculations on the variation of the focal length with the excitation parameter $NI/V_r^{\frac{1}{2}}$ included a number of variable geometrical parameters.

Each specific lens geometry was represented by a separate curve rather than representing all lenses by a "universal" curve (Juma, 1972). The importance of rotation-free lenses in eliminating some of the aberrations that are common in single lenses is another advantage of such lenses.

1.5 Aberrations of magnetic lenses

The images produced by light and electron optical lenses are not perfect reproductions of the object but suffer defects or aberrations. The effect of each aberration is to distort the image of every point in the object in a particular way, leading to an overall loss of quality and resolution in the image.

Mechanically, all magnetic lenses suffer from astigmatic defects. This is due as much to inhomogeneities of the polepiece iron as to machining inaccuracies and to lack of symmetry in the coil winding itself. In a single-pole lens, for example, the surface of the snout should be extended beyond the surface of the flat coil to reduce the effect of asymmetries in the coil winding since the snout can be made more accurately than the winding.

The importance of a particular aberration depends on the function of the magnetic lens. For an objective lens, only the spherical and the chromatic aberrations are important since the electron-optical limit of resolution is set by the combined effects of electron wavelength and the spherical aberration. For intermediate and projector magnetic lenses, the radial (isotropic) and spiral (anisotropic) distortions are the most important; they cause a shift of the image point but no blurring.

Spherical aberration

The most important image defect in an objective lens is spherical aberration, which causes each object point to appear in the image as a

disc. This occurs because the power of the lens is greater for off-axis rays. The diameter, d_s, of the aberration disc in the Gaussian image plane is $2C_s\alpha^3$. Here α is the half-angle subtended at the object by the lens aperture, and C_s is known as the spherical aberration coefficient.

The variation of the spherical aberration coefficient, C_s, with the excitation parameter $NI/V_r^{\frac{1}{2}}$ for the new objective lenses described in Chapter Seven was determined from the axial field distribution data, making use of a program written by Marai (1974). In this program the coefficient C_s is calculated from the Scherzer's equation:

$$C_s = \left(\frac{e}{96\, m_o V_r}\right) \int_{Z_o}^{Z_i} \left(\frac{2e}{m_o V_r} B_z^4 + 5 B_z^{1^2} - B_z B_z''\right) h_z^4 \, dZ \qquad \ldots\ldots 1.5.1$$

where,

Z_o = the position of the object plane,

Z_i = the position of the image plane,

B_z^1 = the derivative of the flux density B_z with respect to Z, and h_z represents a paraxial electron trajectory that intersects the optical axis at $Z = Z_o$ with unit slope, i.e. $h(Z_o) = 0$, $h^1(Z_o) = 1$.

Chromatic aberration

These are of two types; one of which, defined by the coefficient C_c is particularly harmful for an objective while the other, defined by the coefficient C_M is primarily associated with the intermediate and projector lenses. Both aberrations produce blurring. These are a consequence of the fact that fluctuations in the lens focal length, due to a spread in electron energy and fluctuations in lens excitation, result in the superposition on the final screen of a number of images of different size with a consequent loss of image definition. With

present-day solid-state current supplies, the lens current can now be stabilised to one or two parts in 10^6 at which level the contribution of chromatic aberration by the power supplies is negligible. However, chromatic aberration arising from energy loss of electrons in the specimen remains a serious problem for all except the very thinnest specimens.

The chromatic aberration coefficients, C_c and C_M can be calculated from the field distribution of the lens. The coefficient of chromatic change in magnification C_M is given by

$$C_M = \frac{e}{8 m_o V_r} \int_{-\infty}^{+\infty} B_z^2 \, GH \, dz \qquad \ldots\ldots 1.5.2$$

where,

G = G(Z) which represents a ray incident from field-free space outside the projector lens at unit distance from the axis and parallel to it where at the image plane $G_i = M$, the magnification.

H = H(Z) which represents a ray incident from field free-space in such a way that it would intersect the axis at the object plane with unit slope; at the image plane dH_i/dZ is the angular magnification which equals 1/M. This coefficient has not been calculated for the newly developed projector lenses because it has a negligible value.

The coefficient of chromatic aberration, C_c is an important property for the design of magnetic objective lenses. The values of C_c as a function of the excitation parameter $NI/V_r^{\frac{1}{2}}$ have been computed for the newly developed objective lenses described in Chapter Seven. The computations were carried out by inserting the data of the lens field distribution into Marai's program (1974) which is based on

solving the equation

$$C_c = \frac{e}{8m_o V_r} \int_{Z_o}^{Z_i} B_z^2 h^2 \, dZ \qquad \ldots\ldots 1.5.3$$

The results are compared with the well known data on double-pole lenses as will be shown in Chapter Seven.

Radial distortion

Radial distortion of the image in a weak lens is a consequence of the spherical aberration of the lenses which causes marginal rays to encounter a focal length different from that for axial rays. The variation in focal length with distance from the lens axis causes a variation in magnification of the image with distance from the axis and the image is therefore distorted.

In the schematic ray diagram of Figure 1.5.1, consider a ray incident parallel to the optical axis, at a distance r from it, refracted by a magnetic projector lens whose bore radius is R. If $r/R \ll 1$, the ray will pass through the paraxial focus F_o and intersect the image screen at a distance ρ from the axis. For a larger off-axis distance, r, of the incident ray, it will pass through another focal point which is shifted from F_o, and intersect the screen at a distance $(\rho + \Delta\rho)$ from the axis. It has been shown (Liebmann, 1952) that the radial distortion, $(\Delta\rho/\rho)_{rad}$ is given by

$$\left(\frac{\Delta\rho}{\rho}\right)_{rad} = C_d \left(\frac{r}{R}\right)^2 \qquad \ldots\ldots 1.5.4$$

where C_d is the radial distortion coefficient. When C_d is positive the distortion is called "pin-cushion distortion". This is shown in Figure 1.5.2a. There, a broken line indicates the Gaussian image (distortion-free) of a square-pattern, the solid line shows the stretched, actual image. If, on the other hand, the outer parts of the image are on too

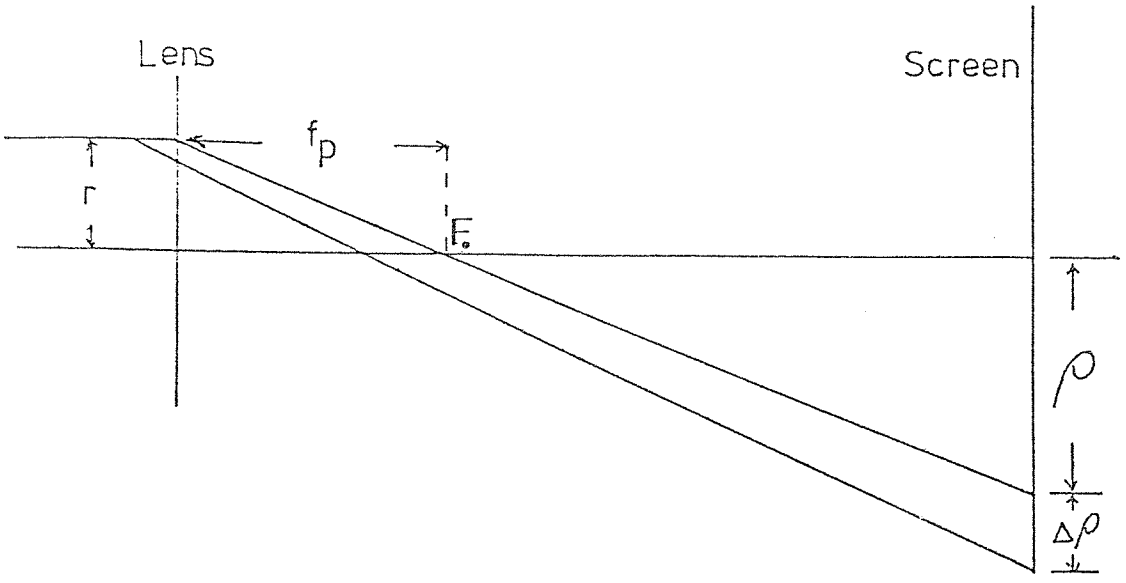

Fig. 1.5.1 Ray duagram illustrating the origin of the radial distortion $(\Delta\rho/\rho)_{rad}$.

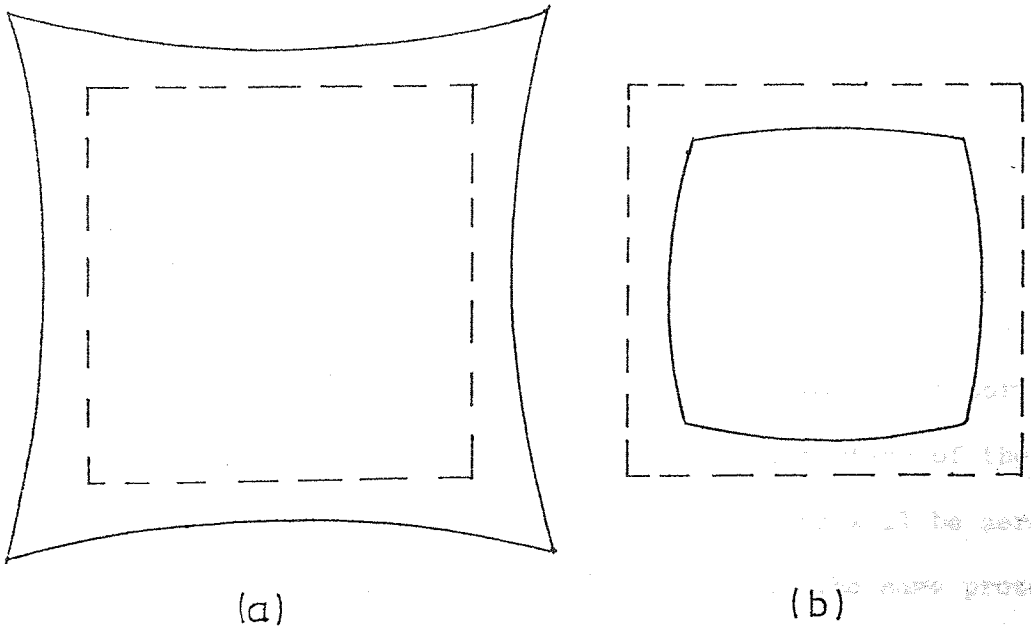

Fig. 1.5.2 Radial distortion: (a) pin-cushion, (b) barrel.

small a circle, the distortion coefficient C_d is negative and so called "barrel-distortion" will occur. This is illustrated by Figure 1.5.2b, the Gaussian image again being indicated by a broken line.

The radial distortion coefficient depends on the lens geometry and its excitation. For double-pole magnetic lenses, C_d has been calculated by Liebmann (1952) for different S/D ratio, which is shown in a modified form in Figure 1.5.3. These curves will be used later to compare them with the radial distortion coefficient of the single-pole lenses.

The data of the field distribution of the magnetic lens inserted in Marai's computer program (1975) to determine C_d as a function of $NI/V_r^{\frac{1}{2}}$. For any magnetic projector lens of bore radius R and focal length fp, the coefficient C_d is represented by the Scherzer's equation

$$C_d = \frac{3R^2}{8\,fp^2} + \frac{e\,R^2}{96\,m_o V_r} \int_{-\infty}^{+\infty} \left(\frac{2e}{m_o V_r} B_z^4 + 5 B_z'^2 - B_z B_z'' \right) G^3 H \, dz \quad \ldots\ldots 1.5.5$$

which is used by Marai in his computer program. The accuracy of the computer program was checked by comparing the results with those of Liebmann for double-pole lenses as will be shown in Chapter Seven.

It should be mentioned that in an electron microscope radial distortion is usually corrected by compensating the barrel distortion of the weak intermediate lens by the pin-cushion distortion of the strong projector lens; thus the net radial distortion will be zero (Haine and Page, 1956; Kynaston and Mulvey, 1963). The same procedure was used with the rotation-free intermediate and projector lenses, as shown in Chapter Eight, over a wide range of magnification.

Spiral distortion

The anisotropic distortion is often called rotational distortion or spiral distortion. In this case, the angle of rotation Θ, is no longer independent of the radial distance of the image point from the

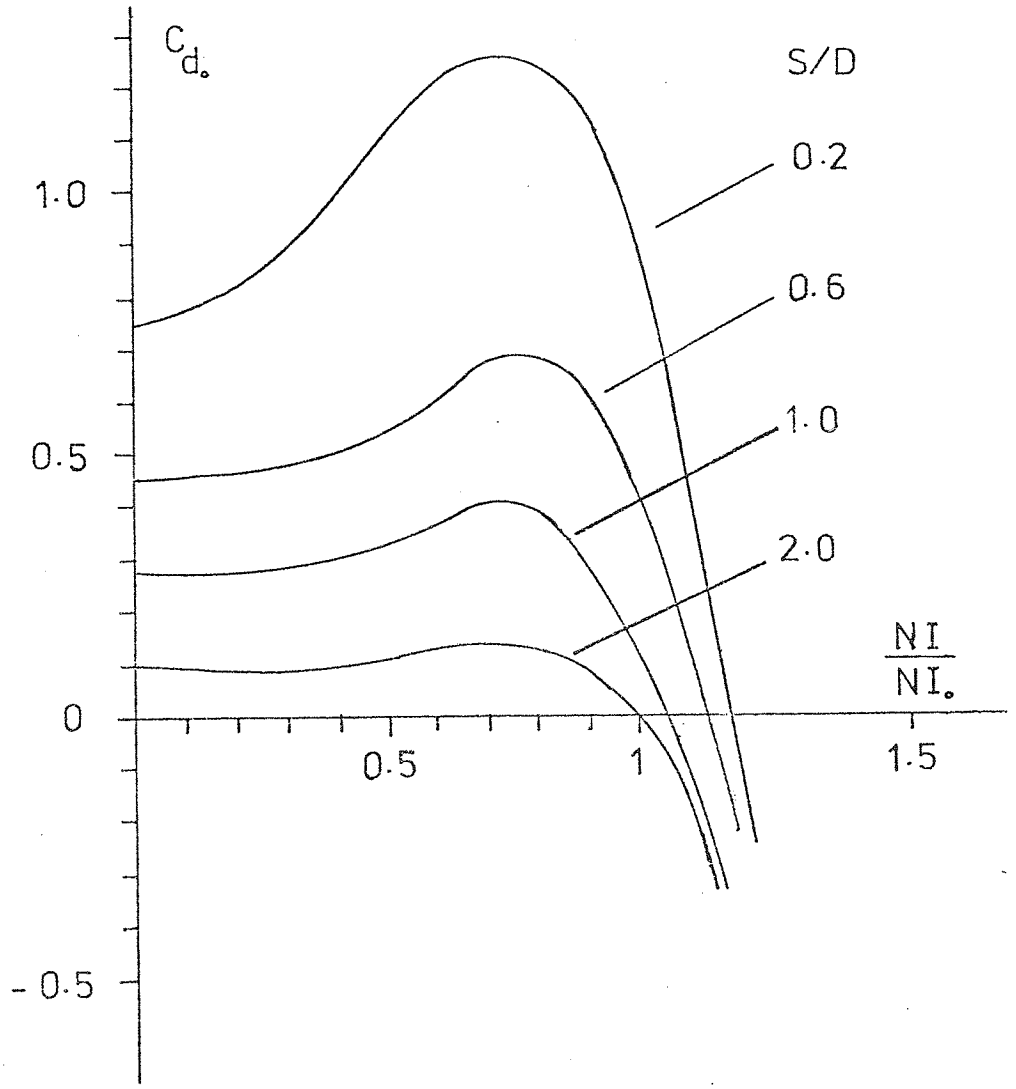

Fig. 1.5.3 Variation of the radial distortion coefficient of symmetrical double-polepiece lenses with excitation for different S/D ratios.

axis. It increases by a small amount for an off-axis ray, giving rise to spiral distortion, as shown in Figure 1.5.4. The broken lines represent Gaussian images while the solid lines show the distorted images; these are spiral shaped from which the name is derived. When the current through the lens is reversed, the direction of the field B and the sense of the circulation of the electron is changed. As a consequence the image of Figure 1.5.4a changes into the image of Figure 1.5.4b, the latter being the mirror image (a) by reflection in the axes.

Under the imaging conditions of the electron microscope projector lens, as shown in Figure 1.5.1, it has been shown by Liebmann (1952) that the spiral distortion $(\Delta\rho/\rho)_{sp}$ is given by

$$\left(\frac{\Delta\rho}{\rho}\right)_{sp} = C_{sp} \left(\frac{r}{R}\right)^2 \qquad \cdots\cdots 1.5.6$$

which is analogous to Equation 1.5.4. In Equation 1.5.6, C_{sp}, the spiral distortion coefficient, depends on the lens geometry and the excitation; $\Delta\rho$ represents the lateral displacement in the image plane shown in Figure 1.5.4. In his investigations on double-pole lenses, Liebmann (1952) found that the coefficient, C_{sp} of a microscope projector lens increases with increasing lens excitation (this is in contrast to C_d) but decreases with increasing S/D ratio. Spiral distortion will be more pronounced than the radial distortion if the lenses are operated near their minimum focal length; however for decreasing excitation spiral distortion will decrease rapidly compared with radial distortion. Radial distortion changes the shape and the area of an image element (Figure 1.5.2), whereas spiral distortion changes its shape only, leaving its superficial area constant, (Figure 1.5.4c).

The coefficient C_{sp} is given by Scherzer's formula:

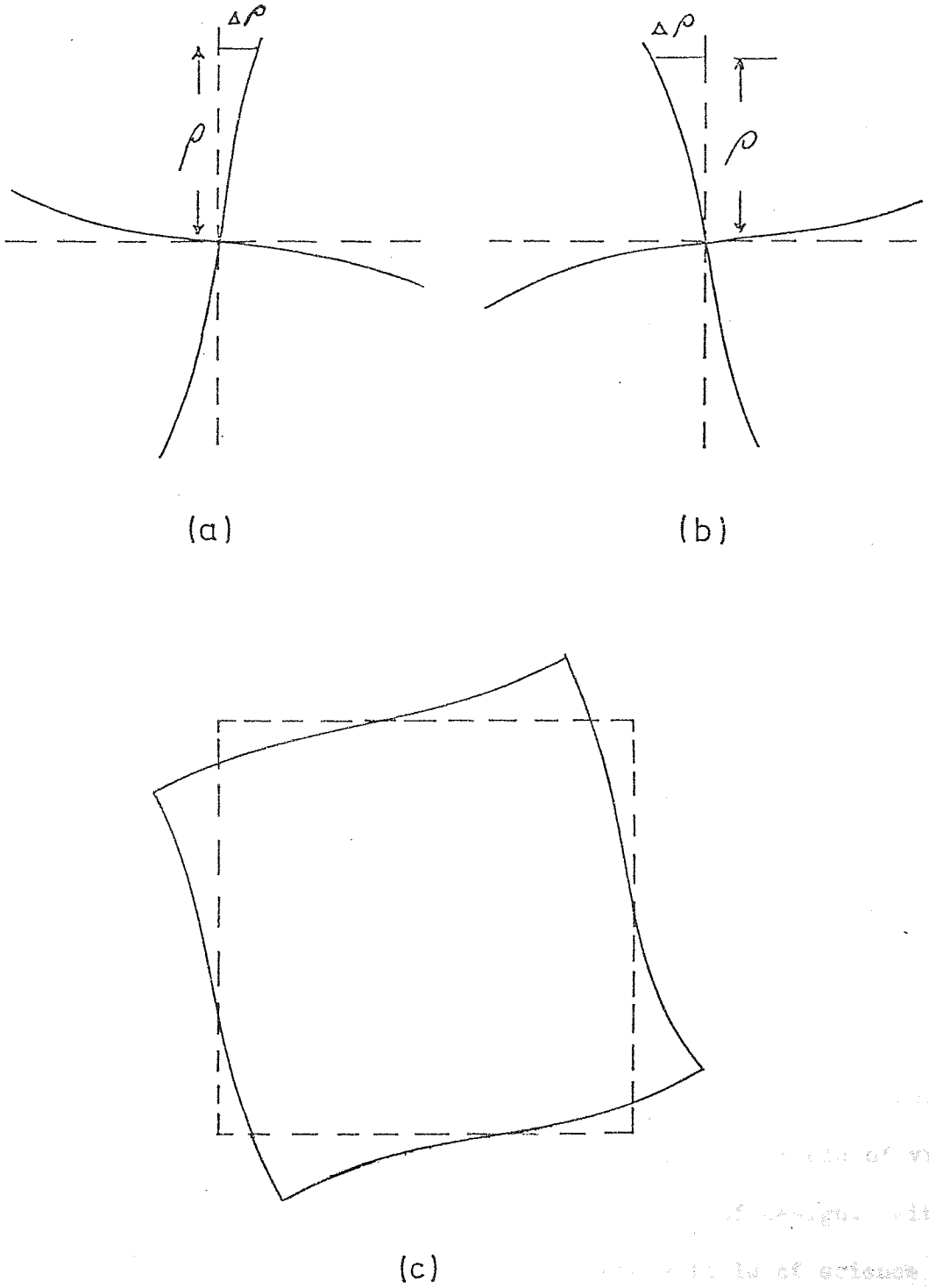

Fig. 1.5.4 Spiral distortion, $(\Delta\rho/\rho)_{sp}$.

$$C_{sp} = -\frac{M^3}{4R^2}\left(\frac{e}{m_o}\right)^2 \int_{-\infty}^{+\infty} \left(\frac{3eV_r}{8m_o}^{-3/2} B_z^3 G^2 + V_r^{-\frac{1}{2}} B_z G^1{}^2 \right) dz \qquad \ldots\ldots 1.5.7$$

The computer program of Marai (1975) computes C_{sp} as a function of the excitation parameter $NI/V_r^{\frac{1}{2}}$. From Equation 1.5.7 for any magnetic lens once its field distribution B_z is known. The values of C_{sp} for the newly developed single-pole lenses have been determined from this program. This program was also checked (see Chapter Seven) by comparing it with Liebmann's results (1952) for double-pole lenses.

It will be shown in Chapter Four how the spiral distortion of magnetic lenses could be minimised by using rotation-free lenses. To minimise the spiral distortion in conventional commercial electron microscopes, the lenses of the imaging system are usually connected so that the total value of the image rotation is a minimum. In a three stage microscope (Figure 1.1.1), for instance, this occurs when the second projector lens rotation θ_2 is in opposite sense to objective rotation θ_o and first projector lens rotation θ_1 should be in the same sense as θ_o.

1.6 New concepts

As mentioned above the principal defects of electron microscopes may be characterised by large size, heavy weight, small field of view, image rotation, alignment difficulty and complexity of design. With the electron microscope finding new uses in every field of science and industry, the need for a simple and more reliable microscope has grown rapidly. In order to fill this need, new concepts have developed for the use of rotation-free lenses which are described in the next chapters and in the recent publications of the author. Because of the inconvenient size of rotation-free lenses made from conventional lens designs (Juma, 1972), theoretical and experimental investigations showed the possibility of using these lenses in miniaturised form (Chapter

Three). Juma and Mulvey (1974, Appendix II), reported the successful performance of miniature rotation-free projector lenses of both double-pole and single-pole types. Each of these rotation-free projectors consisted of two identical magnetic lenses mounted back to back with the ampere-turns of one lens equal and opposite to that of the other i.e. $(NI)_1 = -(NI)_2$, so that the net rotation of the doublet is zero. Recently, a new experimental miniature rotation-free imaging system of simple design, has been described by Juma and Mulvey (1975). Further results with a rotation-free electron microscope will be given in Chapter Eight.

2. MINIATURE COILS

FOR HIGH CURRENT-DENSITY ELECTRON LENSES

It has been shown in Chapter One that the miniaturisation of magnetic electron lenses is important, and even essential for the development of electron-optical instruments. Magnetic lenses can be reduced in size if the current density in the energizing coil is increased. The temperature of the windings can be controlled conveniently if the coil is in direct contact with the cooling fluid. One of the most efficient and readily available cooling fluids is water. The coils under investigation were flat 'pan-cake' coils of small width, cooled by flowing water over their surfaces. In the following calculations it is assumed that the heat generated in the energized coil is removed from the flat surfaces only, and that it is transferred in an axial direction.

2.1 Heat-transfer and fluid flow rate

The heat-transfer is an important factor limiting the use of miniature coils in magnetic electron lenses. The heat-transfer coefficient, h, is defined as the amount of heat transferred from a unit surface area for a unit degree rise of the cooled surface temperature T_s above that of the coolant, i.e.

$$h = \frac{q}{T_s - T_w} \qquad \ldots\ldots 2.1.1$$

where q = heat flux per unit area, (Watts/cm^2.)

T_w = temperature of the fooling fluid (^oC).

The flow rate of the cooling water plays an important role in the transfer of heat generated in the coils. The movement of the fluid

particles over the surface of the coil can either be 'laminar' or 'turbulent' depending on the velocity. In laminar flow, the fluid stream lines run in a well-ordered manner with adjacent layers of fluid sliding relative to one another without any motion or exchange taking place normal to the streamlines of the main flow. During turbulent flow, this ordered flow is completely disrupted. This disruption leads to a violent mixing of the particles in the flow, which causes a transfer of momentum between different liquid layers in a direction normal to the flow. Whether the flow will be laminar or turbulent can be predicted by considering the dimensionless quantity R_e, the Reynold's number defined by the equation

$$R_e = \frac{d v D_h}{\mu} \qquad \ldots\ldots 2.1.2$$

where d = density of the field,

v = velocity of the field,

μ = coefficient of viscosity of the fluid,

D_h = hydraulic diameter of the fluid passage.

Provided $R_e \leqslant 2000$, the flow will be laminar. If $R_e \geqslant 4000$, the flow will be turbulent. In the range $2000 \leqslant R_e \leqslant 4000$, there exists a transition region in which the degree of turbulence steadily increases with R_e. The terms d and μ are temperature dependent, thus, for water at 50°C

$$R_e = 180 v D_h \qquad \ldots\ldots 2.1.3$$

Chapman (1967) gives a comprehensive treatment of both laminar and turbulent cases of forced convective heat transfer for plane surfaces and for cylindrical pipes. He gives his results in terms of the dimensionless quantities: Reynold's number (proportional to v) and Nusselt's number (proportional to h). Nusselt's number is defined by

the equation

$$Nu = \frac{h D_h}{k} \qquad \ldots\ldots 2.1.4$$

where k is the thermal conductivity of the fluid. The results of Chapman, converted into relationships between h and v, and assuming the properties of the fluid being constant, are given below:

	Plane Surface	Cylindrical Pipe
Laminar Flow	$h = \text{const.}\ v^{0.5}$	$h = \text{const.}\ v^{0.5}$
Turbulent Flow	$h = \text{const.}\ v^{0.8}$	$h = \text{const.}\ v^{0.8}$

The relationship between h and v for the water-cooled coils of electron lenses has not been studied thoroughly, (Maclachlan, 1973) particularly under the conditions of laminar flow. Although there is a considerable advantage for heat transfer in having the flow turbulent, this is not appropriate to electron lenses because of the danger that the coil will be caused to vibrate mechanically. It is therefore necessary to remain within the laminar flow or at least the quasi-turbulent region, and that $R_e = 4000$ is the maximum acceptable in electron optical instruments.

In large electromagnets where vibration is not so important, the coils are water-cooled under turbulent flow, and the relationship between h and v is then given by (Montgomery, 1969),

$$h = 9 \times 10^3 (1 + 1.5 \times 10^{-2} T_w)\ v^{0.8}/D_h^{0.2} \qquad \ldots\ldots 2.1.5$$

where v is the average velocity of the water in cm/sec. Equation 2.1.5 is also applicable to electron lenses if they were cooled with turbulent water flow.

2.2 Velocity of water and hydraulic diameter in miniature electron lenses

For thin pan-cake coils, which are cooled on both flat surfaces inside the electron lens, an expression for the effective hydraulic diameter of the water passage is required.

The water velocity at any point of its passage inside the electron lens can be determined from the cross-sectional area and the flow rate (volume per unit time). Figure 2.2.1 shows that the velocity of water changes from a maximum at MM' (v_1) to a minimum at OO' (v_2) and then increases to another but lower maximum at CC' (v_3). As a first approximation one may assume that the velocity of water inside an electron lens is the average value of the three velocities, i.e. $v_{av} = (v_1 + v_2 + v_3)/3$ remembering that only half the total value of water is flowing over each of the two flat surfaces of the coil. It was found in practice that it is possible to write the relation as

$$(v_{av})^n = (v^n)_{av} \qquad \ldots\ldots 2.2.1$$

Here $(v^n)_{av} = (v_1^n + v_2^n + v_3^n)/3$ where $0 \leq n \leq 1$. Equation 2.1.5 is useful in calculating the heat-transfer coefficient.

When the cooling passage is not round, it is customary to define an equivalent "hydraulic diameter" as follows:

$$D_h = \frac{4A_p}{P_w} \qquad \ldots\ldots 2.2.2$$

where A_p = passage cross-sectional area (cm^2),

P_w = wetted perimeter (cm).

This equivalent diameter can be easily verified, in the case of a circular passage of radius r, to be

$$D_h = \frac{4(\pi r^2)}{2\pi r} = 2r$$

and has been shown experimentally to give consistent values in standard

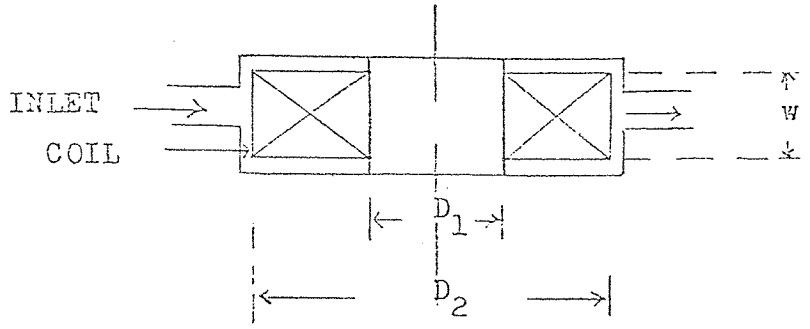

(a)

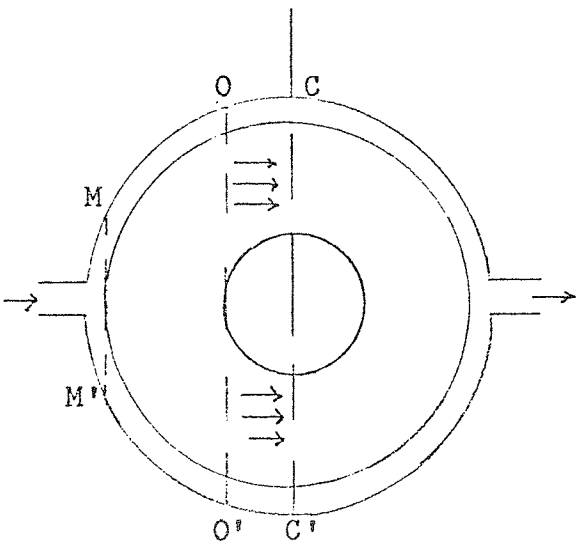

(b)

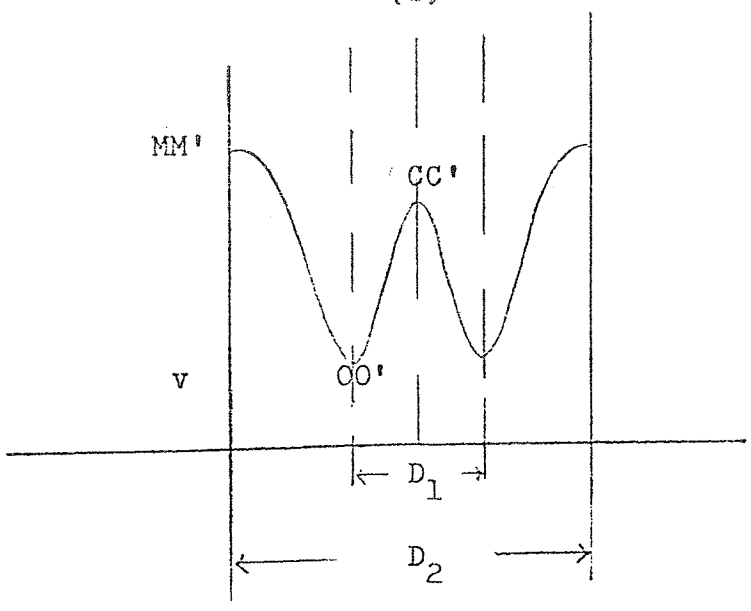

(c)

Fig. 2.2.1 (a),(b) Coil parameters. (c) Variation of the cooling water velocity inside an electron lens.

hydraulic formulae when used with annular or rectangular passages, (Montgomery, 1969). In the case of thin pan-cake coils in an electron lens, the cooling passage above the surface of the coil is a rectangular slit of width t, Figure 2.2.2. The cross-sectional area of the passage $A_p = t\ell$ and the wetted perimeter $P_w = 2(\ell + t)$. Since over most of the coil's surface $t \ll \ell$, $P_w = 2\ell$. Substituting for A_p and P_w in Equation 2.2.2, the hydraulic diameter of the water passage in a miniature electron lens will be given by

$$D_h = 2t \qquad \ldots\ldots 2.2.3$$

It can be seen that D_h is independent of the coil geometry and is a constant, depending only on the gap t above surface of the coil. In practice, t is usually of the order of 1-2mm. Equation 2.2.3 is very useful in determining the hydraulic diameter for all miniature magnetic lenses energized by thin flat coils.

2.3 Physical and geometrical parameters of the coil

Consider the coil winding shown in Figure 2.2.1a. The coil of width w, consists of N turns of a conductor whose cross-sectional area is A and length L.

The total length L of a coil winding (Figure 2.2.1a) is given by the product of the mean circumference and the number of turns, i.e.

$$L = \pi D_m N \qquad \ldots\ldots 2.3.1$$

where $$D_m = (D_1 + D_2)/2 \qquad \ldots\ldots 2.3.2$$

When power is dissipated in the water-cooled coils, their average temperature rises above that of the flowing water. A useful criterion of internal temperature rise is the average temperature rise, obtained from a measurement of the increase in total resistance of the winding.

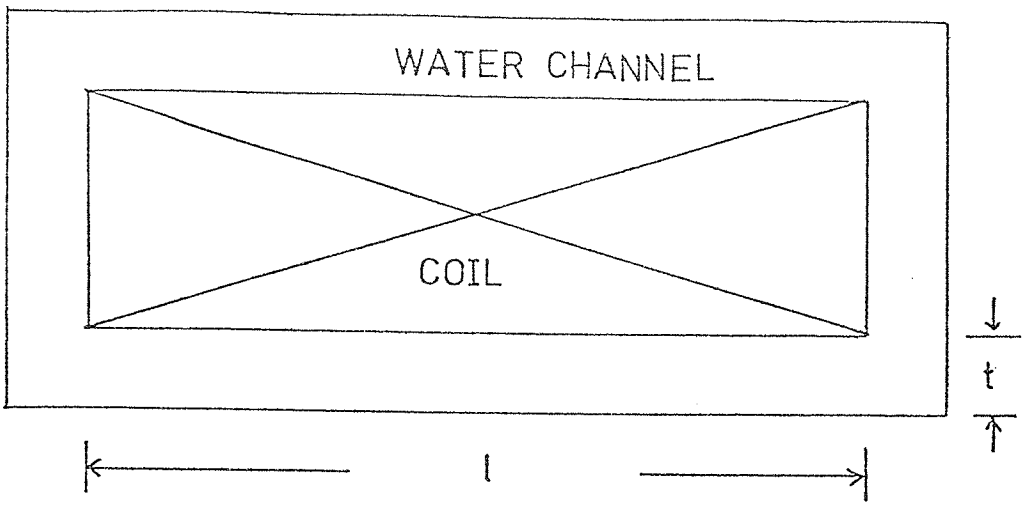

Fig. 2.2.2 Cross-section of the water passage inside a miniature lens.

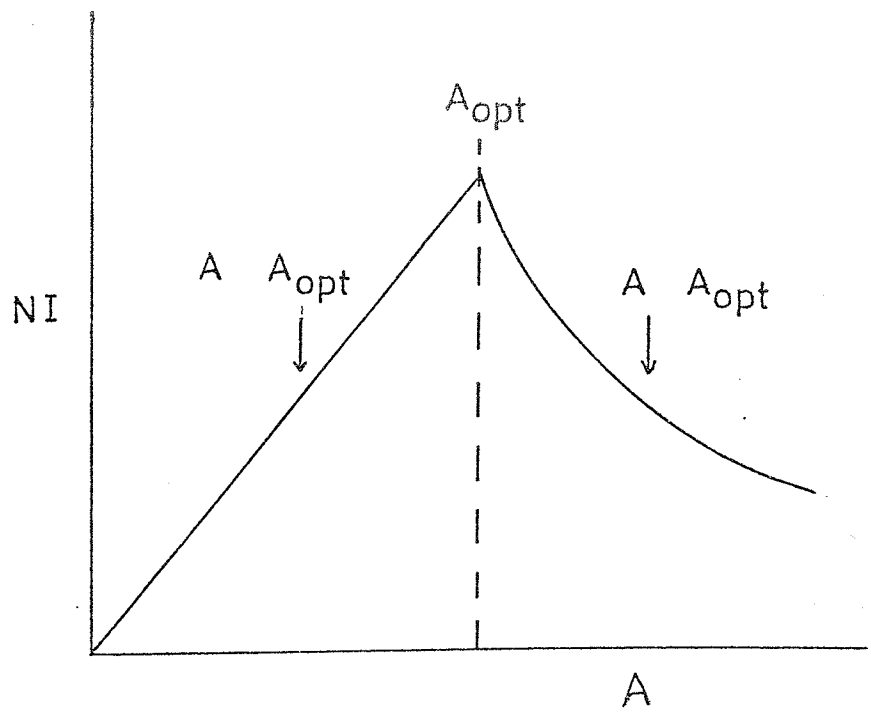

Fig. 2.4.1 Variation of the ampere-turns NI of a wire coil with the wire cross-sectional area A for a given power supply.

The average temperature is defined as the uniform temperature to which the entire coil would have to be raised in order to have the same increase in resistance as that measured under working conditions. The resistance R of the winding is given by

$$R = \rho L/A \qquad \ldots\ldots 2.3.3$$

where ρ is the resistivity of the conductor. The resistance is temperature dependent; i.e.

$$R_T = R_o (1 + \beta T) \qquad \ldots\ldots 2.3.4$$

where

R_T = resistance at temperature T^o

R_o = resistance at temperature 0^o

β = temperature coefficient of the conductor ($0.0041/^oC$ for copper).

Hence Equation 2.3.3 can be written as

$$R_T = \pi \rho_T D_m N/A \qquad \ldots\ldots 2.3.5$$

The total power P required to establish a current I in the coil is I^2R, i.e.

$$P = \pi \rho_T D_m (NI)^2/NA \qquad \ldots\ldots 2.3.6$$

where ρ_T is the resistivity of the conductor at temperature T and D_m is the mean diameter of the coil. Equation 2.3.6 can be written in terms of the current density, $\sigma = I/A$ as

$$P = \pi \rho_T \sigma D_m (NI) \qquad \ldots\ldots 2.3.7$$

The coil winding consists of a metallic conductor surrounded by an insulating coating. The term "insulating" refers to both thermal and electrical properties. The packing factor, λ, can be defined as

the ratio of the current-carrying cross-sectional area (NA) to the total cross-sectional area α, where $\alpha = (D_2 - D_1)w/2$, i.e.

$$\lambda = \frac{2\,NA}{(D_2 - D_1)\,w} \qquad \ldots\ldots 2.3.8$$

Hence in terms of the packing factor, λ, the total power is given by

$$P = \frac{\pi \rho_T (NI)^2}{\omega \lambda} \left[\frac{\frac{D_2}{D_1} + 1}{\frac{D_2}{D_1} - 1} \right] \qquad \ldots\ldots 2.3.9$$

If D_2/D_1 is large compared with unity

$$P = \frac{\pi \rho_T}{\omega \lambda} (NI)^2 \qquad \ldots\ldots 2.3.10$$

i.e. the power required for a given number of ampere-turns depends inversely on the width but it is independent of the diameter of the coil. If the ratio of outer to inner diameter becomes comparable with unity, the power required for a given number of ampere-turns increases rapidly. It is therefore desirable that D_2 should be large compared with D_1.

The increase of the ratio (D_2/D_1) increases the surface area of the coil $2\left[\frac{\pi}{4}(D_2^2 - D_1^2)\right]$. For the same total power and ampere-turns, the mean temperature of the coil decreases as the surface area increases, since the task of extracting heat from the surface becomes easier. In other words, the increase in the surface area will reduce the power q dissipated per unit area. The power per unit area of the coil surfaces is given by

$$q = \rho_T \sigma^2 \lambda \frac{\omega}{2} \qquad \ldots\ldots 2.3.11$$

or

$$q = \frac{\rho_T \sigma (NI)}{(D_2 - D_1)} \qquad \ldots\ldots 2.3.12$$

The volume of the coil is given by $\frac{\pi}{4}(D_2^2 - D_1^2)\omega$, hence the power per unit volume, H can be written as

$$H = \rho_T \sigma^2 \lambda \qquad \ldots\ldots 2.3.13$$

Therefore, it can be seen from Equation 2.3.11 that the power per unit surface area of the coil faces is

$$q = H\frac{\omega}{2} \qquad \ldots\ldots 2.3.14$$

2.4 Matching of a lens winding to a given power supply

Consider the coil winding shown in Figure 2.2.1a. From Equations 2.3.6 and 2.3.8 the power that is dissipated in the coil can be written as

$$P = \frac{\pi^2 \rho_T D_m}{\lambda \alpha} (NI)^2 \qquad \ldots\ldots 2.4.1$$

From 2.4.1, it follows that the excitation NI is not dependent on the number of turns and the cross-section of the wire, provided that there are no restrictions on the voltage and current from the power supply.

Consider the case where the power supply has a maximum current I_{max} which cannot be exceeded, and a limited output power P_{max}. Since from Equation 2.4.1, $(NI)^2 = P\lambda\alpha/(\pi^2 \rho_T D_m)$, therefore

$$(I_{max} N)^2 = P_{max}\lambda\alpha/\pi^2\rho_T D_m \qquad \ldots\ldots 2.4.2$$

Clearly, this will occur for an optimum number of turns N_{opt} given by

$$(N_{opt})^2 = \left(\frac{P_{max}}{I^2_{max}}\right)\frac{\lambda\alpha}{\pi^2\rho_T D_m} \qquad \ldots\ldots 2.4.3$$

and since $N_{opt} = \lambda\alpha/A_{opt}$ from Equation 2.3.8, thus the corresponding

optimum cross-sectional area of the conductor will be given by

$$(A_{opt})^2 = \pi\lambda\alpha\rho_T D_m (I_{max})^2/P_{max} \quad \ldots\ldots 2.4.4$$

Equation 2.4.4 shows that A_{opt} increases as $\alpha^{\frac{1}{2}}$, $\rho_T^{\frac{1}{2}}$ and D_m. Since $A_{opt} = \frac{\pi}{4} a^2_{opt}$ where a_{opt} is the optimum diameter of the round wire, therefore, from Equation 2.4.4,

$$a_{opt} = 2\left(\frac{\lambda\alpha\rho_T D_m I^2_{max}}{\pi P_{max}}\right)^{\frac{1}{4}} \quad \ldots\ldots 2.4.5$$

The maximum ampere-turns from the optimum wire is given by Equation 2.4.2, i.e.

$$(NI_{max}) = \left(\frac{P_{max}\lambda\alpha}{\pi\rho_T D_m}\right)^{\frac{1}{2}} \quad \ldots\ldots 2.4.6$$

Equations 2.4.5 and 2.4.6 are important in designing the appropriate wire coil for a given power supply and a given space in the electron lens.

If the cross-section A of the conductor is not optimized, the ampere-turns will fall. Thus if $A < A_{opt}$ the current will be less than I_{max}, and if $A > A_{opt}$ the current will be constant ($= I_{max}$) but the voltage across the coil will be less than V_{max}.

(i) $A < A_{opt}$

From Equation 2.3.6, the current I in the coil is given by,

$$I = V_{max} A/\pi\rho_T D_m N \quad \ldots\ldots 2.4.7$$

or

$$NI = V_{max} A/\pi\rho_T D_m \quad \ldots\ldots 2.4.8$$

where V_{max} is the maximum voltage of the power supply. i.e. NI is directly proportional to A.

(ii) $A > A_{opt}$

In this case $I = I_{max}$, thus $V = I_{max}R$. Substituting in Equation 2.3.5 for R, therefore,

$$V = \pi \rho_T D_m N I_{max}/A \qquad \ldots\ldots 2.4.9$$

From Equation 2.3.8,

$$NI_{max} = \left(\frac{\lambda \alpha}{A} \right) I_{max} \qquad \ldots\ldots 2.4.10$$

i.e. the maximum ampere-turns is inversely proportional to A The results of the cases (i) and (ii) are shown graphically in Figure 2.4.1.

In designing a coil, therefore, to suit a given power supply, the wire cross-section should be chosen to be A_{opt} or if there is a choice between two available values of A, the higher should be chosen. It should be noted that the value of ρ_T was assumed constant. Its value should be chosen which corresponds to the mean operating temperature. For a copper wire, this value will generally be in the region of $\rho = 2 \times 10^{-6}$ ohm-cm corresponding to an average temperature of 60°C.

2.5 Maximum current density, ampere-turns and power in lens windings

Windings of copper tape are important in miniature lenses. Consider the cross-section of a disc winding of inner and outer diameters D_1 and D_2 respectively, as shown in Figure 2.5.1a, b. The discs are of width (a) separated by an insulating material of thermal conductivity coefficient k_{in} and thickness 2b (i.e. each disc is originally covered by an insulating material of thickness b).

Let an amount of heat P be generated in the discs whose end surfaces only are cooled by water flow. If the conductivity of insulation is much lower than that of the metal, the temperature gradient across the metal can be neglected. Further, if the insulation is thin, as a first approximation a linear distribution of temperature

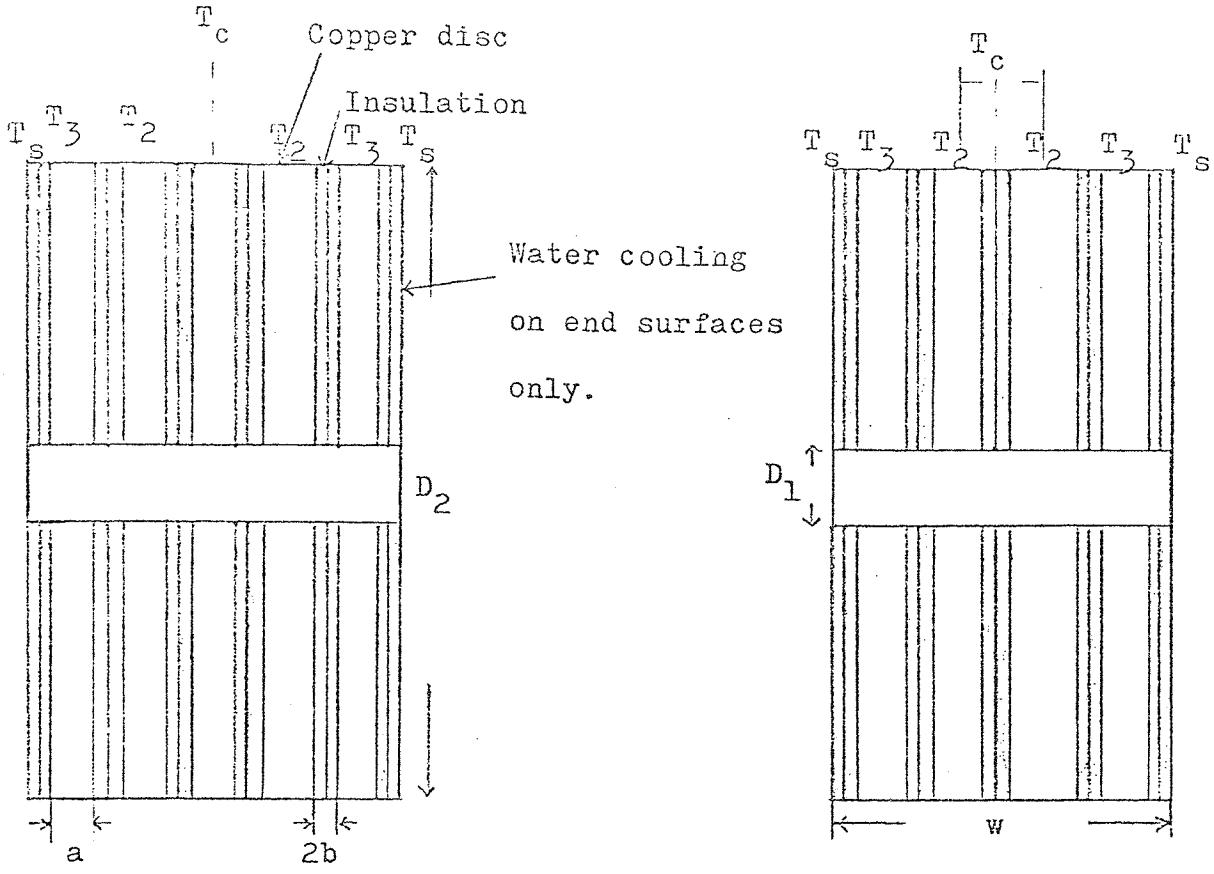

ODD NO. OF LAYERS

(a)

EVEN NO. OF LAYERS

(b)

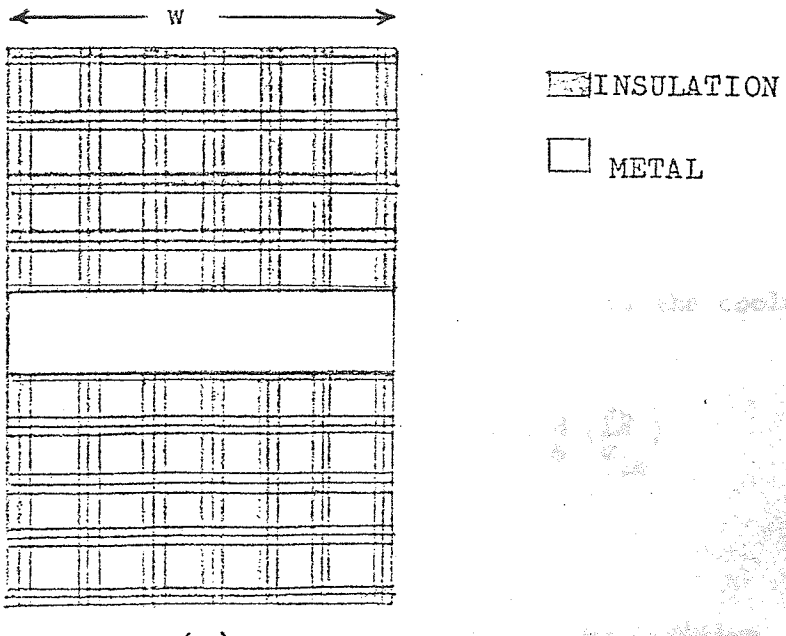

(c)

Fig. 2.5.1 Cross-section of an insulated disc winding .

can be assumed across the insulation, (Figure 2.5.2a). If the temperature of the cooled surfaces is held at a value T_s, from symmetry considerations the maximum temperature T_c will occur at the centre, (Figure 2.5.2b). The radial heat-flow is neglected since the temperature gradient is negligible. Therefore, even wire coils wound as shown in Figure 2.5.1c can also be assumed to be a series of flat discs in close contact. Hence it is important to consider the temperature distribution along the width. From symmetry, only one half of the coil need be considered.

Current density in a wire coil of even number of layers

Consider the coil shown in Figure 2.5.1b, c. It consists of 2n layers along the width w, where n = 1, 2, 3 ..... etc. This pancake coil is water-cooled on the two flat end surfaces; hence the power per unit surface area, q is given by:

$$q = \frac{P}{2\left[\frac{\pi}{4}(D_2^2 - D_1^2)\right]}$$

Therefore, the power per unit area per layer = q/n. Since the temperature gradient along the metal is negligible, hence the heat transmitted per unit area per layer is:

$$K_{in} \frac{(T_1 - T_2)}{(\text{Thickness of insulation})}$$

Considering each layer from the centre of the width to the cooled surface at the steady state temperature one has

$$T_c - T_2 = \frac{q}{n}\left(\frac{2b}{k_{in}}\right), \quad T_2 - T_3 = 2\frac{q}{n}\left(\frac{2b}{k_{in}}\right), \quad T_3 - T_4 = 3\frac{q}{n}\left(\frac{2b}{k_{in}}\right)$$

i.e. $$T_{n-1} - T_n = (n-1)\frac{q}{n}\left(\frac{2b}{k_{in}}\right)$$

where $T_n = T_s$, the temperature of the cooling surface. By addition one obtains

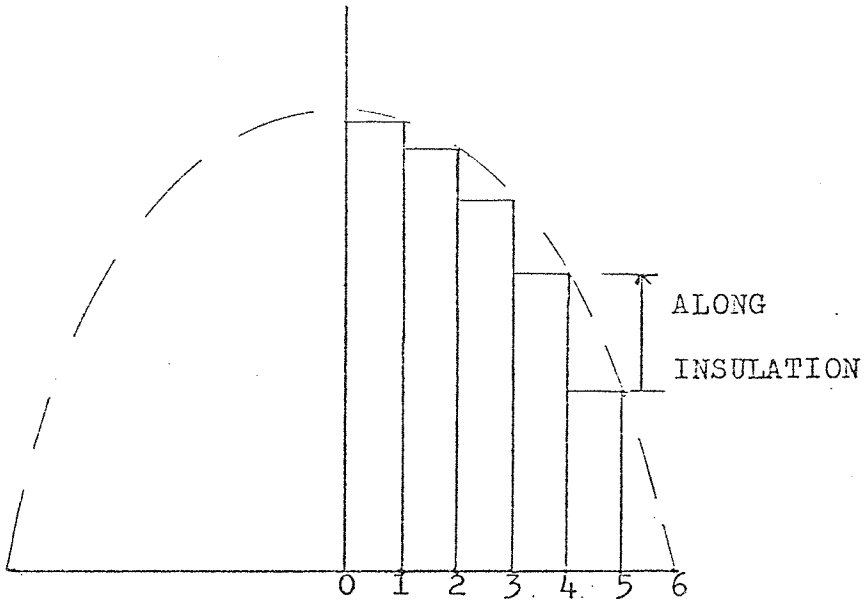

(a)

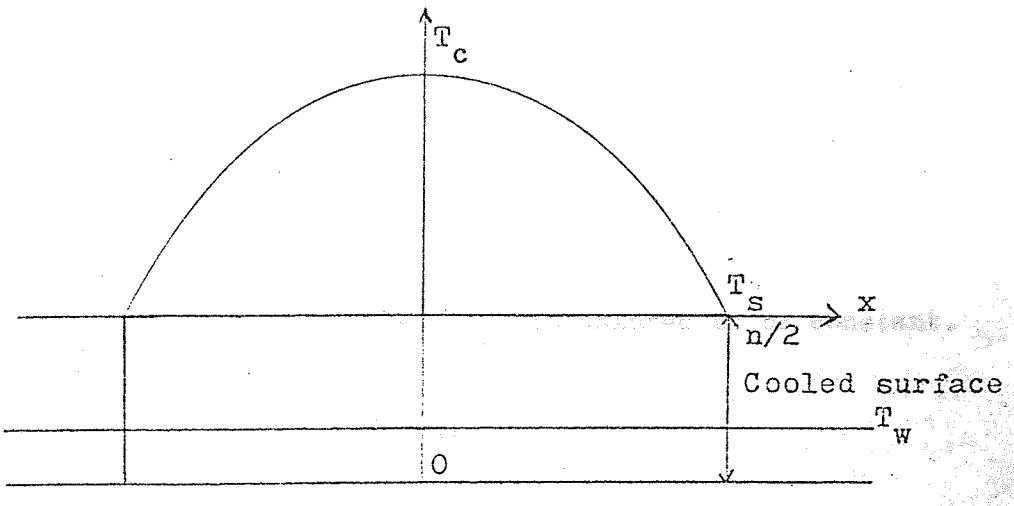

(b)

Fig. 2.5.2 Temperature distribution across the disc arrangement model.

$$T_c - T_s = \frac{q}{n}\left(\frac{2b}{k_{in}}\right)(1 + 2 + 3 + \ldots\ldots n - 1)$$

$$= \frac{q}{n}\left(\frac{2b}{k_{in}}\right)\frac{n}{2}(n - 1) \qquad \ldots\ldots 2.5.1$$

It can be seen that when n = 1 (i.e. a two-layer arrangement) there is no temperature drop across the coil. Thus a coil consisting of two wires thick should behave exactly as a single-layer coil as far as thermal conductivity is concerned. It is found from the wire data that the ratio of the insulation thickness to conductor diameter normally decreases with increasing wire diameter (Appendix III, Figure B), therefore, the above result suggests that in designing a coil the thickest possible wire should be used, arranged in double thickness, each pair being separated by a water channel. From the definition of the heat-transfer coefficient,

$$T_s - T_w = q/h \qquad \ldots\ldots 2.5.2$$

and from Equations 2.5.1 and 2.5.2

$$T_c - T_w = q\left[\frac{b}{k_{in}}(n-1) + \frac{1}{h}\right]$$

But

$$q = \rho\lambda\sigma^2\frac{w}{2}$$

where the resistivity ρ of the discs is assumed to be constant.

$$\lambda = \frac{a}{(a + 2b)}$$

$$W = 2n(a + 2b)$$

Hence $$q = n\rho a\sigma^2$$

If $2n = n_e$ where n_e is an even number, 2, 4, 6 ..... etc., then

$$T_c - T_w = \frac{n_e}{2} \rho a \sigma^2 \left[\frac{b}{k_{in}} \left(\frac{n_e}{2} - 1 \right) + \frac{1}{h} \right]$$

From Appendix III

$$2b = m \sqrt{a}$$

where m is a constant, hence

$$T_c - T_w = \frac{n_e}{2} \rho \sigma^2 a \left[\frac{m\sqrt{a}}{2k_{in}} \left(\frac{n_e}{2} - 1 \right) + \frac{1}{h} \right] \quad \ldots\ldots 2.5.3$$

$$\text{i.e. } \sigma_{wire} = \left[\frac{2(T_c - T_w)}{\frac{m \rho n_e (n_e - 2) (a)^{3/2}}{4k_{in}} + \frac{\rho n_e a}{h}} \right]^{\frac{1}{2}} \quad \ldots\ldots 2.5.4$$

Equation 2.5.4 gives an expression for the current density in a wire coil of even number of layers. It can be seen that when $n_e = 2$ the first term in the denominator is zero and the system behaves exactly like a tape. It is important to note that the first term in the denominator of Equation 2.5.4 is only present due to the presence of the insulation between the layers except that when $n_e = 2$. In the case of tape windings the first term in the denominator is always zero since the tape represents one layer of solid metal along the width $w(= n_e a/\lambda)$, i.e.

$$\sigma_{tape} = \left[\frac{2(T_c - T_w)h}{\rho \lambda w_{tape}} \right]^{\frac{1}{2}} \quad \ldots\ldots 2.5.5$$

Equation 2.5.5 shows that $\sigma_{tape} \propto \frac{1}{w^{\frac{1}{2}}}$. Hence if a tape of width w is divided into two halves each of width w/2 with an insulation between them, the same current density will be obtained at the same maximum temperature. It can also be concluded that the two-layer coil should

show a linear relationship between the average rise in the temperature of the coil above that of water and the input power, from which the amount of heat per unit area per degree is equal to the heat-transfer coefficient.

Current density in a wire coil of odd number of layers

Suppose that the water-cooled coil under consideration has an odd number of layers along its width w (Figure 2.5.1a). If the number of layers is (2n + 1) where n = 0, 1, 2, 3 ..... etc., this means that there are n layers on each side of the central layer; hence half the heat generated in the central layer will be transferred to the n-layers on either side. The heat generated per unit area per unit layer is

$$q/\frac{(2n+1)}{2} \quad \text{or} \quad q/(n+\tfrac{1}{2}).$$

In the steady state the temperature of the central layer is T_c and that of the cooling surface is T_s; therefore

$$T_c - T_1 = \tfrac{1}{2}\left[\frac{q}{(n+\frac{1}{2})}\right]\frac{2b}{k_{in}}$$

$$T_1 - T_2 = \left[\frac{q}{(n+\frac{1}{2})}\right]\frac{2b}{k_{in}}\quad(\tfrac{1}{2}+1)$$

$$T_2 - T_3 = \left[\frac{q}{(n+\frac{1}{2})}\right]\frac{2b}{k_{in}}\quad(\tfrac{1}{2}+2)$$

$$T_{n-1} - T_s = \left[\frac{q}{(n+\frac{1}{2})}\right]\frac{2b}{k_{in}}\left[\tfrac{1}{2}+n-1\right]$$

By addition one obtains

$$T_c - T_s = \left[\frac{q}{n+\frac{1}{2}}\right]\left(\frac{2b}{k_{in}}\right)\left[\frac{n}{2}(n-1)+\frac{n}{2}\right] \qquad \ldots\ldots 2.5.6$$

Hence from Equations 2.5.2 and 2.5.6

$$T_c - T_w = q \left\{ \frac{2b}{(n+\frac{1}{2})k_{in}} \left[\frac{n}{2}(n-1) + \frac{n}{2} \right] + \frac{1}{h} \right\}$$

Since the width

$$w = (2n+1)(a+2b), \quad \text{therefore,}$$

$$q = \rho \sigma^2 a(n+\tfrac{1}{2})$$

also $2b = m\sqrt{a}$; hence,

$$T_c - T_w = \rho \sigma^2 a(n+\tfrac{1}{2}) \left\{ \frac{m\sqrt{a}}{(n+\frac{1}{2})k_{in}} \left[\frac{n}{2}(n-1) + \frac{n}{2} \right] + \frac{1}{h} \right\}$$

If $2n+1 = n_o$ where n_o is an odd number e.g. 1, 3, 5 ..... etc.,

$$T_c - T_w = \frac{\rho \sigma^2 a n_o}{2} \left[\frac{m\sqrt{a}}{4k_{in}} \cdot \frac{(n_o-1)^2}{n_o} + \frac{1}{h} \right] \quad \ldots\ldots 2.5.7$$

i.e.

$$\sigma = \left[\frac{2(T_c-T_w)}{\rho m a^{3/2} \frac{(n_o-1)^2}{4k_{in}} + \rho \frac{n_o a}{h}} \right]^{\frac{1}{2}} \quad \ldots\ldots 2.5.8$$

When the coil is of a single-layer wire i.e. $n_o = 1$, Equation 2.5.8 is similar to Equation 2.5.5, showing that the tape, single and double-layer wire coils behave exactly the same under the same working conditions. When (T_c-T_w) is maximum, the current density given in Equations 2.5.4 and 2.5.8 is also maximum.

It can be seen that as far as the thermal conductivity is concerned it is always advantageous to have an <u>even</u> number of layers since the insulation at the centre of the width of an even number of layers has no effect at all. As an example, the heat in the 3-layer coil will pass through one layer of insulation of thickness 2b on each side of the

centre of the width; similarly in the four layer coil the heat will pass through one layer of insulation of thickness 2b on either side of the centre of the width since the central insulating layer has no effect in heat generation and it maintains the temperature of the surrounding layers. Also the single and double-layer coil have the same thermal behaviour.

Maximum ampere-turns in coil windings

The ampere-turns that can be obtained from a coil winding can be determined from the current density, σ ($=I/A$) and N, [$=\lambda w(D_2-D_1)/2A$]. Thus

$$NI = \lambda w\left(\frac{D_2-D_1}{2}\right)\sigma \qquad \text{..... 2.5.9}$$

Equation 2.5.9 applies to both tape and wire coils. For a wire coil, Equation 2.5.9 can be written in terms of the wire diameter, a, and the number of layers, n, across the width w, [$=n(a+m\sqrt{a})$]; i.e.

$$(NI)_{wire} = n\lambda(a+m\sqrt{a})\left(\frac{D_2-D_1}{2}\right)\sigma \qquad \text{..... 2.5.10}$$

For a specific coil geometry, the ampere-turns is a maximum when the current density is a maximum. For a tape winding where σ is given by Equation 2.5.6, the ampere-turns can be written as

$$(NI)_{tape} = \left[\frac{2h\lambda(T_c-T_w)}{\rho}\right]^{\frac{1}{2}} (R_2-R_1)w^{\frac{1}{2}} \qquad \text{..... 2.5.11}$$

i.e. the maximum ampere-turns from a tape coil increase with the square root of its width.

Maximum power in coil windings

The power density is a maximum when the current density in the windings is also a maximum. This can be seen from Equation 2.3.13, i.e.

$$(H)_{max} = \rho_T \lambda \sigma^2_{max}$$

Therefore, the maximum power dissipated in a coil is given by

$$(P)_{max} = \rho_T \lambda\left[\frac{\pi}{4}(D_2^2 - D_1^2)\,w\right]\sigma^2_{max} \qquad \text{..... 2.5.12}$$

The maximum input power in wire windings of even and odd number of layers is respectively,

$$(P_{max})_{even} = \frac{\pi}{2} (D_2^2 - D_1^2) \left[\frac{T_c - T_w}{\frac{m\sqrt{a}}{4K_{in}} (n_e - 2) + \frac{1}{h}} \right] \quad \ldots\ldots 2.5.13$$

$$(P_{max})_{odd} = \frac{\pi}{2} (D_2^2 - D_1^2) \left[\frac{T_c - T_w}{\frac{m\sqrt{a}}{4K_{in}} \frac{(n_o - 1)^2}{n_o} + \frac{1}{h}} \right] \quad \ldots\ldots 2.5.14$$

In the case of a tape winding both Equations 2.5.13 and 2.5.14 give the same expression

$$(P_{max})_{tape} = \frac{\pi}{2} (D_2^2 - D_1^2) (T_c - T_w) h \quad \ldots\ldots 2.5.15$$

Equation 2.5.15 is an illustration of the definition of the heat-transfer coefficient since the expression $\frac{\pi}{2} (D_2^2 - D_1^2)$ represents the total surface area of the coil. It also shows that the power required in a tape winding is independent of its width w, if w is small; it is a function of the water-cooled surface area. If the surface area is increased the temperature of the coil will decrease since more heat will be extracted, hence more power can be dissipated in the coil to raise it to the maximum permissible temperature. However, it should be mentioned that Equations 2.5.13, 2.5.14 and 2.5.15 show that the power in any winding is independent of the conductor resistivity.

2.6 Experiments on wire and tape coils

The theoretical ideas developed in the previous sections need to be verified experimentally, particularly the validity of the disc model. When power is dissipated in the coil, the average temperature

will rise above that of the cooling water. This average temperature can be measured from the change in coil's resistance. In the steady state, i.e. when the power per unit area is constant, the mechanism of heat transfer from the surface of a multi-layer wire coil is similar to that of a single-layer coil. Hence the temperature of the first layer which is in contact with water is the same as that of the single-layer coil operating under the same conditions. Due to the temperature difference between the centre of the coil and its cooled flat surfaces, the heat may be assumed to be flowing axially towards the cooled surfaces. In order to test these assumptions single and multi-layer wire coils were designed and tested under the conditions likely to be experienced in an electron lens.

Single-layer wire coils

Two single-layer wire coils, A and B, of different wire diameter were designed. Coil A consisted of an insulated copper wire of 24S.W.G. with $D_2/D_1 \simeq 3$; this ratio of D_2/D_1 was chosen because it is commonly used in miniature water-cooled electron lenses. Insulated wire was used to eliminate current leakage through the water. The thickness of the insulation was 0.0025 cm (0.001 in) which is small compared with the diameter of the copper; hence it was assumed that the temperature of the surface was very nearly the same as that of the copper. All the water-cooled coils under investigation were mounted in a "Perspex" box, (Figure 2.6.1). The cooling water was passed over the exposed surfaces of the windings through a 1mm gap between the inside surface of the box and the coil. The "Perspex" box enables the windings to be observed continuously and also ensures that the main heat transfer takes place between the windings and the water and not through the container. The thermal conductivity of the "Perspex" is 2×10^{-3} watt/cm$^{\circ}$C, which is very low compared with that of metals.

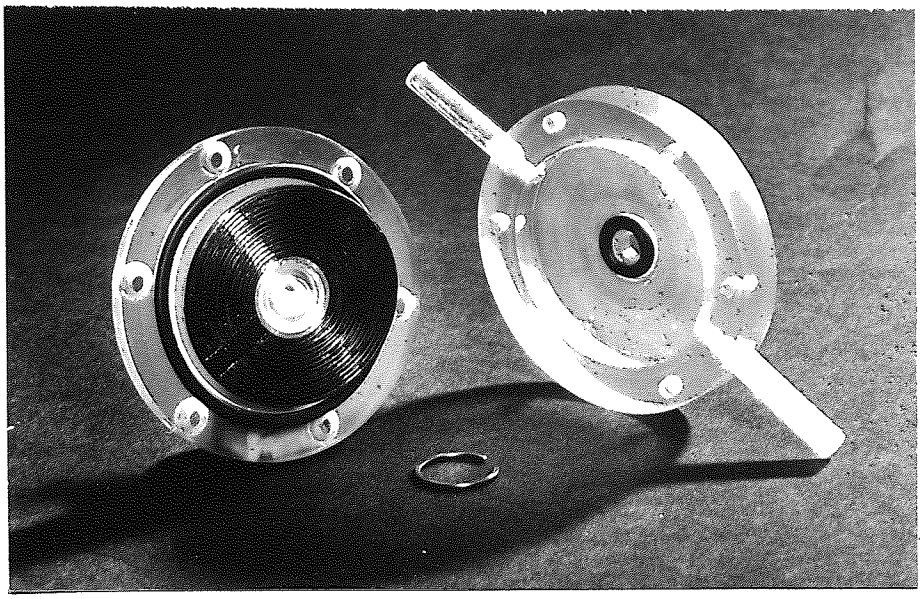

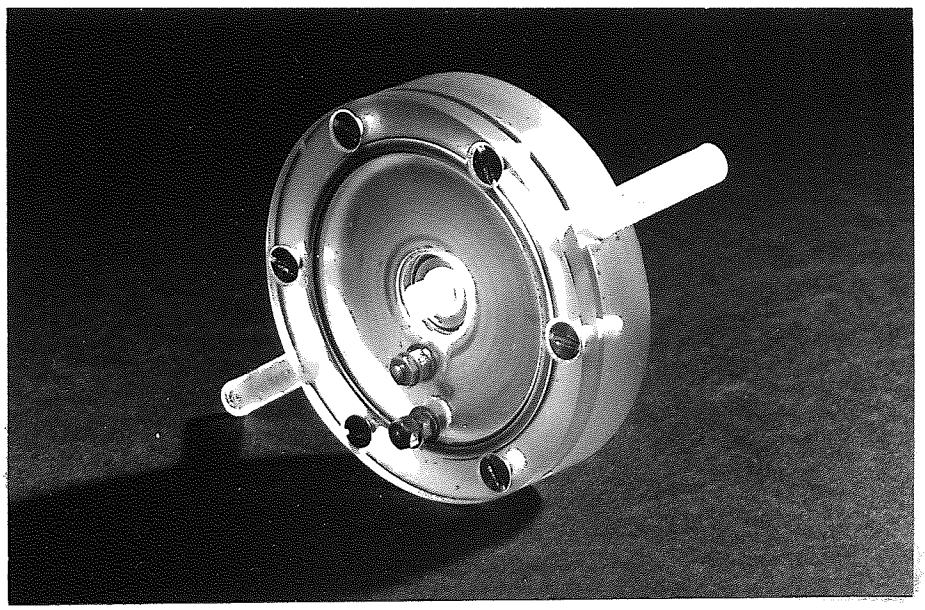

Fig. 2.6.1 Experimental water-cooled copper wire winding in "Perspex" box.

The electrical characteristics of coil A are shown in Figures 2.6.2 and 2.6.3 at different water velocities showing the deviation from a linear relationship of voltage and current. It should be noted that at the maximum current available (24 amps.) the power was limited to 100 watts. The rise in the temperature of the coil was about 20°C for a flow of 0.5 litres/minute and 15°C for a flow of 3.5 litres/minute. At this power, the maximum ampere-turns obtained was about 600A-t. and current density of 10^4 amp/cm^2. This current density is about the same as that obtained by Prior (1967) from superconducting materials. At 3.5 litres/minute, the temperature rise was difficult to measure due to fluctuations in water pressure. These experimental results can be checked against the equation

$P = \pi \rho_T \sigma D_m (NI)$, if NI is 600A-t, (24 amp x 25 turns),

$D_m = 3.2$cm, $\sigma = 10^4$ amp/cm^2 and $\rho_T = 1.7 \times 10^{-6}$ ohm.cm;

P = 103 watts, which is consistent with the experimentally measured value.

Due to experimental errors estimated at about 4% an error of $\pm$ 10°C in the coil's average temperature is to be expected over the available power range. Since no more power was readily available, it proved more convenient to construct a second single-layer coil B. The wire of coil B was 32 S.W.G. i.e. half the diameter of that of coil A.

The characteristic of coil B are shown in Figures 2.6.4 and 2.6.5. These curves were extrapolated in order to determine the current density and the ampere-turns at 120°C. It can be seen that at a coil temperature of 120°C, 1250 A-t can be obtained at 3.5 litres/minute water flow and a current density of 4.2×10^4 amp/cm^2. This current density is about the same as that obtained by Laverick (1967) using a superconducting wire (NbZr) of nearly the same diameter (0.0254 cm) carrying a current of 20 amperes. This

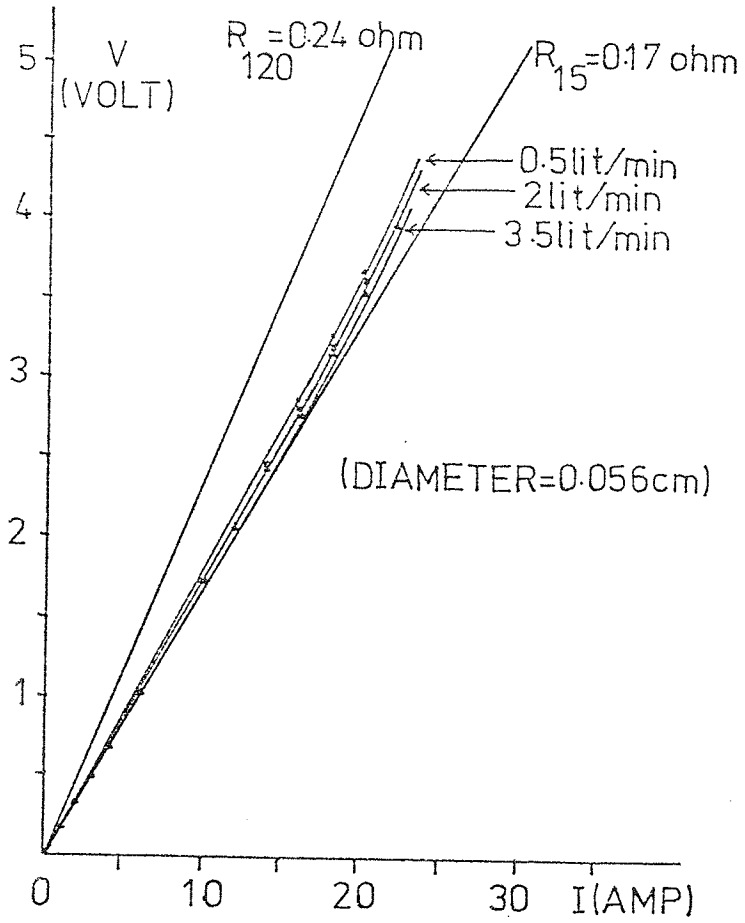

Fig. 2.6.2 Variation of voltage and current in a water-cooled single -layer wire coil 24 S.W.G. (Coil A).

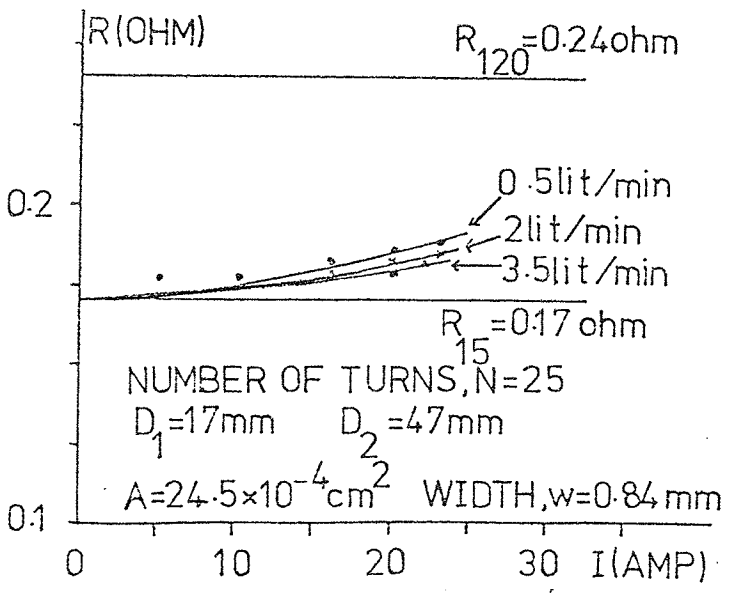

Fig. 2.6.3 Variation of resistance with current in the water-cooled single-layer wire coil 24 S.W.G. (Coil A).

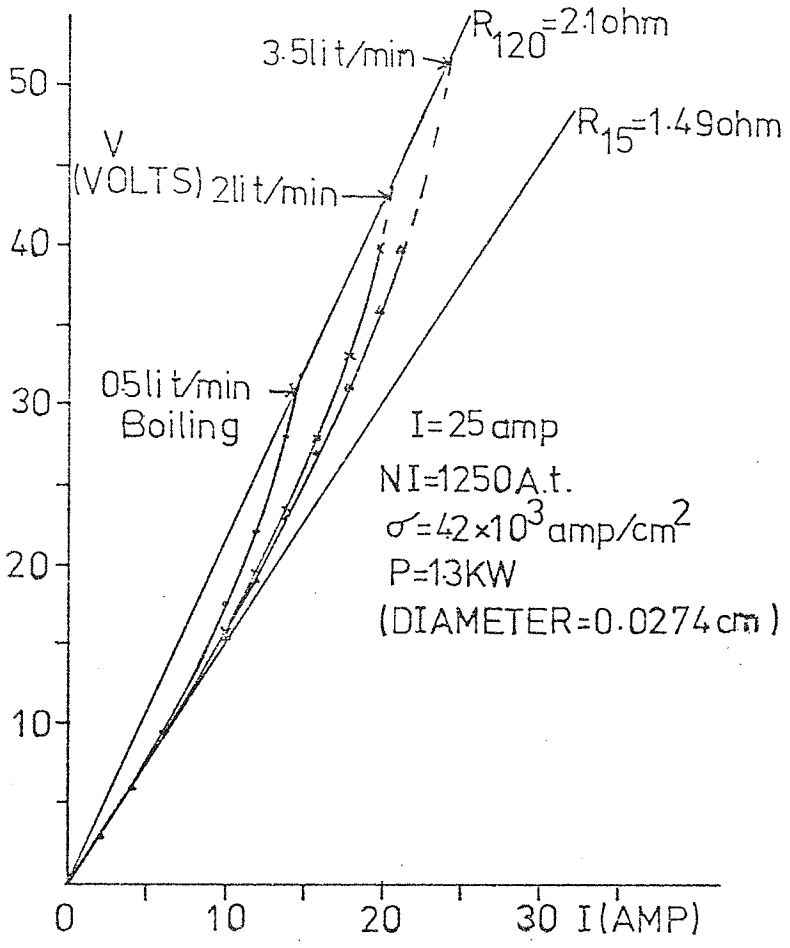

Fig. 2.6.4 Variation of the voltage with the current in the water-cooled single-layer wire coil of 32 S.W.G. (Coil B).

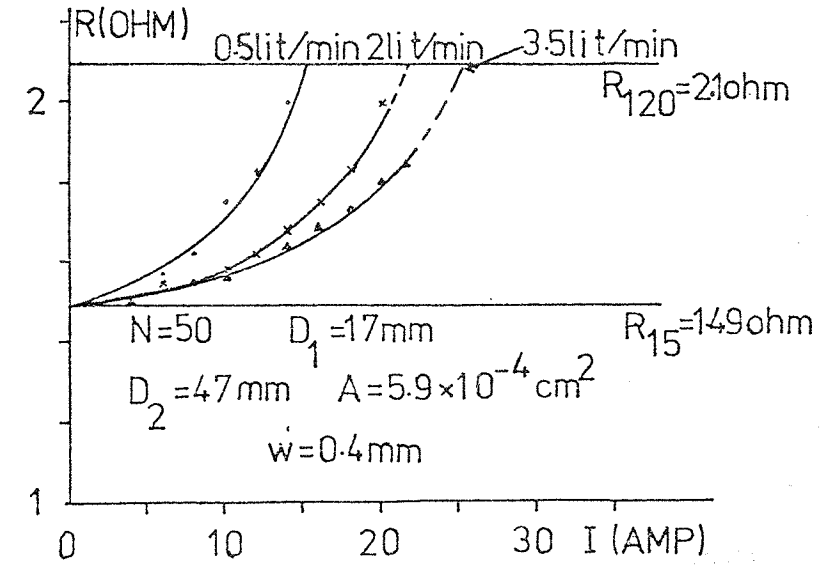

Fig. 2.6.5 Variation of the resistance with the current in the water-cooled single-layer wire coil of 32 S.W.G. (Coil B).

interesting result also means that 2×10^4 A-t/cm^2 is obtainable from water-cooled copper wire coil similar to that from a superconducting coil (Ozasa, et al, 1966) which has the same D_2/D_1 ratio and wire diameter.

It should be noted that at the rate of flow of 0.5 litre/minute, boiling of the cooling water took place when the average temperature of the coil was 120°C at an input power of 480 watts (corresponding to a current of 15 amps (i.e. NI = 750 A-t). As a theoretical check, the power P calculated from equation $P = \pi \rho_T D_m \sigma (NI)$, where $\rho_{120} = 2.4 \times 10^{-6}$ ohm.cm, $\sigma = 25.5 \times 10^3$ amps/cm^2 and $D_m = 3.2$cm; is equal to 460 watts which is only 5% less than the experimentally measured value. At this rate of flow large vapour bubbles were accumulated. Because of these bubbles the heat transfer through the water was poor and hence certain regions of the coil under the bubbles were very hot while others were at a lower temperature. The insulation was damaged in the hot regions.

With the water flowing at 2 litres/minute vapour bubbles were formed at a power input of 800 watts. These vapour bubbles were relatively small. At higher rates of flow, bubbles were absent and hence the coil was not damaged. It is therefore essential to ensure a minimum rate of flow of water for a given power.

Figure 2.6.6 shows the variation of the temperature rise of coil B with input power at different rates of water flow. The curves are essentially straight lines bearing in mind that the experimental points at low powers are unreliable since the error here is high. From the slope of the curve, it was found that the amount of power per unit area per degree centigrade is 0.46 watt/cm^2.°C at 3.5 litres/minute. This relatively high value of heat-transfer coefficient was obtained although the water is flowing in the quasi-laminar region.

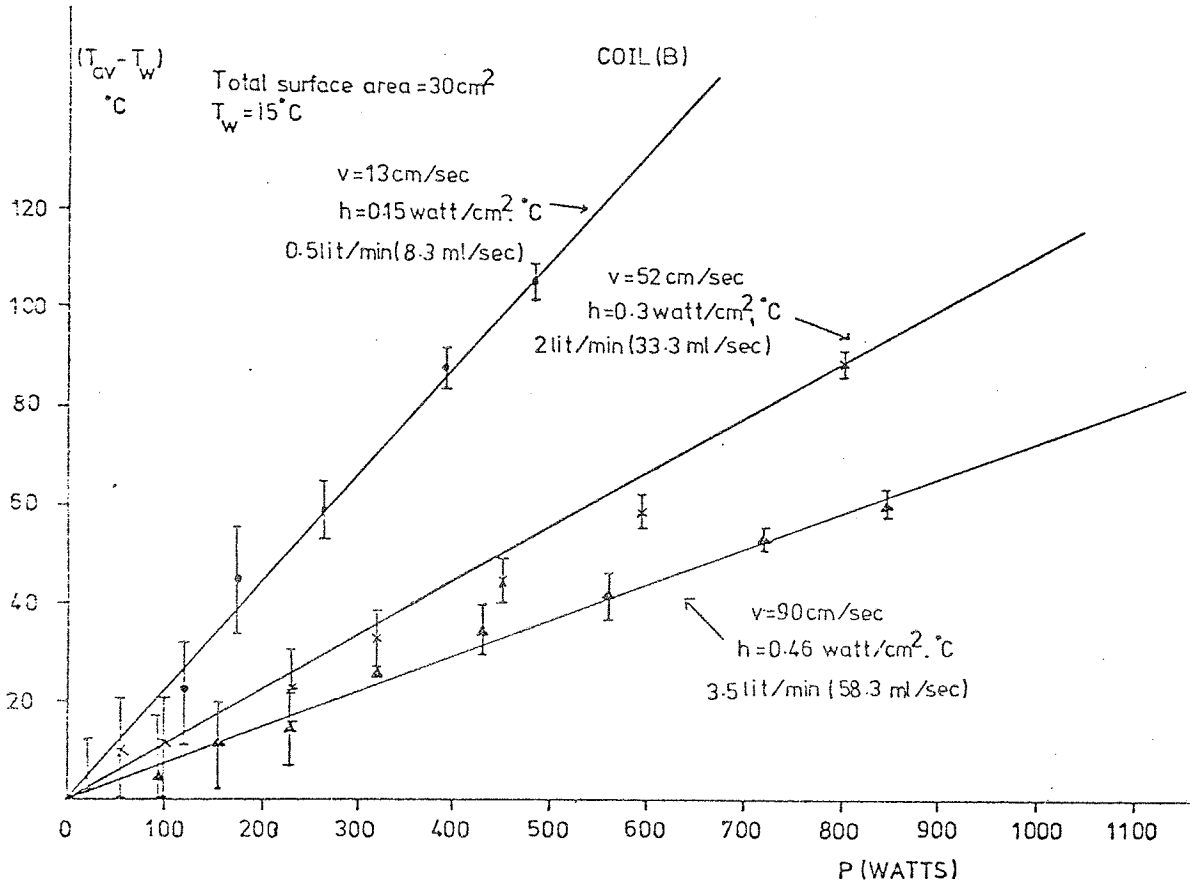

Fig. 2.6.6 Variation of the average temperature rise with the input power of a water-cooled single-layer wire coil of 32 S.W.G.

If coil B is considered to be formed of a cylindrical wire of length L and radius R, the surface area is $2\pi RL$. Coil A has a length L/2 and radius 2R compared with that of coil B; hence its surface area is also $2\pi RL$. Since these two coils have the same surface area, water passage and water temperature, the heat-transfer coefficients of both coils at the same water velocity would be expected to be indentical.

It can be assumed to a good approximation that the average temperature of a single-layer coil is nearly the same as that of the coil's surface. Therefore, it can be concluded from Figure 2.6.6 that the difference between the temperature of the coil's surface, T_s and the input temperature of the water, T_w is proportional to the input power P, i.e.

$$(T_s - T_2) \propto P \qquad \ldots\ldots 2.6.1$$

when the water flow Q is constant.

If the power input, P in coil B at 120°C (Figures 2.6.5 and 2.6.6) is plotted against the flow rate Q, a straight line on a logarithmic scale will be obtained as shown in Figure 2.6.7. From the slope, this figure shows that

$$P = \text{constant } Q^{\frac{1}{2}} \qquad \ldots\ldots 2.6.2$$

when the temperature is constant. Since $P \propto h$ and $Q \propto v$,

$$h = \text{constant } v^{\frac{1}{2}} \qquad \ldots\ldots 2.6.3$$

Therefore, in such electron lenses, the cooling is similar to that of laminar flow on plane surfaces. Heat transfer varies only slowly with water velocity and thus no special precautions are needed to ensure a uniform velocity distribution across the coil face. Equation 2.6.3 shows that the heat transfer coefficient is not

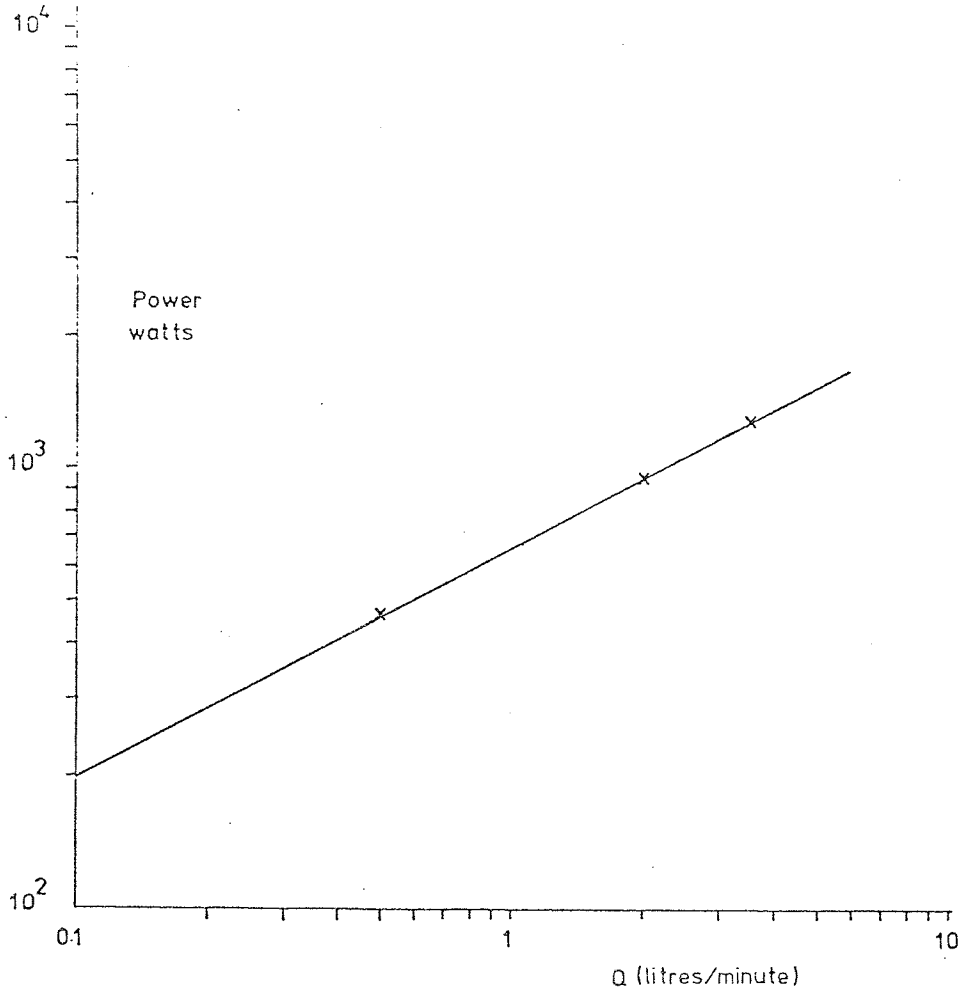

Fig. 2.6.7 Variation of power in single-layer coil (B) with water-flow rate.

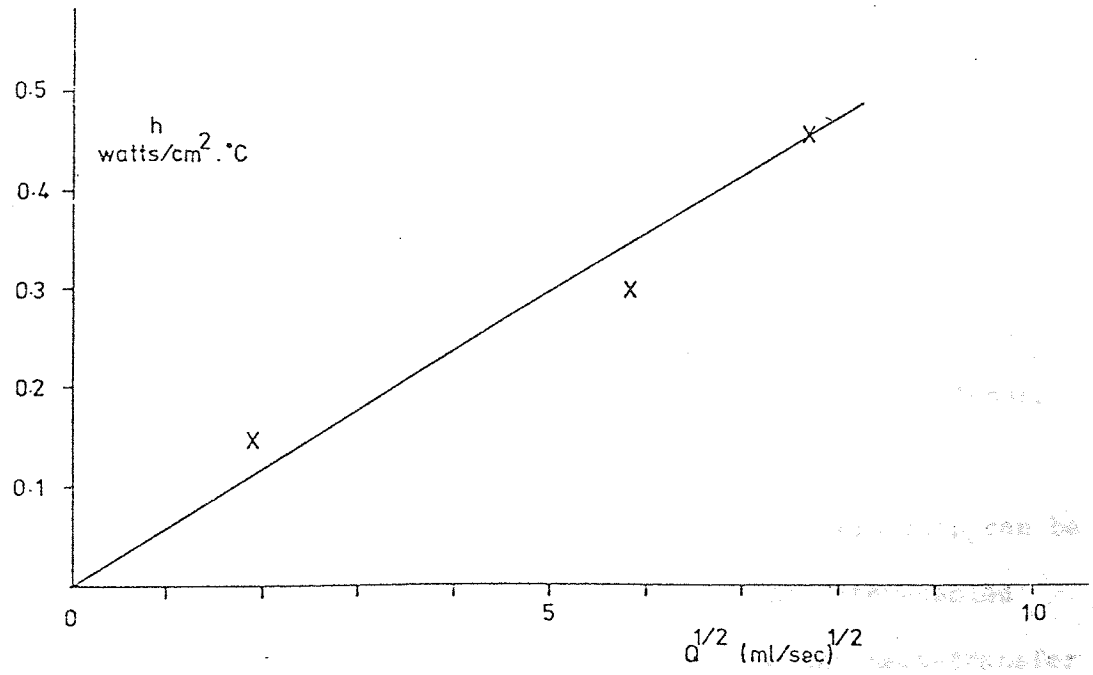

Fig. 2.6.8 Variation of heat-transfer coefficient with the square-root of water-flow rate.

strongly dependent on water velocity provided the flow remains quasi-laminar. In fact to double h, the value of v would have to be increased four times. The average velocity, v, of the cooling water is about 90 cm/sec, when the flow rate is 3.5 litres/minute as calculated by the method described previously.

The type of flow can also be checked from the Reynolds number, $R_e = vdD_h/\nu$. The hydraulic diameter, D_h = 2t where t = 1mm, i.e. D_h = 0.2cm. The viscosity ν = 0.01 poise (gm/cm.sec) at 20°C and d = 1 gm/cc. Therefore, for a 90 cm/sec water velocity, R_e = 1800 which shows that the water flow is within the laminar or quasi-laminar flow range, and not in the turbulent range.

Since it is easier to measure the rate of flow, Q (ml/sec), it is better to write Equations 2.6.2 and 2.6.3 in the form

$$h = \text{constant } Q^{\frac{1}{2}} \qquad \ldots\ldots 2.6.4$$

The constant can be determined from the slope of the curve of h vs. Q (Figure 2.6.8). Therefore, the heat-transfer coefficient for the pan-cake coils of the miniature electron lenses cooled by a water flow at room temperature through a 1mm gap is given by

$$h = 0.06\, Q^{\frac{1}{2}} \qquad \ldots\ldots 2.6.5$$

where Q is in ml/sec. Equation 2.6.5 has been found very useful in determining the heat-transfer coefficient for the miniature lenses which will be described in the next chapters.

From Equations 2.6.1 and 2.6.2 an empirical relationship can be derived relating P, Q and (T_s-T_w) applicable to all water-cooled pan-cake coils for miniature electron lenses since the heat-transfer mechanism is identical in tape, single and multilayer wire coils, i.e.

$$P \propto (T_s-T_w)\ Q^{\frac{1}{2}} \qquad \ldots\ldots 2.6.6$$

From the curves shown in Figure 2.6.6, the constant of proportionality was determined; thus

$$(T_s - T_w) \simeq \frac{0.6\ P}{Q^{\frac{1}{2}}} \qquad \ldots\ldots\ 2.6.7$$

where P is in watts and Q in ml/sec. Equation 2.6.7 gives values of $(T_s - T_w)$ within $\pm$ 5% accuracy and it does not depend on the surface area of the coil. Hence, the temperature difference between the cooled surface and the cooling water can now be easily determined since P and Q are the only variables and these are easily measured experimentally.

The temperature in any part of the coil should not exceed 200°C above water temperature (15°C) otherwise the insulating materials will deteriorate. If coil A, shown in Figures 2.6.2 and 2.6.3, is cooled by a 3.5 litres/minute water flow through a 1mm gap around it, the heat-transfer coefficient will be 0.46 watts/cm^2.°C. If coils A or B are operated under these working conditions, a power of more than 2 kW would be needed to raise their temperatures 150° above that of water. In this case coil A will give more than 2000 A-t at a current density of about 3.5×10^4 amp/cm^2 and coil B will give just less than 1500 A-t at a current density of 5×10^4 amp/cm^2. These figures show that a current density within the range of super-conductors can be achieved from water-cooled single-layer coils. It can be seen from the above figures that the coil with the smaller wire diameter operated at 30% greater current density than the other, for the same power dissipation and temperature, but produced 30% fewer ampere-turns. This illustrates that it is advantageous to use a relatively large wire diameter although it will require a power supply of high current output. The above results are clear from Equation 2.5.11 where the ratio of the ampere-turns of the two coils is equal

to the ratio of the square root of their widths; i.e. $(NI)_A/(NI)_B = (w_A/w_B)^{\frac{1}{2}}$. Since $w_A = 2\ w_B$, therefore the ampere-turns of coil A is 40% higher than that of coil B which agrees within the experimental errors with that determined practically.

Tape Coils

Consider a copper tape covered on both sides by a thin (9 μm) "Mylar" tape which acts as an insulator between adjacent turns, Figure 2.6.9. The coil is cooled by a water flow of 2 litres/minute across its flat surfaces, through a 1mm gap. Figure 2.6.10 shows the measured variation of the average temperature rise above water temperature with the input power. The curve is straight line; from its slope it is found that the amount of heat per unit area per degree rise in temperature (i.e. heat-transfer coefficient) is 0.33 watts/$cm^2.{}^oC$ which is in good agreement with that for the single-layer wire coil (h = 0.3 watt/$cm^2.{}^oC$) operated under the same conditions. Since the tape width is relatively small, the average temperature, T_{av} is nearly the same as that of the surface T_s. For a power of 800 watts, Equation 2.6.7 gives a value of 83^o for (T_s-T_w) while experimentally, it is 80^oC showing the validity of this equation.

The thermal conductivity of a tape coil in the direction of heat flow through the tape is that of the conductor. In calculating the area of conductor the packing factor must be taken into account. The insulation between layers has a conductivity smaller than that of the conductor by a factor of 10^3 and so radial heat flow can be neglected. Typically the packing factor of the tape coils is 75%. The thermal conductivity of copper is 3.86 watts/$cm.{}^oC$.

To illustrate a typical temperature distribution across the width of a tape coil, consider the copper tape coil whose

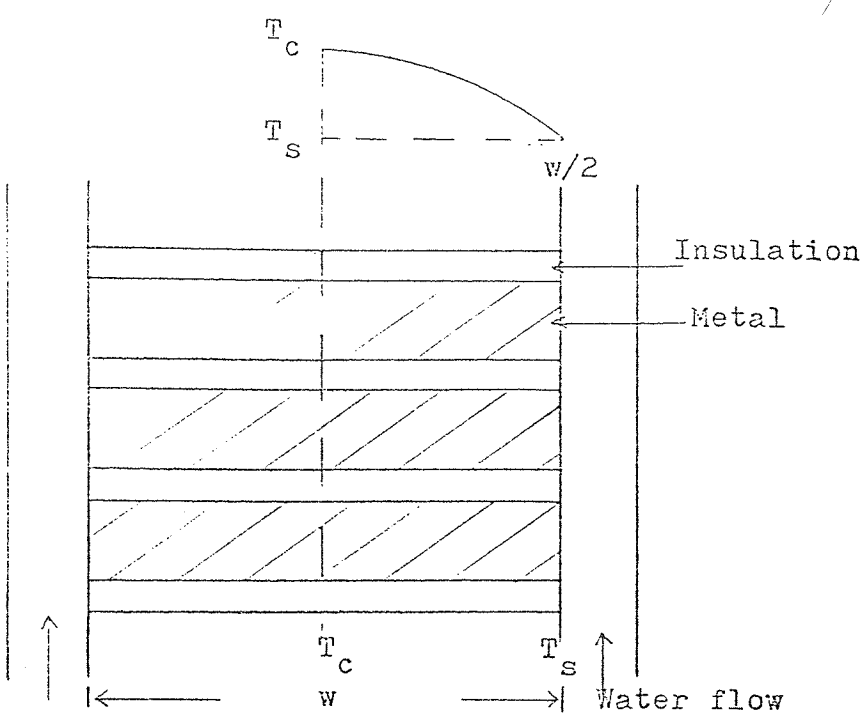

Fig. 2.6.9 Cross-section of a tape winding.

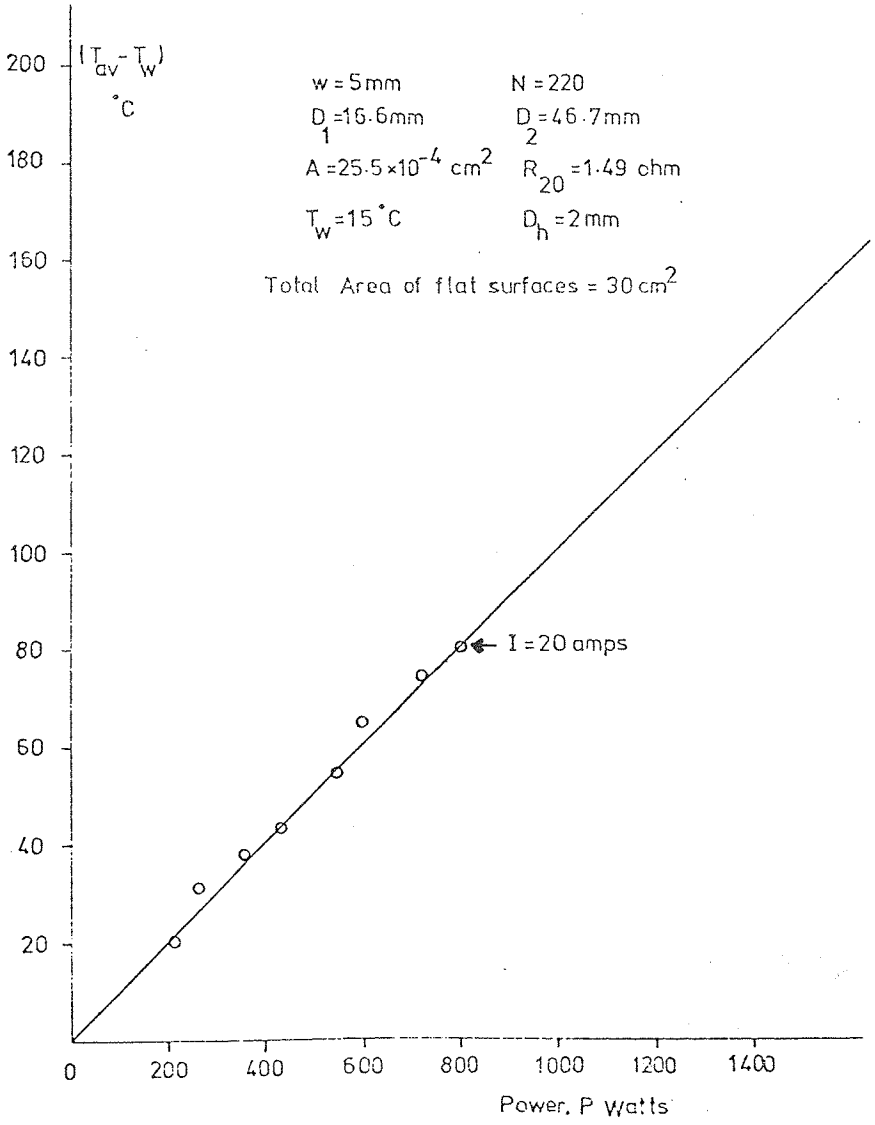

Fig. 2.6.10 Variation of the average temperature rise with the input power of a water-cooled copper tape coil.

characteristics are given in Figure 2.6.10. The power required to raise the average temperature of the coil to 200°C above water is 2000 watts (Figure 2.6.10). Therefore, the resistance at this temperature is 2.7 ohms; hence

$$I = 27 \text{ amperes}$$

$$\sigma = 10700 \text{ amp/cm}^2$$

$$\rho_{215} = 3 \times 10^{-6} \text{ ohm.cm}$$

It has been shown that the power density $H = \rho\sigma^2\lambda$ where $\lambda = 0.75$; therefore, $H = 258$ watts/cm^3. Also it has been shown in Appendix IV that

$$T_c - T_s = \frac{Hw^2}{8k_c} \qquad \ldots\ldots 2.6.8$$

where the width w is 5mm and k_c is the coefficient of thermal conductivity of the coil, i.e. $T_c - T_s = 2°C$. This shows that the temperature difference between the centre of the tape and its cooled surface is negligible. The difference between the average temperature of the coil and that of the cooling surface is given in Appendix IV by

$$T_{av} - T_s = \frac{2}{3}(T_c - T_s) \qquad \ldots\ldots 2.6.9$$

i.e. $T_{av} - T_s = 1.3°C$ at 1.5mm from the centre of the tape's width. Since T_{av} is taken as 215°C, thus $T_s = 213.7°C$. This surface temperature shows that the flowing water would be expected to boil.

Alternatively, the surface temperature can be calculated from the equation $T_s - T_w = q/h$ since the values of q, h and T_w at $T_{av} - T_w = 200°C$ are known from Figure 2.6.10; i.e.

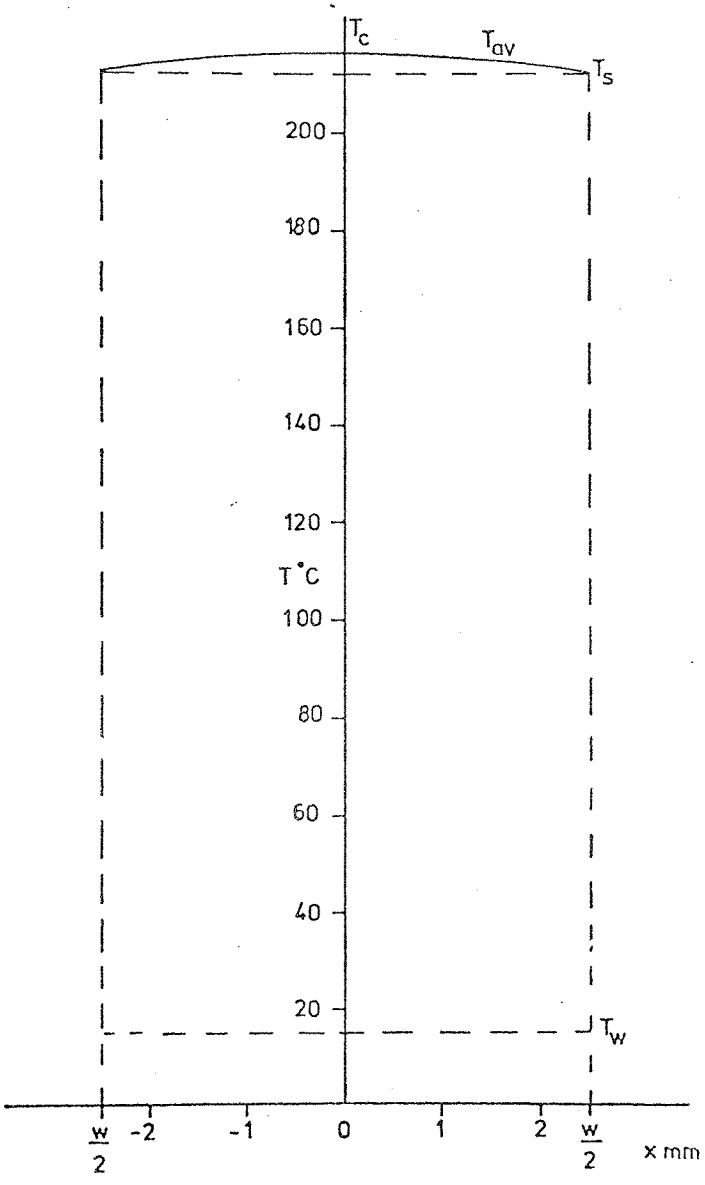

Fig. 2.6.11 Temperature distribution across the width of the copper tape coil in Figure 2.6.10.

$$q = 66 \text{ watts/cm}^2$$

$$h = 0.3 \text{ watt/cm}^2.^{\circ}C$$

$$T_w = 15^{\circ}C$$

hence $$T_s = 215^{\circ}C$$

which is in a very good agreement with the above result.

The temperature distribution across the width of the tape is shown clearly in Figure 2.6.11. If the velocity of water is increased, the heat-transfer coefficient will increase and hence more input power will be required to raise the average temperature of the coil to say 200°C above water. In this case the temperature difference between the centre and the surface of the tape will still be negligible but more current density and ampere-turns will be obtained.

From Equation 2.6.8 it can be seen that the maximum temperature can be reduced by a factor of four if the coil of width w is replaced by two coils, each of width w/2, using the same power density and with the water flowing between the coils. If the power density is increased, the two coils can produce more ampere-turns than the one coil of width w when the two are at the same maximum temperature as the one coil.

Consider the theoretical expressions for the current density (Equation 2.5.5) and the ampere-turns (Equation 2.5.11) of a tape coil derived from the disc model. The maximum current density and ampere-turns from the tape coil as a function of the width cooled under the same conditions as that in Figure 2.6.10, are shown in Figures 2.6.12 and 2.6.13. It can be seen that as the coil width increases the ampere-turns increase also while the current density decreases. These figures show also very good agreement between the theory and experiment.

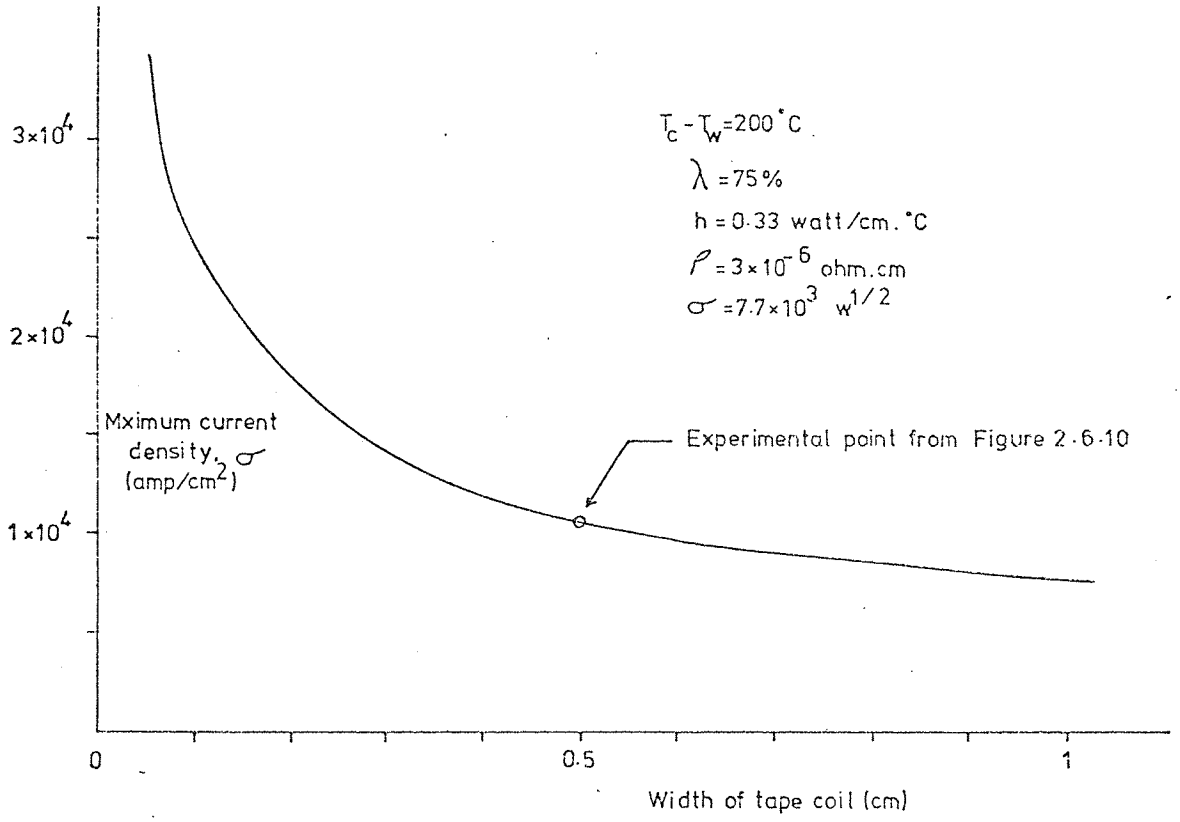

Fig. 2.6.12 Variation of the maximum current density in a tape coil with coil width at constant maximum temperature.

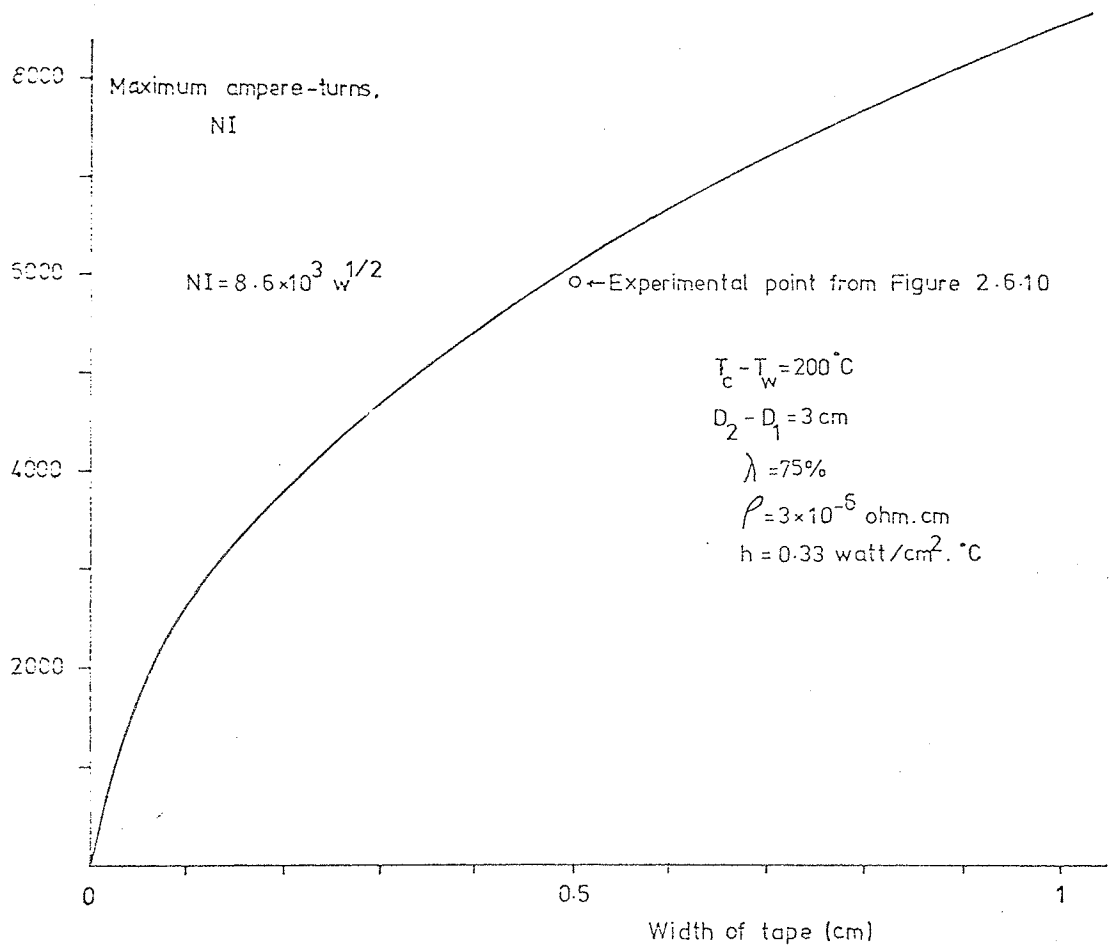

Fig. 2.6.13 Variation of the maximum ampere-turns in a tape coil with coil width at constant maximum temperature.

Wire Coils

Wire coils having two, four and eight layers were wound with 24. S.W.G. wire with the same outer and inner diameters as the single-layer and the tape coils. The characteristics of these coils are shown in Figures 2.6.14, 2.6.15, 2.6.16. The width of the eight-layer coil is 5mm which is the same as that of the tape. The coils were cooled under the same cooling conditions as the single-layer coil; therefore, at a water flow of 3.5 litres/minute, the heat-transfer coefficient was 0.46 watt/$cm^2.^oC$. From these characteristic curves, results were deduced for the maximum current density and ampere-turns and compared with the theoretical values which are calculated from the disc model (Equations 2.5.4 and 2.5.10). For the same power dissipated in the double-layer coil and the single-layer coil A, the double-layer coil gives more ampere-turns at a lower current density than the single-layer coil A when the maximum temperature is the same in both coils since they behave thermally the same; this is explained by the difference in the width. Figure 2.6.17 shows good agreement between theory and experiment for the variation of the maximum current density in a wire coil with the number of layers along the width. The disc model therefore seems an adequate description of coil behaviour. It can be seen that the current density decreases rapidly as the number of layers increase. It should be mentioned that for the 24 S.W.G. wire the two terms in the denominator of Equation 2.5.4 are nearly equal when the number of layers is eight. Below eight, the second term, which represents the equivalent tape, is the effective one, while above eight the first term becomes dominant. Hence, there is no considerable advantage in having a coil of more than eight layers along its width, as can be seen clearly in Figure 2.6.18.

The coils were wound on a brass ring mounted between two brass

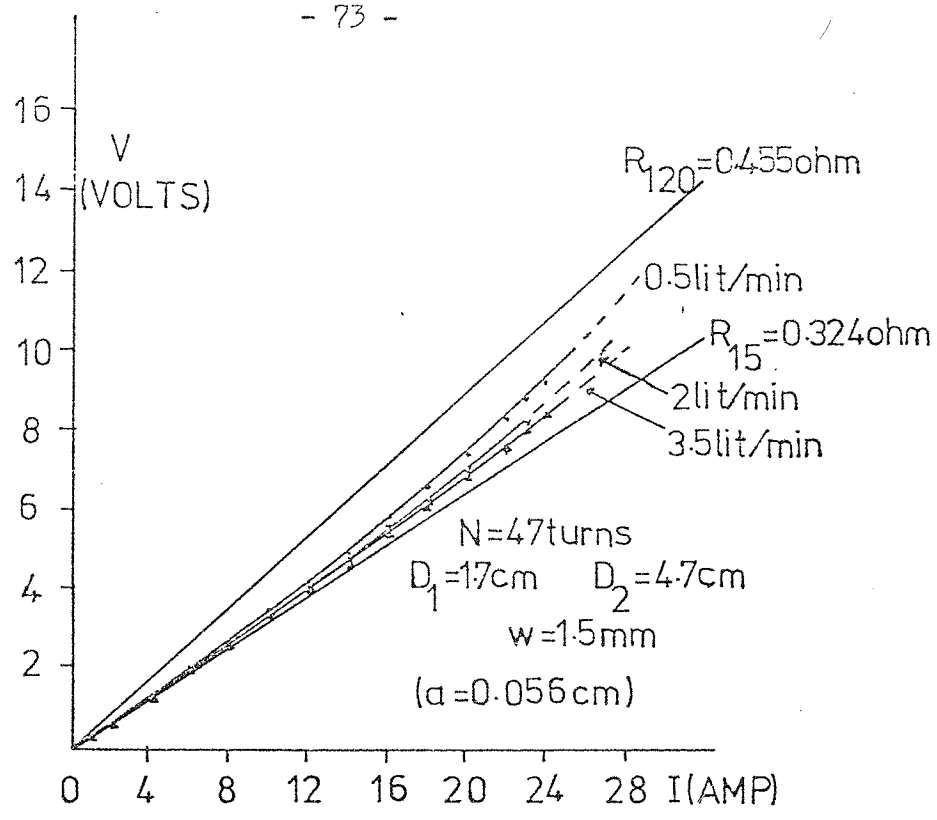

Fig. 2.6.14 Variation of the voltage with the current in the water-cooled double-layer wire coil of 24 S.W.G.

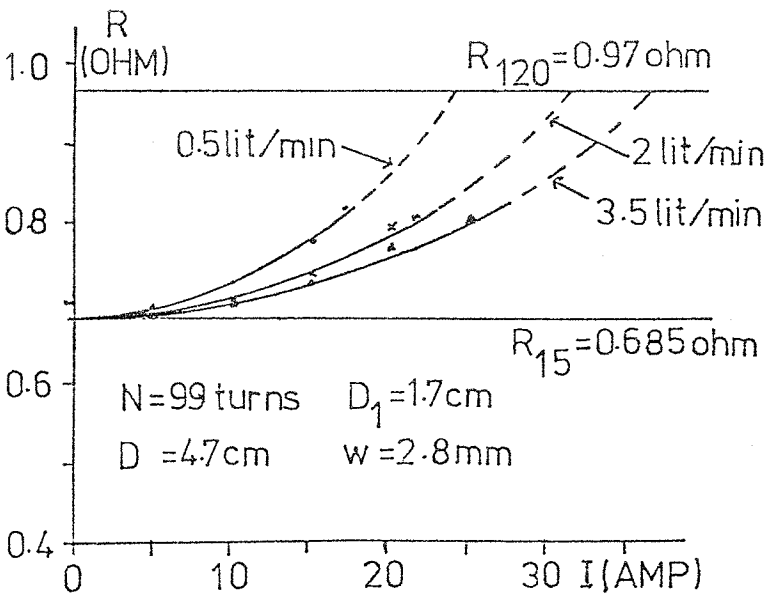

Fig. 2.6.15 Variation of the resistance with the current in the water-cooled four-layer coil of 24 S.W.G.

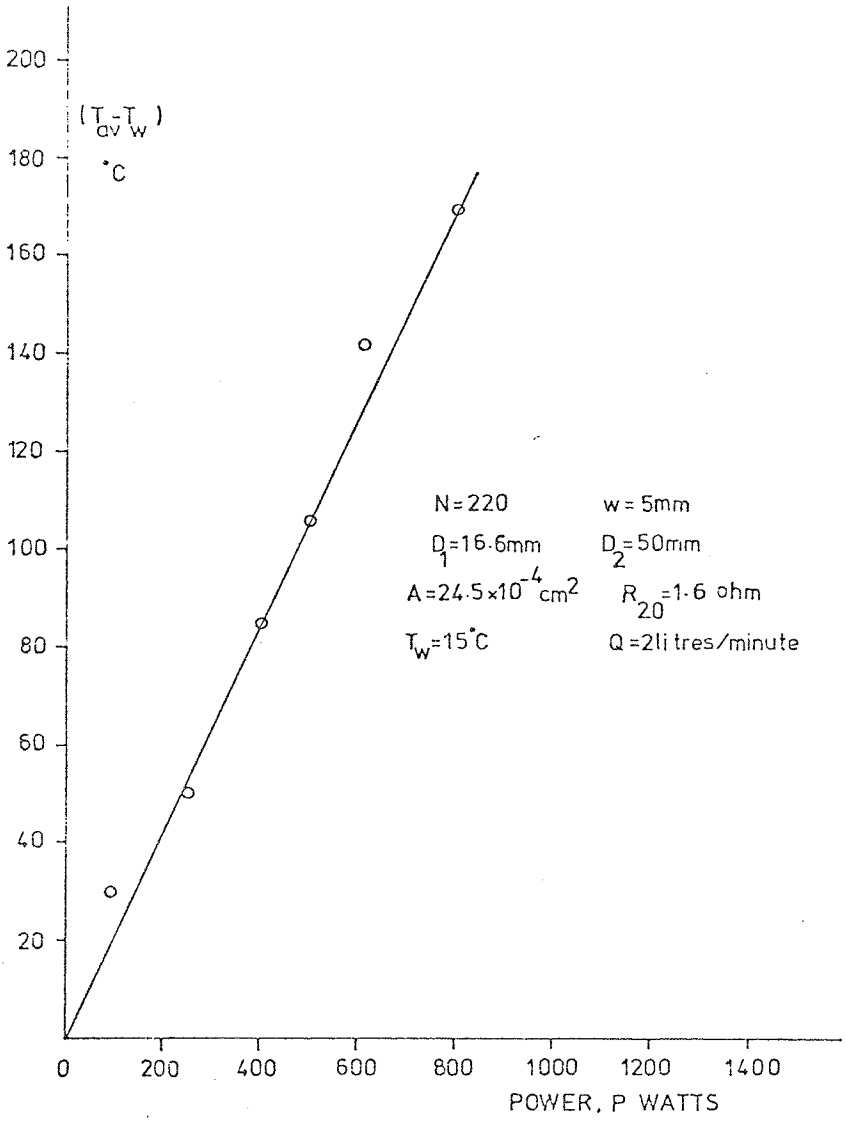

Fig. 2.6.16 Variation of the average temperature rise with input power of water-cooled eight-layer wire coil of 24 S.W.G.

formers. During the winding of the wire on the brass ring, it was painted with 'Araldite' to avoid air voids. In the theoretical calculations given in Figures 2.6.17 and 2.6.18 the effective coefficient of thermal conductivity of the 'Araldite' and the insulating enamel was taken from manufacturer's data as 3×10^{-3} watt/cm.°C. This is an approximate value only and since the wires are cylindrical, air spaces were almost certainly present between the layers this will tend to decrease the thermal conductivity of the whole coil ($k_{air} \simeq 10^{-4}$ watt.cm^{-1}.°C^{-1}). This uncertainty about the value of k_{in} is the main reason for the slight deviation between theory and experiment. This method of coil winding differs from that described by Kroon (1968) and applied to electron lenses by Maclachlan (1973) where the coil consisted of sub-coils wound on a former between cooling discs.

The overall thermal conductivity coefficient, k_c of the multi-layer coil ($n > 2$) can be derived from the disc model. It has been shown (Appendix V) that for a wire coil with an even number of layers

$$(k_c)_{even} = k_{in} \frac{n_e}{(1-\lambda)(n_e-2)} \qquad \ldots\ldots 2.6.10$$

and that for an odd number of layers

$$(k_c)_{odd} = k_{in} \frac{n_o^2}{(1-\lambda)(n_o-1)^2} \qquad \ldots\ldots 2.6.11$$

These two equations show that, for the same wire gauge, the three and four layer wire coils (five and six, etc.) have nearly the same thermal conductivity coefficient; hence it is important to use an even number of layers along the width.

Figure 2.6.19 summarizes the important parameters of wires as a function of wire diameter. This figure is useful in practical lens design in determining the number of layers along a specific width, the

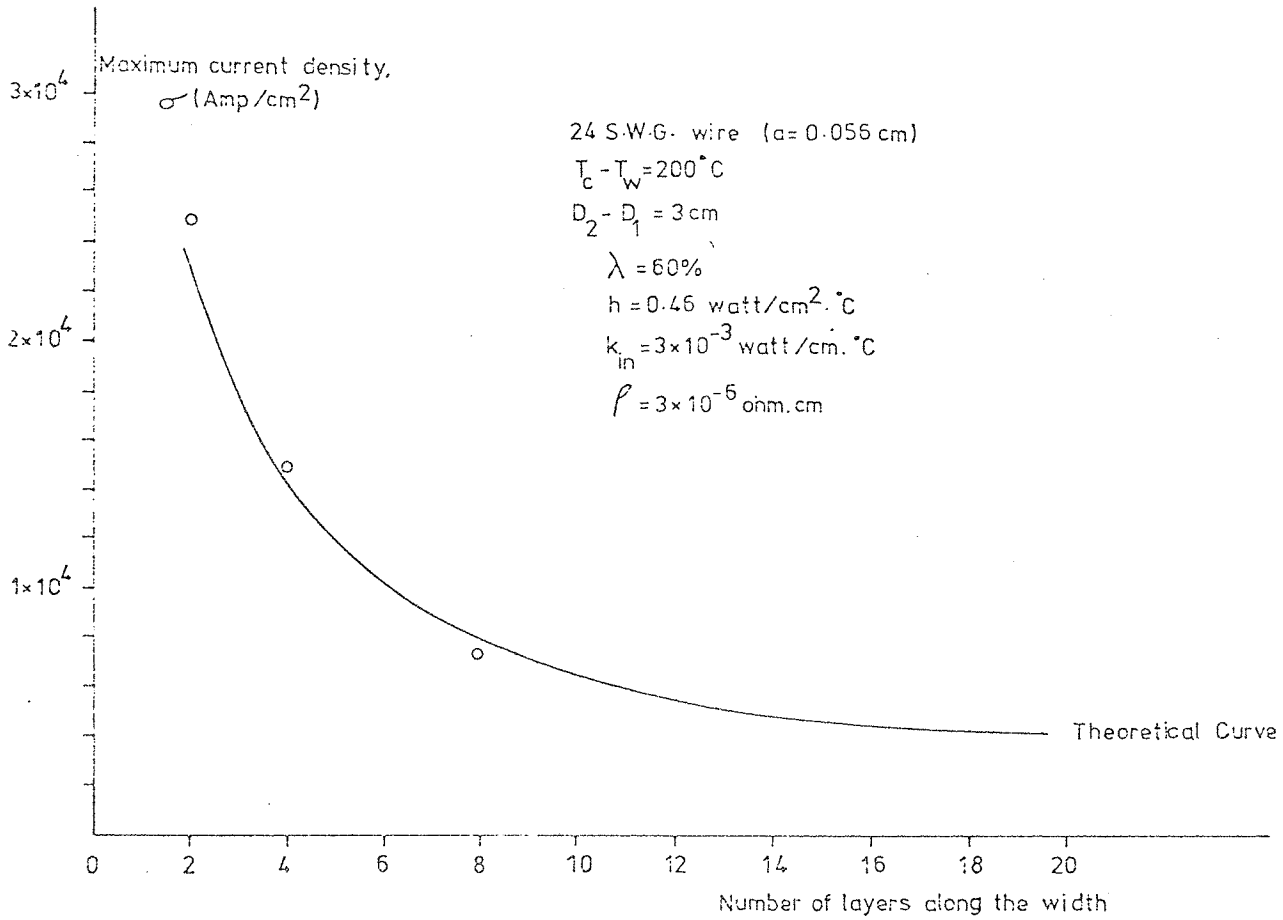

Fig. 2.6.17 Variation of the maximum current density in a water-cooled 24 S.W.G. wire coil with the number of layers across its width at constant maximum temperature.

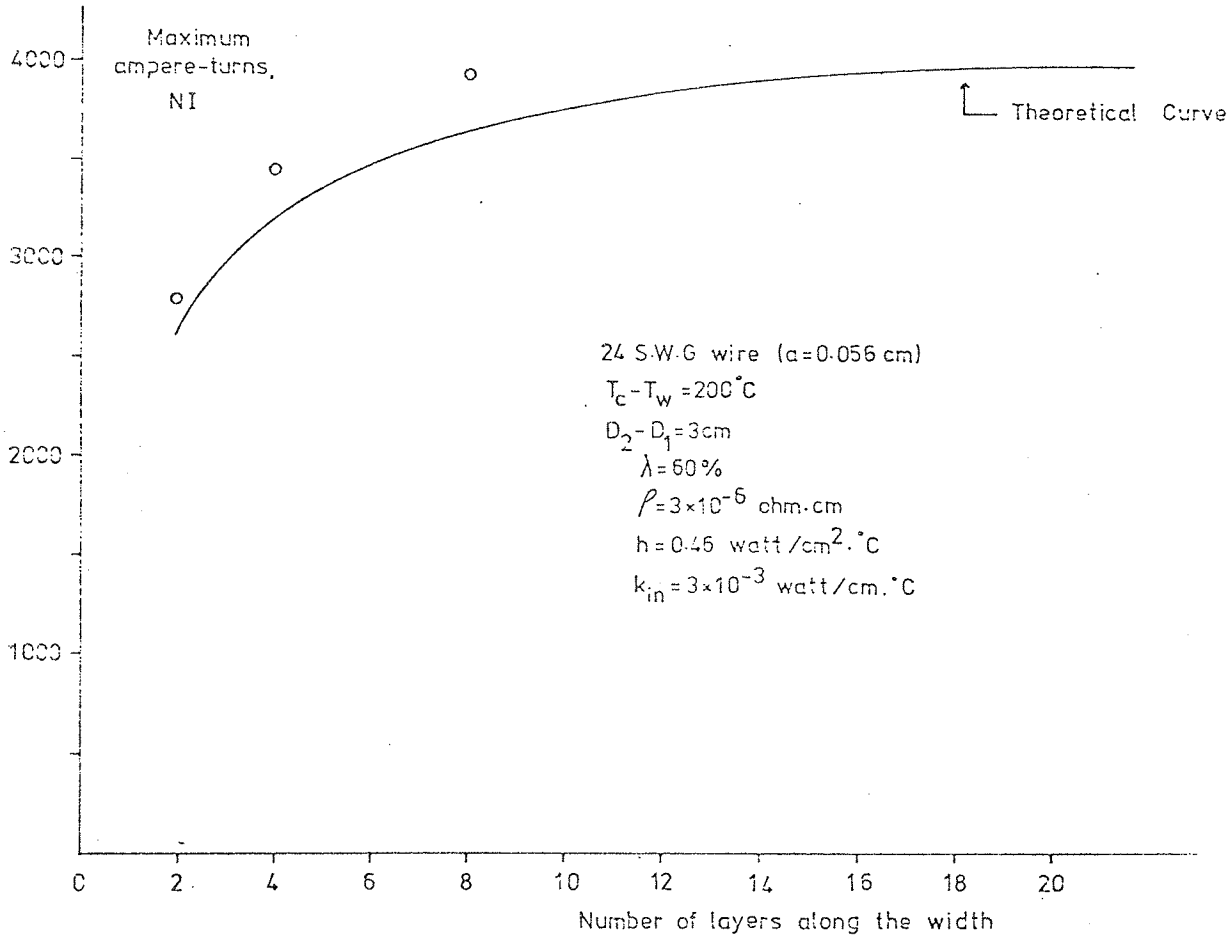

Fig. 2.6.18 Variation of the maximum ampere-turns in a water-cooled 24 S.W.G. wire coil with the number of layers along its width at constant maximum temperature.

percentage of insulation and the thermal conductivity. This figure shows that to ensure high thermal conductivity, as big a wire diameter as possible should be used.

To illustrate the temperature distribution across the width of a wire coil, consider the 5mm wide, eight-layer enamelled-copper wire coil (Figure 2.6.16). This figure shows that for multi-layer coils, the rise in the average temperature above that of water is a linear function of the input power as shown in Appendix IV. The coil is cooled by a water flow (T_w= 15°C) of 2 litres/minute through a 1mm gap (D_h= 2mm). The heat-transfer coefficient calculated from Equation 2.6.5 is 0.34 watt/cm.°C. The power required to raise the average temperature of the coil 150°C above water is 700 watts. Since the surface area of the flat faces of the coil is 35 cm^2, q = 20 watt/cm^2. Hence, the surface temperature is T_s= 74°C as calculated from Equation 2.1.1. Also since $(T_{av} - T_s) = \frac{2}{3}(T_c - T_s)$ where T_{av}=165°C, the maximum temperature T_c=210°C at the mid plane of the width is just on the limit of the insulation. However, this calculation is slightly pessimistic since it neglects the cooling over the curved edge of the coil. Figure 2.6.20 shows the parabolic temperature distribution across a wire coil 5mm wide. The temperature difference (136°C) between the centre and the cooled surface is very high compared with that of a comparable tape 2°C. The average temperature of the coil is less than that of the tape shown in Figure 2.6.11 when the maximum temperature T_c is the same for both. The power input to the tape was 2000 watts.

An alterative method of finding the temperature difference between the centre and the cooled surface is to determine the thermal conductivity of the whole coil. The accuracy of this method depends on the accuracy of the thermal conductivity of the insulation which accounts for about 10% of the coil width. It is the poor thermal

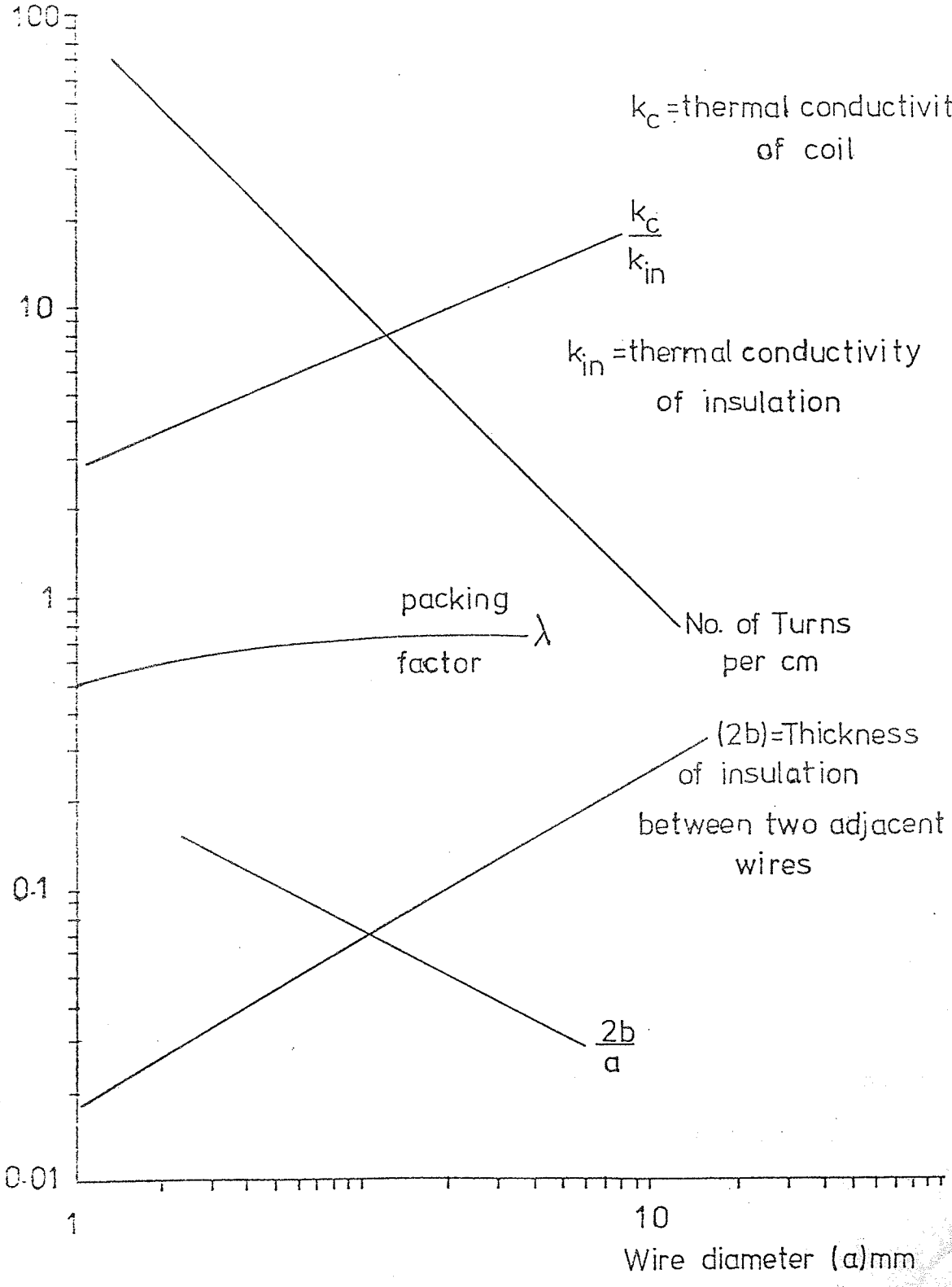

Fig. 2.6.19 Wire parameters as a function of wire diameter.

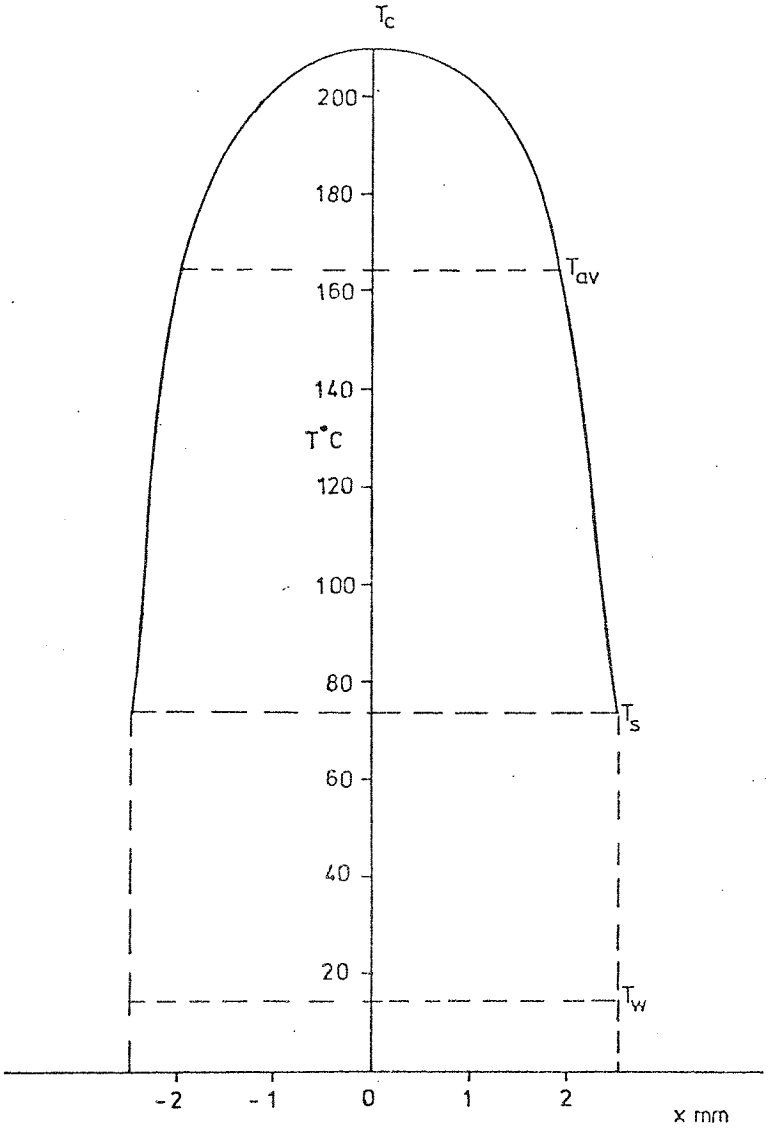

Fig. 2.6.20 Temperature distribution across the width of the copper wire coil shown in Figure 2.6.16.

conductivity of the electrical insulation that allows the build up of high temperature gradients along the width; this thermal conductivity is smaller than that of the conductor by a factor 10^3 and the temperature drop across the insulation is about 100 times greater than that across the conductor. The latter can therefore be neglected. The coefficient of thermal conductivity of the insulation is of the order 10^{-3} watt per cm per $^{o}C.$, k_c is therefore of the order 10^{-2} watt/cm.$^{o}C.$

2.7 Comparison between a tape and wire coil

The ampere-turns efficiency of a coil is defined as the number of ampere-turns NI gained per unit volume V. It can be seen from Equations 2.3.7 and 2.3.13 that the ampere-turns per unit volume of a coil is given by

$$\left(\frac{NI}{V}\right) = \frac{\sigma \lambda}{\pi D_m} \qquad \ldots\ldots 2.7.1$$

Equation 2.7.1 shows that for two identical tape and wire windings having the same current density, the ampere-turns per unit volume of a tape coil is more than that of a wire coil by the ratio of their packing factors. Also Equation 2.7.1 shows that coils of small mean diameter have better ampere-turns efficiency. This shows that the Le Poole's mini-lens of a long solenoid has higher ampere-turns efficiency than other types of lens windings.

Figure 2.7.1 shows the variation of ampere-turns with input power for a tape and wire coils cooled under the same conditions. The percentage difference in the packing factors of the two coils is equivalent to that in their volumes, i.e. $(\lambda V)_{tape} = (\lambda V)_{wire}$. Thus Figure 2.7.1 shows a good comparison between a tape and wire coil which are identical in all aspects. The figure shows that for a constant power, the ampere-turns of a tape coil is always more than that of a wire and at a lower average temperature. Also for the same number of

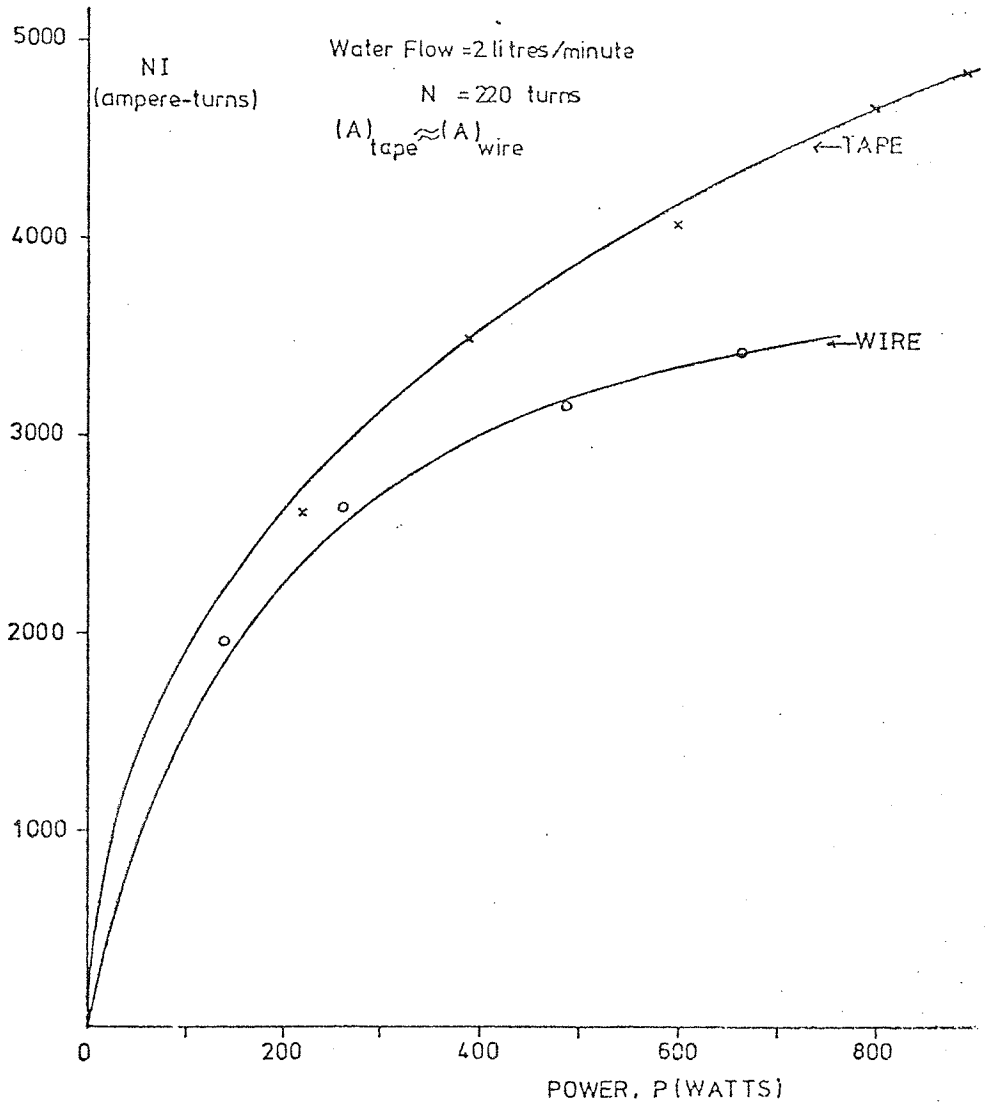

Fig. 2.7.1 Comparison between a tape coil and an identical wire coil cooled under the same conditions.

ampere-turns the tape coil requires always less power than the wire. At high power input the deviation between the two curves increases where the ampere-turns of the wire coil becomes approximately constant with the increase of power due to the heating-up of the wire. Therefore, the ampere-turns efficiency of a tape coil is always higher than that of an identical wire coil.

However, tape coils were not used in the miniature electron lenses described here because of the difficulty at present in obtaining supplies of suitable tape. It is found more convenient to use wire coils since they are easier to wind and insulate.

2.8 Conclusions

(a) In miniature water-cooled lenses the heat-transfer coefficient is not strongly dependent on flow rate, provided the water flow is laminar or quasi-laminar. Under these conditions there is very little danger of mechanical vibration caused by the water flow.

(b) In well designed coils, current densities normally associated with superconducting region can be obtained from water-cooled copper wire coils.

(c) In designing a wire coil it is important to have an even number of layers across its width; this number should preferably not exceed eight. Single and double-layer wire coils behave thermally exactly as a tape coil. Therefore, to gain a large number of ampere-turns at a small power dissipation it is preferable to use a series of double-layer coils separated from each other by water channels.

(d) A tape coil is always more efficient than the identical wire coil when operated under the same cooling conditions.

3. DOUBLE-POLE ROTATION-FREE LENSES

The basic principles of double-pole electron magnetic lenses have been discussed briefly in Chapter One. Since most commercial microscopes use double-pole lenses, it is relevant to consider the properties of double-pole rotation-free lenses. These consist of two double-pole lenses mounted in close proximity to each other and arranged so that the ampere-turns of one oppose the ampere-turns of the other. Hence the rotation produced by each field will be equal and opposite, since the angle of rotation, Θ depends directly on the strength of the field B_z. The focusing power of each of the two lenses on the other hand depends on B_z^2 and hence is independent on the direction of rotation. The focal properties of a double-lens system having $(NI)_1 = -(NI)_2$ are therefore the same as that with $(NI)_1 = +(NI)_2$.

The principal parameters of a magnetic lens are: magnification, focal length, principal planes and the angle of rotation. The magnification and the focal length of a double-lens projective system of conventional construction can be studied to a good approximation by using the rectangular field mentioned in Chapter One.

3.1 Magnification of a rotation-free projector lens

Consider the two rectangular field distributions, L_1 and L_2 (Figure 3.1.1) of two double-pole lenses of different geometries and different excitations. In Figure 3.1.1, ℓ represents the distance between the centre lines of the two fields, i.e. $\ell = \ell' + \frac{L_1}{2} + \frac{L_2}{2}$. The two fields represent the double-lens system. This double-system is assumed to be used as a final projector lens in a microscope. It is shown in (Appendix VI) that by solving the paraxial ray equation

$\frac{d^2r}{dz^2} + k^2r = 0$ for the trajectory of a parallel electron beam

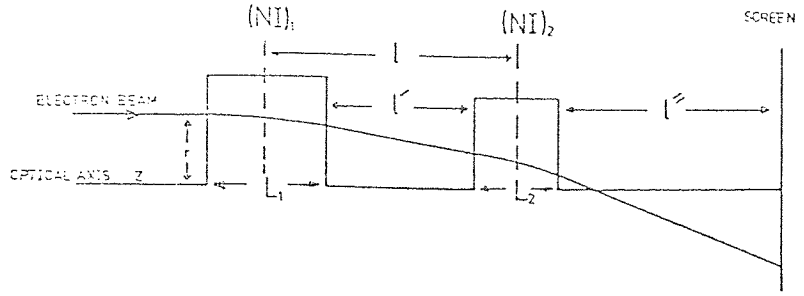

Fig. 3.1.1 Ray path of a parallel electron beam entering two displaced rectangular fields which form the double-lens system.

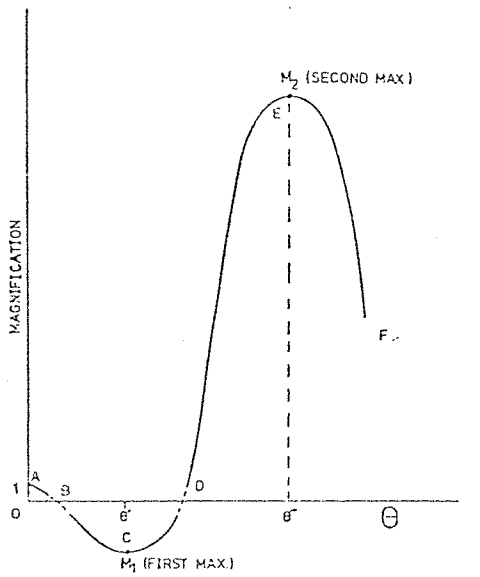

Fig. 3.1.2 Variation of the magnification of a rotation-free lens with the excitation function, O.

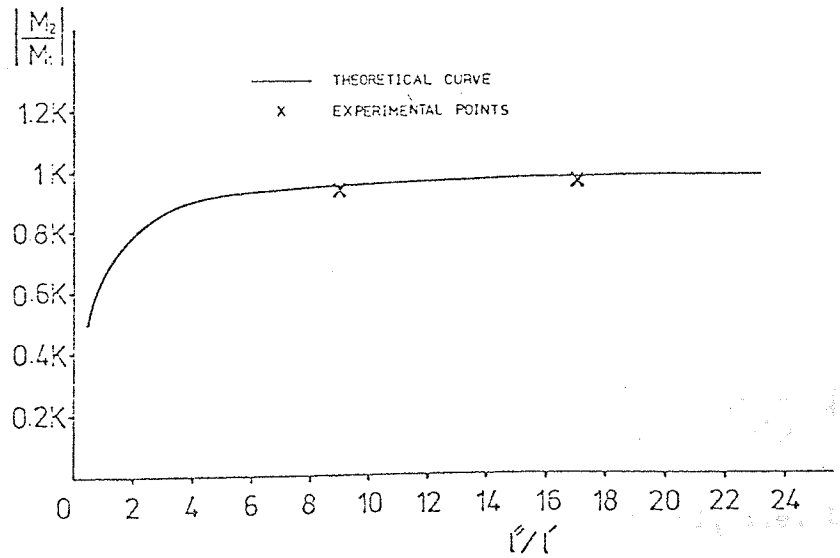

Fig. 3.1.3 The ratio of the first two maximum magnifications M_2/M_1 as a function of the l''/l' ratio.

entering the first field and projecting an image on the screen or photographic plate, the magnification M of this double lens system is given by:

$$M = \cos\theta_1 \cos\theta_2 - \ell'\frac{\theta_1}{L_1}\sin\theta_1\cos\theta_2 - \frac{\theta_1}{\theta_2}\cdot\frac{L_2}{L_1}\sin\theta_1\sin\theta_2 -$$

$$\ell''\left[\frac{\theta_1}{L_1}\sin\theta_1\cos\theta_2 + \frac{\theta_2}{L_2}\cos\theta_1\sin\theta_2 - \ell'\frac{\theta_1\theta_2}{L_1L_2}\sin\theta_1\sin\theta_2\right] \quad \ldots\ldots 3.1.1$$

where $\theta = 0.186\ NI/V_r^{\frac{1}{2}}$

Equation 3.1.1 shows that when the two lenses are not excited, i.e. NI = 0, the magnification is unity as expected. The magnification is independent of the sign of θ as expected. If only one lens is excited, the magnification becomes

$$M = \cos\theta_2 - \frac{\ell''}{L_2}\theta_2\sin\theta_2$$

which is the same expression as that of a single projector lens.

Since the magnetic field is a function of the lens excitation, the two fields can be made equal and opposite by having the ampere-turns of both lenses equal and opposite, i.e. $(NI)_1 = -(NI)_2$ or $\theta_1 = -\theta_2 = \theta$. This double gap system can thus produce an image on the screen free from rotation. The magnification given by

$$M = \cos^2\theta - \frac{\ell'}{L_1}\theta\sin\theta\cos\theta - \frac{L_2}{L_1}\sin^2\theta -$$

$$\ell''\left[\left(\frac{1}{L_1} + \frac{1}{L_2}\right)\theta\sin\theta\cos\theta - \frac{\theta^2}{L_1L_2}\ell'\sin^2\theta\right] \quad \ldots\ldots 3.1.2$$

If the two conventional lenses are identical, i.e. $L_1 = L_2 = L$, where $L = \sqrt{S^2 + 0.45D^2}$, the magnification M given in Equation 3.1.2 can be written as

$$M = \text{Cos } 2\theta - \left(\frac{\ell'}{2} + \ell''\right) \frac{\theta}{L} \text{ Sin } 2\theta + \ell' \ell'' \left(\frac{\theta}{L} \text{ Sin } \theta\right)^2 \quad \ldots\ldots 3.1.3$$

where in this case $\ell' = \ell - L$. It should be noted that if the two fields are brought side by side such that $\ell' = 0$, Equation 3.1.3 becomes

$$M = \text{Cos } 2\theta - \frac{\ell''}{L} \theta \text{ Sin } 2\theta$$

which is the expression expected for a single lens with a field width of 2L. If the second lens is placed near the screen, so that $\ell'' = 0$, Equation 3.1.3 becomes

$$M = \text{Cos } 2\theta - \frac{\ell'\theta}{2L} \text{ Sin } 2\theta$$

which is the expression for the magnification by a single lens. If high magnification is required, the second lens must be placed away from the first lens and the screen. The maximum magnification is obtained when the second lens is midway between the screen and the first lens i.e. $\ell' = \ell''$.

Figure 3.1.2 shows the general shape of the curve given by Equation 3.1.3. It should be noted that from unit magnification at A to the first minimum at B, the term Cos 2θ is the dominant one while the rest are negligible. From B, the (θ Sin 2θ) term becomes effective and it is always higher than the term $\ell' \ell'' \left(\frac{\theta}{L} \text{ Sin } \theta\right)^2$. At C the first maximum magnification M_1 is obtained; and due to the effect of the $\text{Sin}^2\theta$ term, then the absolute value of M_1 can approximately be written as

$$|M_1| \simeq \frac{1}{2} \left(\frac{\ell'}{2} + \ell''\right) \frac{\theta'}{L} \text{ Sin } 2\theta' \quad \ldots\ldots 3.1.4$$

The $\text{Sin}^2\theta$ term increases considerably after the first maximum magnification until it becomes the dominant term from D to E. At the point E, the second maximum magnification M_2 is obtained where

$$|M_2| \simeq \frac{\ell' \ell''}{L^2} (\theta'' \text{ Sin } \theta'')^2 \quad \ldots\ldots 3.1.5$$

Hence the ratio of the two maxima M_1 and M_2 is given by

$$\left|\frac{M_2}{M_1}\right| \simeq \frac{2\ell''}{(2\ell'' + \ell')} \left[\frac{2\ell' (\theta'' \text{ Sin } \theta'')^2}{L\,\theta' \text{ Sin } 2\theta'}\right] \quad \ldots\ldots 3.1.6$$

The term $\left[2\ell'(\theta'' \text{ Sin } \theta'')^2/L\theta' \text{ Sin } 2\theta'\right]$ depends on the lens geometry and is therefore a constant for a specific lens arrangement. Equation 3.1.6 shows that, for a given lens system, the ratio $\left|\frac{M_2}{M_1}\right|$ is approximately independent of the lens-to-screen distance ℓ'' when the field separation ℓ' is small compared with $2\ell''$. Figure 3.1.3 shows that the $\left|\frac{M_2}{M_1}\right|$ ratio is independent of ℓ'' when $\ell''/\ell' \geqslant 6$ for the same lens system.

3.2 Focal length of a double-pole rotation-free projector lens

The focal length of a double-gap projector lens can be derived from the paraxial ray equation. Considering Figure 3.1.1. It is shown in (Appendix VI) that the projector focal length F_p of this system, consisting of two double-pole lenses of different geometry, is given by

$$F_p = -\left[\frac{\theta_1}{L_1} \text{ Sin } \theta_1 \text{ Cos } \theta_2 + \frac{\theta_2}{L_2} \text{ Cos } \theta_1 \text{ Sin } \theta_2 - \frac{\theta_1\theta_2}{L_1L_2}\, \ell' \text{Sin } \theta_1 \text{ Sin } \theta_2\right]^{-1}$$

$\ldots\ldots 3.2.1$

Equation 3.2.1 shows that the projector focal length of the double-gap lens is independent of the field direction. For a double-gap rotation-free lens, where $\theta_1 = -\theta_2 = \theta$, the focal length becomes

$$F_p = -\left[\left(\frac{1}{L_1} + \frac{1}{L_2}\right)\frac{\theta}{2} \text{ Sin } 2\theta - \frac{\ell'}{L_1L_2} (\theta \text{ Sin } \theta)^2\right]^{-1} \quad \ldots\ldots 3.2.2$$

Equations 3.2.1 and 3.2.2 show also what is expected electron-optically that when NI = 0 in both gaps the refractive power of the whole system is zero, i.e. $F_p = \infty$. Considering the case when both

gaps are identical, i.e. $L_1 = L_2 = L$, the projector focal length of this rotation-free lens is

$$F_p = -\left[\frac{\Theta}{L}\,\mathrm{Sin}\,2\Theta - \frac{\ell'}{L^2}\,(\Theta\,\mathrm{Sin}\,\Theta)^2\right]^{-1} \qquad \ldots\ldots\ 3.2.3$$

Normalising the focal length in terms of the gap width L, Equation 3.2.3 becomes

$$\left(\frac{F_p}{L}\right) = \frac{-1}{\Theta\,\mathrm{Sin}\,2\Theta - \frac{\ell'}{L}\,(\Theta\,\mathrm{Sin}\,\Theta)^2} \qquad \ldots\ldots\ 3.2.4$$

Equation 3.2.4 shows that if $\frac{\ell'}{L}$ is infinite, $\frac{F_p}{L}$ approaches zero. Figure 3.2.1 shows a family of curves which represent Equation 3.2.4 where the relative projector focal length (F_p/L) is plotted as a function of the excitation parameter $NI/V_r^{\frac{1}{2}}$ for different values of $\frac{\ell}{L}$ ratio. It can be seen that for $NI/V_r^{\frac{1}{2}}$ increasing from zero to say 15, two minimum values of $\frac{F_p}{L}$ appear; one is negative, giving rise to the first maximum magnification M_1 at C in Figure 3.1.2 and the other is positive and small where the second maximum magnification M_2 at E is obtained.

It should be noted that for $\ell'/L = 0$ (i.e. $\ell/L = 1$), Equation 3.2.4 reduces to that for a single projector lens of gap width 2L; and Figure 3.2.1 shows that the first minimum value of F_p/L is one, at an excitation $NI/V_r^{\frac{1}{2}} = 5.3$. As the ratio of ℓ/L increases, the value of the first minimum (F_p/L) increases linearly (Figure 3.2.2), while the second minimum (F_p/L) decreases, Figure 3.2.3. The excitation parameter $NI/V_r^{\frac{1}{2}}$ required for minimum (F_p/L), decreases as the ratio of ℓ/L increases, Figure 3.2.4, and as $\ell/L \gtrsim 6$, $(F_p/L)_{min}$ in both loop becomes nearly independent of $NI_o/V_r^{\frac{1}{2}}$.

Figure 3.2.2 shows that the first minimum projector focal length

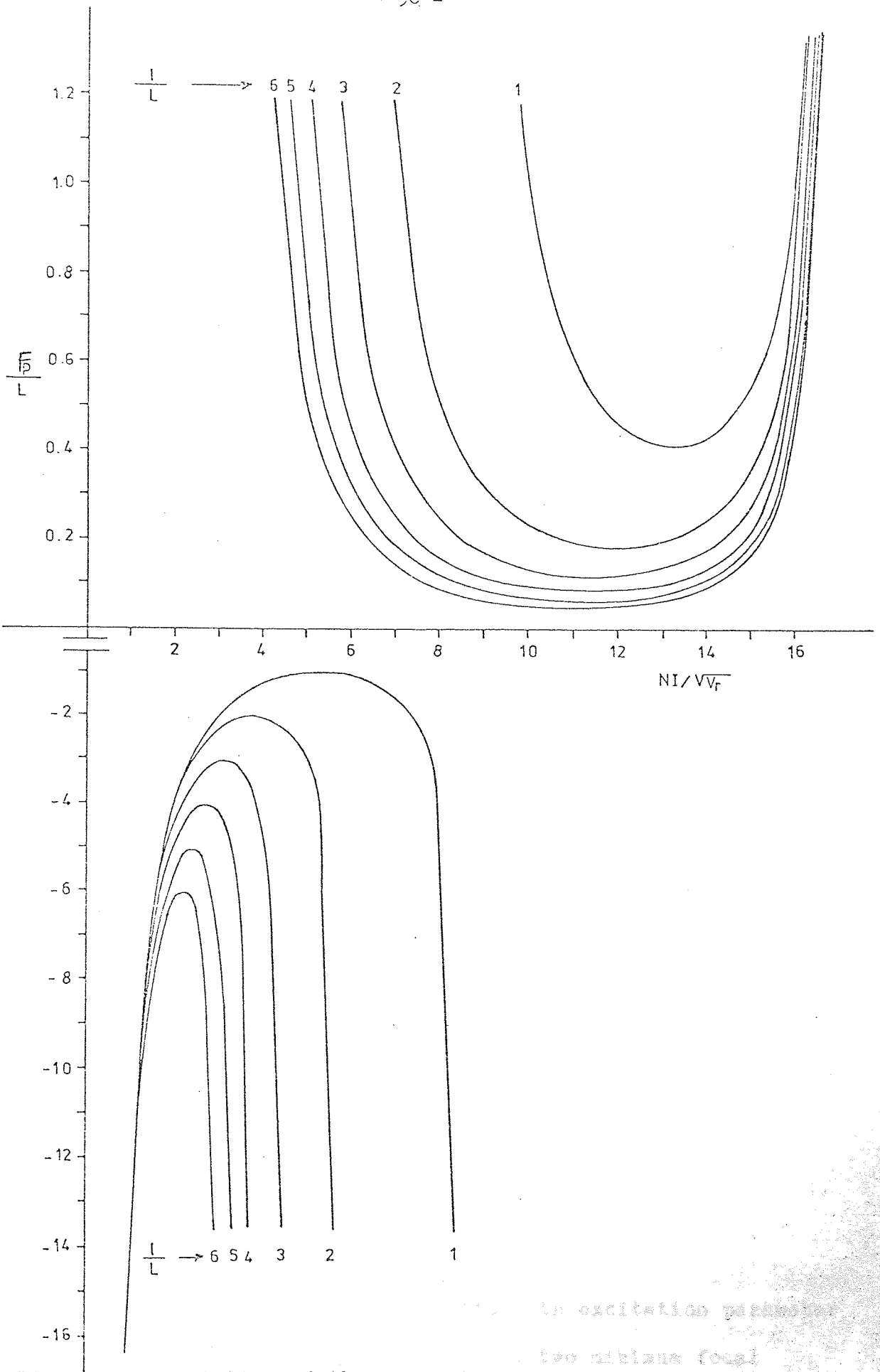

Fig. 3.2.1 Variation of the normalised projector focal length F_p/L with the excitation parameter $NI/V_r^{\frac{1}{2}}$ for different ratio of ℓ/L at the first two loops.

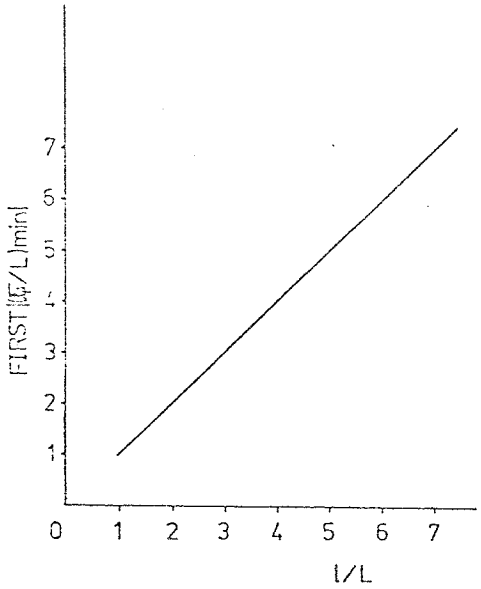

Fig. 3.2.2 Relationship between the minimum value of F_p/L in the first loop and the ℓ/L ratio.

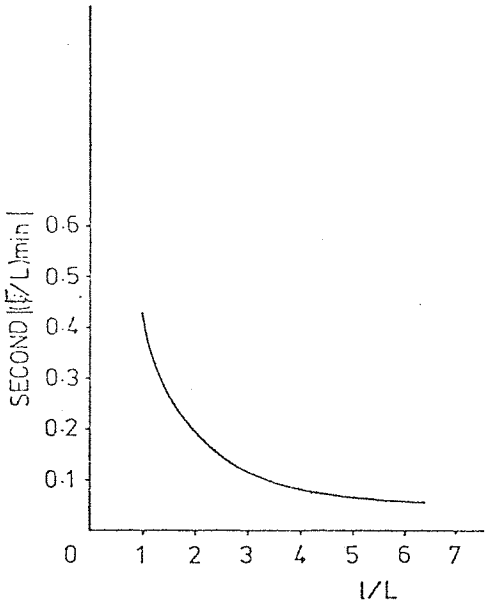

Fig. 3.2.3 Decrease of the minimum value of (F_p/L) in the second loop with the increase of the ℓ/L ratio.

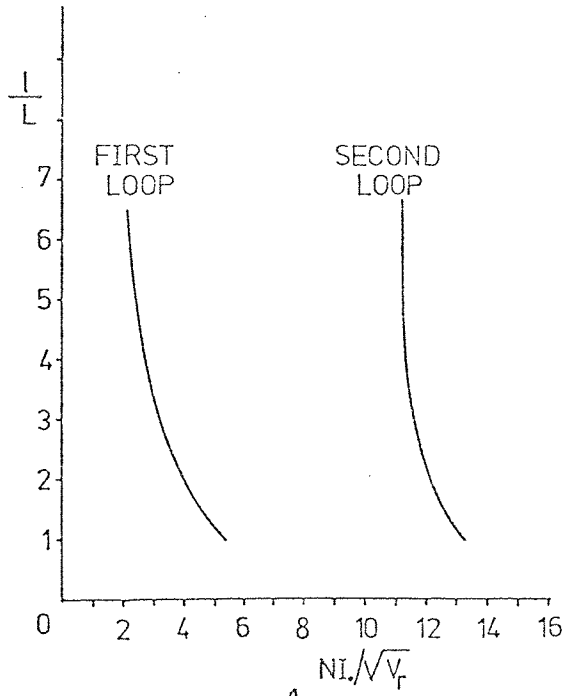

Fig. 3.2.4 Variation of the ℓ/L ratio with excitation parameter $NI_o/V_r^{\frac{1}{2}}$ required at the first two minimum focal lengths of a rotation-free lens.

is always equal to the gap separation ℓ; i.e. $F = \ell$. The ray diagram (Figure 3.2.5) for this special case shows that: (a) the focal length f_p of the first lens is also equal to the projector focal length of the rotation-free lens, (b) the second lens is located at the focal point of the first lens and (c) the image is inverted and at its first maximum magnification. This image is expected to be distortion-free according to Hillier's theory which was discussed in Chapter One.

In light optics, the general equation which represents two thin lenses in air of focal lengths f_1 and f_2 separated by a distance ℓ is

$$\frac{1}{F^1} = \frac{1}{f_1} + \frac{1}{f_2} - \frac{\ell}{f_1 f_2}$$

i.e. $$F^1 = f_1 f_2 / (f_1 + f_2 - \ell)$$

where F' is the focal length of the combined system. In electron optics, when the rotation-free projector lens is operated at low excitations, i.e. in the region of the first loop, the two gaps can be considered as thin lenses. If the lenses are identical with $(NI)_1 = -(NI)_2$ thus $f_1 = f_2 = f_p$. But $f_p = \ell$ at the first maximum magnification; hence by putting ℓ for f_1 and f_2 in the above equation, the combined focal length $F^1 = \ell$, as predicted in the previous theory. Therefore, in the first loop, the projector focal length F_p of the rotation-free lens can be determined by using the above equation and conditions. Hence $F_p = f_p^2/(2f_p - \ell)$ applies up to the value of $f_p = \ell/2$ where F_p will be infinite i.e. the beam leaves the last lens parallel to the optical axis as can be seen by the ray diagram shown in Figure 3.2.6.

At high excitations, the term Sin 2Θ in Equation 3.2.4 is small compared with the $\text{Sin}^2\Theta$ term; hence the equation can be reduced to

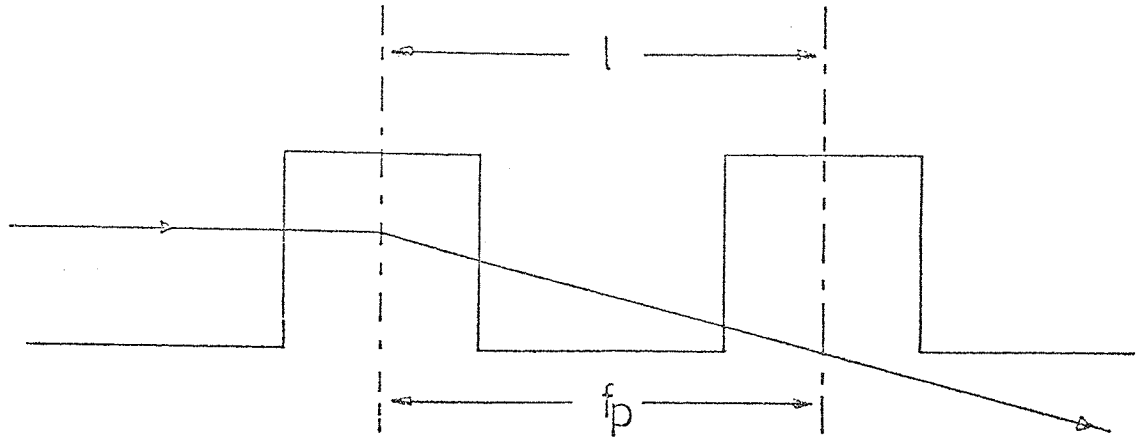

Fig. 3.2.5 Ray path of the electron beam when the rotation-free lens is at its first minimum projector focal length.

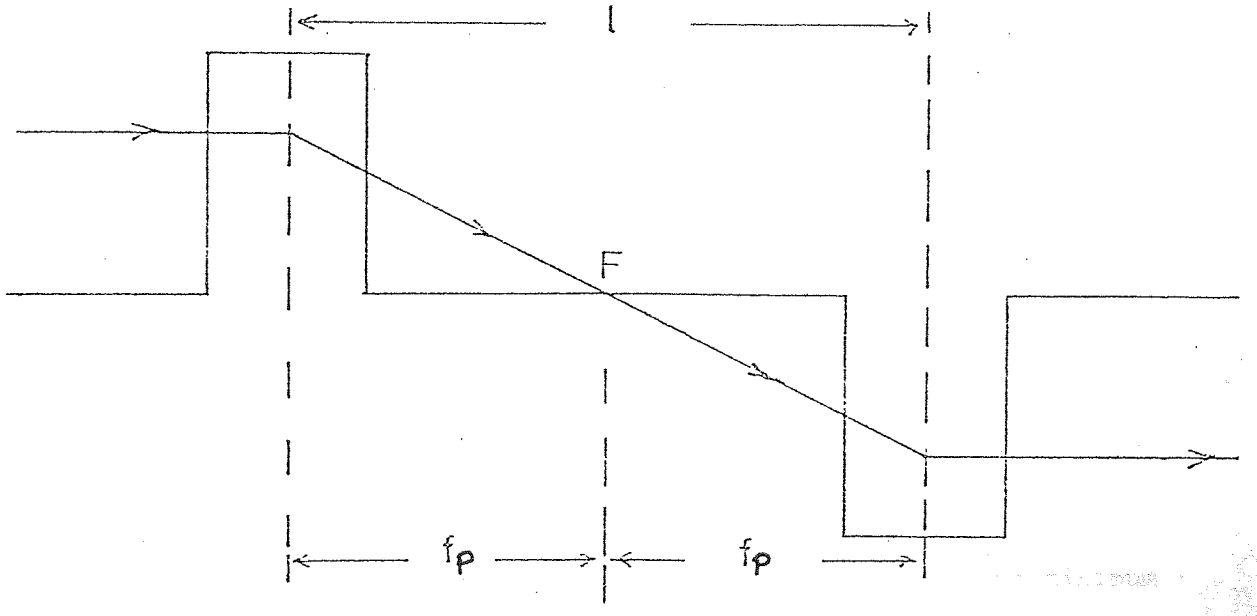

Fig. 3.2.6 Ray path of a parallel elector beam passing through the fields of a rotation-free lens at an infinite focal length (telescopic ray path).

$$F_p = \frac{L_1 L_2}{\ell' (\theta \sin \theta)^2} \qquad \ldots\ldots 3.2.5$$

Since the projector focal length of the two double-pole lenses is given by $f_{p_1} = \frac{L_1}{\theta \sin \theta}$ and $f_{p_2} = \frac{L_2}{\theta \sin \theta}$, hence

$$F_p = \frac{f_{p_1} f_{p_2}}{\ell'} \qquad \ldots\ldots 3.2.6$$

This applies only at high excitations near the second minimum focal length. Hence, Equation 3.1.5 can be written as

$$M_2 \simeq \frac{\ell' \ell''}{f_{p_1} f_{p_2}} \qquad \ldots\ldots 3.2.7$$

Equation 3.2.7 shows that M_2 is approximately equal to the product of the magnifications of the two gaps. If the two gaps are identical in geometry and excitation, i.e. $f_{p_1} = f_{p_2} = fp$

$$(Fp)_{min} = \frac{(f_p)^2_{min}}{\ell'} \qquad \ldots\ldots 3.2.8$$

and

$$(M)_{max} = \ell''/(Fp)_{min} \qquad \ldots\ldots 3.2.9$$

Equations 3.2.8 and 3.2.9 are very useful in calculating the minimum focal length and maximum magnification of a rotation-free lens whose gaps are identical.

Universal curves of the rotation-free projector lenses for the first two loops are shown in Figure 3.2.7. The figure shows the relative focal length $(F_p/L)/(F_p/L)_{min}$ as a function of the relative excitation NI/NI_o, where NI_o is the excitation required to obtain the minimum projector focal length, at a given accelerating voltage.

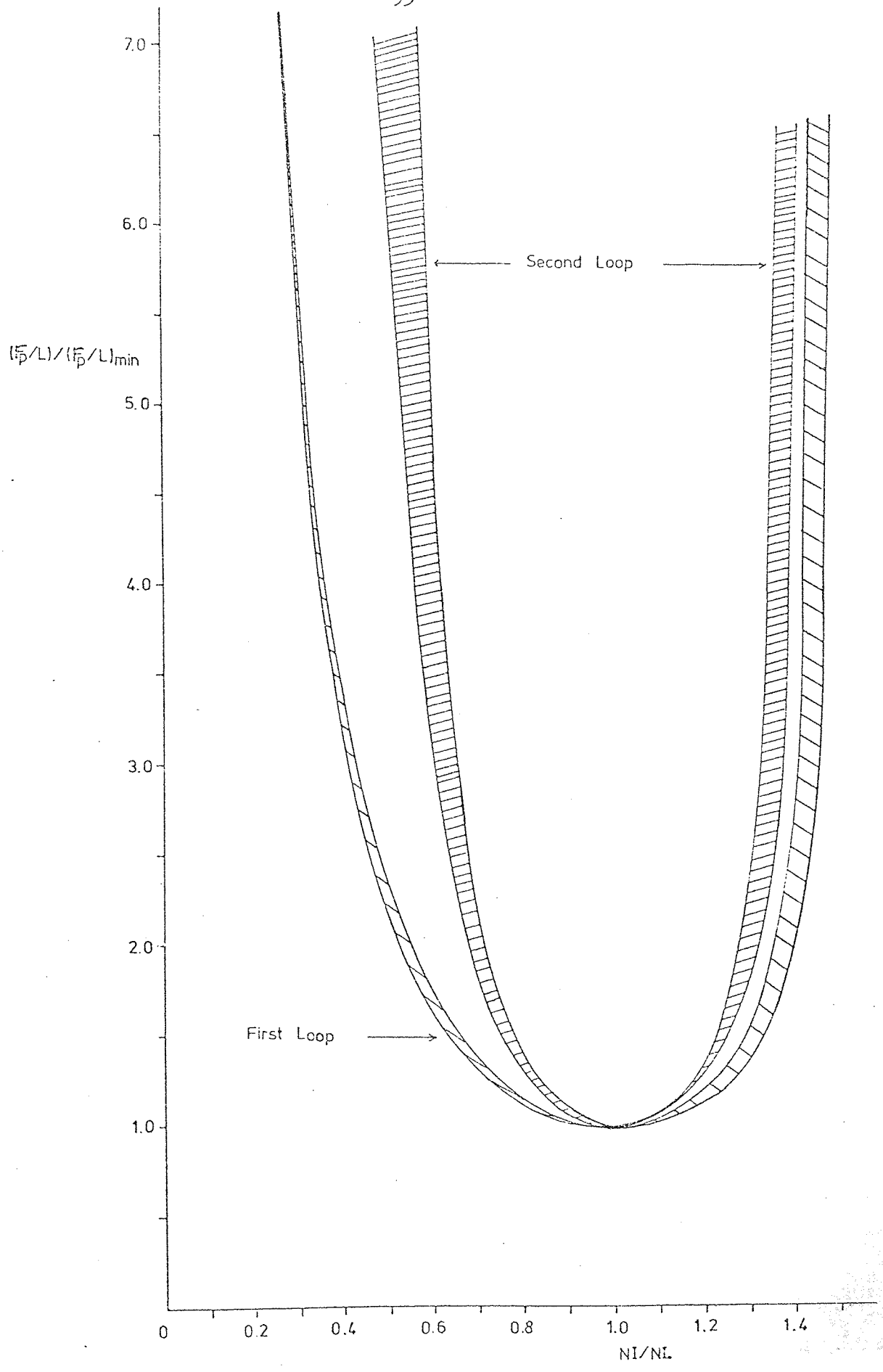

Fig. 3.2.7 Universal curves of the first two loops for all double-pole rotation-free lenses which have $\ell/L > 1$.

These curves include all conventional double-gap lenses whose ℓ/L ratio is greater than unity. In fact there is no advantage in having a rotation-free lens whose ℓ/L ratio is one. In practice, such a lens will suffer from field interaction; it can also be difficult to construct. Hence, from a practical point of view, the ratio ℓ/L will generally be greater than one.

Table 3.1 shows the computed results of the minimum values of (F_p/L) at the first six loops and their corresponding excitation parameter $NI_o/V_r^{\frac{1}{2}}$. It can be seen that for a specific ratio of ℓ/L the values of $(F_p/L)_{min}$ decrease with the increase of $NI_o/V_r^{\frac{1}{2}}$. Loops 1, 3 and 5 i.e. when (F_p/L) is negative show that $(F_p/L)_{min}$ increases with the increase of ℓ/L ratio while $NI_o/V_r^{\frac{1}{2}}$ decreases. Loop 6 shows that when $\ell/L \geq 4$, $(F/L)_{min}$ will occur at the same excitation parameter $NI_o/V_r^{\frac{1}{2}} = 43$.

Loop		1	2	3	4	5	6
$\frac{\ell}{L}=1$	$(\frac{F}{L}p)_{min}$	-1.1	0.415	-0.253	0.1812	-0.1412	0.1156
	$NI_o/V_r^{\frac{1}{2}}$	5.4	13.2	21.4	29.8	38.2	46.6
$\frac{\ell}{L}=2$	$(F_p/L)_{min}$	-2.051	0.19	-1.085	0.0386	-1.031	0.01526
	$NI_o/V_r^{\frac{1}{2}}$	3.8	12	18.2	27.2	34.6	43.4
$\frac{\ell}{L}=3$	$(\frac{F}{L}p)_{min}$	-3.03	0.1184	-2.056	0.0254	-2.05	0.00783
	$NI_o/V_r^{\frac{1}{2}}$	3.2	11.6	17.6	26.8	34.2	43.2
$\frac{\ell}{L}=4$	$(\frac{F}{L}p)_{min}$	-4.03	0.0855	-3.032	0.01394	-3.01	0.00526
	$NI_o/V_r^{\frac{1}{2}}$	2.8	11.4	17.4	26.7	34	43
$\frac{\ell}{L}=5$	$(\frac{F}{L}p)_{min}$	-5.022	0.668	-4.174	0.0105	-4.4	0.004
	$NI_o/V_r^{\frac{1}{2}}$	2.4	11.2	17.2	26.6	34	43
	$(\frac{F}{L}p)_{min}$	-6.016	0.05475	-5.02	0.008476	-7.369	0.00317
	$NI_o/V_r^{\frac{1}{2}}$	2.2	11.2	17.2	26.6	33.8	43

Table 3.1

Computed values of $(F_p/L)_{min}$ and their corresponding excitation parameter $NI_o/V_r^{\frac{1}{2}}$ for the first six loops at different ratios of ℓ/L.

3.3 Thickness of the central pole of a rotation-free lens

The two lenses forming the double-pole projector doublet are separated by an iron plate which is common to both lenses. Since the flux of both passes through it, it is important to choose its thickness correctly in order to avoid magnetic saturation. Figure 3.3.1 shows a simple construction of a doublet. For simplicity let all bores and gaps be identical and the flux density B_p in the gaps be uniform. If this double lens is operated so that $(NI)_1 = +(NI)_2$, the flux from one gap will oppose the flux from the other in the central plate region; therefore, there will be no problem of saturation. If the double gap lens is operated in the rotation-free mode, the two fields in the gaps oppose each other and the flux in the central plate will be doubled as shown by the dotted lines in Figure 3.3.1. The flux ϕ in each gap out to a distance, D' is $\pi(D'/2)^2 Bp$. Neglecting the leakage flux, the total flux entering the central plate out to D' is $2\pi(D'/2)^2 Bp$. Thus the flux passes through a cylinder of diameter D' and height d which gives a flux density B' in the central plate of

$$B' = 2\pi\left(\frac{D'}{2}\right)^2 Bp/(\pi D'd)$$

i.e. the plate flux density at D' is D'B/2d. B_p in gauss is given by

$$Bp = \frac{4\pi}{10} \cdot \frac{NI}{S},$$

where NI is the ampere-turns in each gap and S in centimetres. Hence the plate flux density B' at D_1 is

$$B' = \frac{\pi}{5} \quad \frac{D'}{d} \quad \frac{NI}{S}$$

or $$B' = \frac{\pi}{5} \cdot \frac{(D'/D)}{d} \cdot \frac{NI}{(S/D)} \qquad \ldots\ldots 3.3.1$$

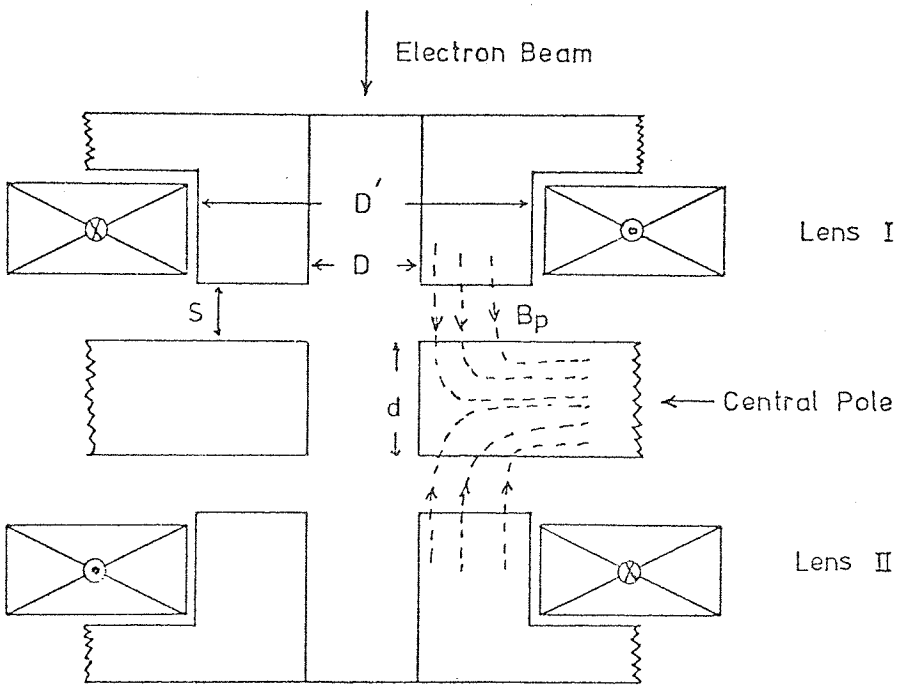

Fig. 3.3.1 The polepieces of two identical lenses with equal and opposite flux densities.

Equation 3.3.1 gives the flux density in the common pole in terms of the lens geometry. If the maximum permissible flux density in the central plate is $(B')_{max}$ corresponding to the maximum ampere-turns in each gap $(NI)_{max}$, the plate thickness d in centimetres is given by

$$d \geqslant 0.63 \frac{(D'/D)}{S/D} \cdot \frac{(NI)_{max}}{(B')_{max}} \qquad \ldots\ldots 3.3.2$$

where B' is in gauss. Equation 3.3.2 is very useful in the design of double-pole rotation-free projector lenses. If the two lenses are designed to operate at an accelerating voltage of 100 kV, $(NI)_{max}$ will be about 4500A.t, also taking the maximum permissible $(B')_{max}$ as 15000 gauss (1.5T) and the minimum value of (D'/D) being 2, hence

$$d \geqslant \frac{3.8}{(S/D)}$$

Thus the minimum value of d for a lens of S/D = 1 is 3.8mm, a conveniently small value.

3.4 An experimental double-pole miniature rotation-free lens

Since many commercial electron microscopes employ double-pole lenses although not in the rotation-free mode, and usually operate at an accelerating voltage of 100 kV, a 100 kV, miniature, double-pole, rotation-free projector lens was constructed and tested.

Lens design

The miniature rotation-free lens consisted of two identical lenses. Figure 3.4.1 shows a cross-section of the two lenses mounted in close proximity to each other and their windings connected in series opposition so that the composite lens is free from image rotation. Each miniature lens has two pole-pieces of gap width S = 3mm and diameter D = 2mm, (S/D = 1.5). The calculated minimum projector focal length of each lens is 1.8mm. The distance, ℓ,

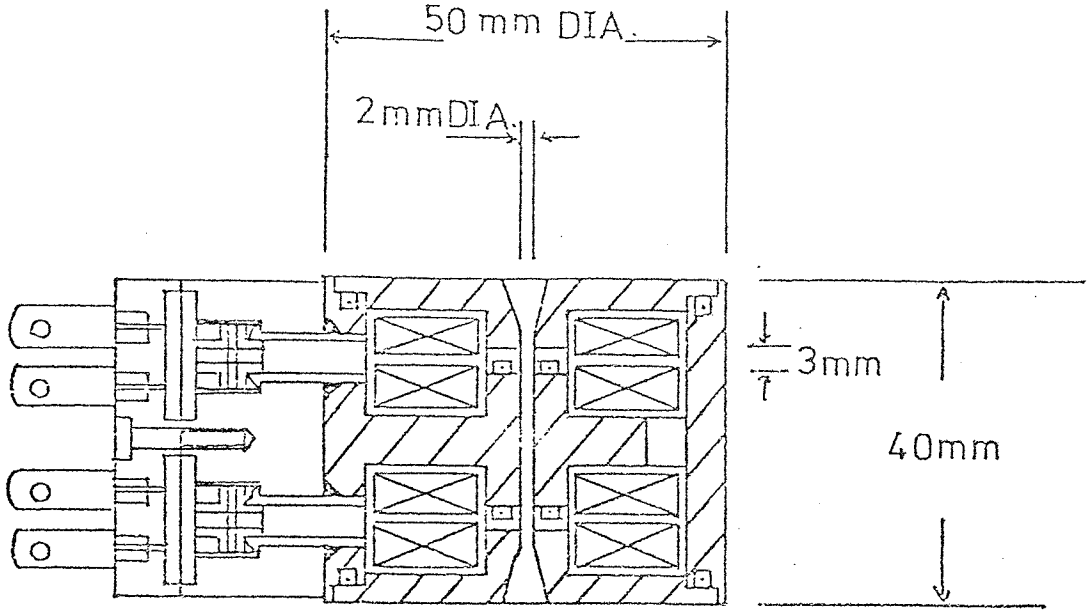

Fig. 3.4.1 Cross-section of a 100kV miniature rotation-free lens. Scale: full-size.

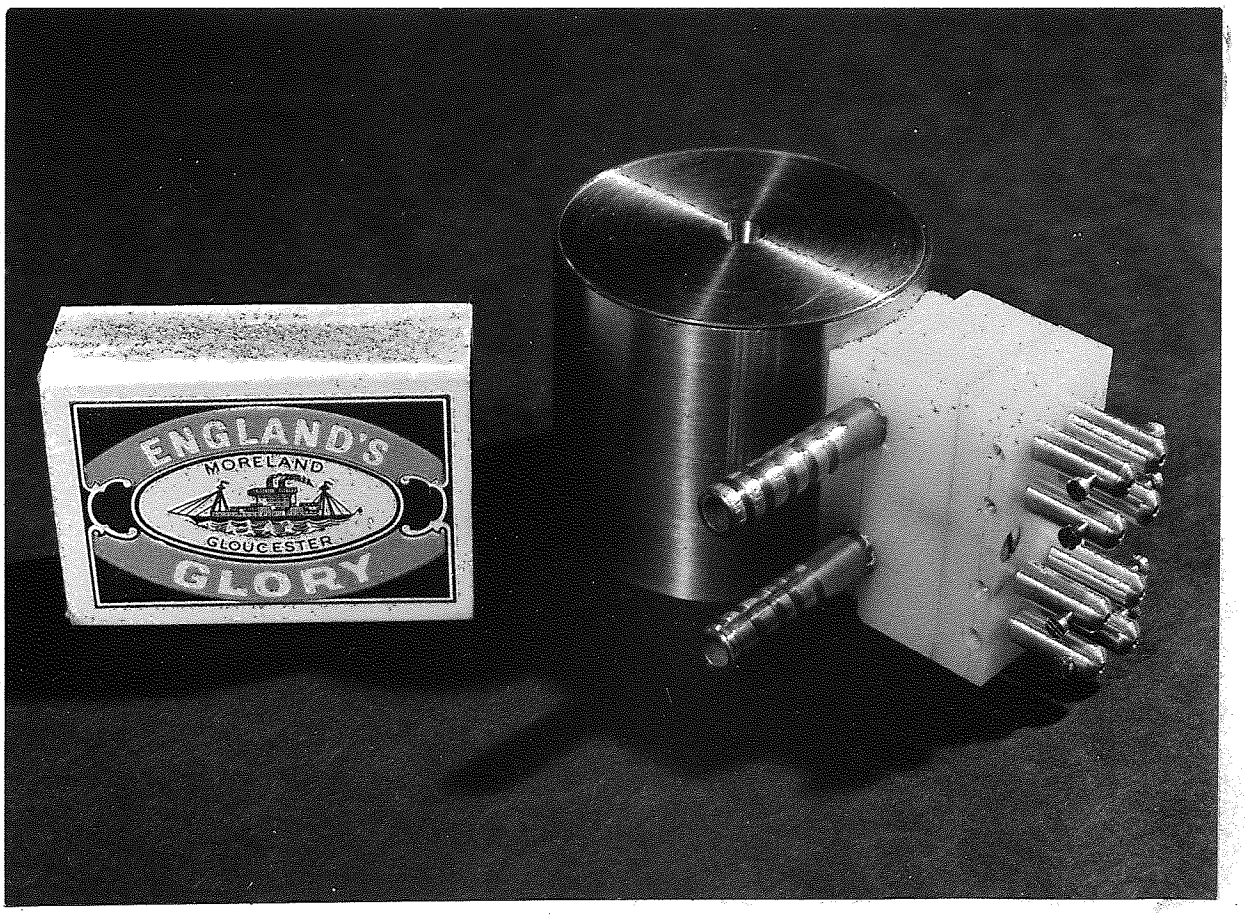

Fig. 3.4.2 100kV miniature rotation-free projector lens.

between the centre-lines of the two gaps is 20mm. The effective focal length of this rotation-free lens is 0.17mm as calculated from the Equation 3.2.8. Since the width of the rectangular field in each gap is L = 3.35mm, the ratio of ℓ/L is 6, which gives $(F_p/L)_{min}$ = 0.05 as given by Figure 3.2.1. Figure 3.4.2 shows a photograph of the lens, whose height is 40mm and diameter of 50mm; the length of the match box is 50mm.

Each gap is excited by two coils which provide sufficient excitation for operation up to an accelerating voltage of 100kV. The advantage of two coils is the reduction in temperature as was shown in Chapter Two. Each coil is wound with 24 S.W.G. (0.56mm diameter) insulated copper wire and has an inner diameter D_1 = 12mm and outer diameter D_2 = 38mm, (D_2/D_1 = 3.17). The coil has eight layers of wire along its 5mm width. The number of turns in each coil is 191 turns; this makes the total number of turns in each gap equal to 382 turns; so when the lenses are connected in series they will produce the same number of ampere-turns. The resistance of each coil is 1.1 ohms at 17°C and hence the total resistance of the coil of the rotation-free lens is 4.4 ohms. All the coils are in direct contact with the cooling water which flows through a channel of one millimeter height all around the coils.

The thickness of the central plate is 6mm, (See Equation 3.2.2). Since the outer diameter D' of each pole-piece is 10mm with a bore D of 2mm, hence, D'/D=5. Assuming that the ampere-turns in each gap is 4500A-t and the maximum permissible flux density in the central plate is 1.5 tesla, the minimum thickness d of the plate should be 6mm. In practice, the maximum permissible flux density can be higher than 1.5 T and the ampere-turns required are less than 4500; thus the value of the plate thickness is on the safe side. A hole of 5mm in diameter was drilled in the central plate in order to allow for the

Fig. 3.4.3 The miniature rotation-free projector lens mounted on the optical bench of the 'Intercol' electron microscope.

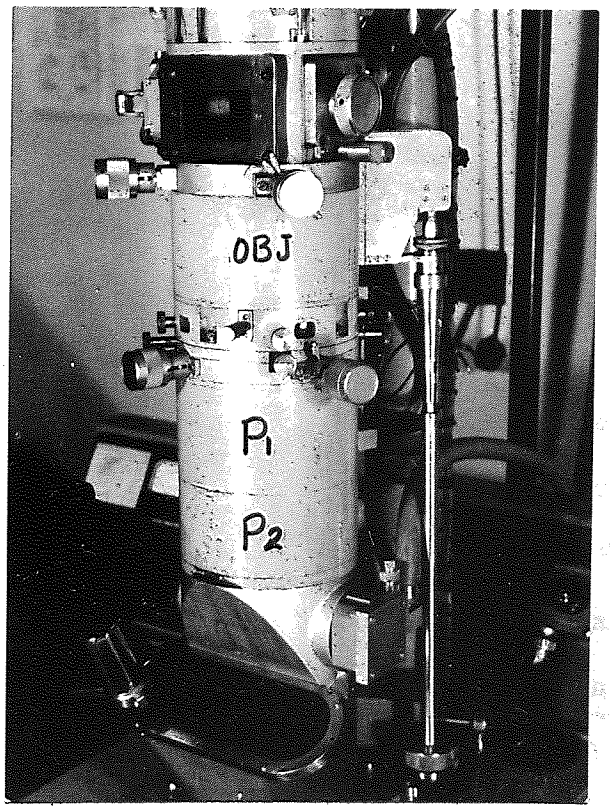

Fig. 3.4.4 The imaging system of the AEI-EM6 microscope where the lens P_2 will be replaced by the rotation-free lens.

water circulation from the upper lens to the bottom one. The effect of this small hole on the magnetic circuit is negligible.

Lens stage

The rotation-free projector lens was tested on two electron-optical benches. A primary test was performed on the 30kV 'Intercol' type electron optical bench using the electron gun only, (Figure 3.4.3), which illuminates a specimen placed close to the first gap. The screen was mounted on top of a round iron tube 150mm long. The lens successfully projected rotation-free images at 30kV with the ratio of the two maximum magnifications being 900:9 i.e. $M_2/M_1=100$. This experimental result is shown in Figure 3.1.3 for the ratio of $\ell''/\ell'=9$.

The most important test of the lens was that performed in the 100KV-EM6 type electron microscope. The imaging system of this microscope is shown in Figure 3.4.4. The rotation-free lens was designed to replace the final projector lens (P_2) of the microscope.

First, a special stage was designed, (Figure 3.4.5) to occupy the space formerly occupied by the second projector lens. It consisted of two iron discs separated by four iron pillars supporting the whole electron-optical column. The front righthand-side pillar was designed to be removable (Figure 3.4.6) in order to have a large space for inserting the lens between the two iron discs. The space between the lens and the two iron discs was filled by two brass discs as shown in Figures 3.4.5 and 3.4.6. The lens could be aligned in the X-Y directions by means of four brass screws. These alignment screws were mounted on four rectangular brass bars supported by the four pillars, Figure 3.4.7. The lens cooling system of the original final projector was used without modification. An external current supply capable of delivering up to 10 amperes was provided to energize the windings of the miniature lenses.

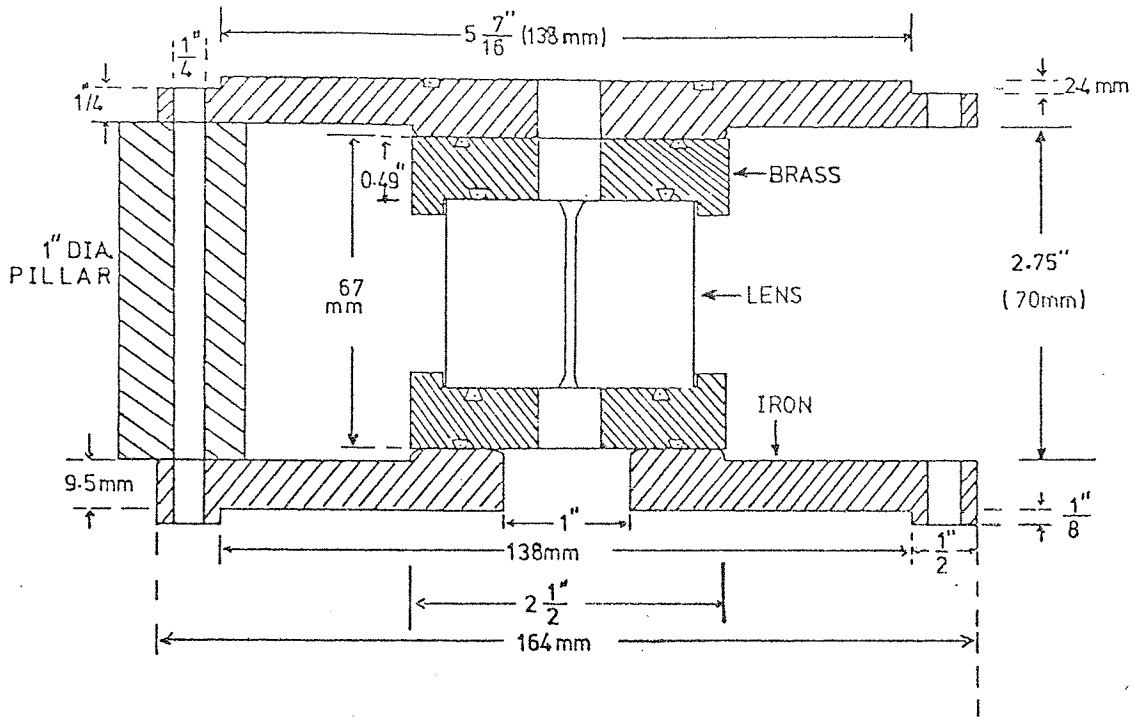

Fig. 3.4.5 Cross-section of the stage which replaced the final projector lens of the EM6 microscope.

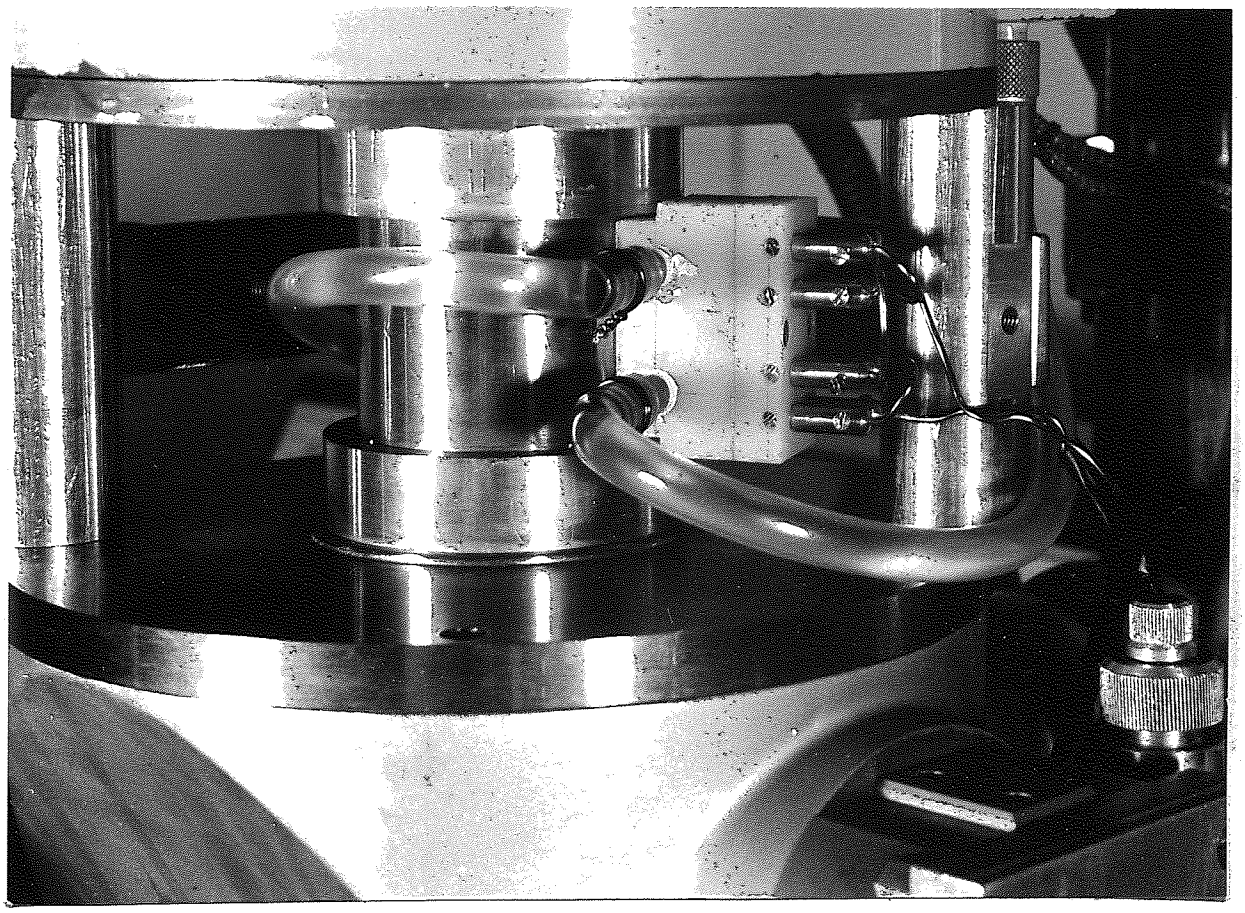

Fig. 3.4.6 The miniature rotation-free lens and its special stage replacing the final projector of the EM6 microscope.

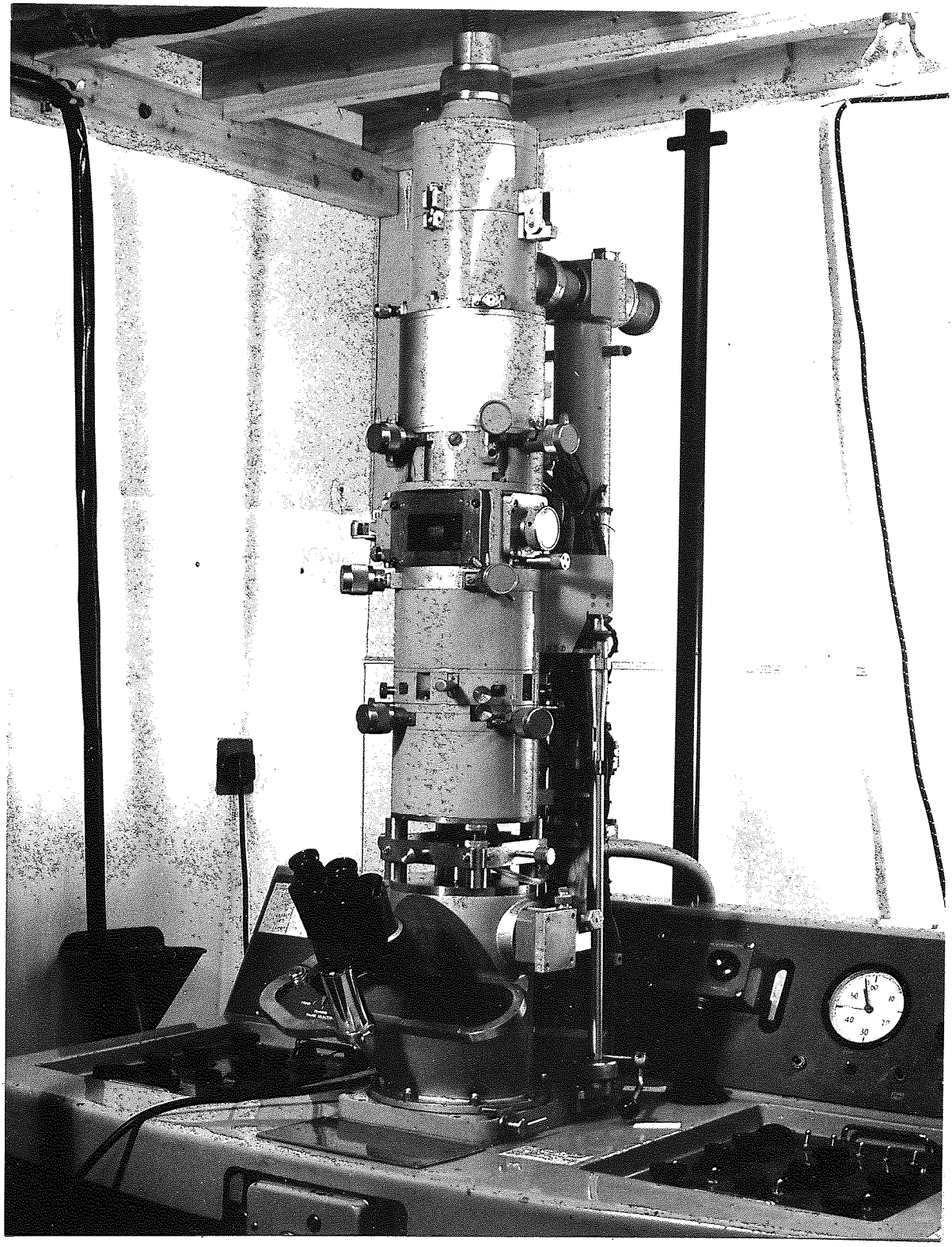

Fig. 3.4.7 The EM6 electron microscope with the miniature rotation-free final projector lens.

Focal properties of the miniature rotation-free lens

The important lens properties to be measured are magnification, focal length and image rotation. Careful experiments showed that the image rotation had been entirely cancelled. The magnification was measured at 75kV by illuminating a copper grid placed in the position of the selected-area aperture of the microscope, all other lenses were switched off in order to provide an essentially parallel beam. Figure 3.4.8 shows the magnification characteristics of the rotation-free lens as calculated for the EM6 microscope image throw (ℓ"=380mm) using a "rectangular-field" model. The corresponding experimental results are in very good agreement; the top magnification is more than 2000X at the photographic plate, an unusually high value.

The magnification curve of Figure 3.4.8 is plotted against the excitation parameter $NI/V_r^{\frac{1}{2}}$ where NI is the number of ampere-turns in each lens of the unit and V_r is the relativistically corrected accelerating voltage. At the first maximum (20X), the radial and spiral distortion is completely corrected and the image appears inverted as shown in micrograph A of Figure 3.4.8, as predicted theoretically. One other important property which is shown clearly in micrograph A is the large field of view. The micrograph shows an area of diameter 720 μm, completely distortion-free and at a very low magnification which is not obtainable in conventional lenses.

At high magnifications, the distortion characteristics are determined by the distortion coefficient of the last lens in the chain and in this respect the unit does not differ from a conventional lens. This is illustrated by the micrographs B, C and D of Figure 3.4.8 in which the complete freedom from lens rotation of the erect image may be observed. Below a magnification of 150X, the distortion becomes intolerably large. However, since the ratio of the two maximum magnifications is more than 100:1 Figure 3.4.8 shows that a high

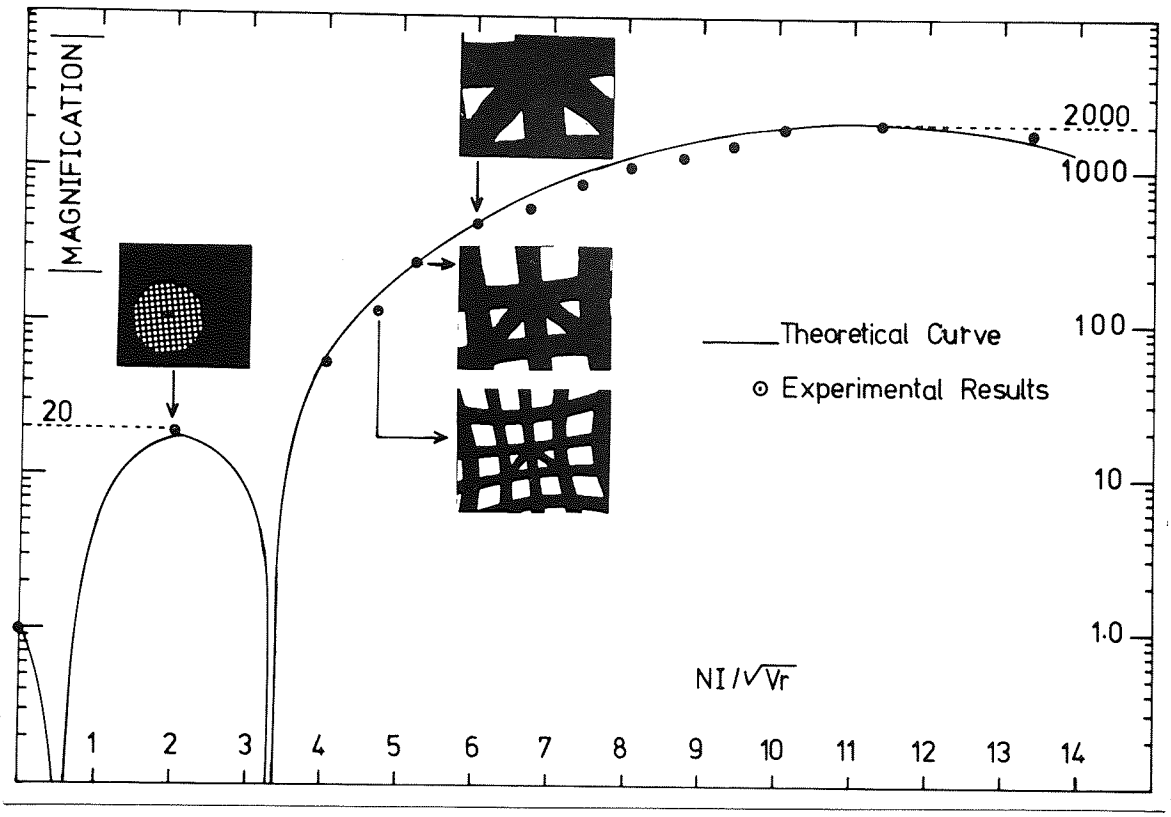

Fig. 3.4.8 Variation of the magnification of the miniature rotation-free lens with excitation parameter $NI/V_r^{\frac{1}{2}}$. The micrographs show the absence of image rotation.

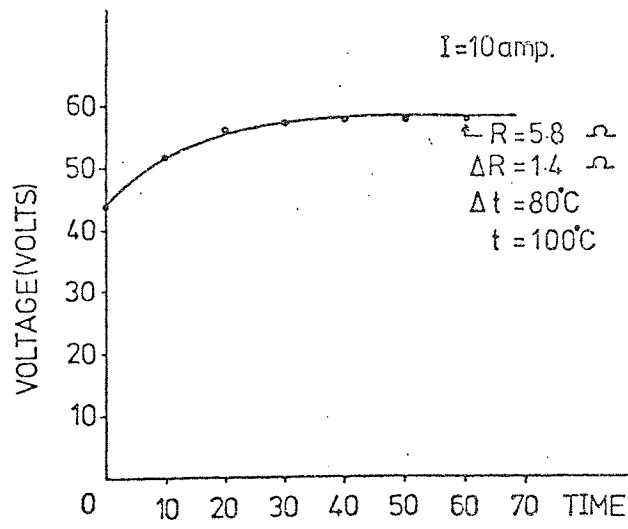

Fig. 3.4.9 The rise in voltage with time when a current of ten amperes is passed through the coils of the miniature rotation-free lens.

range of magnification can be obtained with negligible distortion. This value of M_2/M_1 is shown in Figure 3.1.3 for the ratio $\ell''/\ell' = 17$. The maximum magnification of this lens is more than ten times higher than that of the original final projector lens of the EM6 microscope while its volume is twenty times smaller. On the other hand it consumes ten times more power. In practice a balance must be sought between these conflicting factors in a particular design.

If the lens is operated at 100kV it will require a current of ten amperes which means that the number of ampere-turns will be about 4000A-t. Figure 3.4.9 shows that at a current of 10 amperes, the mean temperature rise in the coils is about 100°C, a perfectly safe value. The heating-up time constant of the windings is of the order of one minute. The current density under these conditions is 4000 amp/cm^2 at a water flow of 1 litre/minute and a total power conumption of 580 watts. The mean temperature and hence the power required can be reduced if the two lenses are cooled separately. With the arrangement adopted the cooling water enters the bottom lens at a temperature higher than its initial value when it enters the upper lens. This makes the average temperature of the bottom two coils higher than that of the upper two, which is the main reason why the two lenses are not connected in parallel, since the ampere-turns in both lenses will not be equal.

The focal length of the rotation-free lens is shown in Figure 3.4.10 as a function of the excitation parameter $NI/V_r^{\frac{1}{2}}$. It shows good agreement between theory and experiment. The first minimum focal length is about 20mm. The effective focal length of the lens is 0.17mm which is ten times less than that of the original projector lens of the microscope. Hence it is possible to design a practical lens unit which has a very short focal length when it is

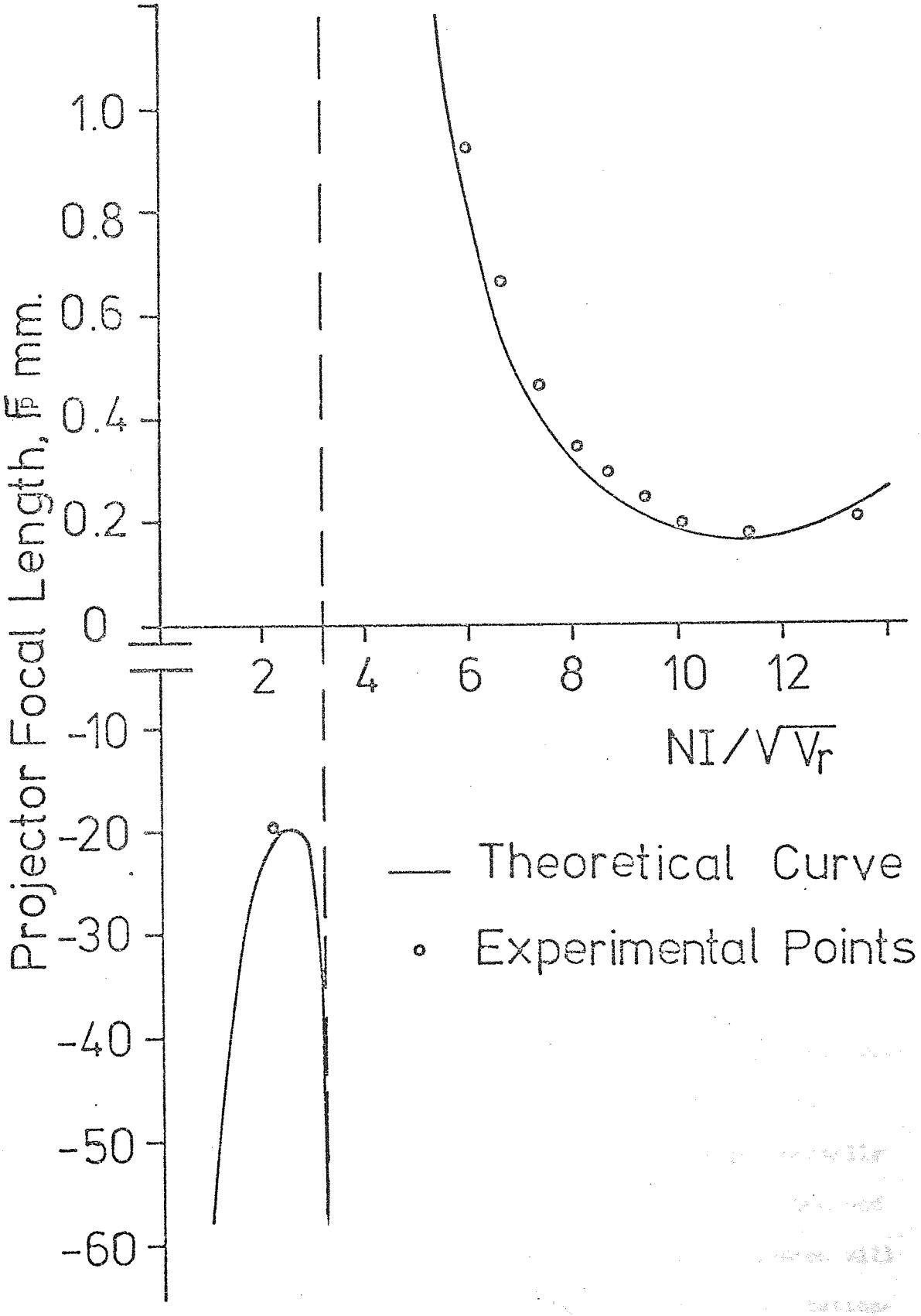

Fig. 3.4.10 Variation of the projector focal length of the miniature rotation-free lens with the excitation parameter $NI/V_r^{\frac{1}{2}}$.

operated in the second loop of the curve and a long focal length when it is operated in the first loop.

It is often desirable to have a double-pole rotation-free projector lens with an effective focal length comparable with those used in commercial microscopes i.e. of the order 1-2mm. This is now feasible following the successful use of water-cooled flat helical coils and rotation-free lenses. The dimensions of such lenses should be large so that the square of the focal length of each of the two gaps is of the order of the gaps's centre-lines separation. For example, let the required rotation-free lens consist of two identical double-pole lenses of S/D = 1.5. If the bore diameter D is 10mm, the gap width S of each lens will be 15mm. Hence $L = \sqrt{S^2 + 0.56D^2} = 16.8$mm and the focal length of each gap will be $f_p = 0.55L = 9.2$mm, i.e. $f^2 = 85\text{mm}^2$. To avoid any kind of field interaction, the distance ℓ between the centres of the two gaps should be greater than L. Let $\ell = 3L = 50$mm. Therefore, the effective projector focal length of this rotation-free lens will be $F_p = f_p^2/\ell = 1.7$mm which is of the same order as that of the final projector lens of the EM6 microscope. The value of F_p can be reduced further if ℓ is increased; it becomes 1mm when $\ell = 85$mm. The size of the lens will be smaller than conventional ones with the practical advantage of having large bores, giving rotation-free images. Furthermore this lens will have a distortion-free image at a very low magnification since $F_p = \ell$ is large in this case. However, if the 2mm bore and the two 3mm gaps of the experimentally tested rotation-free unit are scaled up three times, i.e. S=9mm and D=6mm, the projector focal length, f_p of each of the two lenses will become 5.5mm and the effective focal length, F_p of the new rotation-free lens will be $(5.5)^2/20 = 1.5$mm. Thus, the present rotation-free unit can also be designed for a focal length comparable with that of a conventional lens, but with a wide bore, typically with a diameter/

focal length ratio of four to one.

The focal length can be varied to any desired value by changing the dimensions and the ratio of S and D. In particular, for a lens of a specific focal length and geometry, its focal length can be changed by a factor n if its geometry is changed by the same factor.

The ray trajectories of a parallel beam distant r above the optical axis, passing through the miniature rotation-free lens was calculated by assuming that the two fields have a rectangular-field distribution. The maximum value of the magnetic flux density was calculated for the 4000A.T. required at an accelerating voltage of 100kV, i.e. B_o=1.44 Tesla which is less than the saturation limit of the iron. Figure 3.4.11 shows the ray trajectories of the electron beam at different excitations; the first maximum magnification occurs at $NI/V_r^{\frac{1}{2}}$ between 2 and 3 as it was confirmed experimentally. The second maximum magnification occurs at $NI/V_r^{\frac{1}{2}}$ between 11 and 12 where the beam emerges with a maximum slope and positive r, i.e. erect image.

3.5 Conclusion

It has been shown, both theoretically and experimentally, that it is possible to construct double-pole miniature rotation-free lenses. The size of the lenses is very small compared with conventional ones and they have very useful focal properties which are not met in single-gap lenses. Miniature rotation-free lenses of large bores and gaps can be designed for use as intermediate lenses. It is therefore possible to construct a rotation-free projection system which is small in size but with lenses still having the same basic design features of conventional lenses.

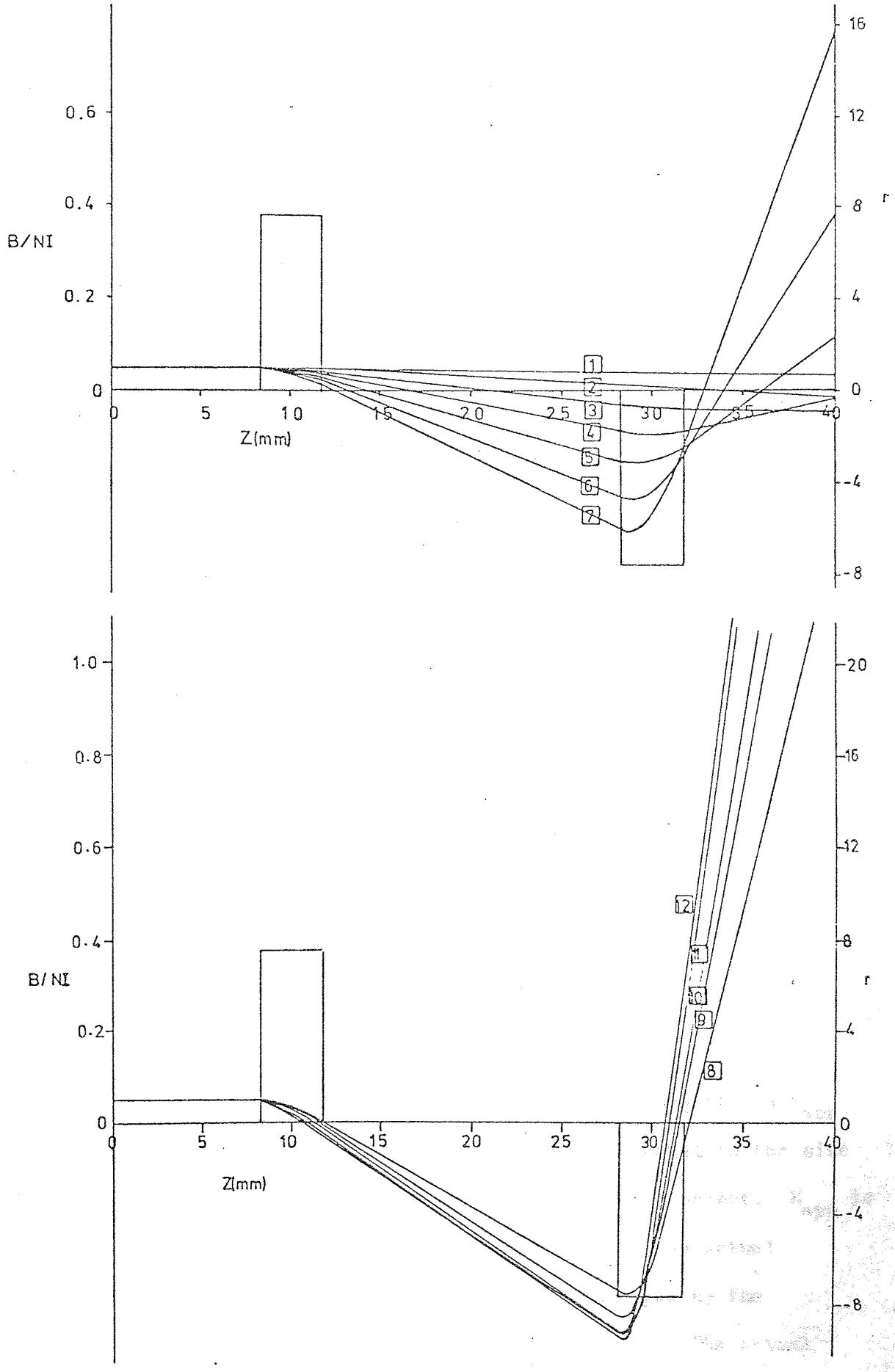

Fig. 3.4.11 Ray trajectories for a parallel beam of electrons entering the fields of the miniature rotation-free lens, drawn for different values of $NI/V_r^{1/2}$ as shown in small squares for each corresponding ray.

4. SINGLE-POLE ROTATION-FREE LENSES

Single-pole (snorkel) lenses are a new type of magnetic lens. Like all magnetic lenses, they suffer from spiral (rotational) distortion. One method of reducing spiral distortion is to have a double lens system which has $(NI)_1 = -(NI)_2$.

A double snorkel lens unit has been designed. Its focal properties as a double and single lens have been studied practically and theoretically. The focal length of a snorkel lens is a function of a number of factors such as the outer and inner diameters of the coil and the geometry of the snout.

4.1 Focal length and magnification of a single projector lens

Suppose an object is illuminated by an electron beam from a source at a distance u from the projector lens, Figure 4.1.1. The lens projects an image of the object on the screen which is at a distance L from the lens. It is shown in (Appendix VII) that the projector focal length is given by

$$f_p = \frac{Lu}{M_{app} S_o + L + u} \qquad \ldots\ldots 4.1.1$$

where S_o is the distance between the source and the object and M_{app} is the apparent magnification of the lens which is equal to the size of the image on the screen divided by the size of the object. M_{app} is called the apparent magnification because it is not the actual magnification of the lens since the object is enlarged by the illuminating beam before being projected by the lens. The actual magnification M of the projector lens and its focal length are related by the following equation (Appendix VII),

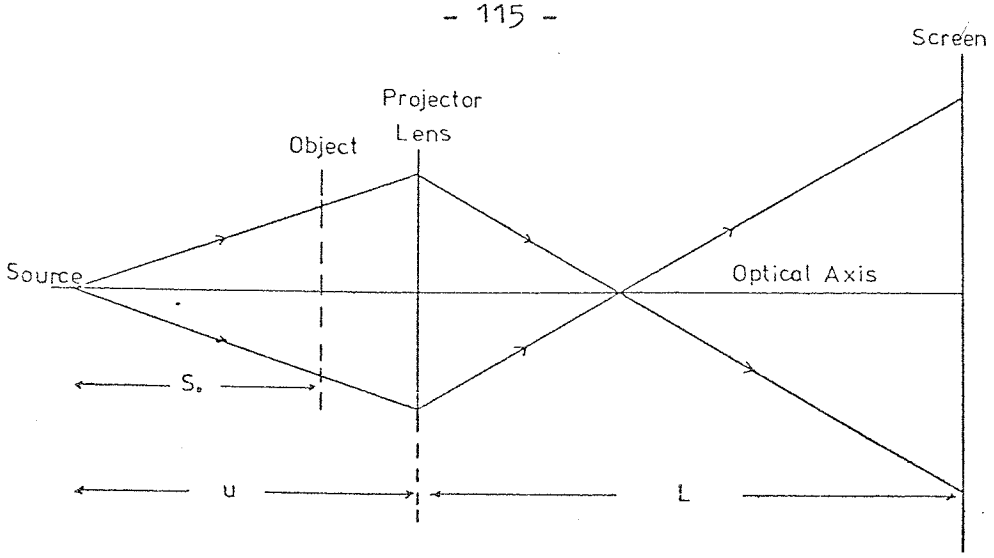

Fig. 4.1.1 Single magnetic lens projecting an image on the screen of an object illuminated by an electron source.

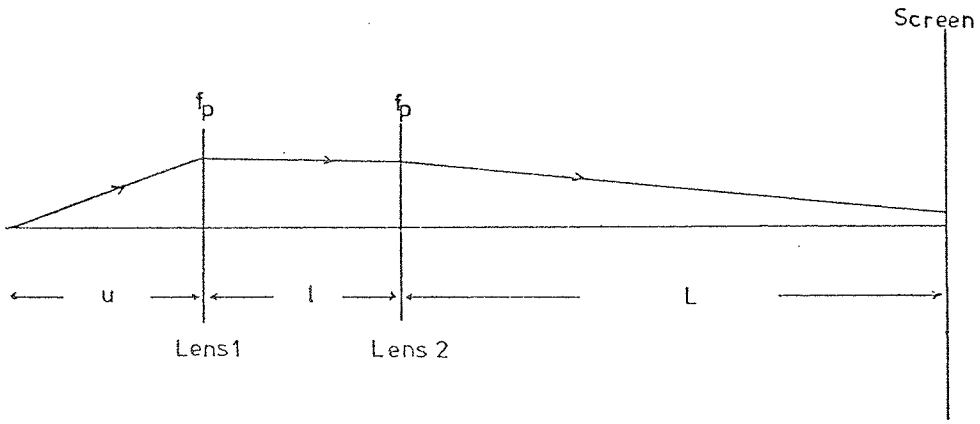

Fig. 4.2.1 Double lens unit consisting of two identical lenses projecting an image on the screen.

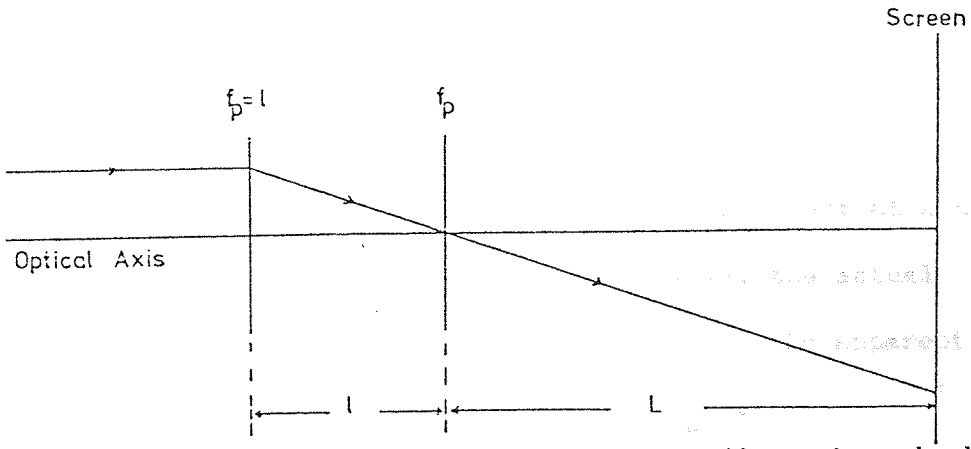

Fig. 4.2.2 Trajectory of paraxial electrons through a double-lens unit excited to give the first maximum magnification where the projector focal length of each of the two lenses is equal to separation of their principal planes.

$$f_p = \frac{Lu}{u(M+1) + L} \qquad \ldots\ldots 4.1.2$$

since $Mu = M_{app} S_o$. If the object is illuminated by an electron beam travelling parallel to the optical axis, M_{app} will equal the actual magnification, M of the lens and the projector focal length will be

$$f_p = \frac{L}{M+1} \qquad \ldots\ldots 4.1.3$$

Equations 4.1.1, 4.1.2 and 4.1.3 are very useful in calculating the projector focal length of any single lens from the magnification.

4.2 Focal length and magnification of a double projector lens

Consider the double projector lens unit shown in Figure 4.2.1. It consists of two lenses identical in geometry and ampere-turns, and assumed to be thin lenses such that their principal planes are separated by a distance ℓ. The unit refracts an electron beam from a source at a distance u from the first lens. The beam is incident on a screen at a distance L from the second lens. It is shown in Appendix VII that the magnification M of this double projector lens is given by

$$M = 1 + \frac{\ell+L}{u} - \frac{1}{f_p}\left[\frac{\ell L}{u} + \ell + 2L\right] + \frac{\ell L}{f_p^2} \qquad \ldots\ldots 4.2.1$$

However, if the electron beam is illuminating an object at a distance S_o from the source as that shown in Figure 4.1.1, the actual magnification, M of the double lens is related to the apparent magnification M_{app} by the equation $M = M_{app} \cdot \frac{S_o}{u}$.

If the electron beam is parallel to the optical axis i.e. u is infinite, Equation 4.2.1 becomes

$$M = 1 - \frac{\ell+2L}{f_p} + \frac{\ell L}{f_p^2} \qquad \ldots\ldots 4.2.2$$

Equation 4.2.2 gives the following information:

(i) If the lenses are not excited, i.e. $(NI)_1 = \pm (NI)_2 = 0$, f_p is infinite and hence M = 1 which is exactly what is expected electron-optically.

(ii) If M is differentiated with respect to f_p for maximum or minimum, a maximum magnification is obtained when $f_p = \frac{2\ell L}{\ell+2L}$. Since 2L is usually large compared with ℓ, f_p approximately equals ℓ and hence $M_{max} \simeq \frac{-L}{\ell}$. These expressions for f_p and M_{max} mean that:

(a) the second lens is approximately in the back focal plane of the first; hence it corrects the aberrations of the first and the combined focal length of the system is also ℓ,

(b) from the negative sign of the magnification, the image is inverted (Figure 4.2.2) and

(c) this first magnification is independent of the lens bore or geometry, it only depends on the distance of separation ℓ.

(iii) When f_p is minimum, a second maximum magnification of the double lens is obtained and approximately given by

$$M_{max} \simeq \frac{\ell L}{f_p^2} \qquad \ldots\ldots 4.2.3$$

which is the product of the maximum magnification of each individual lens.

(iv) There are two values of f_p for every value of M given by

$$f_p = \frac{(\ell+2L) \pm \sqrt{(\ell+2L)^2 - 4\ell L(1-M)}}{2(1-M)}$$

When $M \ll 1$, f_p becomes

$$f_p = \frac{(\ell + 2L) \pm \sqrt{\ell^2 + 4L^2}}{2}$$

Since L is usually very large compared with ℓ, hence

$$f_p \simeq \frac{(\ell + 2L) \pm 2L}{2}$$

such that $(f_p)_1 \simeq 2L$ (Figure 4.2.3) and $(f_p)_2 \simeq \ell/2$ (Figure 4.2.4). In fact $(f_p)_2$ is slightly less than $\ell/2$, but when it is exactly $\ell/2$ the magnification is (-1) and an inverted image is obtained Figure 4.2.5

The information given in Sections 4.1 and 4.2 applies to all kinds of geometries of magnetic lenses.

4.3 An experimental single-pole rotation-free lens

A miniature double-snorkel lens was designed to operate at 30KV. Its design is very simple as shown in Figures 4.3.1 and 4.3.2. It consists of two lenses of the single-pole type mounted back to back and made of soft iron except the upper and lower lids and the water pipes which are made of brass. The whole unit is 50mm in diameter and 25mm thick and has a hole of 4mm in diameter bored through the snouts which are 19mm apart. Each half of the lens is excited by a single coil of a 24 SWG (0.56mm diameter) copper wire. The coil has an outer diameter of 37mm and 12mm inner diameter; its width is 5mm which has an even number (eight) of wire layers along it. Each coil has 175 turns and resistance of 1 ohm at 15°C and are connected in series in order to produce the same number of ampere turns. The cooling water which flows in the inlet pipe is divided into two as it enters the lens; so when 2 litre/minute of water flow in the pipes, each coil is cooled by a flow of 1 litre/minute through a 1mm channel all around each coil. The ampere-turns required from each coil is

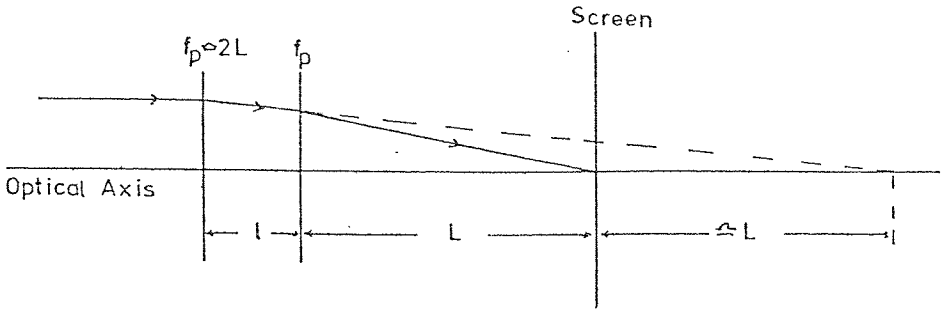

Fig. 4.2.3 Ray path of a parallel electron beam entering a double lens unit when the projector focal length of each lens is approximately 2L.

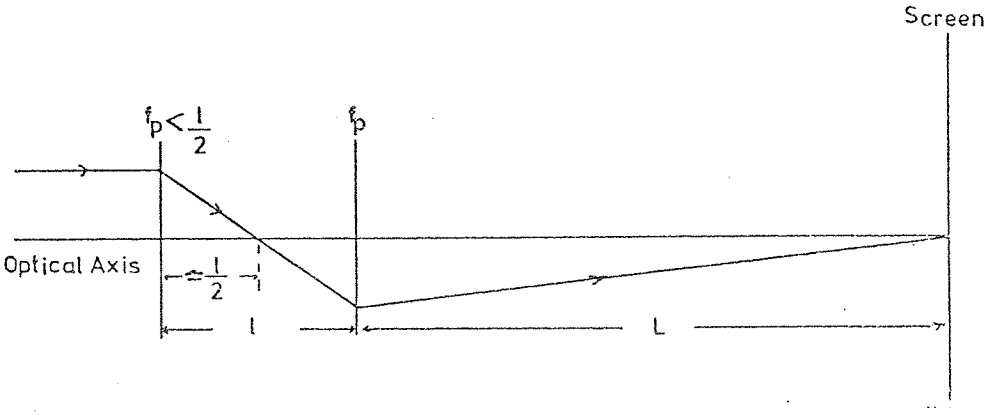

Fig. 4.2.4 Ray path of a parallel electron beam entering a double lens unit when the projector focal length of each lens is slightly less than $l/2$.

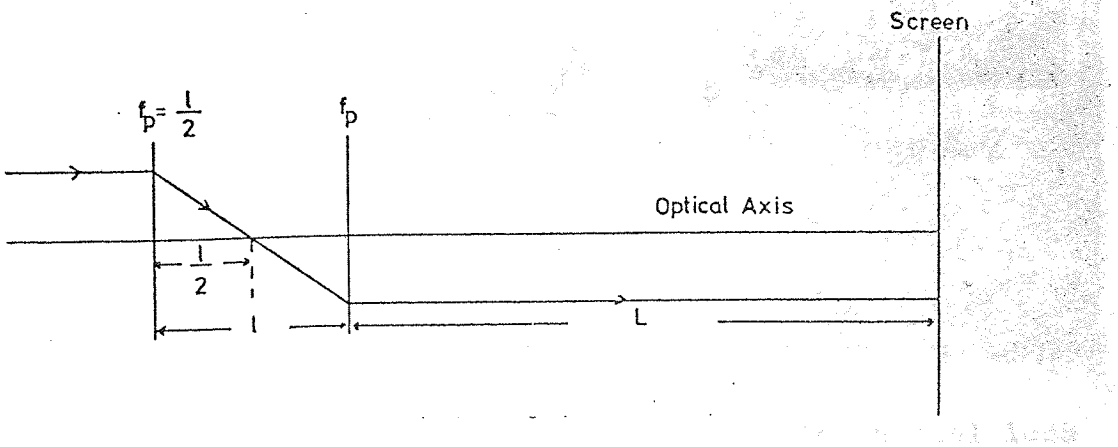

Fig. 4.2.5 Telescopic ray path of a parallel electron beam entering a double lens unit when the projector focal length of each lens is $l/2$.

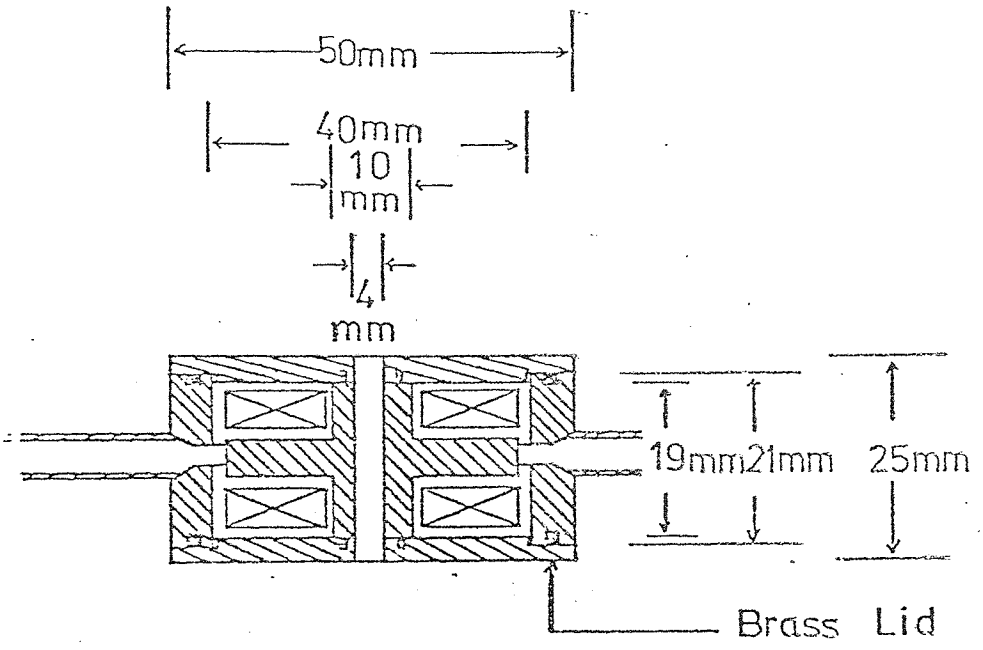

Fig. 4.3.1 Cross-section of the miniature 30kV double-snorkel lens. Scale: full-size.

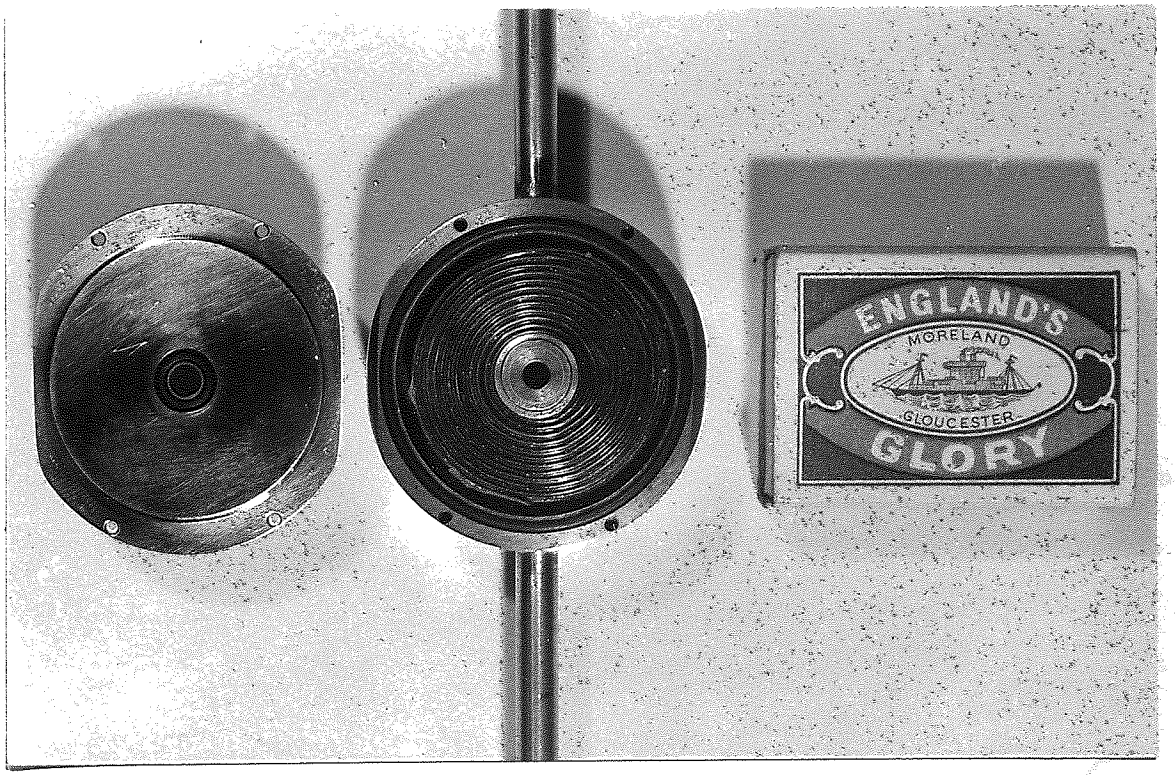

Fig. 4.3.2 One side of the miniature 30kV double-snorkel lens with its brass lid.

2500 A-t in order to operate the lens at 30 kV. For such an excitation (I = 14 amps), the whole lens consumes a total power of 500 watts and the average temperature of each coil is 100°C at a water flow of 1 litre/minute.

A magnetic test was carried out by exciting one half of the double lens. The axial magnetic field was measured by a small Hall-probe detector. The maximum flux density was at a distance of 2.5mm from the snout's surface. At this position the magnetic saturation test (B-H) curve) has shown no sign of saturation at the 2500 A-t and the maximum magnetic flux at this excitation is 0.3T (3000 gauss)

4.4 Focal properties of the single snorkel lens

The minimum projector focal length of any lens can be determined from its field distribution. By means of the Hall-probe, the field distribution of the single snorkel lens was measured at 2500 ampere-turns, Figure 4.4.1. As the probe measures the field at a distance of 1mm from its tip and since its diameter is greater than the 4mm of the bore, the field distribution could only be measured up to a distance of 1mm from the snout. Figure 4.4.1 shows that as the probe is moved away to the right of the snout, initially, the magnetic field increases sharply and approximately linearly until it reaches the maximum. As the probe is moved further away, the field starts decreasing until it becomes exponential as shown by the straight line in Figure 4.4.2. The exponential part of the curve can be used to determine the minimum projector focal length. As shown in Figure 4.4.2, $(f_p)_{min}$=4.8mm. An approximate value of $(f_p)_{min}$ can be obtained by finding the distance between the positions of the peak and its half value for which Figure 4.4.2 shows a value of 5mm. The shape of the field distribution curve shown in Figure 4.4.1 is characteristic of all single-pole lenses with a bore in their snout.

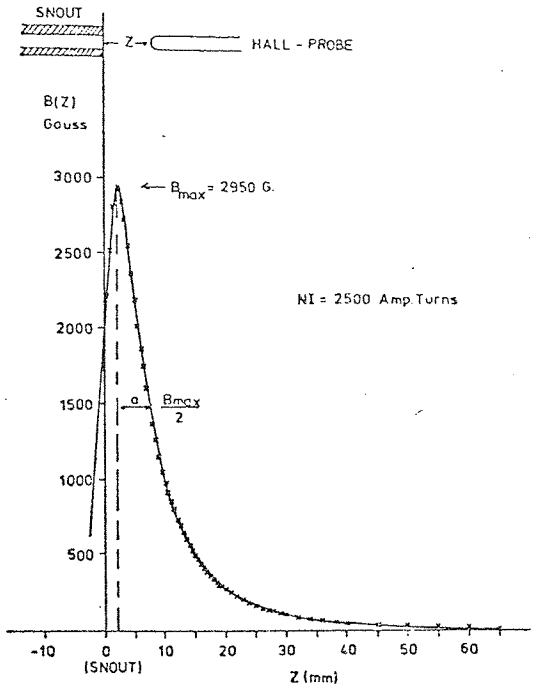

Fig. 4.4.1 Experimentally determined axial flux density distribution in the single snorkel lens of the 30kV double lens.

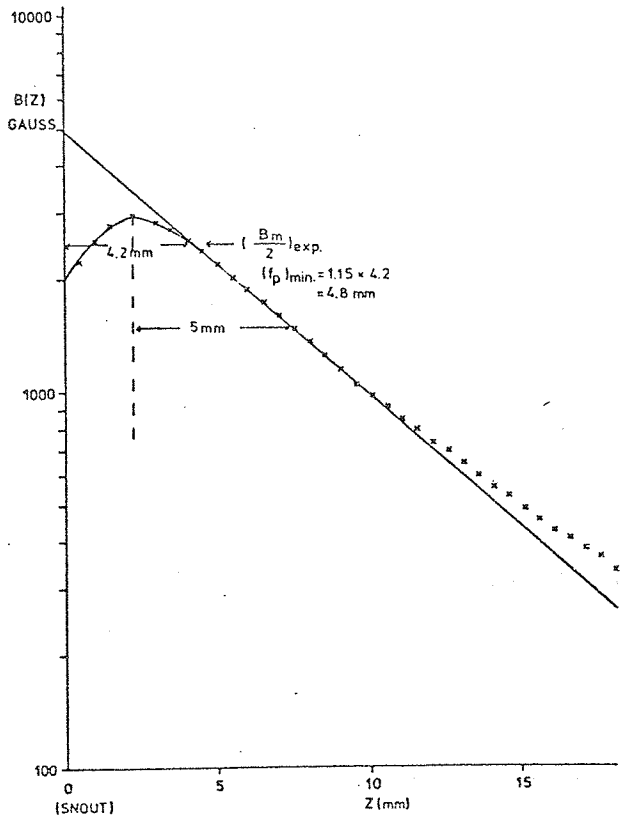

Fig. 4.4.2 The exponential part of the axial flux density distribution, in the single snorkel lens, shown in Figure 4.4.1.

The field to the left hand side of the snout surface drops steeply and was assumed to be linear (Figure 4.4.1) and terminates with a small tail such that the area under the curve agrees to within 10% with that calculated from the excitation $\mu_o NI$.

The variation of the projector focal length with the excitation parameter $NI/V_r^{\frac{1}{2}}$ is shown in Figure 4.4.3. It shows good agreement between the computed and the measured focal length of the single lens. The lens was tested at 30 kV on the Intercol electron-optical bench in a similar way to the test that was done on the 100 kV double lens shown in Figure 3.4.3. The focal length was determined from Equation 4.1.1 by measuring the magnification when the lens nearest to the screen was excited. Figure 4.4.3 shows that the measured minimum focal length is 4.5mm at $NI_o/V_r^{\frac{1}{2}} = 14.5$. This focal length is of the order of the snout's bore but it occurs at a higher excitation than that required for double-pole lenses.

When the experimental results are normalised in terms of the parameter $f_p/(f_p)_{min}$ as a function of NI/NI_o, the focal properties conform approximately to the "universal" curves (Figure 1.2.7) as shown in Figure 4.4.4, which were calculated for double-pole lenses of different geometries. A good check of any experimental results is that at $NI/V_r^{\frac{1}{2}} = (1/2)NI_oV_r^{\frac{1}{2}}$ the value of f_p is nearly twice $(f_p)_{min}$; this can be seen very clearly in Figures 4.4.3 and 4.4.4.

4.5 Focal properties of the double-snorkel lens

A double lens can be excited in two modes i.e. $(NI)_1 = \pm (NI)_2$. In both modes, the lens will have the same focal length at a given excitation. The projector focal length of this doublet was calculated by measuring the magnification of the projected images in the Intercol electron optical bench at 30 kV.

Figure 4.5.1 shows the focal length as a function of the

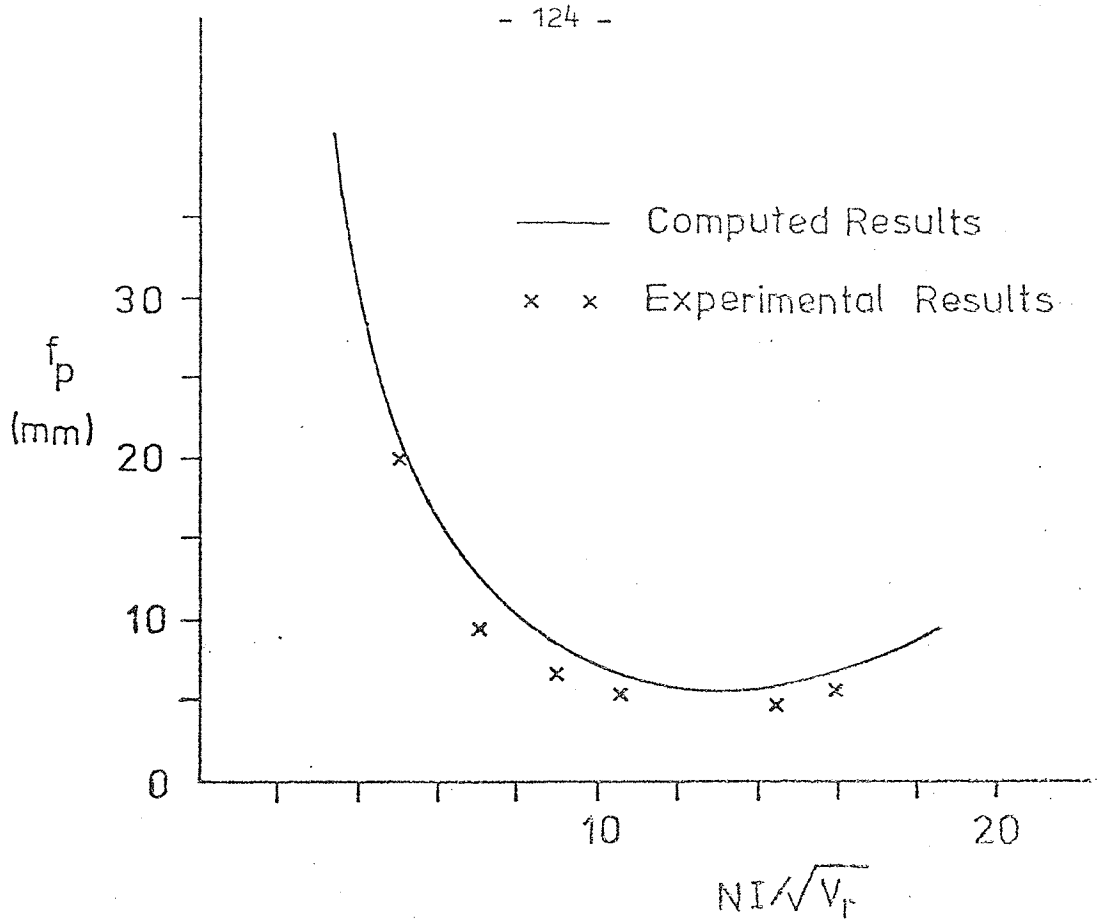

Fig. 4.4.3 The computed and experimentally measured projector focal length of single snorkel lens as a function of the excitation parameter $NI/V_r^{\frac{1}{2}}$.

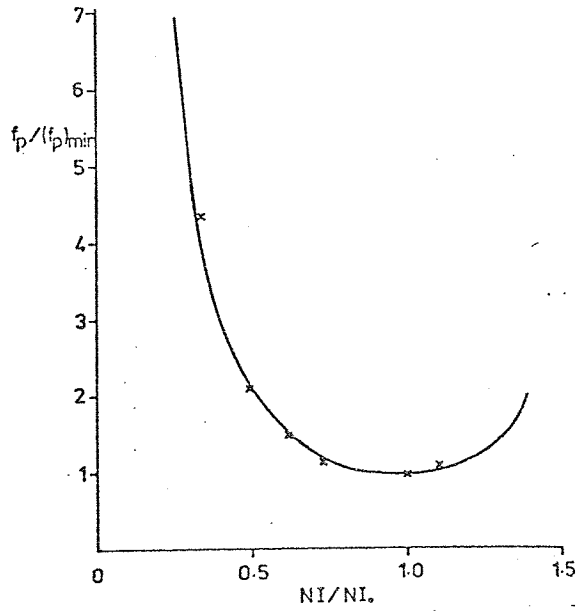

Fig. 4.4.4 The focal properties of the single-pole lens conform approximately to the "universal curves" calculated for the double-pole lens.

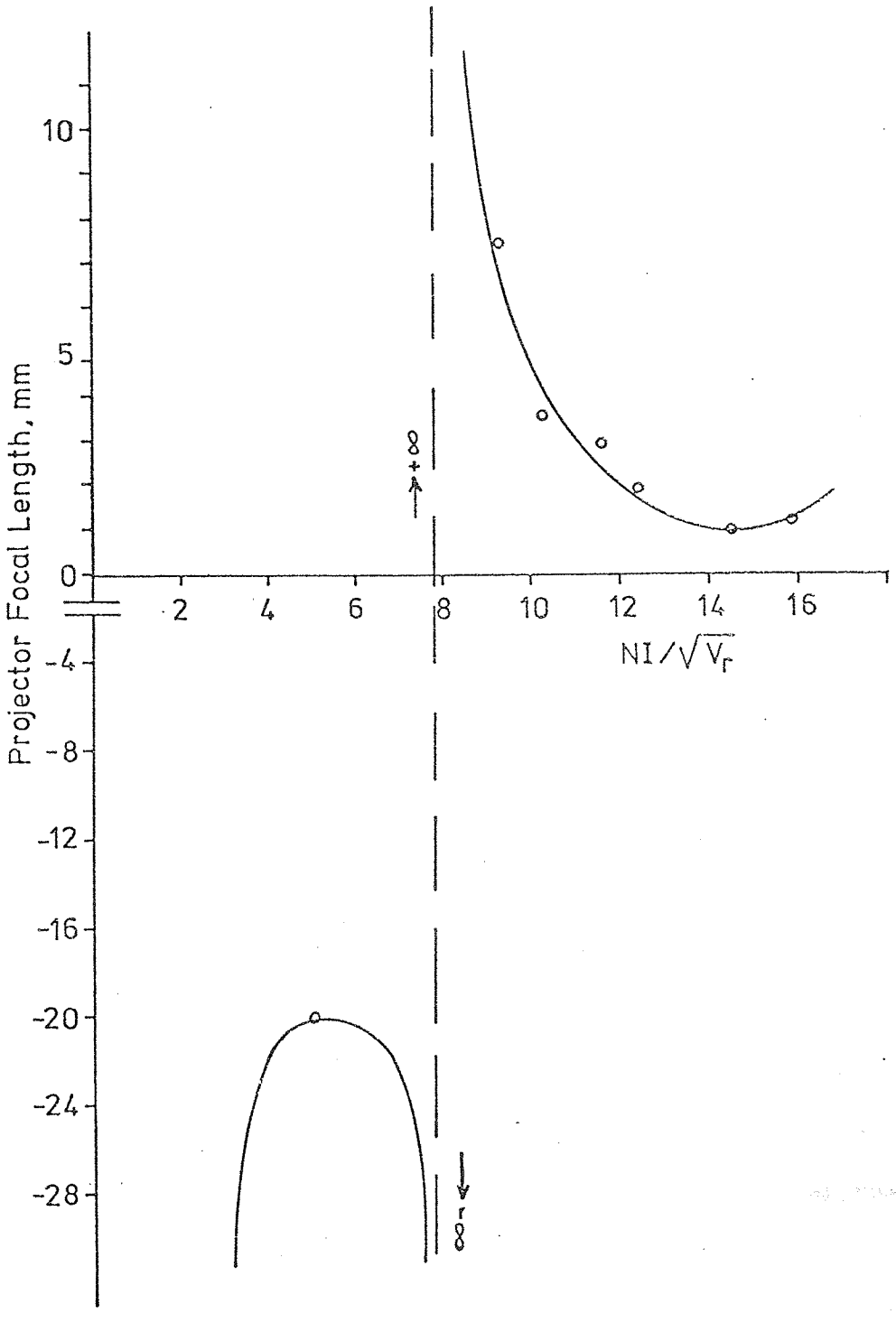

Fig. 4.5.1 The focal length of the 30kV miniature rotation-free snorkel lens as a function of the excitation parameter $NI/V_r^{\frac{1}{2}}$.

excitation parameter $NI/V_r^{\frac{1}{2}}$. The first minimum focal length $(F_p)_{min\ 1}$ at $NI/V_r^{\frac{1}{2}} = 5$ is 20mm which is of the same order as the separation of the snouts. At this focal length a distortion-free inverted image was obtained since the second lens is in the back focal plane of the first and the focal length of each of the two lenses is also 20mm. The second minimum focal length $(F_p)_{min\ 2}$ is 1mm at $NI/V_r^{\frac{1}{2}} = 14.5$. Hence the minimum focal length of a double snorkel lens can be approximately determined from the equation

$$(F_p)_{min\ 2} \simeq \frac{(f_p)^2_{min}}{S} \qquad \ldots\ldots 4.5.1$$

where $(f_p)_{min}$ is the minimum projector focal length of each of the two lenses and S is the distance between the faces of the two snouts. The focal properties of this lens conform approximately to the "universal" curves plotted in Figure 3.2.7 which were calculated for double-pole, rotation-free lenses.

The magnification characteristic curve of this lens is similar to that of the double-pole rotation-free lens shown in Figure 3.4.8. The ratio of the two maximum magnification M_2/M_1 is independent of the projection distance L if it is large compared with the snouts separation S; it depends on the geometry of the lenses and hence on their focal length. It was found that M_2/M_1 for this lens is 20. The ratio M_2/M_1 for a rotation-free lens can hence be approximately written as

$$\left|\frac{M_2}{M_1}\right| \simeq \frac{(F_p)_{min\ 1}}{(F_p)_{min\ 2}} \qquad \ldots\ldots 4.5.2$$

where $(F_p)_{min\ 1}$ is approximately equal to the snouts separation S.

The lens was also tested in the AEI EM6 electron microscope at 50 kV by fitting it into the diffraction stage immediately below the normal second projector lens. The lens was filed off the edges as can

be seen in Figure 4.3.2 in order to push it through the circular holes of the diffraction stage. It was cooled by the same water cooling system of the microscope. A copper grid was placed in the selected area aperture of the microscope and a series of images with a complete freedom from rotation (Figure 4.5.2) was projected by the lens. It should be noted that micrograph (A) (Figure 4.5.2) which is the first maximum of magnification and also a distortion-free image, has the very large field of view of 1.5mm in diameter. This field of view is twice that obtained from the double-pole rotation-free lens which has half the bore diameter of the double snorkel lens. Hence this large bore lens has the advantage of increasing the field of view which is usually small in conventional microscopes.

If the lens geometry is doubled, a rotation-free lens will be obtained of an 8mm bore and an effective focal length of 2mm, capable of working at an accelerating voltage of 100 kV. The 2mm projector focal length is of the same order as commonly used in the final projector lenses in commercial microscopes, but such lenses usually have very small bores. The large-bore snorkel lens also has the advantage of a larger angle of projection compared with that of conventional lenses. The advantage of this large angle of projection lies in the fact that the total length of a microscope can be reduced by reducing the projection distance between the final lens and the screen.

4.6 Image distortion in the experimental single-pole lens

The distortion of magnetic lenses, in particular radial and spiral distortion, was discussed in Chapter One with a reference to the well known distortion coefficients of the double-pole lenses. The radial and spiral distortion coefficients of single-pole lenses has not previously been investigated experimentally. The importance of these

Fig. 4.5.2

A series of rotation-free micrographs projected by the double snorkel lens in the EM6 microscope at 50kV at a projection distance L of 300mm.

Micrograph (A): first maximum, inverted and distortion-free image of a 1.5mm diameter field of view, at $NI/V_r^{\frac{1}{2}} = 5$, $M = 15X$, $F_p = 20mm$.

Micrograph (B): erect image (obtained after the second minimum magnification) at $NI/V_r^{\frac{1}{2}} = 11.6$, $M = 100X$, $F_p = 3mm$.

Micrograph (C): $NI = 2800A.t$ where the lens starts to saturate and the coil temperature becomes high. The field of view is still large. $NI/V_r^{\frac{1}{2}} = 12.4$, $M = 150X$, $F_p = 2mm$.

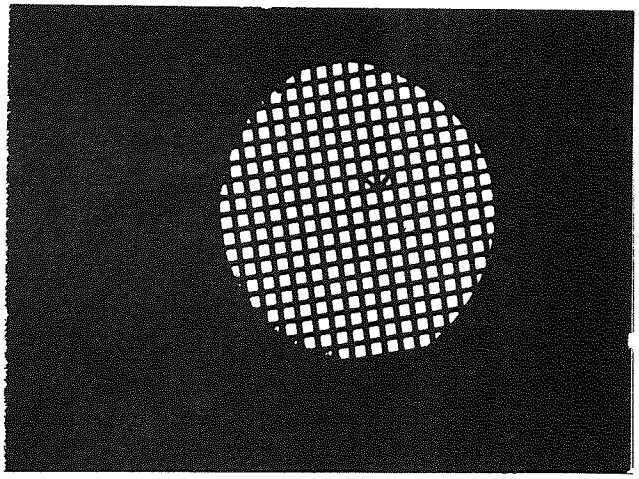

(A)

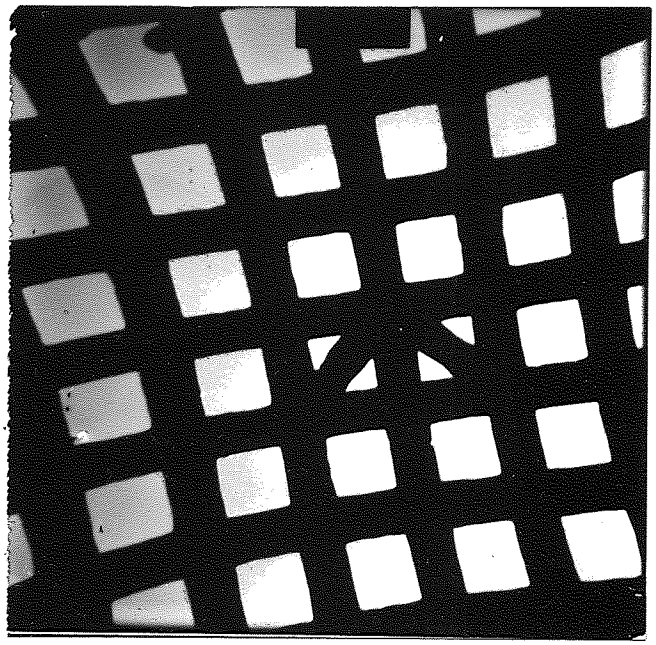

(B)

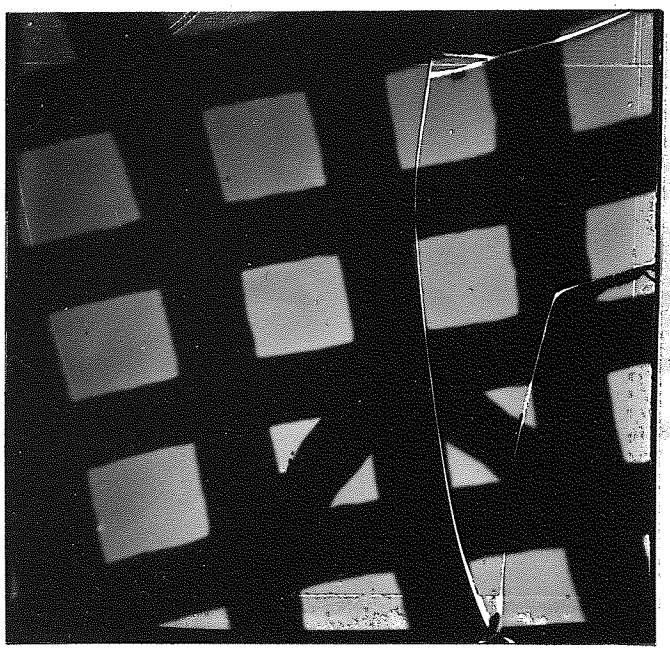

(C)

lenses make it necessary to obtain experimental evidence concerning their distortion coefficients.

The 30 kV snorkel lens was used to find the distortion coefficients for a single lens and to investigate the distortion of a double one. It was mounted on the Intercol electron optical bench to project an image of a copper grid which was used for the measurement of distortion at different excitations.

Distortion in the single snorkel lens

One half of the double snorkel lens was used. The single-pole lens nearest to the screen was excited i.e. the lens whose pole was facing the screen. The imaging process was similar to that of the diagram shown in Figure 4.1.1. The whole bore of the lens was illuminated in order that the radial displacement, r of the electron beam from the optical axis equals to the radius R of the lens bore, i.e. $r/R = 1$. The magnified lens bore filled the screen with the projected image of the copper grid.

At different excitations, the radial and spiral distortions of the projected images were measured across its magnified bore. Due to the fact that the ray incident parallel to the optical axis at a distance r from it, will pass through the paraxial focus only if $r/R \ll 1$, the magnified centre square on the screen was assumed to be distortion-free since its side length, 2r is very much less than the lens diameter, 2R. The rays of a radially undistorted image should intersect the image screen at a distance ρ from the axis whereas the distorted ones intersect at the distance $(\rho + \Delta\rho)$. Since the incident ray was not exactly parallel to the axis, the measured distortion was corrected; this correction was only important at low excitations. the radial distortion $(\Delta\rho/\rho)_{rad}$ $\left[= C_d(r/R)^2\right]$ and the spiral distortion $(\Delta\rho/\rho)_{sp}$ $\left[= C_{sp}(r/R)^2\right]$ will equal C_d and C_{sp}

respectively since the measurements were taken along the magnified bore diameter.

Figure 4.6.1 shows the radial and the spiral distortion coefficients of the snorkel lens as a function of the excitation parameter $NI/V_r^{\frac{1}{2}}$ compared with those computed, using Marai's program (1975), from the date of the field distribution. It can be seen that the computed and measured values of the spiral distortion coefficient C_{sp} are in good agreement within experimental error. The spiral distortion coefficient C_{sp} was computed by Liebmann (1952) for four double-pole lenses S/D = 0.2, 0.6, 1 and 2 at different excitations. The results were expressed in relative units, by plotting $(C_{sp}/C_{sp})_o$ as a function of $(NI/NI_o)^2$. C_{sp_o} is the value of the spiral distortion coefficient for $(NI/NI_o)^2 = 1$, where NI_o is the ampere-turns required to reach the minimum projector focal length at a constant accelerating voltage. Figure 4.6.2 shows that one single curve is obtained which is a straight line on a double logarithmic scale. The experimental results for the single-pole lens (C_{sp_o} =0.185 at $NI_o/V_r^{\frac{1}{2}} = 14.5$) lie along the same straight line whose slope is 1.3. Therefore,

$$\left(\frac{C_{sp}}{C_{sp_o}} \right) = \left(\frac{NI}{NI_o} \right)^{2.6} \qquad \text{..... 4.6.1A}$$

$$\text{or} \qquad (C_{sp})^{\frac{1}{2}} = (C_{sp_o})^{\frac{1}{2}} \left(\frac{NI}{NI_o} \right)^{1.3} \qquad \text{..... 4.6.1B}$$

Considering the radial distortion coefficient, C_d of the single-pole lens in Figure 4.6.1, it can be seen that it varies with the excitation parameter $NI/V_r^{\frac{1}{2}}$ in the same way as for double-pole lenses. For a weak lens, C_d remains nearly constant, then reaches a maximum after which it drops away fairly steeply and changes sign, i.e. "pincushion" distortion changes to "barrel" distortion. Figure 4.6.1

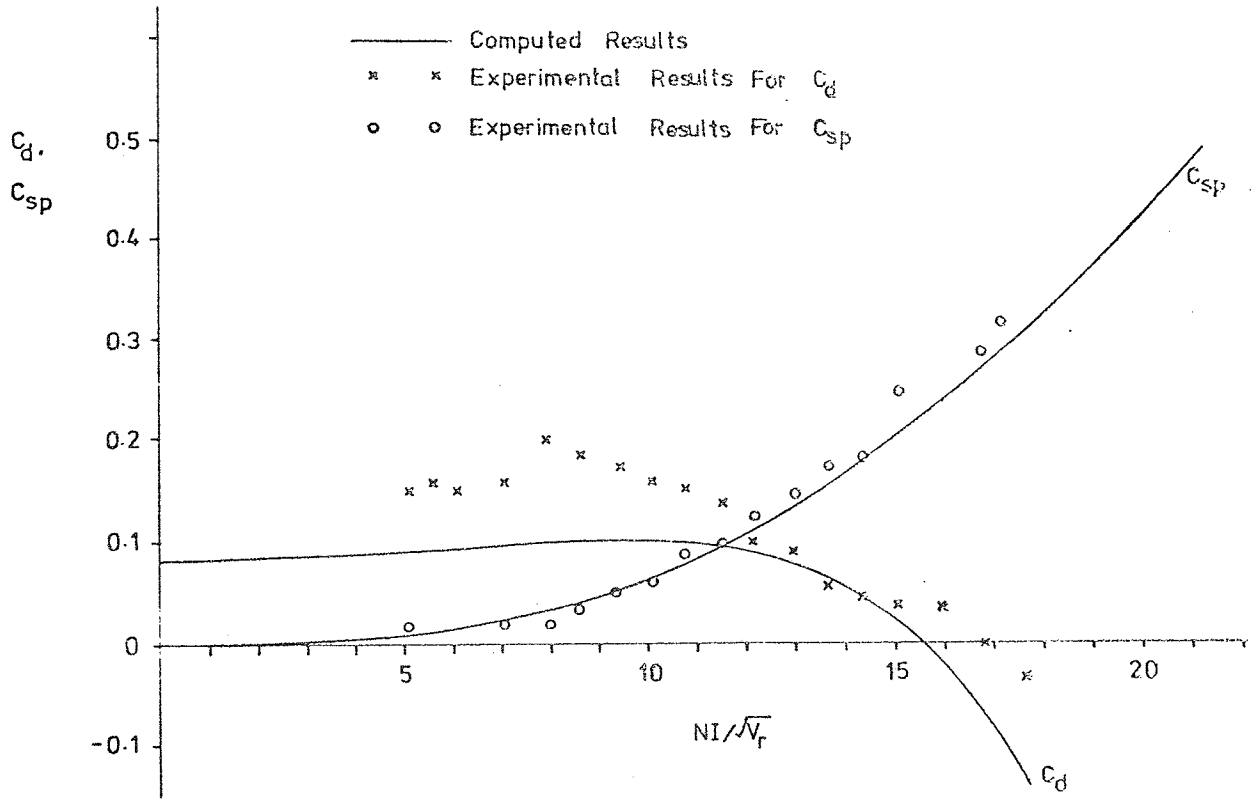

Fig. 4.6.1 Computed and measured radial and spiral distortion coefficients of the 4mm bore single-pole lens,

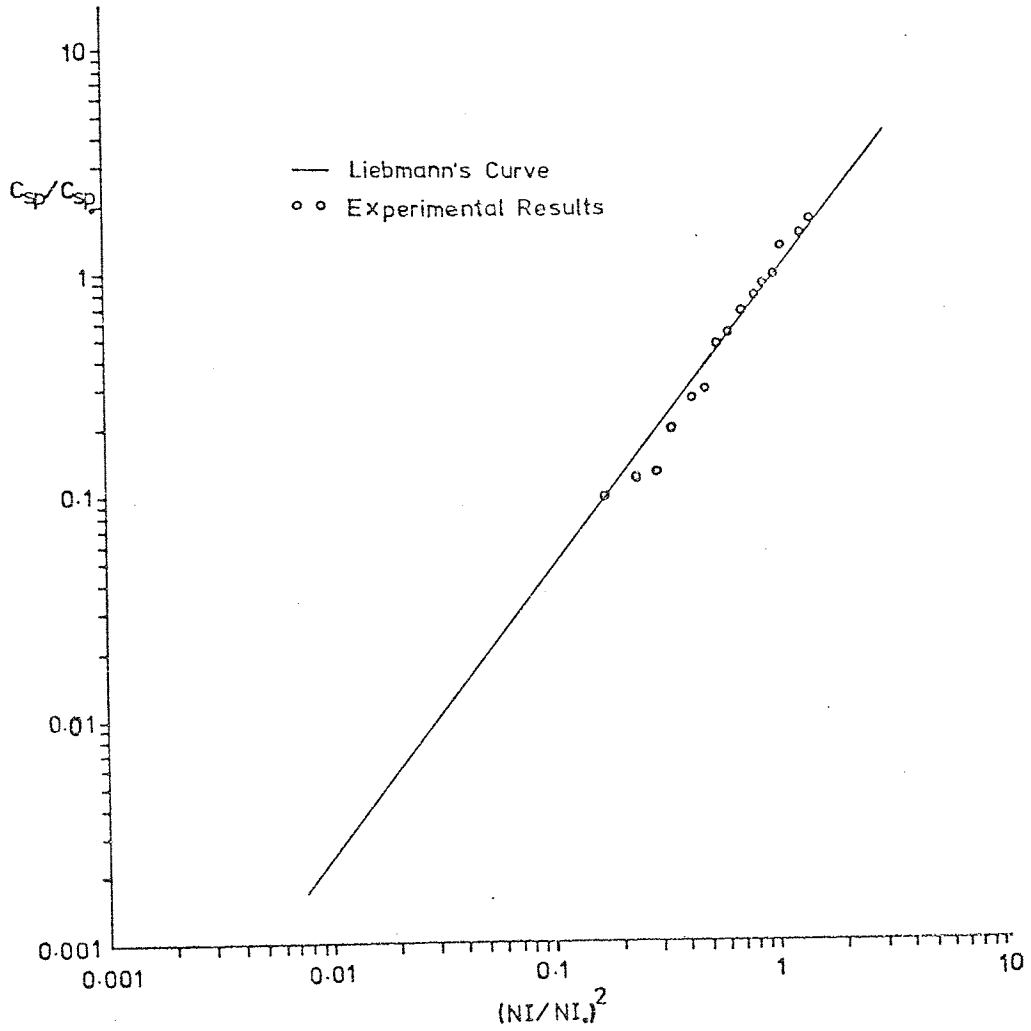

Fig. 4.6.2 Measured relative spiral distortion coefficient (C_{sp}/C_{sp_o}) as function of $(NI/NI_o)^2$ of the 4mm bore single-pole lens compared with that of Liebmann's curve (1952) for the double-pole lenses of $2 \gtrsim S/D \gtrsim 0.2$.

shows that the experimental results are appreciably higher than computed results; this can be ascribed to the difficulty in measuring the radial distortion particularly at low excitations. However, near the minimum projector focal length where the distortion is small Figure 4.6.1 shows good agreement between the experimental and computed results of C_d. It can be seen that spiral distortion is more pronounced than the radial distortion when the lens is operating near its minimum focal length.

Although the computed and the experimental results of C_d and C_{sp} are not in quantitative agreement, the general features of the distortion of this single-pole lens can be compared with that of the well known double-pole lenses. Figure 4.6.3 shows that the radial distortion coefficient of this 4mm bore snorkel lens is equivalent to that of a double-pole lens of S/D = 2 which has very low radial distortion. Its spiral distortion coefficient is equivalent to that of a double-pole lens whose S/D = 3 which has very low rotational distortion, less than that for S/D = 2. Hence this snorkel lens appears to have some of the advantages of two known double-pole piece lenses of particularly good performance.

The distortion $\left(\frac{\Delta\rho}{\rho}\right)$ in an electron micrograph produced by the final projector lens of an electron microscope depends on the projection distance L, between the phtographic plate and the projector lens. It is shown in Appendix VIII that

$$L = \left(\frac{R_p}{R}\right)\left(\frac{\Delta\rho}{\rho}\right)^{-\frac{1}{2}} \quad C^{\frac{1}{2}} f_p \qquad \ldots\ldots 4.6.2$$

where,

R_p = radius of the photographic plate.

R = radius of the lens bore.

C = distortion coefficient (C_d or C_{sp}).

f_p = projector focal length.

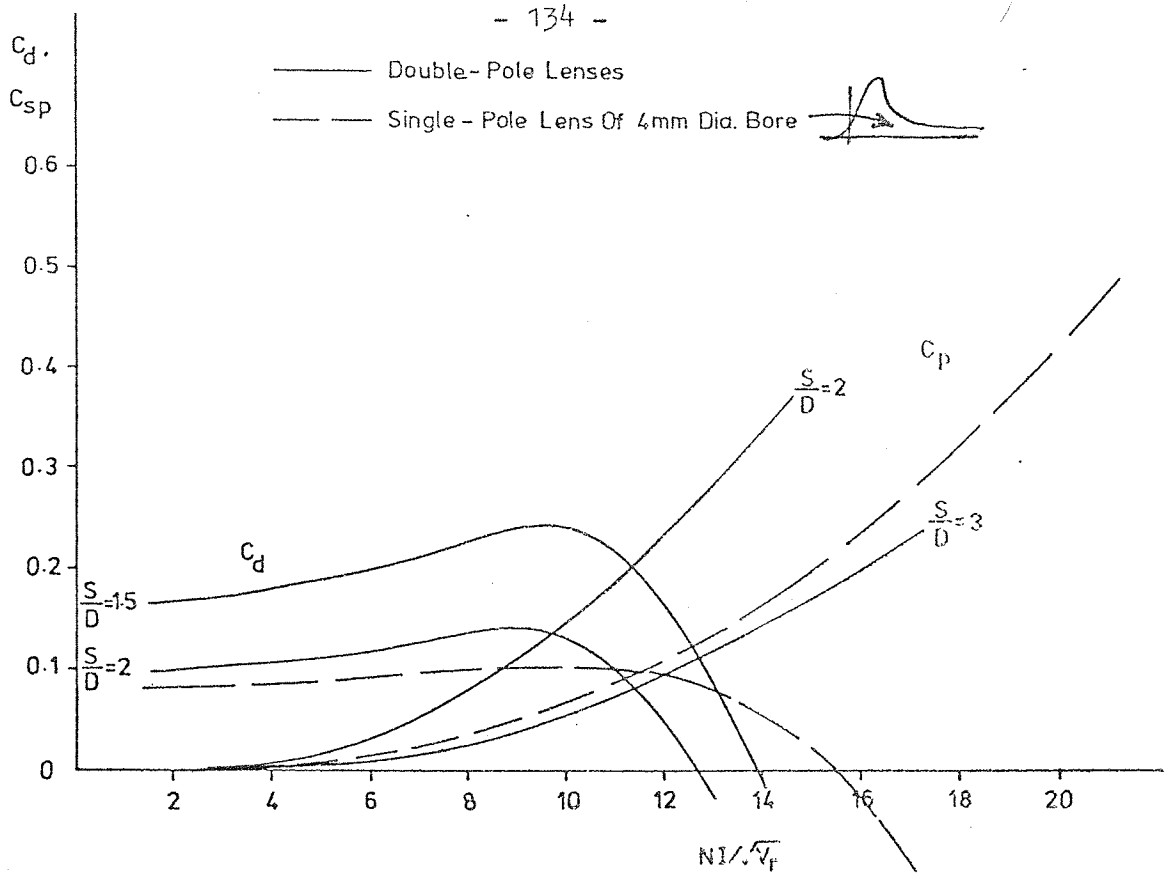

Fig. 4.6.3 Computed radial and spiral distortion coefficients of the 4mm bore single-pole lens compared with those of double-pole lenses.

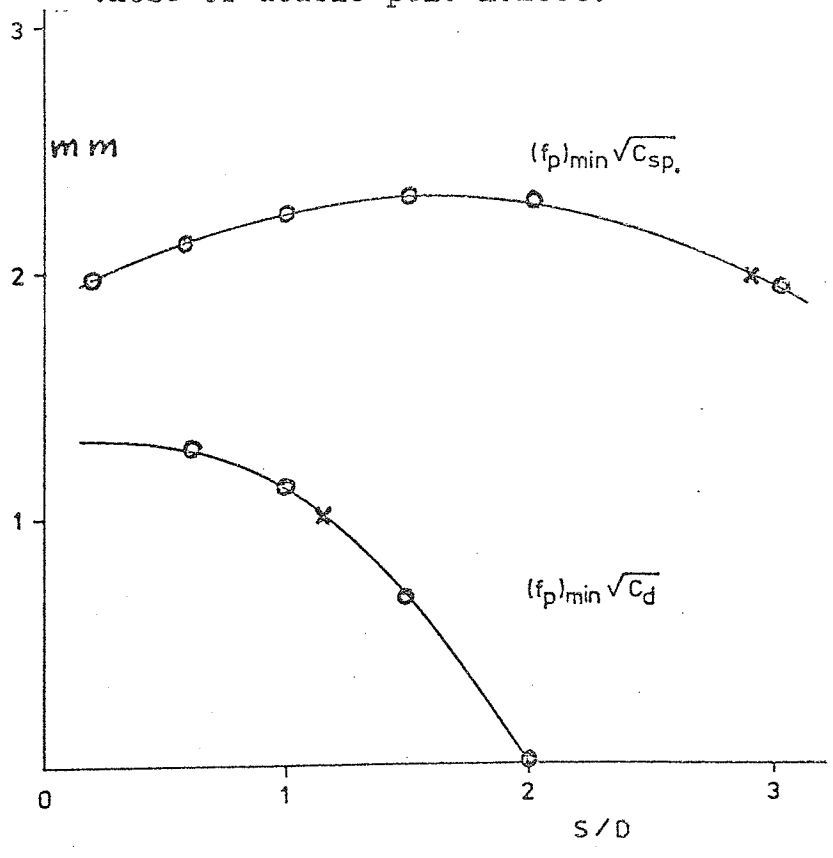

Fig. 4.6.4 Variation of the parameter $(f_p)_{min} C_d^{\frac{1}{2}}$ and $(f_p)_{min} C_{sp}^{\frac{1}{2}}$ at $NI_o/V_r^{\frac{1}{2}}$ with the S/D ratio of 4mm bore double-pole lenses. The cross on each curve represents the corresponding value of the 4mm bore single-pole lens.

For a constant distortion ($\Delta r/r$),

$$L \propto C_{\frac{1}{2}} \; f_p \qquad \ldots\ldots 4.6.3$$

i.e. L depends only on the product of $C_{\frac{1}{2}}$ and f_p since R_p and R are constants. For double-pole lenses, the minimum projector focal length is approximately given by

$$(f_p)_{min} \simeq 0.5 \, (S^2 + 0.45 \, D^2)^{\frac{1}{2}}$$

$$\text{i.e.} \qquad (f_p)_{min} \simeq R \left[(S/D)^2 + 0.45 \right]^{\frac{1}{2}} \qquad \ldots\ldots 4.6.4$$

The projection distance L of the 4mm bore snorkel lens can be compared with that of double-pole lenses of different S/D ratios where D = 4mm also. For equal and constant values of radial and spiral distortions, Figure 4.6.4 shows $(f_p)_{min} \, C_{d}^{\frac{1}{2}}$ and $(f_p)_{min} \, C_{sp_o}^{\frac{1}{2}}$ of the 4mm bore double-pole lenses as a function of the S/D ratio where C_d and C_{sp_o} are the radial and spiral distortion coefficients at the excitation $NI_o/V_r^{\frac{1}{2}}$ required for the minimum projector focal length. It can be seen that as far as the spiral distortion is concerned, the projection distance at the maximum magnification is maximum when the double-pole lens has S/D=1.5, and also the lenses of S/D=0.2 and S/D=3 are both identical and similar to the 4mm bore snorkel lens. At maximum magnification, as far as radial distortion is concerned, the projection distance decreases initially slowly with $1 \gtrsim S/D > 0$ and then steeply with the increase of S/D; the snorkel lens lies below the turning point. However, Figure 4.6.4 shows that the microscopes built of double-pole lenses should have the final projector lens with $S/D > 1.5$. Figure 4.6.4b is typical of all double-pole magnetic lenses with bigger or smaller bores, the lenses with bigger bores will require longer projection distance and vice-versa.

Figure 4.6.5 shows the variation of the projection distance (i.e $f_p C_d^{\frac{1}{2}}$) with the excitation parameter $NI/V_r^{\frac{1}{2}}$ at a constant and equal radial and spiral distortions on the screen for the 4mm bore double-pole lens of S/D = 2 and the 4mm bore snorkel lens using its experimental results. When the radial distortion is under consideration, the projection distance decreases steeply from infinity to zero with the increase of $NI/V_r^{\frac{1}{2}}$ and it has higher values for the snorkel lens than that for the lens of S/D = 2. Considering the spiral distortion, the projection distance increases with the increase of the excitation parameter $NI/V_r^{\frac{1}{2}}$ sharply from zero to a plateau where it becomes independent of excitation and then increases sharply again; in this case the snorkel lens requires shorter projection distance than that for the lens whose S/D = 2. The shape of the two curves $f_p C_d^{\frac{1}{2}}$ and $f_p C_{sp}^{\frac{1}{2}}$ shown in Figure 4.6.5 is the same for all magnetic lenses. It can be seen that the projection distance in a microscope should be a compromise between the two curves, and a good projector lens is that which has a shorter projection distance.

Experience in electron microscopy tends to suggest that in an electron micrograph the acceptable spiral distortion $(\Delta\rho/\rho)_{sp}$ can be twice the acceptable radial distortion $(\Delta\rho/\rho)_{rad}$. A typical radius, R_p of the image on the photographic plate in commercial microscopes is about 50mm. The 4mm bore snorkel lens has $(f_p)_{min} C_d^{\frac{1}{2}} = 1$ and $(f_p)_{min} C_{sp_o}^{\frac{1}{2}} = 2$, Figure 4.6.4. Hence, the projection distance for 1% radial distortion is 250mm ($(\Delta\rho/\rho)_{sp}$ will be 4%) and that for 2% spiral distortion is 350mm ($(\Delta\rho/\rho)_{rad}$ will be 0.5%). Therefore an average projection distance of 300mm will give lower radial distortion (0.7%) and higher but acceptable spiral distortion (2.8%); however, this spiral distortion will be slightly reduced by the other lenses in the microscope which have an opposing current sense. The 300mm projection distance is less than that in commercial microscopes

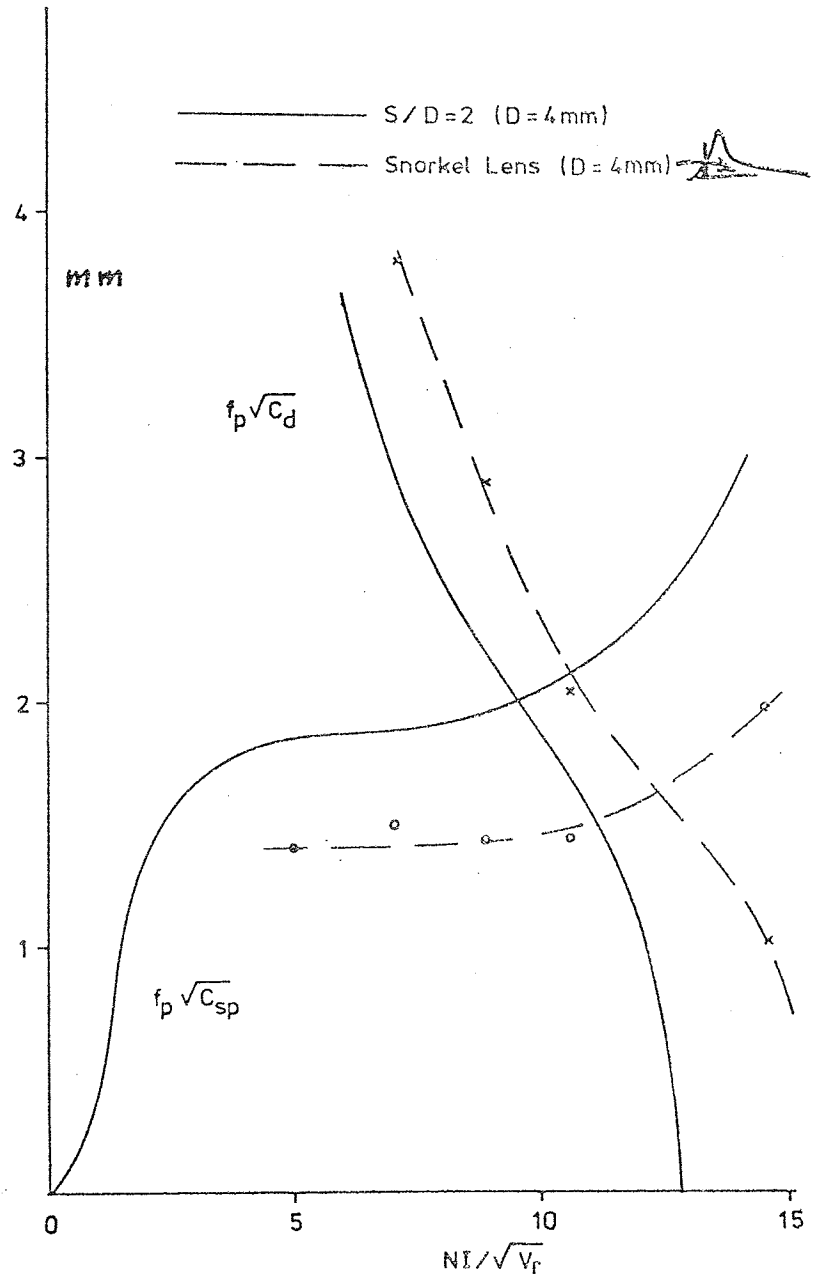

Fig. 4.6.5 Variation of $f_p C^{\frac{1}{2}}$ parameters with the excitation parameter $NI/V_r^{\frac{1}{2}}$ for the 4mm bore single-pole lens compared with that for a 4mm bore double-pole lens whose $S/D = 2$. The snout of the snorkel lens faces the screen.

which is usually of the order of 350mm as in the AEI EM6 microscope. The maximum magnification of the 4mm bore single snorkel lens at the 300mm projection distance is about 70X. Therefore, this snorkel lens is marginally better than double-pole lenses as far as distortion is concerned.

Distortion in the double snorkel lens

The variation of distortion with excitation of a double-pole rotation-free lens was discussed briefly in Chapter Three. The distortion of the present double-snorkel lens is more complicated and will now be studied in more detail.

Magnetic lenses, when weakly excited, show negative (barrel) distortion when they are used to demagnify an existing image from another lens.

At this first minimum magnification of a pair of lenses the radial distortion changes over from $-\infty$ to $+\infty$ since $\rho \rightarrow 0$, hence $(\Delta\rho/\rho) \rightarrow \infty$. As the lens excitation is increased, positive (pin-cushion) distortion begins to appear. The above variations in radial distortion are the same for single and double lenses. However, the distortion in the double lenses decreases faster than the single lens and at lower excitations, which takes place in the first loop of the magnification curve as shown below.

Figure 4.6.6 shows a typical distortion curve of a double lens as a function of excitation. The distortion of the 30 kV double snorkel lens was measured experimentally along the lens bore; i.e. the first lens whose magnification is m_1 illuminated the whole bore of the second lens which is nearest to the screen such that (r/R) of the first lens equals $1/m_1$ and that of the second lens is one. The values of the radial and spiral distortion are highly exaggerated since the measurements were taken across the whole lens bore and at a very short projection distance (60mm).

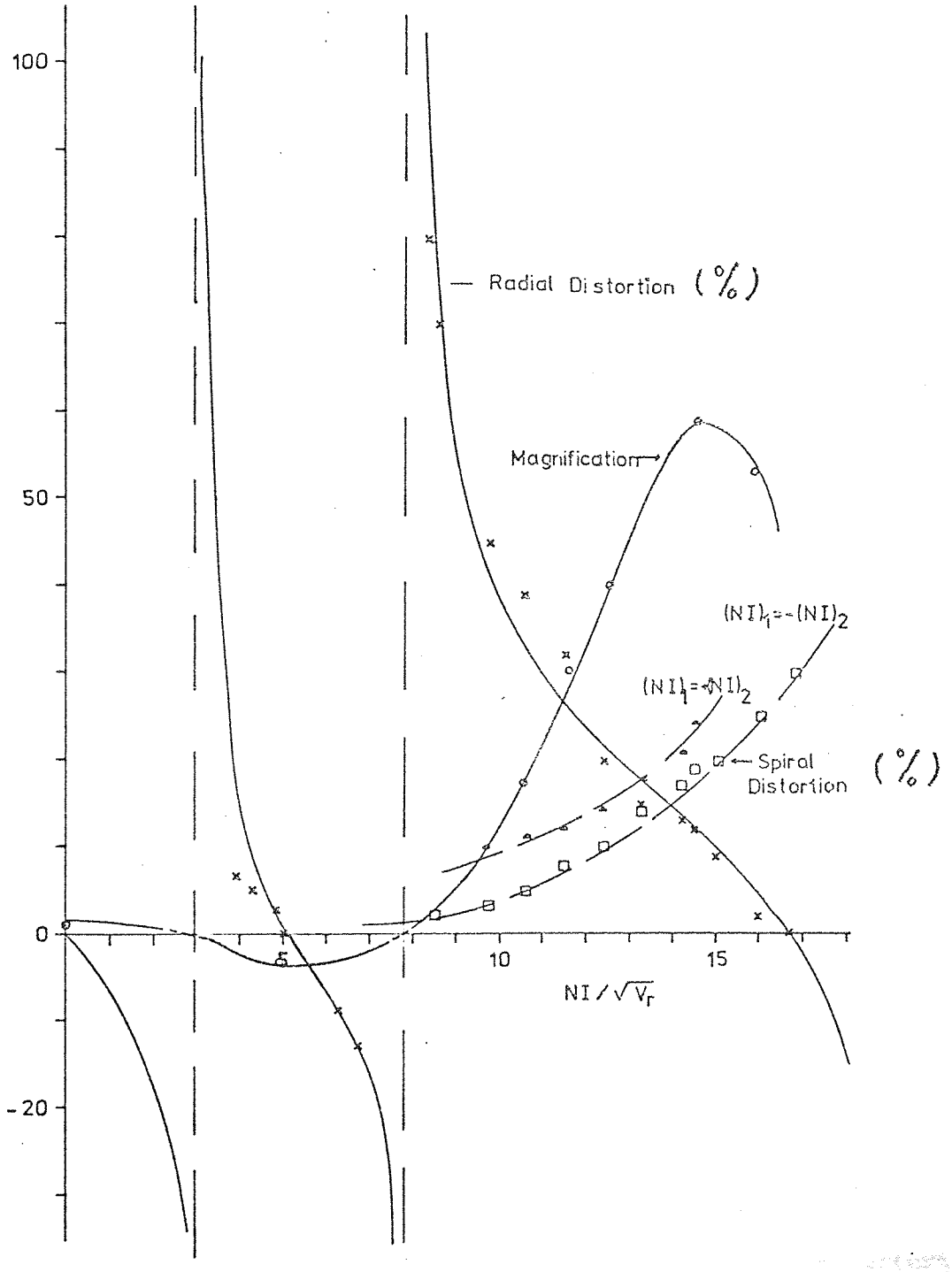

Fig. 4.6.6 Variation of the radial distortion, spiral distortion and magnification of the 30kV double snorkel lens, with the excitation parameter $NI/V_r^{\frac{1}{2}}$.

The radial distortion curve shows the following conclusions which apply to all double lenses:-

(a) The radial distortion of a rotation-free lens is not affected by the absence of image rotation.

(b) In the two loops of the magnification curve the radial distortion varies steeply with the increase of excitation.

(c) Between the first minimum and the first maximum, the second minimum and the second maximum magnifications, the radial distortion is approximately inversely proportional to the magnification.

(d) At the first maximum magnification there is always a distortion-free image where the barrel distortion of the first lens is equal in magnitude to the pin-cushion distortion produced by the second.

(e) Near the second magnification there is always a series of images of very low distortion.

(f) In the second loop of the magnifaction characteristic curve, the distortion of the lens nearest to the screen was found experimentally to be the dominant one, i.e. the contribution to distortion of the first lens is negligible.

(g) The change of distortion from $-\infty$ to $+\infty$ at the two minimum magnifications can be very useful aid to focussing when imaging the diffraction pattern at the back focal plane of the objective lens since on focus the pattern will be distortion-free.

(h) The presence of barrel and pin-cushion distortion at different excitations can be corrected if another double-lens unit is used as a second projector and operated so as to cancel the distortion to the first.

Figure 4.6.6 shows the variation of spiral distortion with

excitation of a double lens used in both modes, $(NI)_1 = \pm (NI)_2$. The spiral distortion in the rotation-free mode is clearly less than in the rotational mode. The spiral distortion curve of the final lens lies between the two curves. The spiral distortion curves of double lenses show the following:

(a) Double lenses consisting of two identical lenses operating with $(NI)_1 = -(NI)_2$ do not eliminate spiral distortion but reduce it below that of a single lens. This is because the spiral distortion is proportional to the square of the displacement of the ray from the optical axis; this displacement is not equal for the two lenses of the unit. If the radial displacement of the electron beam from the optical axis is r in the first lens, it will be $m_1 r$ in the second lens.

(b) The spiral distortion of a rotation-free lens operating in the second loop of the magnification curve was found, experimentally to be dominated by the spiral distortion of the lens nearest to the screen, as expected. Therefore, if two double-lens units are used as projectors in one system, it is important that the excitation of the second lens is opposed to that of the first in order to reduce the spiral distortion.

(c) When a double-lens unit is operating with $(NI)_1 = + (NI)_2$, it increases the spiral distortion by the same amount that the rotation-free lens reduces it below that of a single lens.

4.7 Conclusion

The experimental investigations on the 30 kV single and double snorkel lens revealed very useful properties in this kind of lens. It therefore seemed feasible to construct a scaled up version of this lens capable of working at 100 kV can be used in a new projector system.

5. ELECTRON-OPTICAL PROPERTIES OF DOUBLE AND SINGLE-POLE LENSES

5.1 Effect of lens tilt on image displacement

If an object OO' is viewed through a glass lens as shown in Figure 5.1.1 and the lens is tilted about the optical axis through an angle ε, the image OO'' experiences no displacement. Figure 5.1.1 shows that with the new axis at O'C'' the arrow head remains in the same plane. This phenomena can easily be verified experimentally.

Magnetic electron lenses have the property of rotating the image plane by an amount $\Theta = 0.186\ NI/V_r^{\frac{1}{2}}$ radians. Hence if the experiment is repeated with a magnetic lens the arrow head will be displaced from its position at O by an angle Θ to a position P as shown in Figure 5.1.2. The coordinates of P measured from the origin at O are $S = OP$ and $\phi = \Theta/2$ in polar coordinates. Hence from the geometry $S = 2\ r_i \sin \Theta/2$. Figure 5.1.1 shows that $r_i = v\varepsilon$ where v is the image distance from the lens and ε in radians. Therefore, the shift S of the image by a magnetic electron lens can be written as

$$S = 2\varepsilon v \sin\left(\frac{\Theta}{2}\right) \qquad \ldots\ldots 5.1.1$$

Equation 5.1.1 shows that at constant excitation (i.e. Θ = constant), the image shift is proportional to the angle of tilt.

An experimental verification of Equation 5.1.1 was performed. A 100 kV miniature projector lens shown in Figures 5.1.3 and 5.1.4 whose S/D = 1.5 has been placed in the diffraction stage under the final projector lens of the AEI EM6 microscope. It was supported by two brass flanges, and tilted about the axis of the water pipes. The lens was cooled by the same cooling system of the microscope.

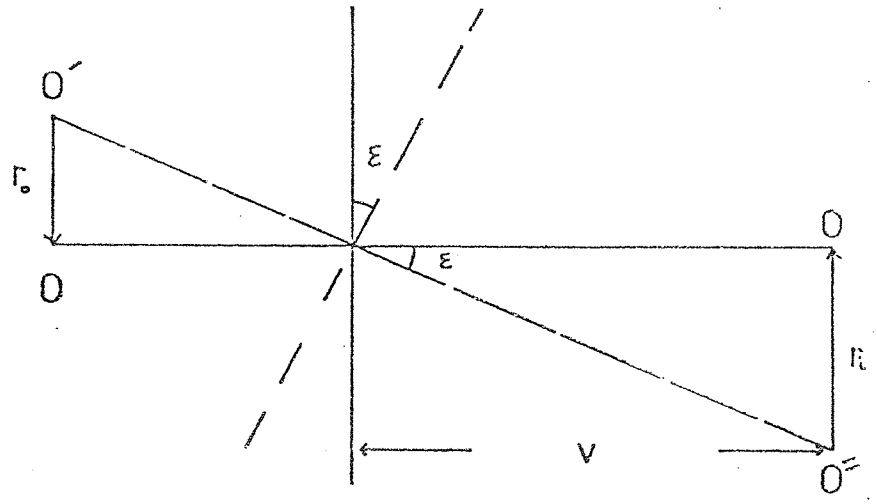

Fig. 5.1.1 Image displacement is zero when a glass lens is tilted about the optical axis.

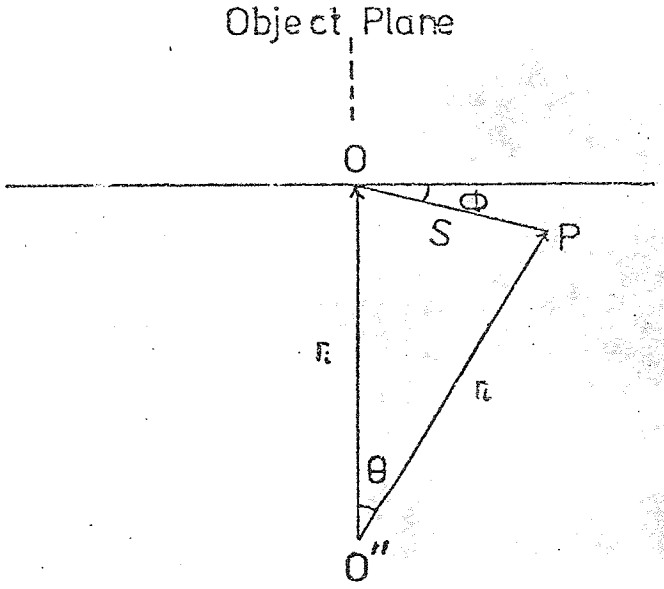

Fig.5.1.2 The displacement of an image formed by a magnetic electron lens from the object plane.

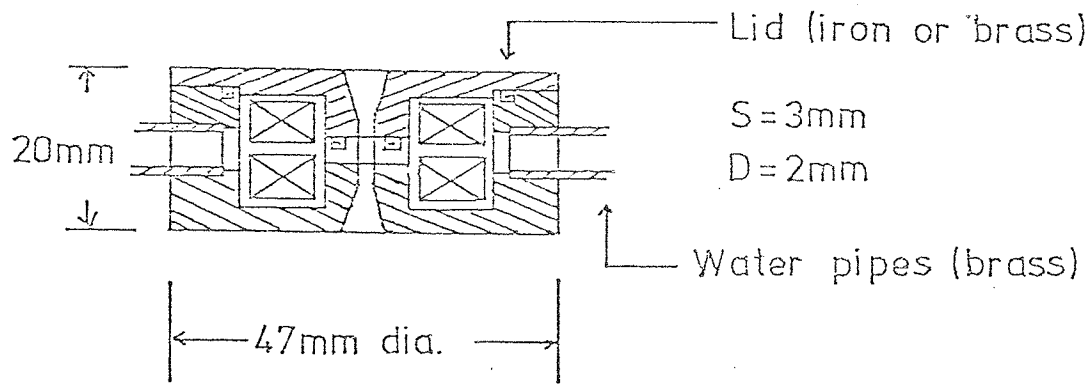

Fig. 5.1.3 Cross-section of the 100kV miniature projector lens.
Scale: full-size.

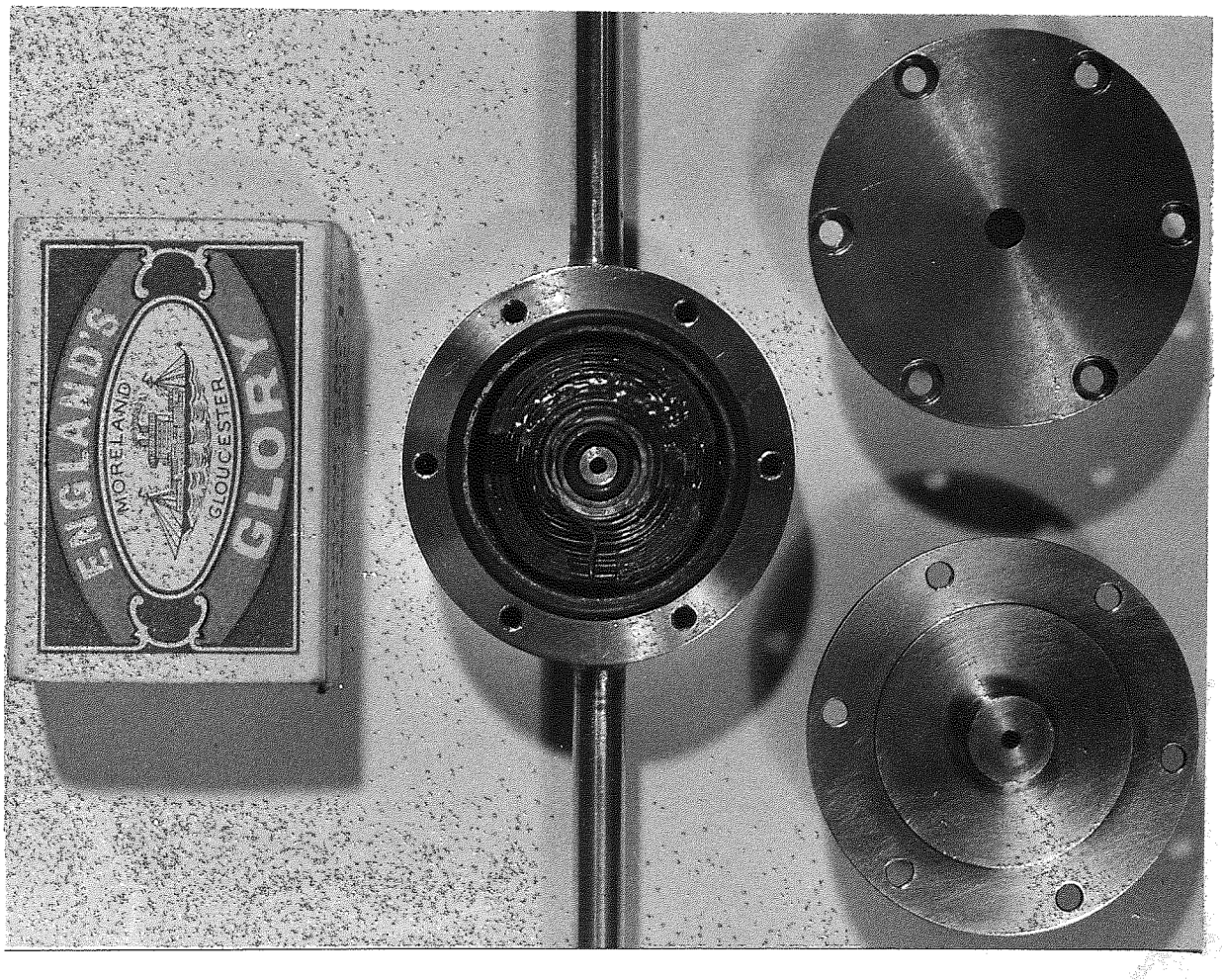

Fig.5.1.4 100kV miniature projector lens with interchangable lid. The lid on the right is of iron and that on the left is of brass.

Figure 5.1.5 shows the variation of the shift S with the excitation parameter $NI/V_r^{\frac{1}{2}}$ for two values of the tilt angle . Within the experimental errors in measuring the shift S and the angle of tilt it can be seen that there is good agreement between theory and experiment. It was also observed experimentally that for a constant lens, Current I, the shift S was proportional to the tilt angle. Hence Equation 5.1.1 has been verified. However, it should be mentioned that at a constant tilt angle the image sweeps around the screen in a clockwise or anti-clockwise direction, depending on the direction of the current in the coils, as the excitation is increased. The miniature projector lens used for investigating the image shift had an iron lid, i.e. the lens was of a double-pole type. When the iron lid was replaced by a brass one, i.e. convering the lens from a double to a single pole lens, there was no change in the image shift at the same angle of tilt, since the image shift depends on excitation.

Equation 5.1.1 shows that if there is an equal shift of an opposing sign by another magnetic lens, the net shift can be eliminated. The rotation-free snorkel lens described in Chapter Four was placed in the diffraction stage below the final projector of the EM6 microscope. This lens was also tilted about the axis of the water pipes. The two single-pole lenses were excited in the rotation-free condition i.e. $(NI)_1 = -(NI)_2$. Initially, the rotation-free lens demagnifies the image from unity to a minimum. In this region where $NI/V_r^{\frac{1}{2}}$ is between zero and 2, the image shift was too small to be detected as the angle of tilt was varied from zero to about 9^o which is the maximum angle that the double lens can be tilted without losing the image. In the region of the first loop, where an inverted, rotation-free image is obtained, it was found that the shift was zero when the magnification was unity, at $NI/V_r^{\frac{1}{2}} = 2.5$, at all

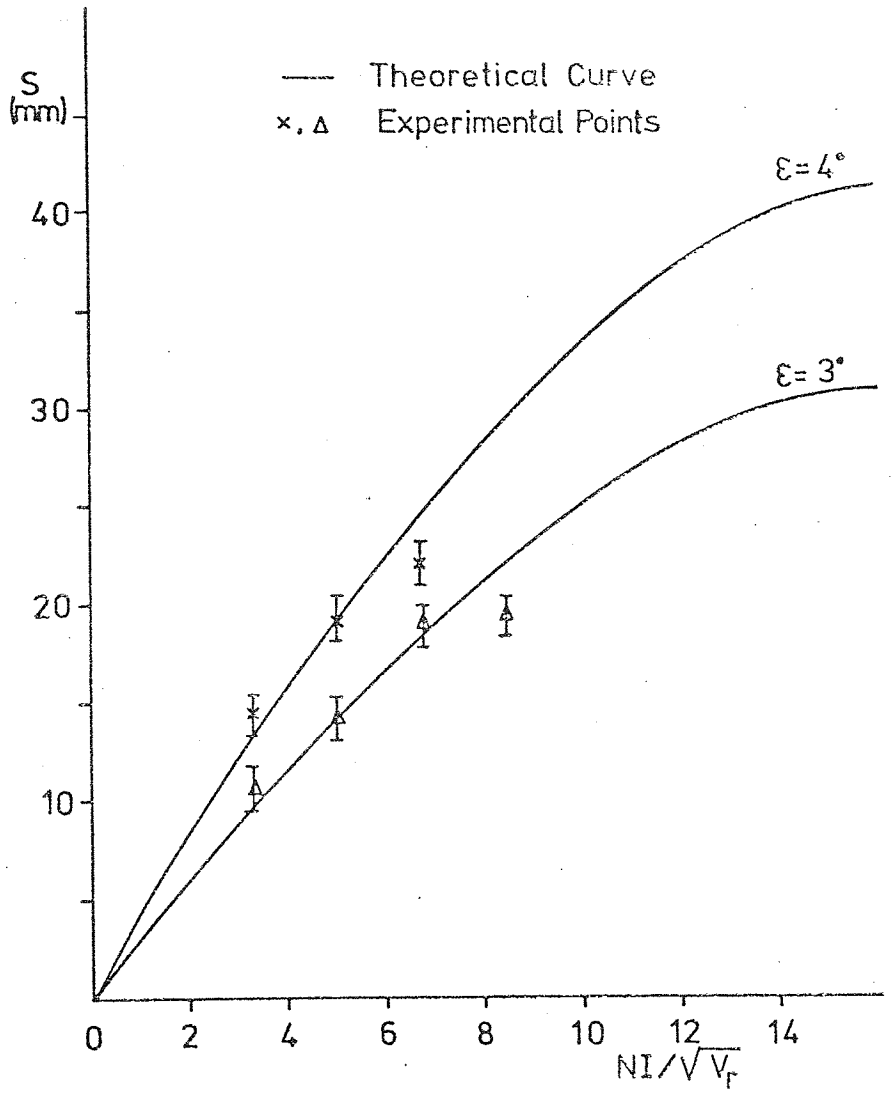

Fig 5.1.5 Image shift produced by titling a magnetic electron lens through an angle ε, as a function of the excitation parameter $NI/V_r^{\frac{1}{2}}$.

angles of tilt. Keeping the tilt angle constant, it was found that by increasing the lens excitation, the image shift increases in a direction normal to the axis of the pipes about which the lens was tilted. The image was still on the screen although the lens was at its first maximum magnification at $NI/V_r^{\frac{1}{2}} = 5$ and the angle of tilt was about 3^o (0.05 rad). It should be mentioned, however, that in practice, 3^o is a highly exaggerated angle of tilt.

The above results can be explained by reference to Figure 5.1.6. Since the two snorkel lenses are working at equal but opposite excitations, the image rotated by the first lens through an angle θ with respect to the object plane will be brought back to the original plane of the object by the second lens. However, the second lens magnifies the image of the first lens m_2 times; this causes the image move in a straight line normal to the axis of rotation and away from it with increase of lens excitation. The condition of no shift at all angles of tilt is only satisfied when $m_2 = 1$. This condition was verified experimentally. Since the focal length of each of the two snorkel lenses at $NI/V_r^{\frac{1}{2}} = 2.5$ is about 100mm as given by the computed results shown in Figure 4.4.3, the magnification m_2 of the second lens is unity on the screen which is 200mm away. The long focal length of each of the two lenses also satisfies the condition of unit magnification of the rotation-free lens at $NI/V_r^{\frac{1}{2}} = 2.5$ where the lens has shown experimentally no image shift at all possible tilt angles.

Hence a tilted rotation-free lens has the property of eliminating the image shift at unit magnification. This property makes the rotation-free lenses have a useful application as an intermediate lens in transmission electron microscopes. Also since the beam shifts in a straight line with excitation when the lens is tilted, this makes it easy to find the beam during the alignment

Image of the first lens shifted from the object plane.

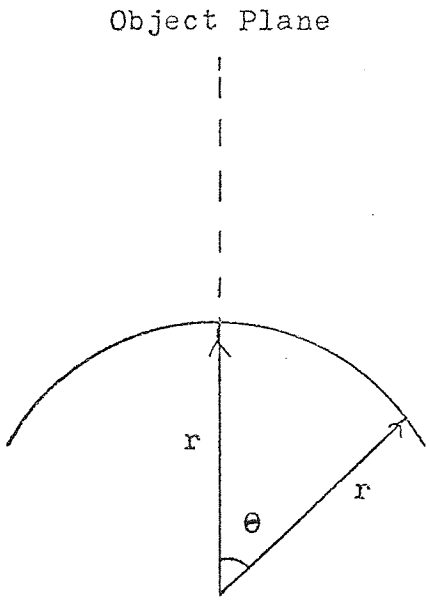

Image brought back to the object plane by the second lens and magnified by m_2X.

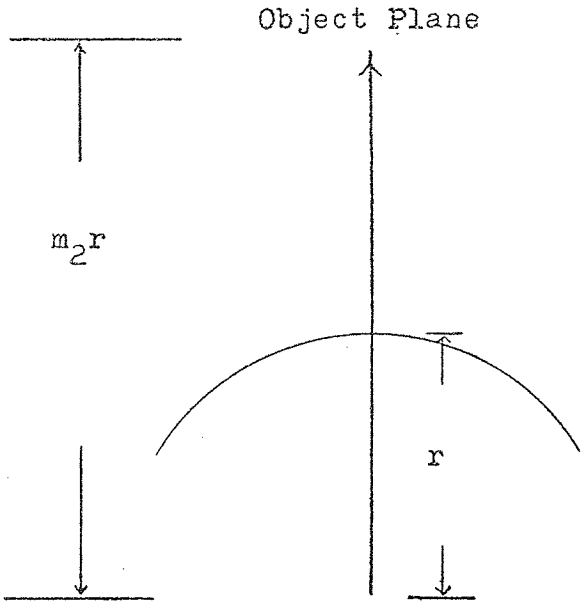

Fig. 5.1.6 Imaging processes by a tilted double-lens which has $(NI)_1 = -(NI)_2$.

procedures.

5.2 Imaging properties of a double and single-pole lens

A comparison of the imaging properties of double and single-pole lenses can be made by considering the 100 kV miniature projector lens shown in Figures 5.1.3 and 5.1.4. This lens can be readily converted from a double-pole lens to a single-pole lens merely by replacing the iron lid by a brass one. This changes the focal properties appreciably. Figure 5.2.1 shows the change in the projector focal length when the lens is converted from a double-pole (iron lid) to a single-pole type (brass lid). The thoeretical curve of the double-pole lens was determined from the universal curves for conventional lenses (Figure 1.2.7) and it agrees with the experimental results; its minimum focal length is 1.8mm at $NI_o/V_r^{\frac{1}{2}} = 13$. The minimum focal length of the single-pole lens is 5.7mm at $NI_o/V_r^{\frac{1}{2}} = 13.6$ which is three times higher than that for the double-pole lens. This experimental value of the focal length is in good agreement with that calculated from the field distribution where the half-width, a, of the exponential field is 4.7mm which gives a minimum projector focal length of 5.4mm. Hence if a double-pole lens is converted to a single-pole lens by simply removing one of its pole-pieces, the minimum focal length will increase and occur at a higher excitation.

This miniature single-pole lens was tested in the EM6 microscope as the final projector lens (the original second projector lens was switched off) at 75 kV in two positions: (A) with the snout's surface facing the incident beam and (B) with the snout's surface facing away from the incident beam and towards the fluorescent screen. This was done in order to record the imaging properties of the lens in both cases for a constant projection distance between snout and screen (or photographic plate) (300mm). The lens

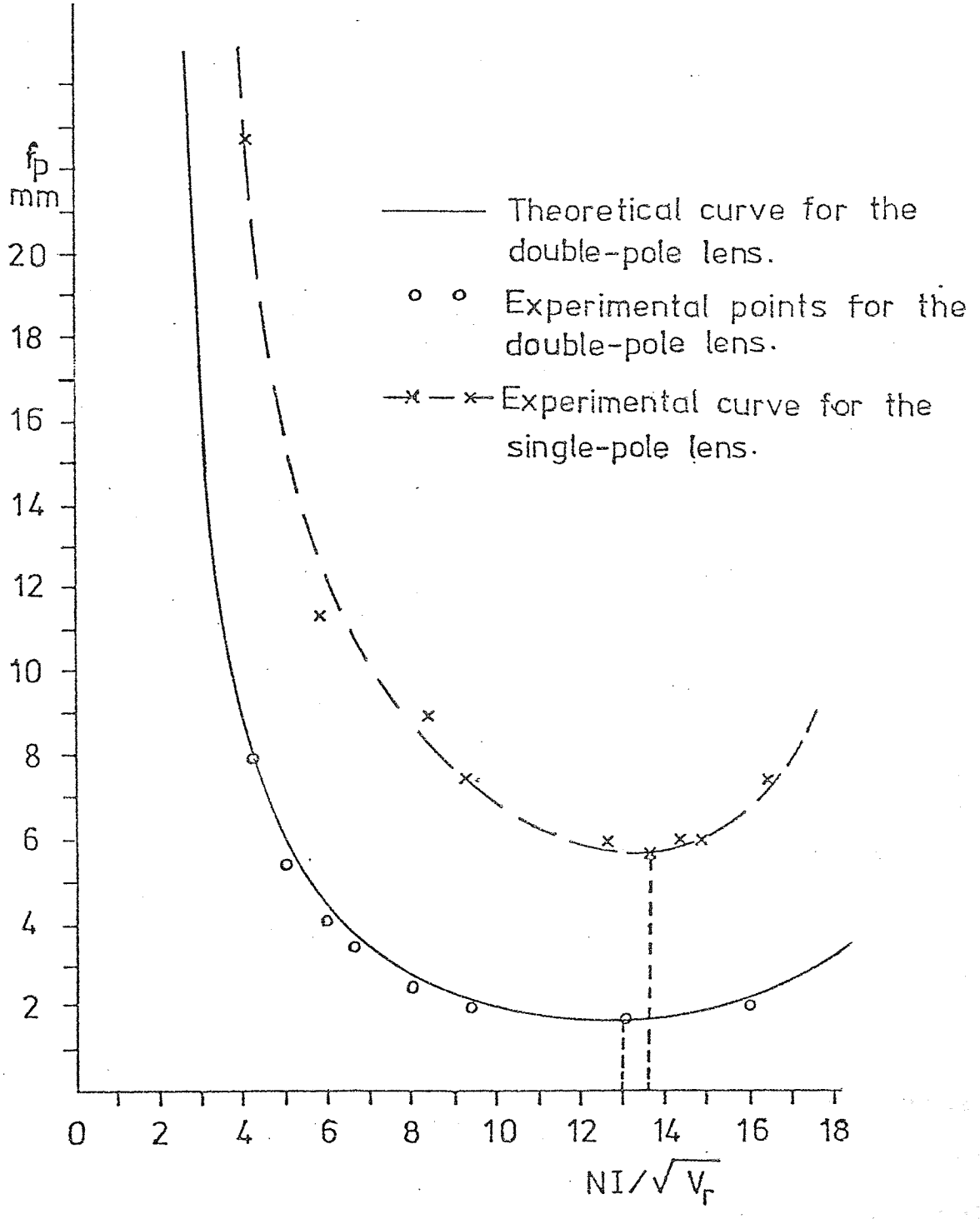

Fig. 5.2.1 Variation of the projector focal length f_p of a 100 kV miniature projector lens as a double and as a single-pole lens with excitation parameter $NI/V_r^{\frac{1}{2}}$.

magnification is the same since the projector focal length at a specific excitation is the same in both cases.

Figure 5.2.2 shows two micrographs taken in this way at $NI/V_r^{\frac{1}{2}} = 8.4$. The micrographs are identical within the limits of measurement. Both have equal radial distortions (about 5% and equal spiral distortions (about 1%). Hence, up to this excitation the lens has similar properties in both modes of operation. The contribution of the intermediate lens to the distortion of the image on the photographic plate is 2.8% radial distortion ($C_d = 0.45$) and 0.3% spiral distortion ($C_{sp} = 0.05$), which shows that the effect of its distortion especially of spiral distortion is small whether the excitations of the intermediate and the final projector are cooperative or opposing. Therefore, the spiral distortion in the final image is due chiefly to the spiral distortion of the final single-pole projector lens.

At excitation parameter $NI/V_r^{\frac{1}{2}} = 14$, the projector focal length of the single-pole lens is 6mm as shown in Figure 5.2.1 and its magnification on the photographic plate is 50X. Figure 5.2.3 shows two micrographs taken when the miniature projector lens was operating under the above conditions, keeping the excitations of the EM6 intermediate and objective lenses unaltered and equal to those at Figure 5.2.2. It can be seen that the field of the micrograph (B) taken with the snout facing the screen is limited by the bore of the lens. This is best explained by referring to Figure 5.2.4 which shows the ray path through the lens structure at $f_p = 6$mm. Filling the whole bore when entering the lens field, the beam leaves the lens structure at 0.45mm from the optical axis and strikes the photographic plate at a radius of 45.5mm i.e. the calculated diameter of the image is 91mm. Experimentally, this diameter is 94mm which agrees within 3% with the calculated value. When the lens is

(A)

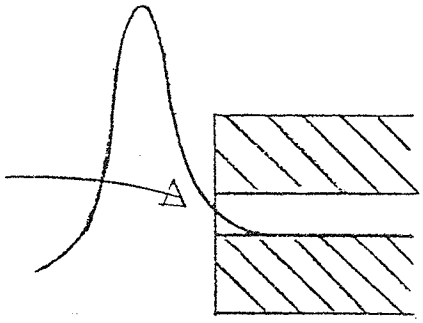

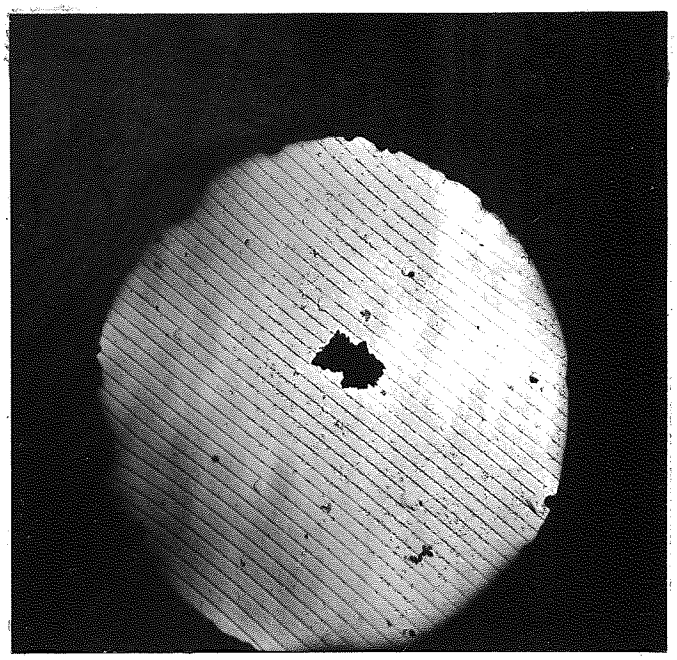

(B)

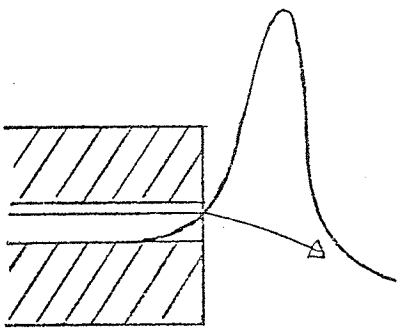

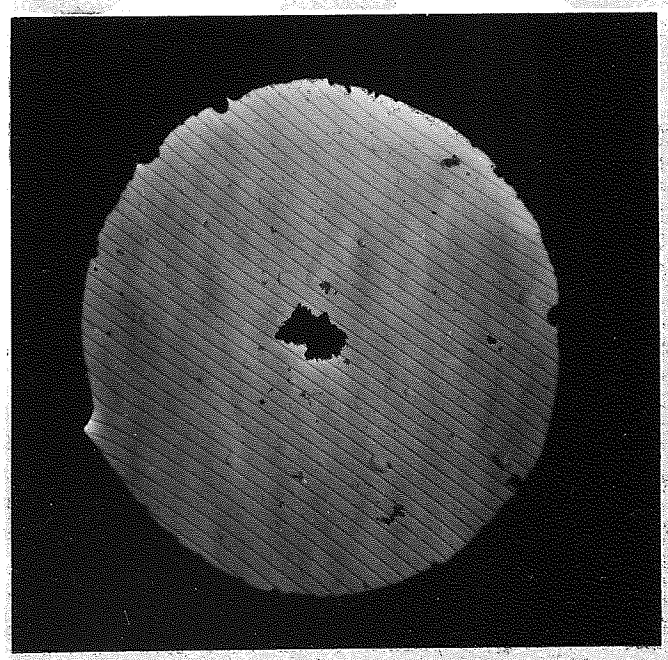

Fig. 5.2.2 Micrographs of a line grating magnified 3600X when the second projector lens in the EM6 microscope is a miniature single-pole lens whose excitation parameter $NI/V_r^{\frac{1}{2}}=8.4$. Direction of the electron beam through the lens indicated on the figure.

(A)

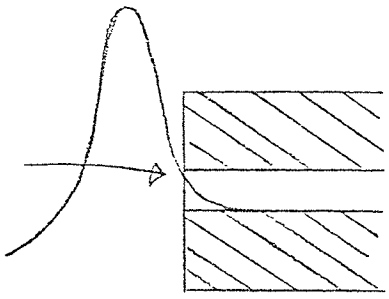

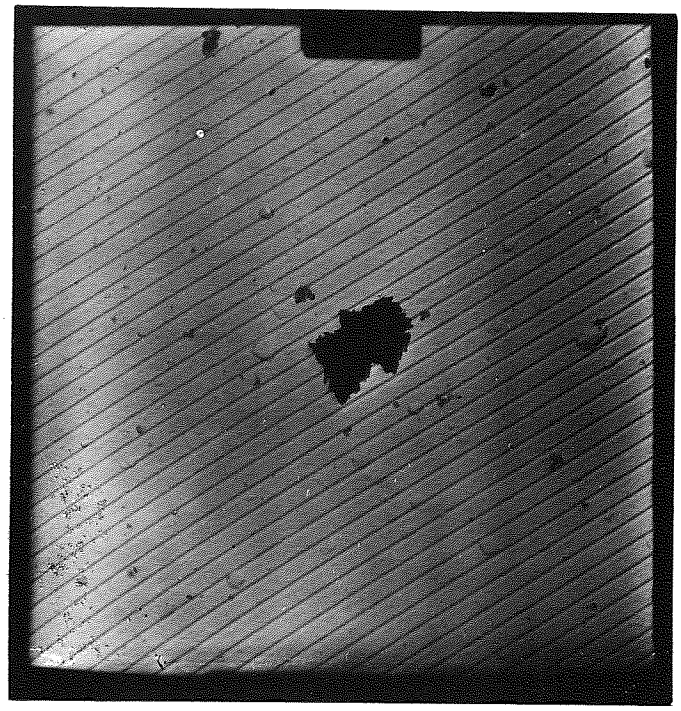

(B)

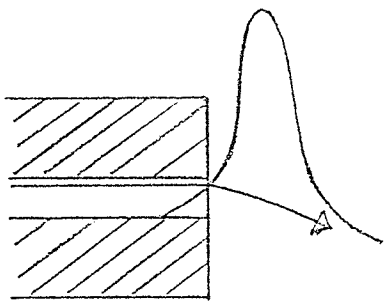

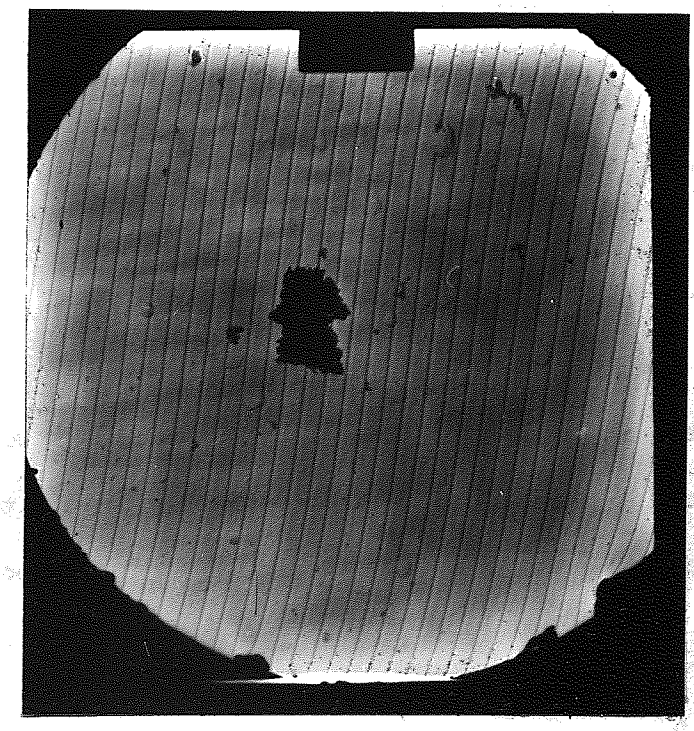

Fig. 5.2.3 Micrograph of a line grating magnified 5500X when the second projector lens in the EM6 microscope is of a single-pole type at $NI/V_r^{\frac{1}{2}} = 14$. Notice that the spiral distortion is sensitive to the direction of the electron beam through the lens.

inverted, so that the snout now faces the incident beam, calculations show that the image just covers the whole photographic plate at a diameter equal to the diagonal of the photographic plate as shown in micrograph (A), Figure 5.2.3. The image plane of the micrograph (A) is rotated relative to that of micrograph (B); this is because the rotation of the final lens changes from a clockwise direction to an anti-clockwise one when the lens is inverted mechanically and the connections of the coil to the power supply are left unaltered. The 60^{o} angle of rotation observed between the two micrographs is what is expected theoretically. Consider the distortions of the two micrographs in Figure 5.2.4. Both micrographs show small and equal radial distortion (about 3%) on about 50mm radius. However, it can be seen that micrograph (B) which is taken with the snout surface facing the screen, has appreciably higher spiral distortion than micrograph (A) with the snout facing the incident beam. This can be seen clearly in Figure 5.2.5 in which the micrographs of Figure 5.2.3 have been reproduced in the same orientation and with an identical field of view. The rotational distortion in micrograph (B) with the snout facing the screen is 6% which is twice that in (A).

The measured distortion from Figures 5.2.2 and 5.2.3 are plotted in Figure 5.2.6 for the two directions of the lens snout. These show conclusively that the distortion of the single-pole lens whose snout is facing the incident beam is considerably less than that whose snout is facing the screen. This interesting result was confirmed later by Marai (1975) who computed the radial and spiral distortion coefficients for the two directions of the lens from the data of the field distribution. Unfortunately, the complete field distribution of the experimental lens could not be measured due to the small bore of the lens; the accessible nearest point to the snout was 9mm away. However, the data of one lens of the 30kV doublet was used to check

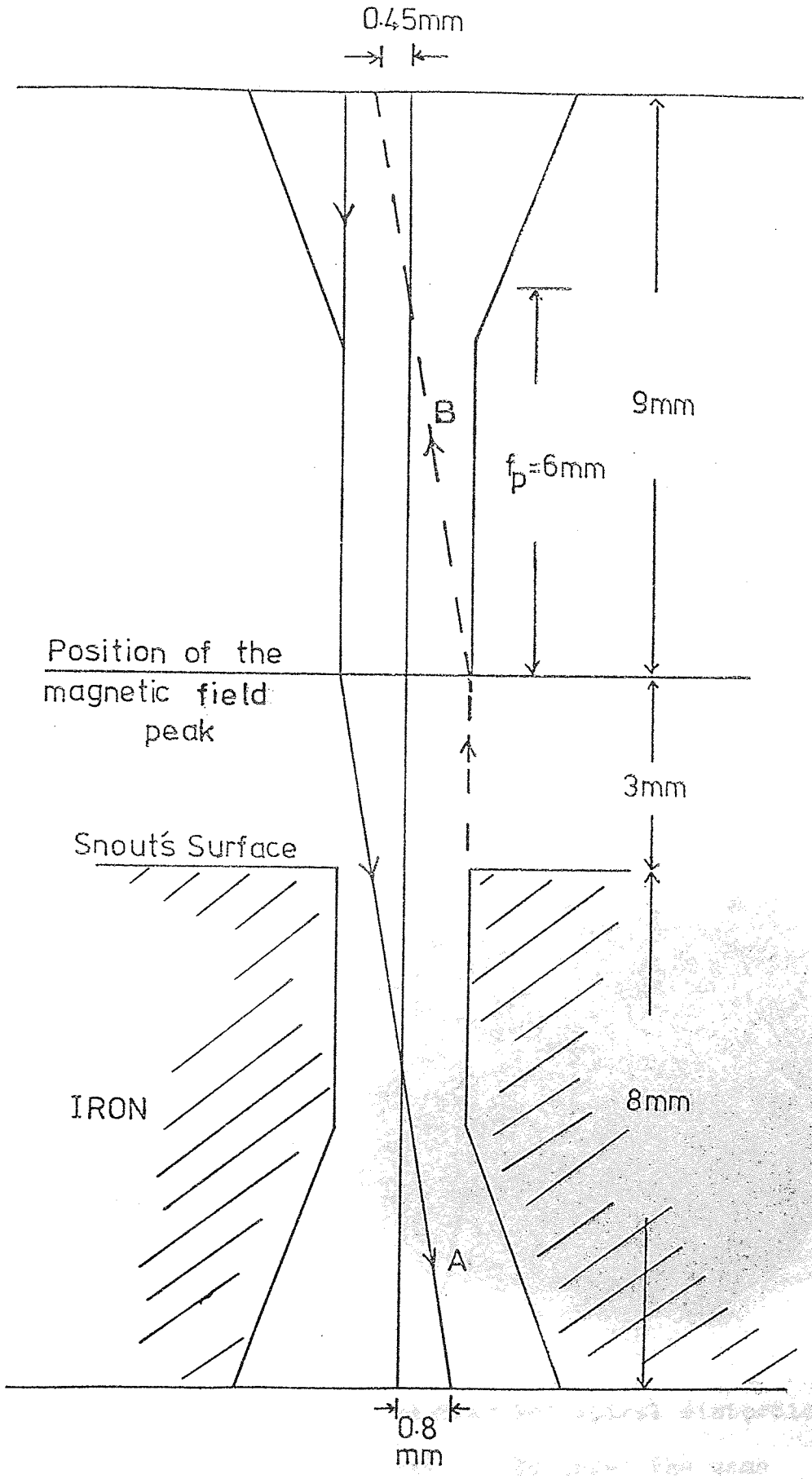

Fig. 5.2.4 Ray path of the electron beam in the experimental single-pole lens of 6mm focal length for beams traversing the field in opposite directions.

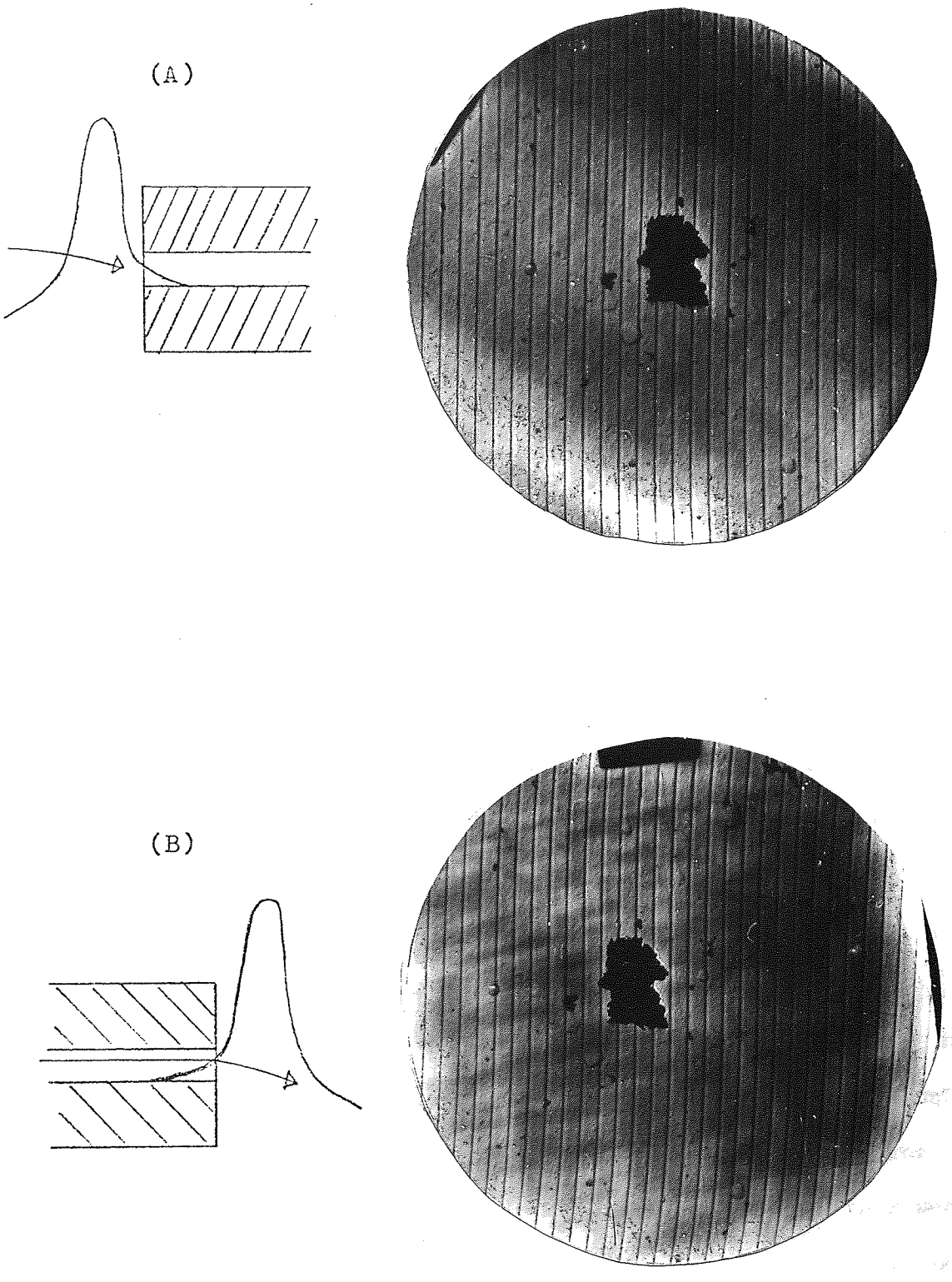

Fig. 5.2.5 Electron micrographs showing the spiral distortion in (A) is less than that in (B) under the same imaging conditions and field of view.

for the presence of a difference in distortion in the two ways of operation. Figure 5.2.7 shows that the computed results of C_d and C_{sp} for the lens with the snout facing the screen is higher than that if the lens is reversed. The change in radial distortion in Figure 5.2.7 is small however; this is the reason why it does not appear in Figure 5.2.6. The change in spiral distortion on the other hand is large and therefore easy to measure experimentally. Hence single-pole projector lenses should be operated with their snouts facing the incident electron beam in order to obtain full advantage of their superior optical properties.

5.3 The effect of the bore diameter of a single-pole lens on its focal properties

It was shown in Chapter Four that it is possible to have miniature single-pole lenses with large bores and relatively short focal lengths. Figure 5.3.1 shows a photograph of a single-pole miniature lens used for testing these properties with the attachments for changing its geometry. It is 50mm in diameter and 29mm high, and has a brass lid around its snout. The lens is excited by three coils (wound with 24 S.W.G. insulated copper wire); D_1=22mm and D_2=44mm. The total number of turns in the lens was 351 and the total resistance was 2.6 ohms at 17°C. The basic snout had a 15mm diameter bore, but the bore diameter could be changed by inserting a cylindrical iron plug. This iron cylinder had a length equal to that of the lens and an outer diameter fitting closely into the 15mm bore of the snout and it is bored through its axis. Figure 5.3.1 shows three iron plugs, which have the following bores: (a) zero bore, (b) 5mm bore diameter and (c) 10mm bore diameter. Hence only one parameter was changed in the lens geometry and that was the bore diameter.

The lens was first tested for magnetic saturation by measuring the maximum axial magnetic flux density at different ampere-turns by

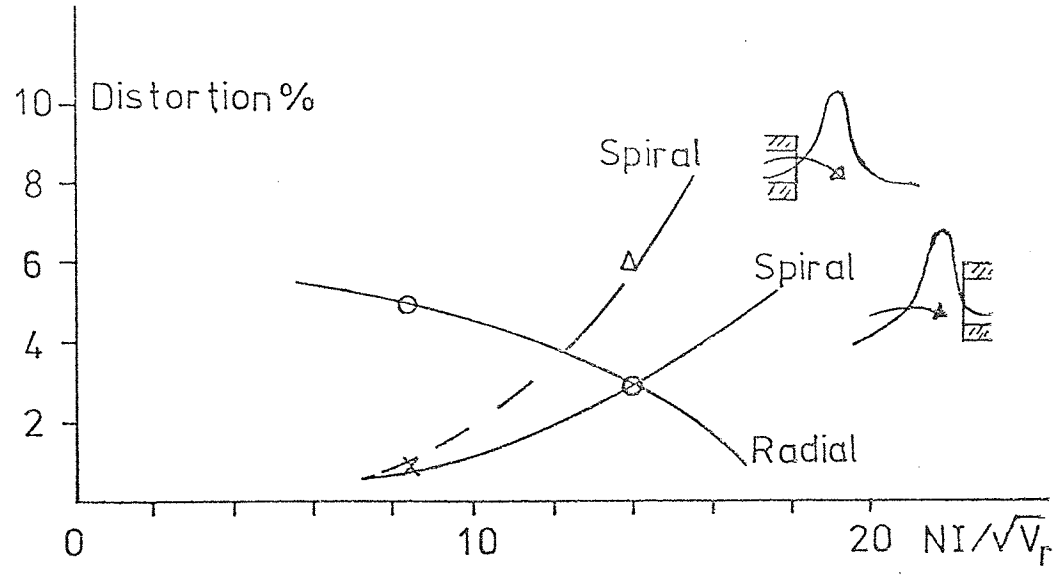

Fig. 5.2.6 Variation of distortion of the experimental single-pole lens with excitation parameter $NI/V_r^{\frac{1}{2}}$ for the two ways of operation.

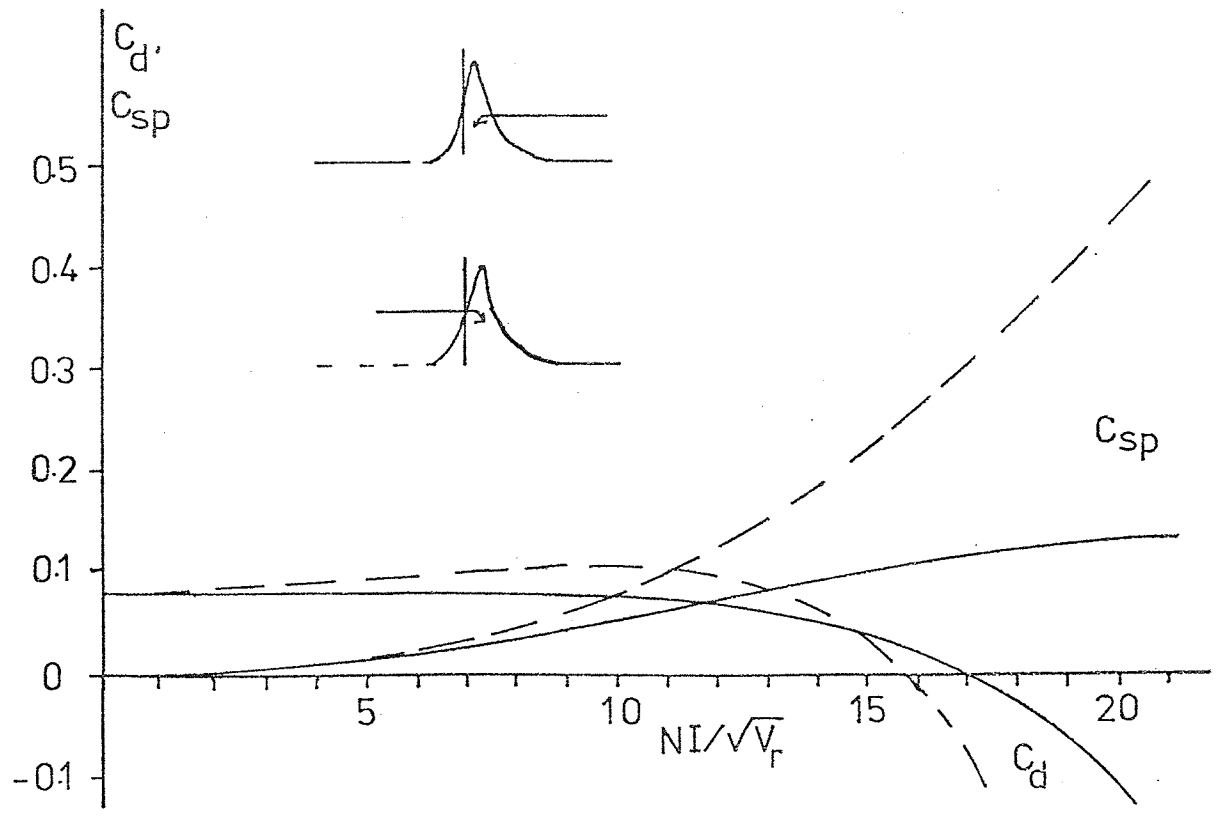

Fig. 5.2.7 Computed radial and spiral distortion coefficients of the 4mm bore single-pole lens when the electron beam enters the field in two opposite direction.

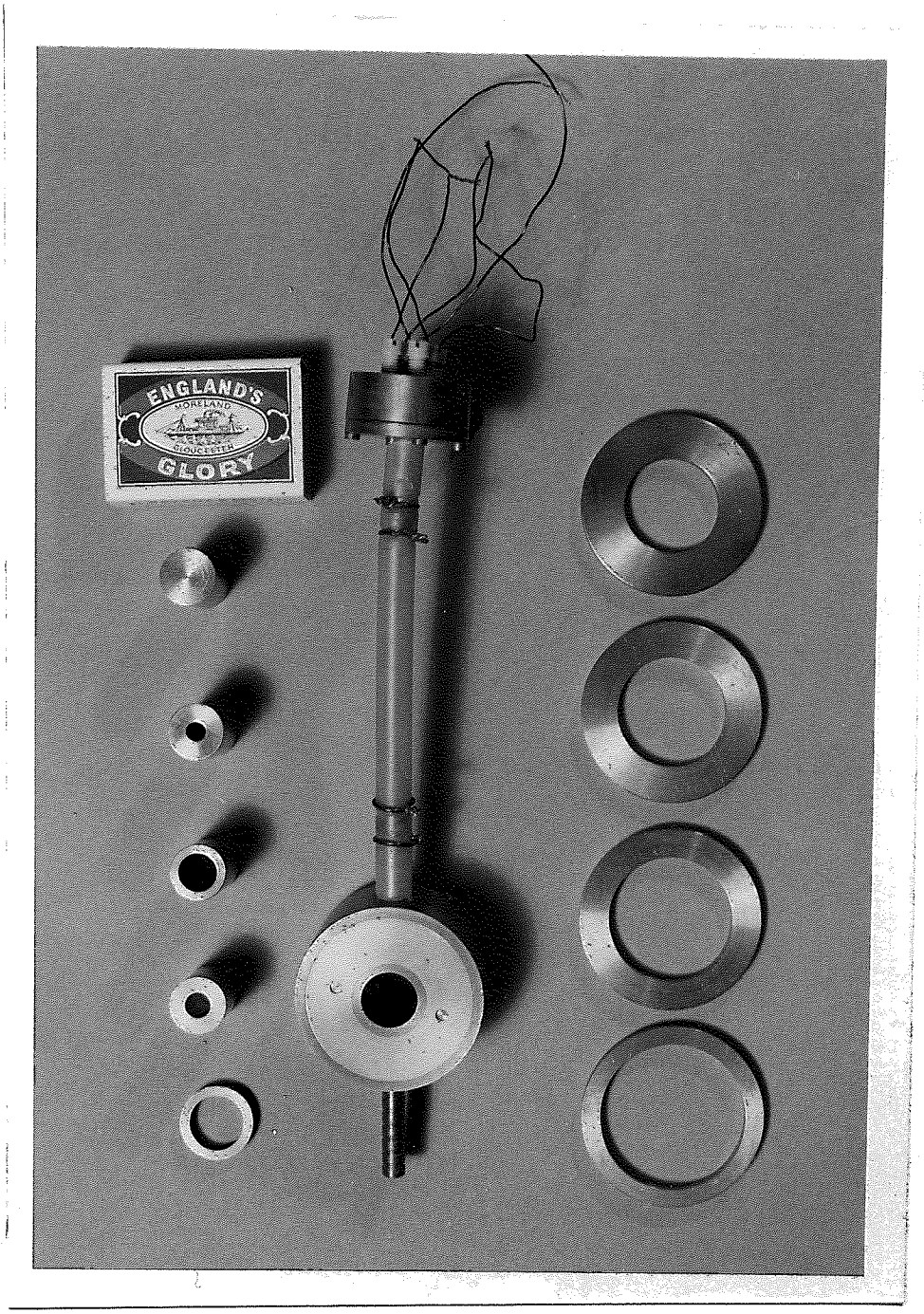

Fig. 5.3.1 Experimental miniature single-pole lens with attachments to change its geometry.

means of a Hall-probe. It was found that the 1755 (I = 5 amp) ampere-turns were enough to produce saturation in the lens with the largest bore (15mm). With smaller bores the lens required more ampere-turns in order to show signs of saturation. Therefore, the field distributions for different lens bores were all measured at an excitation of 1755 ampere-turns.

Figure 5.3.2 shows the cross-section of the lens and the axial field distributions (B_z curves) for different lens bores. It should be mentioned that the areas under the curves are all equal and agree very closely with that calculated from the expression $\int Bdz = \mu_o NI$. This provides a check on the calibration of the Hall-probe gaussmeter. It is seen that the position of the maximum flux density B_m moves towards the snout face as the bore diameter is decreased. Of greater importance for the imaging properties of the lens is the fact that for decreasing values of the bore diameter the maximum value B_m increases, leading to a greater refracting power and thus shorter focal length. The position of the maximum flux density B_m in snorkel lenses with bores is usually of the order of 2 to 5mm away from the snout's structure. The value of B_m depends on the geometry of the snout which in this experiment was a flat ended cylinder. However, the maximum field will be higher if the snout is made conical. The field decreases steeply between the peak and the lens bore itself; the smaller the bore the steeper the curve as shown in Figure 5.3.2. However, except for the B_z curve of the zero bore, all curves have the same flux density of 0.075 Tesla (750 gauss) at the snout face. Inside the lens bore there is a saturation peak in the case of a 15mm bore, and on the flat iron surface there is another peak due to the flux leakage inside the bore at all bore diameters. It can be seen that at distance 20mm and more away from the snout the flux density becomes independent of the bore diameter. In the case of a zero bore

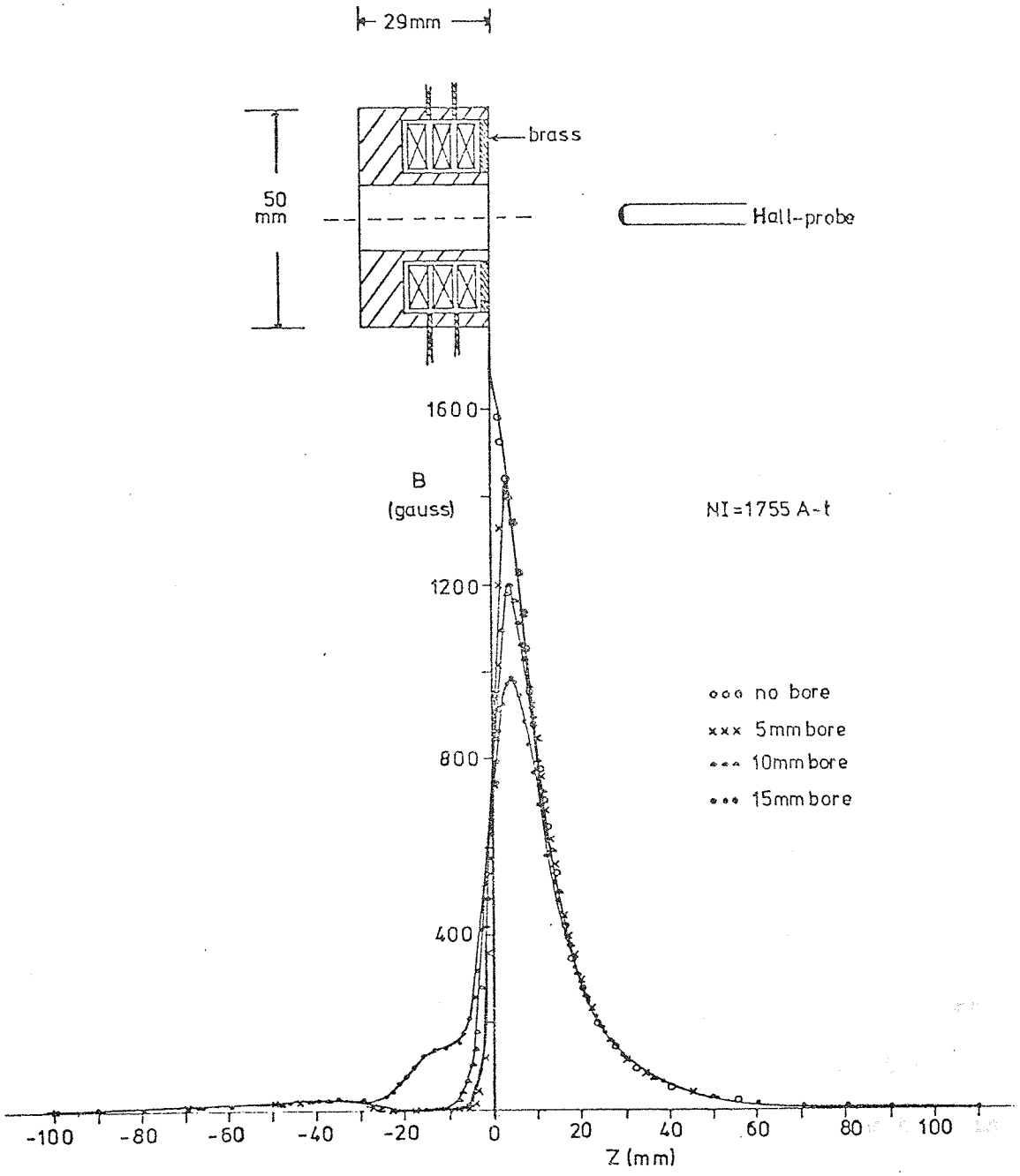

Fig. 5.3.2 Flux density distributions of the experimental single-pole lens with different bores. The saturation effect is shown inside the lens structure along the bore.

lens the field could be measured only up to a distance of 1mm from the snout; the peak value was estimated to be 1700 gauss; however the field started to vary exponentially at a distance of 5mm from the snout which is typical for snorkel lenses with bores also.

The half-width of the field and maximum flux density for different bore diameters were determined from Figure 5.3.2 and plotted in Figures 5.3.3 and 5.3.4 as a function of the diameter D of the bore in the snout. It can be seen that the half-width, a, is not very sensitive to bore size for it increases slowly and becomes constant if the bore diameter is further increased. The value of the maximum field B_m decreases steadily with the increase of the bore size until it becomes nearly independent of its diameter. These results are expected from the field distributions shown in Figure 5.3.2 where all the curves for all bore sizes pass through the same point on the snout and hence they cannot have a maximum of less than that value (750 gauss).

The data of the curves shown in Figure 5.3.2 were used to compute the focal length. Figure 5.3.5 shows the variation of the projector focal length with excitation parameter $NI/V_r^{\frac{1}{2}}$ for different bore sizes. It shows that the change in the bore size from zero to 5mm in diameter has no effect on the excitation required to reach the minimum focal length. The minimum focal length lens of 5mm bore is only 5% higher than that with no bore, a very small difference. Hence, unlike a double pole lens a single-pole lens can have its bore increased with a negligible effect on its focal properties. Thus, the lens bore is doubled (i.e. 10mm diameter bore), its minimum focal length increases by less than 10%; this requires 7% more excitation, but this is still very small. When the lens bore is increased to 15mm diameter, its minimum focal increase about 20% and requires 14% more excitation. This demonstrates a substantial increase in bore

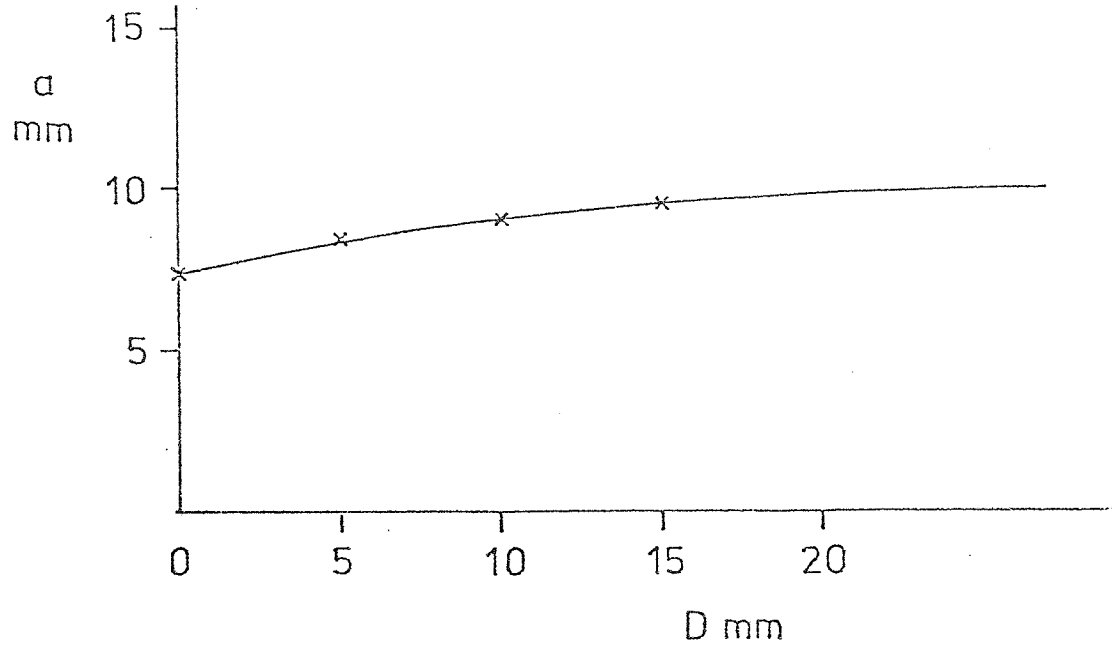

Fig. 5.3.3 Variation of the half-width of the magnetic field with the bore diameter of a single-pole lens.

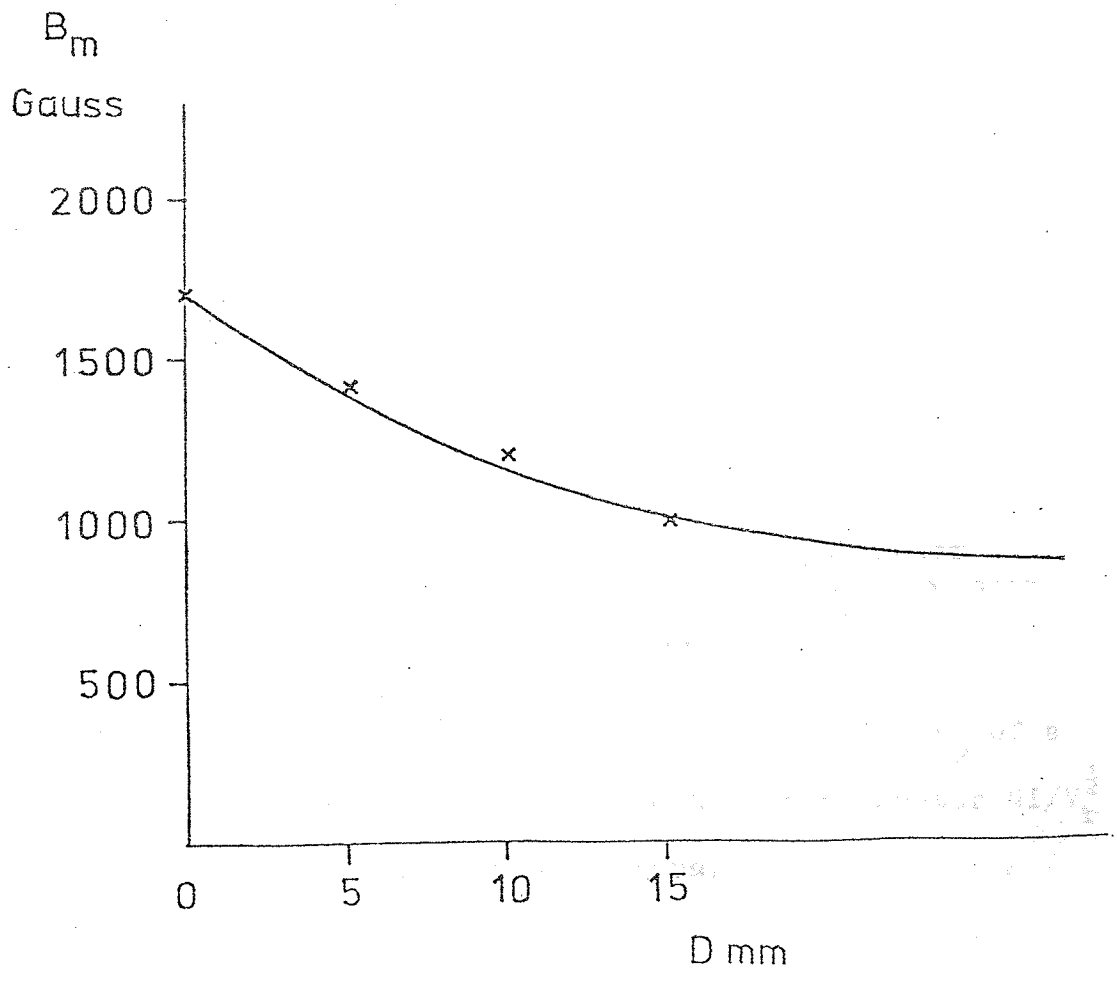

Fig. 5.3.4 Variation of the maximum flux density of the magnetic field with the bore diameter of a single-pole lens.

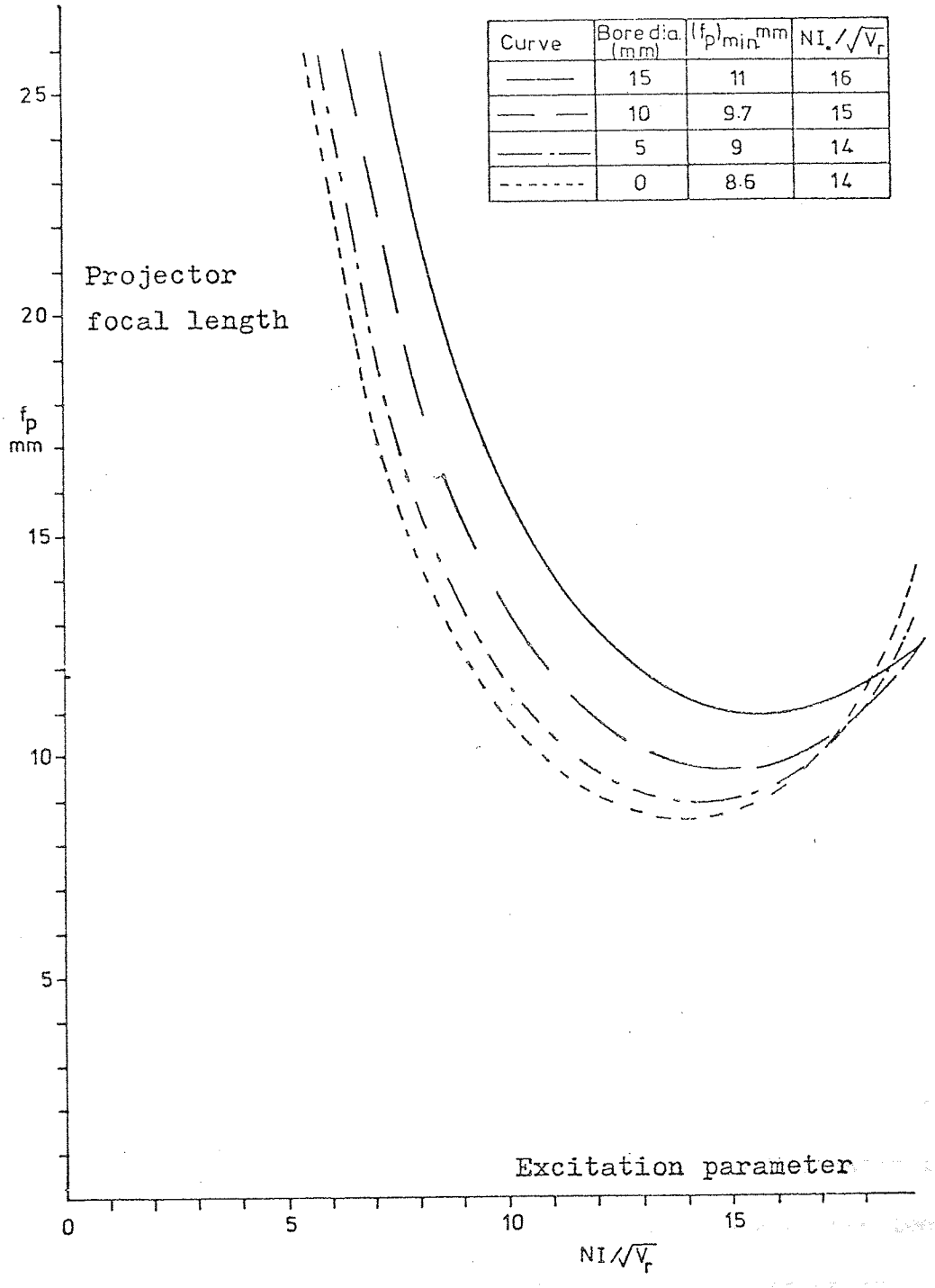

Fig. 5.3.5 Variation of the projector focal length, f_p of a single-pole lens, with excitation parameter $NI/V_r^{\frac{1}{2}}$ for different bore diameters.

diameter causes only small increases in the minimum projector focal length. These results are to be expected from the small changes in the half width shown in Figure 5.3.3 since the half width, a, and minimum projector focal length are closely related.

If such changes were made in the bore of a double-pole lens, keeping the gap width S constant, the percentage change in the focal length would be very much higher than that in a single-pole lens; e.g. if the bore D of a lens with S/D = 1 is doubled, so that S/D becomes 0.5, the focal length will increase by about 40%. This shows that single-pole lenses are much less sensitive to change in diameter than double-pole lenses. This fact can be exploited in the design of wide bore projector lenses.

If an iron ring is placed on the brass lid of the lens, the maximum magnetic field on the axis will be higher than that without it. Hence a new lens structure can be investigated by considering Figures 5.3.1 and 5.3.6. An iron ring of 5mm thickness and of the same outer diameter as the lens (50mm) was placed on top of the brass lid. The snout surface was extended (by means of a small iron cylinder) 5mm in order to make it level with the iron ring. The cylinder had the same inner and outer diameters D and D' respectively as the original snout and aligned it by one of the cylindrical plugs shown in Figure 5.3.1. To retain the original bore of the lens, the snout extension was located by the brass plug also shown in Figure 5.3.1. The inner diameter, D'' of the iron ring was varied in order to change the ratio of D''/D'. Using the same ampere-turns (1755 A-t) as before, it was found that the smaller the D''/D' ratio, the higher the peak of the axial flux density distribution, whichever snout was used. For a given bore it was found that the peak was (a) higher and (b) closer to the snout with an iron ring on the brass lid than without it. For a specific bore, the half-width a,

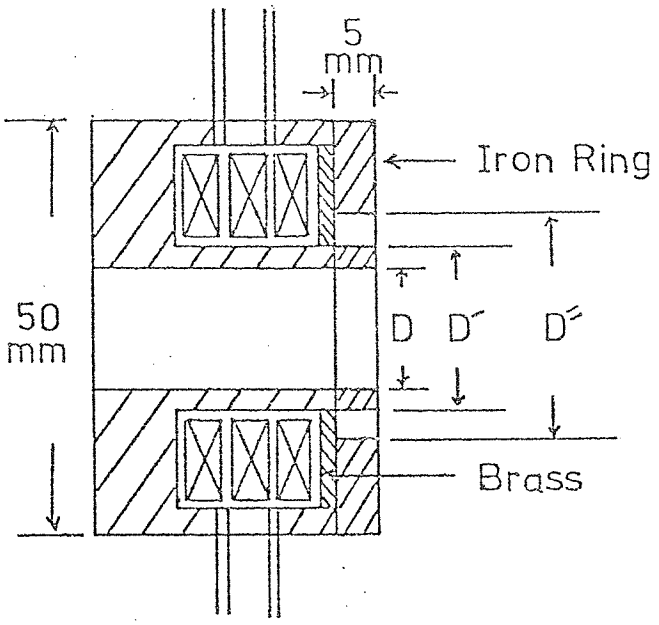

Fig. 5.3.6 Cross-section of the miniature lens of variable bore diameter with an iron ring placed on its brass lid.

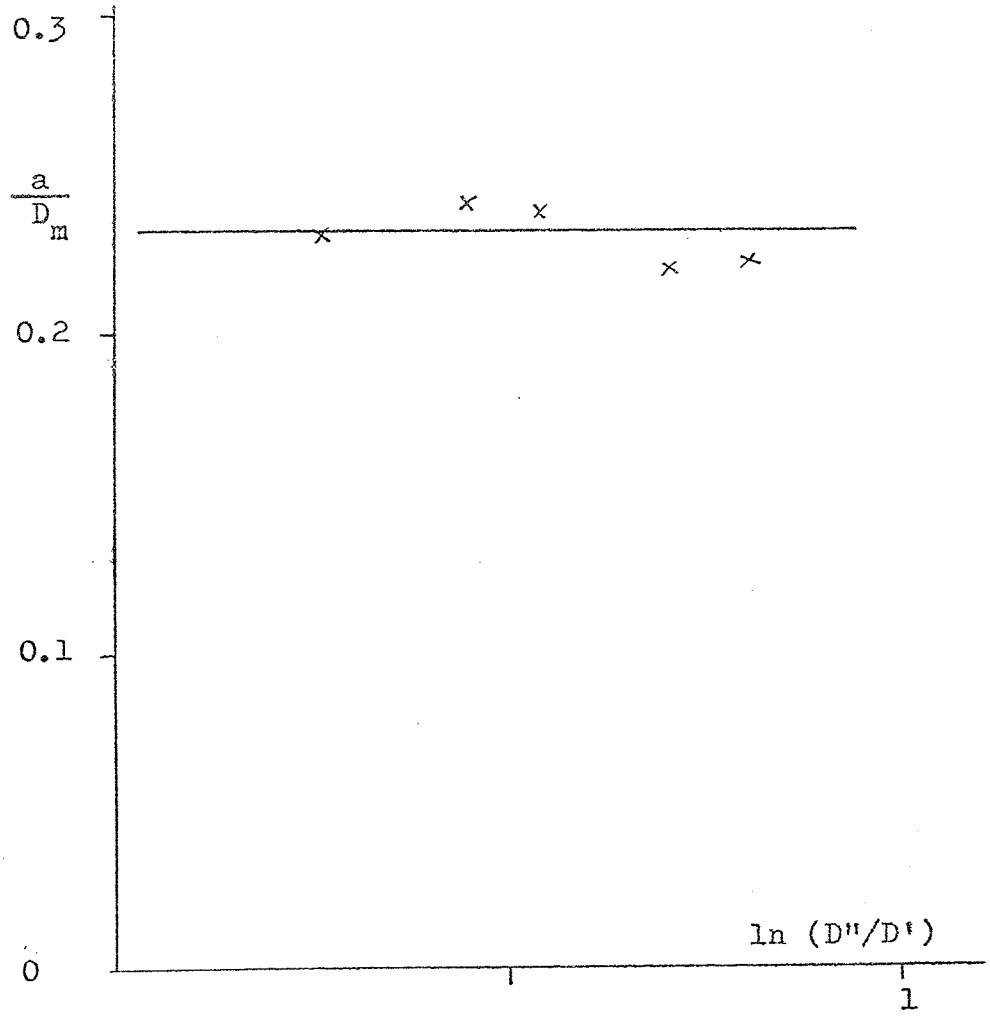

Fig. 5.3.7 Characteristics of the experimental snorkel lens of the construction shown in Figure 5.3.6 with no bore.

increases with the increase of the D''/D' ratio. However, the measurements with the zero bore lens had shown that the range of the D''/D' ratio between 1.2 and 2.2 was not large enough to show its relationship with the a/D_m ratio, where $D_m = (D' + D'')/2$. The ratio a/D_m was found to be independent of D''/D' for the above range of values and it was equal to 0.23, Figure 5.3.7.

This kind of lens has a shorter focal length than that without iron plates. However, a snorkel lens of this construction requires further investigation.

5.4 Conclusion

It has been found that (a) the rotation-free lens has important electron-optical properties which are useful in alignment, (b) the single-pole magnetic lens has different distortion according to direction in which the electron beam traverses the field, and (c) single-pole lenses can be designed to have considerably large bores without an appreciable change in focal length.

6. A MINIATURE ROTATION-FREE PROJECTION SYSTEM

It was concluded in Chapters Four and Five that it should be possible to construct single-pole projector lenses with big bores. Such lenses have relatively long focal length, but this can be reduced to the same order of magnitude as that of conventional lenses by making use of double lenses. The effective focal length of a double lens unit depends on its geometry. Making use of these principles a miniature 100 kV projection system was designed consisting of two identical doublets; these consisted of miniature rotation-free projector lenses with a large bore mounted on a specially designed stage. The projector doublets were designed to be identical since it was found (Chapter Five) that the single-pole lenses are not sensitive to their bore size. One lens was an intermediate projector and the other a final projector. Both lenses were mounted outside the vacuum system which made alignment easy.

6.1 Design of the 100 kV rotation-free single-pole lens

The design of the miniature rotation-free projector lens was based upon the successful performance of the 30kV doublet described in Chapter Four. Figure 6.1.1 shows the cross-section of the iron circuit of the 100kV rotation-free snorkel lens. The iron circuit was conveniently machined from a solid iron bar. A photograph of the dismantled lens with its coils and brass lids is shown in Figure 6.1.2. Unfortunately, an error was made during the machining of the lenses, resulting in the vacuum "O" rings being machined in the lens poles instead of in the non-ferromagnetic lids. Fortunately it turned out that this type of lens is not sensitive to machining errors of this type.

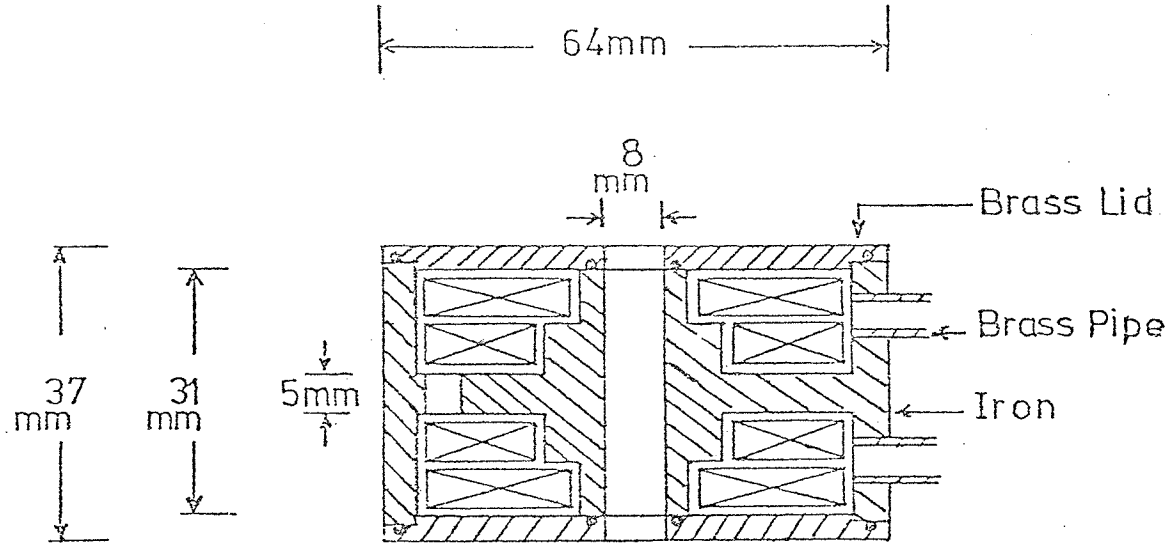

Fig. 6.1.1 Cross-section of the miniature 100kV double snorkel lens. Scale: full-size.

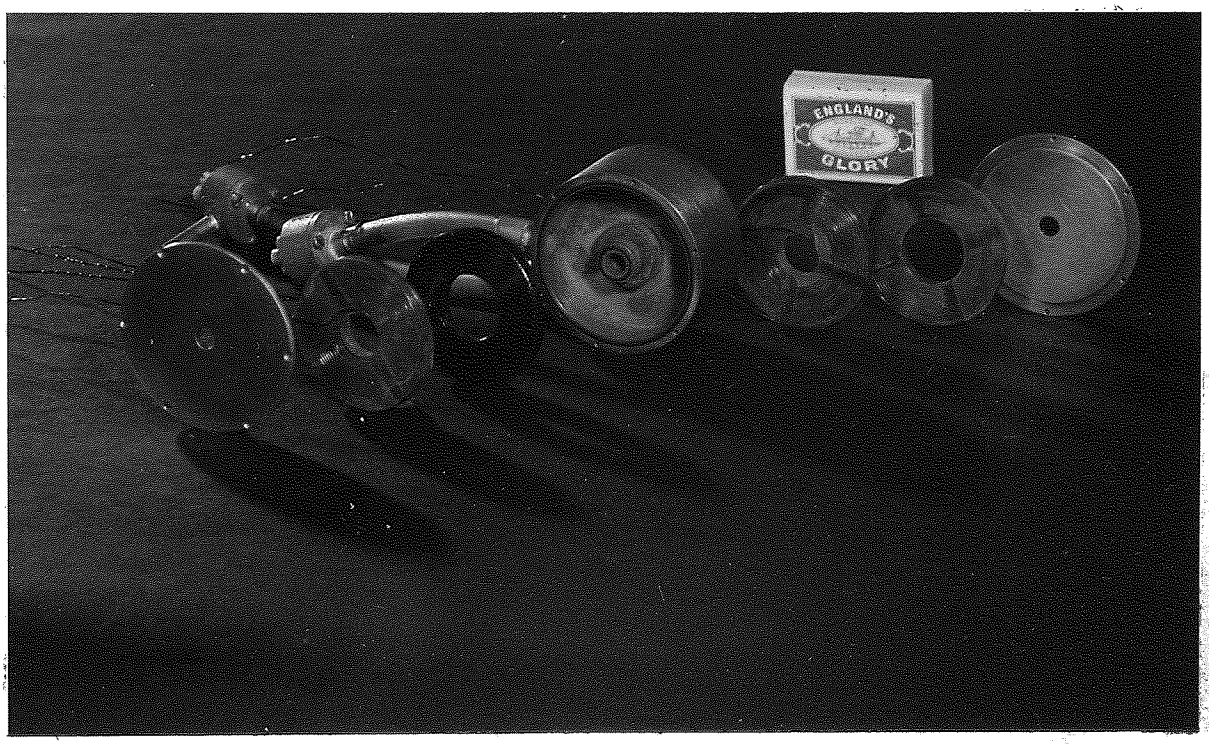

Fig. 6.1.2 The miniature 100kV double snorkel lens.

The lens design is very simple and easy to construct. Its outer diameter is 64mm. The cross-section of the central polepiece was stepped to allow for magnetic leakage flux. Ideally a conical polepiece would be used if high flux densities were required. The lens bore is not critical; it was of 8mm nominal diameter. The axial distance between the flat surfaces of the two snouts is 31mm and the overall height of the lens is 35mm.

Each lens of the doublet had two wire windings connected in series. The two coils had the same outer diameter (52mm) but the inner diameters were 16 and 24mm to suit the steps in the iron circuit. An external current supply capable of delivering up to 25 amps at 60 volts was provided to energize the windings of the double lens, the wire size being chosen to match the output of the power supply. To operate at 100kV, each lens element of the doublet needs an excitation of 4800A-t. The appropriate wire size was 21 S.W.G. (0.8mm diameter) insulated copper wire as determined from the equations given in Chapter Two. The thickness of each coil was 5mm with six layers of wire across the width. The coil of I.D. 24mm had 85 turns and that of I.D. 16mm had 115 turns. The total number of turns of the two coils was 200 with a resistance of 0.8 ohm at 17°C. Hence the whole double lens with the four coils connected in series had a resistance of 1.6 ohms at 17°C. The coils were cooled by direct contact with the water flowing through the 1mm high channels around the coils as shown in Figure 6.1.1. The cooling water entered the upper half of the lens and then proceeded to the lower half via a hole 5mm in diameter in the central plate as shown in Figure 6.1.1.

6.2 Magnetic tests

Single snorkel lens

A magnetic test on a single lens was first performed by energizing

one lens of the doublet unit. The flux density was measured by means of a Hall-probe gaussmeter. The test for magnetic saturation has shown that: (a) the maximum flux density was 3mm away from the snout's surface, i.e. its position was on the surface of the brass lid, (b) from the measurement of the maximum flux density it was found that in spite of the unfortunate presence of the "O" ring on the snout, no saturation was observed in the single lens below 5000 A-t, which is more than sufficient for a 100kV accelerating voltage, (c) the maximum flux density on the axis was 0.42T; this is well below the values usually associated with conventional projector lenses with their small bores and gaps, thus the 5mm thick central plate of the double lens would not be expected to saturate at all in the rotation-free mode, and (d) the single lens consumed a maximum power, P of 0.6Kw at a water flow of 1 litre/minute and current density, σ of 5000 Amp/cm^2, when the average temperature of the coils was 80^{o}C; this is well below the maximum safe operating temperature of the insulation. The measured maximum power consumed in both coils agrees within 5% with that calculated from the equation $P = \pi \rho \sigma D_m (NI)$ as discussed in Chapter Two.

The axial field distribution of a single snorkel lens excited at 4650A-t is shown in Figure 6.2.1. It can be seen that at a distance of 34mm from the snout there is another small peak inside the lens bore which is due to the leakage flux in the second unexcited half of the double lens. The small peak appeared at this distance because the second snout is 31mm away from the first and the peak of the flux density is always 3mm away from any of the two snouts, thus they add up to 34mm. This small peak in the second lens is a linear function of the excitation in the first lens, and at maximum excitation, its maximum value is only 50 gauss.

The shape of the field distribution is similar to those obtained

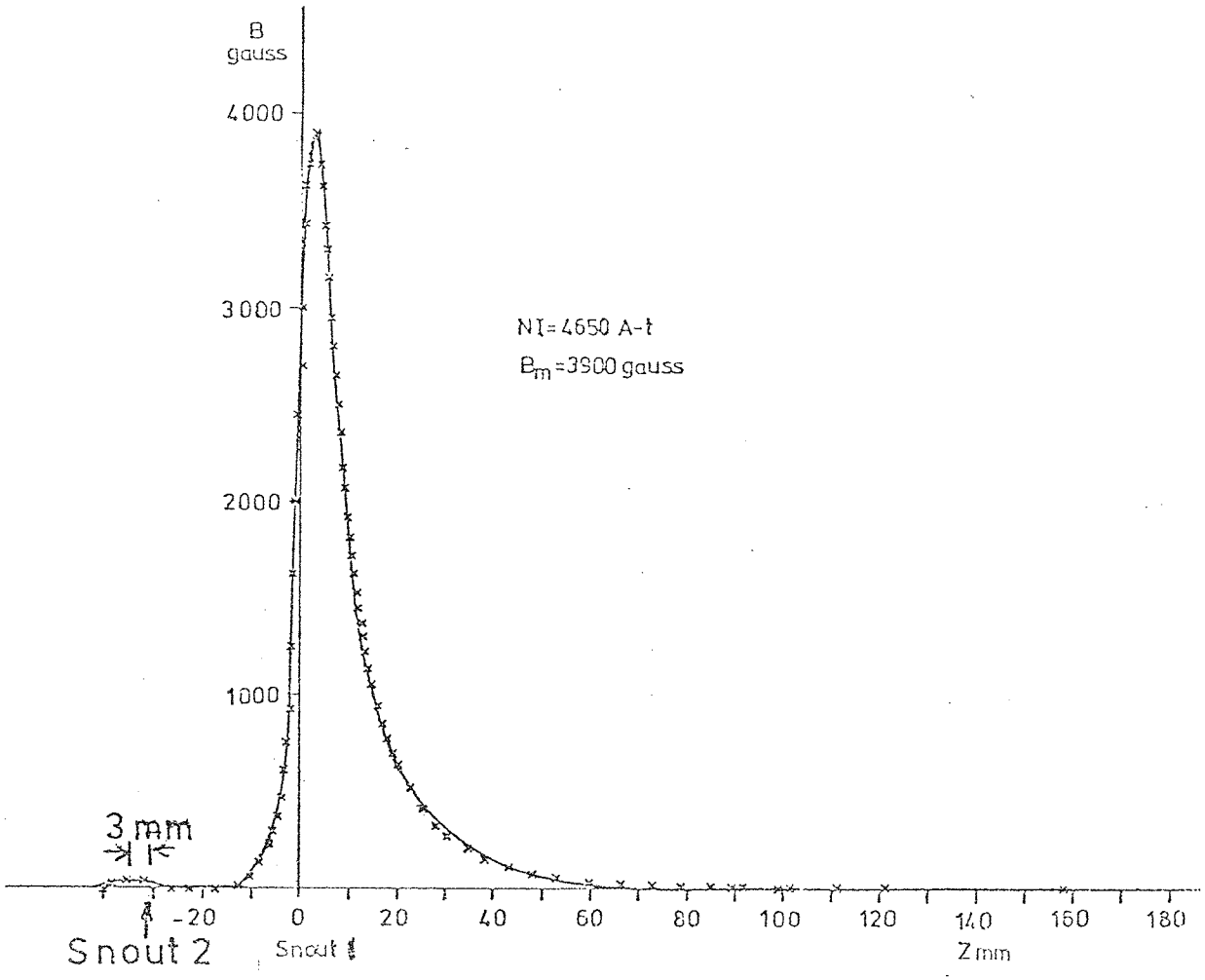

Fig. 6.2.1 Axial flux density distribution of the 8mm bore single snorkel lens.

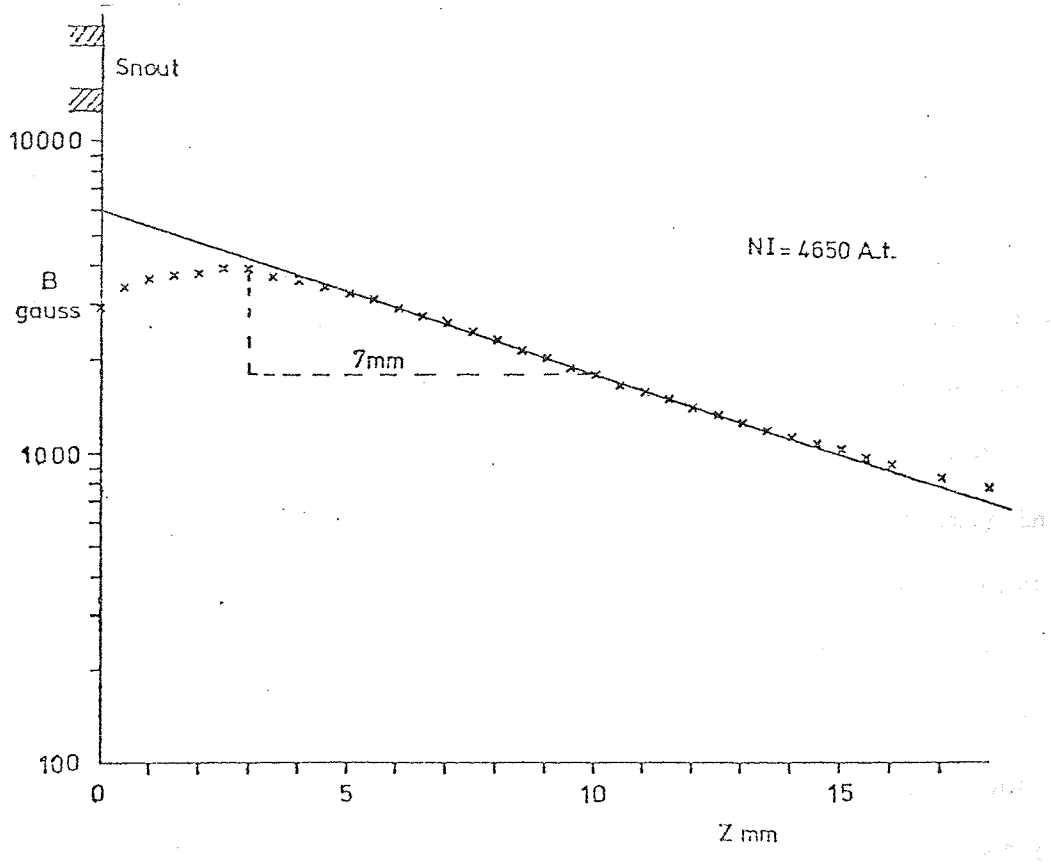

Fig. 6.2.2 Log-linear plot of the axial flux density distribution shown in Figure 6.2.1.

from other snorkel lenses, and can be used to compute the variation of the focal length with the excitation parameter $NI/V_r^{\frac{1}{2}}$. However, an approximate value of the minimum focal length can be obtained from the field itself by plotting it on a bigger, logarithmic scale (Figure 6.2.2). The experimental points which apart from those in the vicinity of the snout, lie on the straight line in Figure 6.2.2 show the approximate exponential nature of the main field distribution. The half-width of the exponential field extrapolates (B_m = 6000 gauss) is 6.1mm, i.e.

$$(f_p)_{min} = 1.15 \times 6.1$$

$$= 7mm$$

The half value of the peak (3900 gauss) of the actual field corresponds to a half-width of 7mm. This suggests that the minimum focal length of a wide bore snorkel lens is of the same order as the diameter of the lens bore.

Plots of the magnetic flux of a specific single-pole lens for different snout geometries are shown in Figure 6.2.3. These flux plots were kindly calculated by Munro of the IBM Research Laboratory at Yorktown Heights, U.S.A. by means of the finite element method. Diagrams (a) and (b) of Figure 6.2.3 show two different outer diameters of the cylindrical pole but the lens bore is constant. These two diagrams show that decreasing the outside diameter of the snout concentrates the field on it, thus the peak of the flux density in diagram (b) is higher than that in (a); therefore the focal length of (b) will be shorter than that of (a). The surface of the snout in diagrams (a) and (b) is well within the body of the lens. If the snout is extended as shown in diagram (c) the flux density in the snout will be higher than that in (a). Therefore, the focal length of the lens in diagram (c) will be shorter than that in (a). When the lens

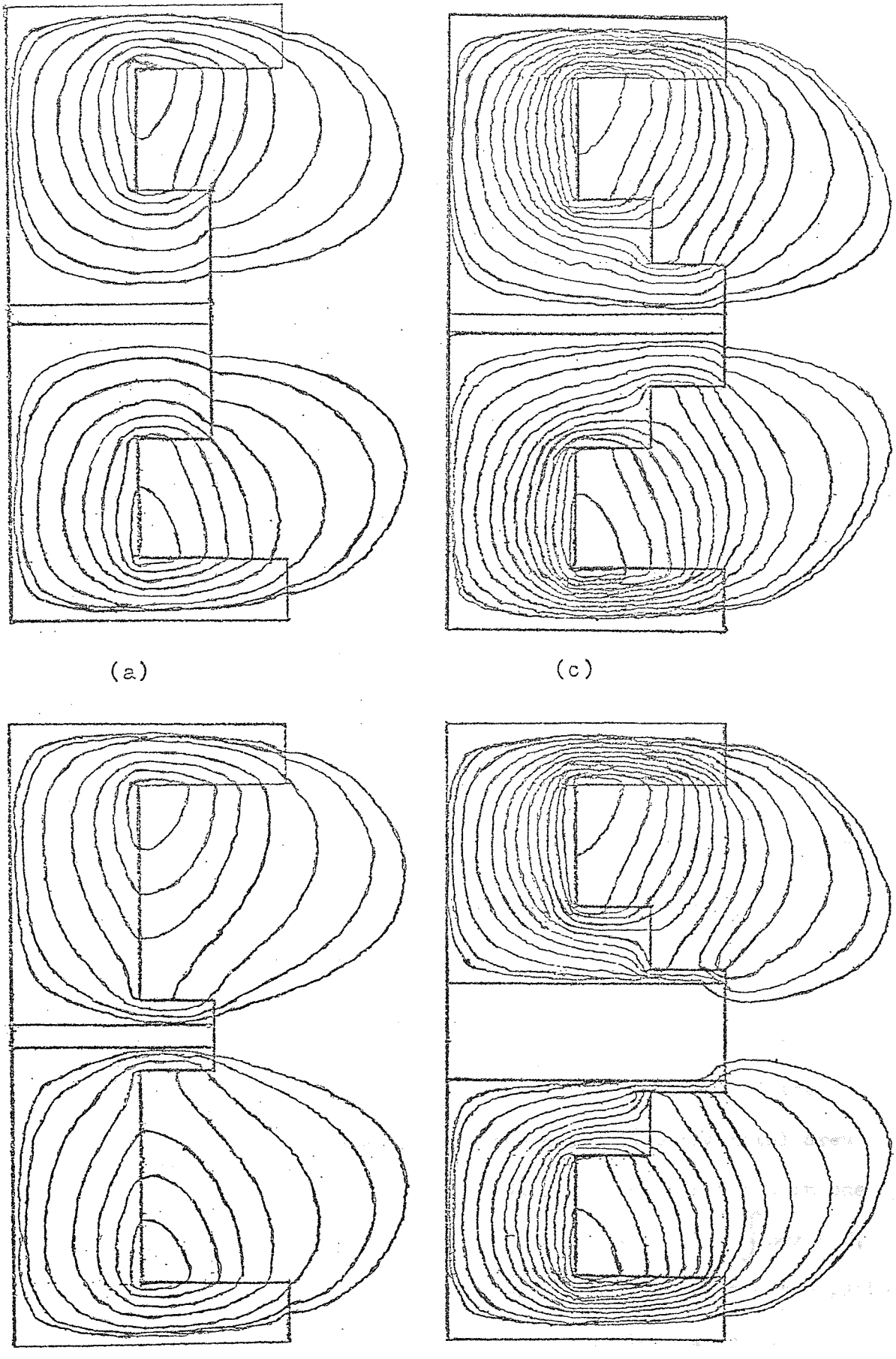

Fig. 6.2.3 Computed magnetic flux plots of a single-pole lens with different snout's geometry.

bore of (c) is increased five times as shown in diagram (d), the flux changes only slightly and saturation is likely to take place inside the lens. Thus there will be a small increase in the focal length; this result was proved in Section 5.3. The cross-section of the lens shown in diagram (c) is similar to a single lens of the 100kV doublet unit shown in Figure 6.1.1; therefore, the flux distribution of the new projector lens is similar to that shown in diagram (c).

Double snorkel lens

The two lenses of the doublet unit with equal ampere-turns can be excited in two ways. The first is when their excitations are in cooperative mode i.e. $(NI)_1 = +(NI)_2$, and the second is when their excitations are opposing each other i.e. $(NI)_1 = -(NI)_2$. Figure 6.2.4 shows the field distribution of the double lens in both modes of excitation. Experiments show that (a) the peak in the opposing mode is 5% less than that in cooperative mode, (b) the field distribution away from the lens structure is the same in both methods of excitation, (c) the two peaks of the field of a double lens are separated by 37mm, (d) as predicted, there is no sign of saturation inside the lens structure even at the maximum opposing excitation of 5000A-t because the maximum flux density is below the saturation limit of the iron, (e) in the cooperative mode of excitation, the two parts of the distribution are on the same side of the axis, i.e. the total area under the curve $\int Bdz = 2 \mu_o$ NI where NI is the ampere-turns in one lens of the doublet; in the opposing mode of excitation $\int Bdz = 0$, (f) for this particular lens, the half-width of each of the two parts of the field distribution is nearly the same at both modes of excitation; thus the focal properties are identical, (g) at the centre of the lens axis, i.e. at 15.5mm from each snout, the flux density changes sign as it passes this point at opposing excitation.

It was shown in Figure 6.2.1 that if one lens of the doublet is

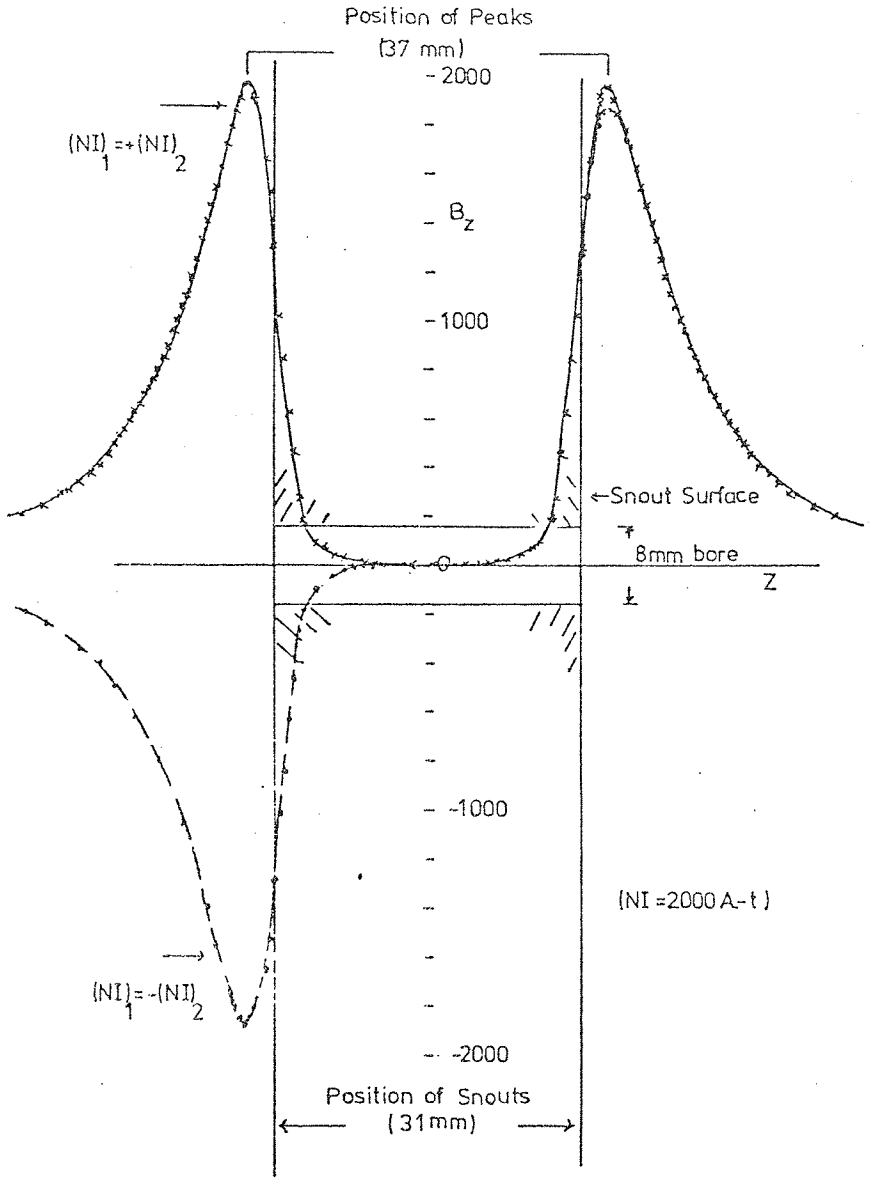

Fig. 6.2.4 Field distribution of the singl-pole doublet in cooperative excitation (full line) and opposing excitation (dotted line).

excited, there will be a leakage flux near the snout of the unexcited lens. Thus, if both single lenses are excited with equal ampere-turns, there will be a leakage flux from one lens to the other. In the opposing excitation mode, this leakage flux in one lens will have an opposing sense to the flux in that lens and thus will reduce the peak of the field in that lens. In the cooperative mode of excitation this leakage flux will add to the flux in that lens. This explains the change in the values of the field distribution around the peak at both modes of excitation.

The effective focal length of this doublet can easily be estimated. Since the minimum focal length of each single lens is of the order of the bore diameter and the surfaces of the snouts are 31mm apart, the minimum focal length of the double snorkel lens would be expected to be of the order of 2mm as calculated from Equation 4.5.1.

6.3 Image distortion

The distortion produced by the projector lens is an important parameter in deciding the final projection distance in an electron microscope. Thus the data of the field distribution of the single lens (Figure 6.2.1) were used to compute the radial and spiral distortion coefficients as a function of the excitation parameter $NI/V_r^{\frac{1}{2}}$ together with the corresponding projector focal length.

Figure 6.3.1 shows the variation of the radial distortion, C_d and the spiral distortion C_{sp} with excitation for the two opposite directions of the snout. With the snout facing the screen, the C_d curve shows that as $NI/V_r^{\frac{1}{2}} \longrightarrow 0$, $C_{d_o} = 0.17$ and goes to a maximum value of 0.21 at $NI/V_r^{\frac{1}{2}} = 9$; after this maximum C_d decreases steeply to zero at $NI/V_r^{\frac{1}{2}} = 15.3$ whereupon it changes sign. The C_{sp} increases with increase of excitation. There is good agreement between the computed results and those measured experimentally. The variation of C_d and C_{sp} with excitation when the snout of the single-pole lens

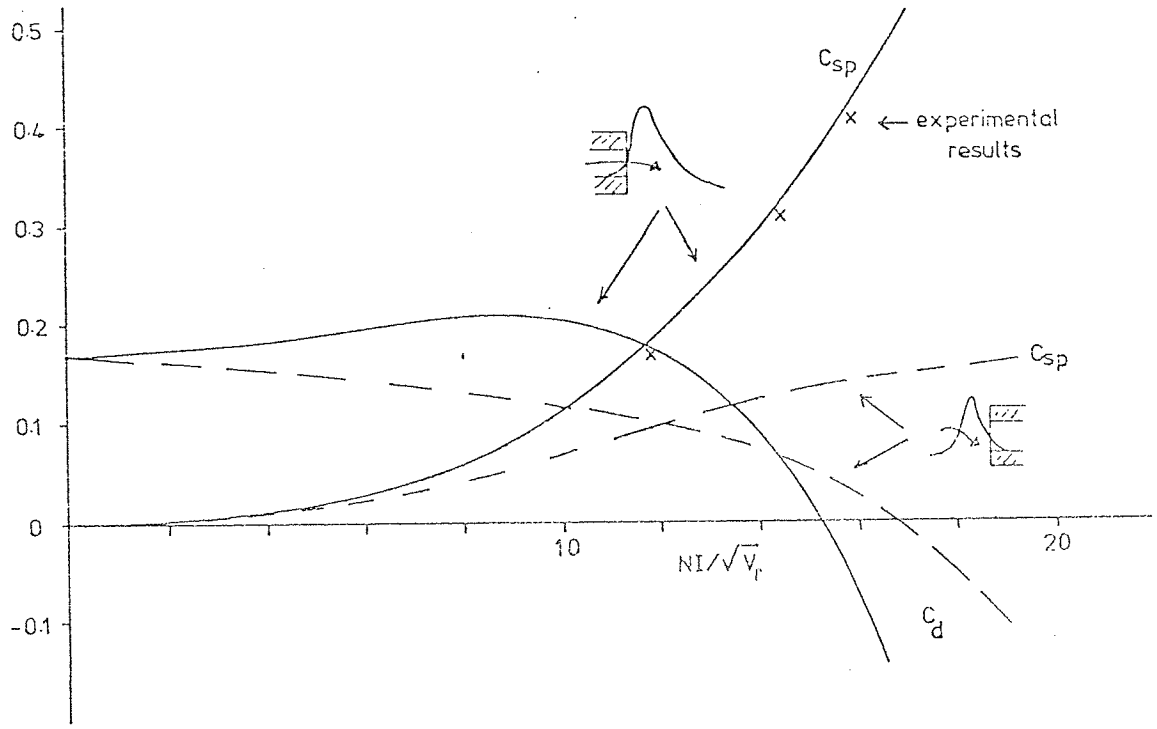

Fig. 6.3.1 Radial and spiral distortion coefficients of the 8mm bore single-snorkel lens as a function of excitation parameter $NI/V_r^{\frac{1}{2}}$, for the two modes of operation.

faces the screen is similar to that of double-pole lenses (see Figure 4.6.3). However, the variation of C_d and C_{sp} is entirely different from conventional lenses when the snout faces the incident beam as shown in Figure 6.3.1. The C_d curve shows that C_{d_o} is also 0.17 but C_d decreases continuously and slowly with increase of excitation while C_{sp} increases very slowly with the excitation. The distortion of the lens in this way of operation is much thus lower than those with the snout facing the screen as was shown experimentally in Section 5.2. It was difficult to measure the distortion of the lens whose snout was facing the incident beam because of the long axial extension of the bore (Figure 6.1.1) which limited the field view of the image. Both experiment and the computation suggest that the two snouts of a snorkel projector doublet should both face the incident beam in order to have images of very low distortion. However, such a design is more complicated than the one chosen for study as shown in Figure 6.1.1, which is very easy to construct.

It is shown in Appendix VIII that the projection distance of a projector lens is given by

$$L = \left(\frac{R_p}{R}\right)\left(\frac{\Delta\rho}{\rho}\right)^{-\frac{1}{2}} C^{\frac{1}{2}} f_p$$

where C is either C_d or C_{sp}. For a specific distortion $(\frac{\Delta\rho}{\rho})$ and radius, R_p of the image on the photographic plate, the distance L is proportional to $f_p C_d^{\frac{1}{2}}$. Figure 6.3.2 shows the variation of $f_p C_d^{\frac{1}{2}}$ and $f_p C_{sp}^{\frac{1}{2}}$ with excitation parameter $NI/V_r^{\frac{1}{2}}$ when the snout is facing the screen. It can be seen that $f_p C_d^{\frac{1}{2}}$ decreases steeply with excitation. Since in an electron micrograph, the acceptable spiral distortion $(\frac{\Delta\rho}{\rho})_{sp}$ can be twice the acceptable radial distortion $(\frac{\Delta\rho}{\rho})_{rad}$, the point where the two curves of $f_p C_d^{\frac{1}{2}}$ and $f_p (\frac{C_{sp}}{2})^{\frac{1}{2}}$ meet gives the projection distance which satisfies this condition for a specific lens. Figure 6.3.2 shows that $(\frac{\Delta\rho}{\rho})_{sp} = 2(\frac{\Delta\rho}{\rho})_{rad}$ when $f_p (\frac{C_{sp}}{2})^{\frac{1}{2}} = f_p (C_d)^{\frac{1}{2}} = 3$

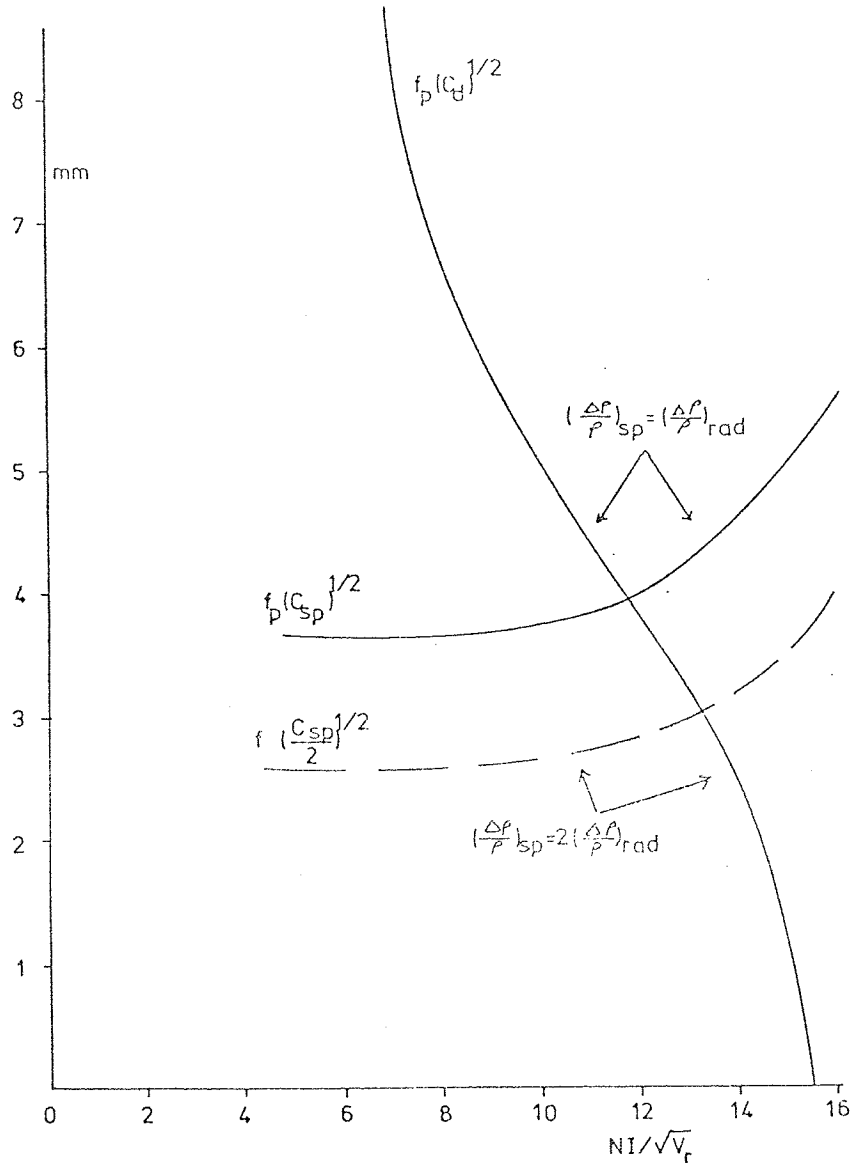

Fig. 6.3.2 Variation of the parameters $f_p C_d^{\frac{1}{2}}$ and $f_\rho C_{sp}^{\frac{1}{2}}$ of the 8mm bore single-snorkel lens with excitation parameter $NI/V_r^{\frac{1}{2}}$ when its snout is facing the screen. The projection distance L is proportional to the parameter $f_p C^{\frac{1}{2}}$.

at $NI/V_r = 13.3$. Thus R_p = 50mm, R = 4mm and $(\frac{\Delta\rho}{\rho})_{rad}$ = 1% the projection distance L will be 375mm before reaching the minimum projector focal length. However, it can be seen that near the minimum focal length at about $NI/V_r^{\frac{1}{2}} = 15$, $f_p C_d^{\frac{1}{2}} = 1.2$ and $f_p C_{sp}^{\frac{1}{2}} = 5$, where for 1% radial distortion L will be 150mm $\left[(\frac{\Delta\rho}{\rho})_{sp} = 17\%\right]$ and for 2% spiral distortion L will be 450mm $\left[(\frac{\Delta\rho}{\rho})_{rad} = 0.1\%\right]$. Therefore at the average projection distance of 300mm, the radial and spiral distortions will be 0.25% and 4% respectively. These results show that the radial distortion is negligible compared with the spiral distortion. At $NI/V_r^{\frac{1}{2}} = 13.3$ where $(\frac{\Delta\rho}{\rho})_{rad} = 2\,(\frac{\Delta\rho}{\rho})_{sp}$ the radial distortion at the 300mm projection distance is only 1.5% which suggests that the lens can be successfully used at an excitation just below that required for minimum focal length. However if the final projector lens is of the rotation-free type similar to that shown in Figure 6.1.1, the spiral distortion at maximum magnification will be reduced without an appreciable increase in the radial distortion.

6.4 The miniature projection stage

The short focal length of the double snorkel lens and the shorter projection distance it requires for a given distortion suggested the design of an improved projection stage for the EM6 electron microscope. The original projector and intermediate lenses in the microscope were therefore removed and replaced by an experimental projection stage which consisted of two identical rotation-free single-pole projector lenses as shown in Figures 6.1.1 and 6.1.2.

Figure 6.4.1 is a cross-sectional diagram of the projection stage which fitted onto the existing viewing chamber of the EM6 electron microscope. The brass and the iron discs were separated by the same four iron pillars described in Section 3.4; these support the whole electron optical column placed on top of the brass disc. The two identical rotation-free lenses were placed over the brass tube (outer

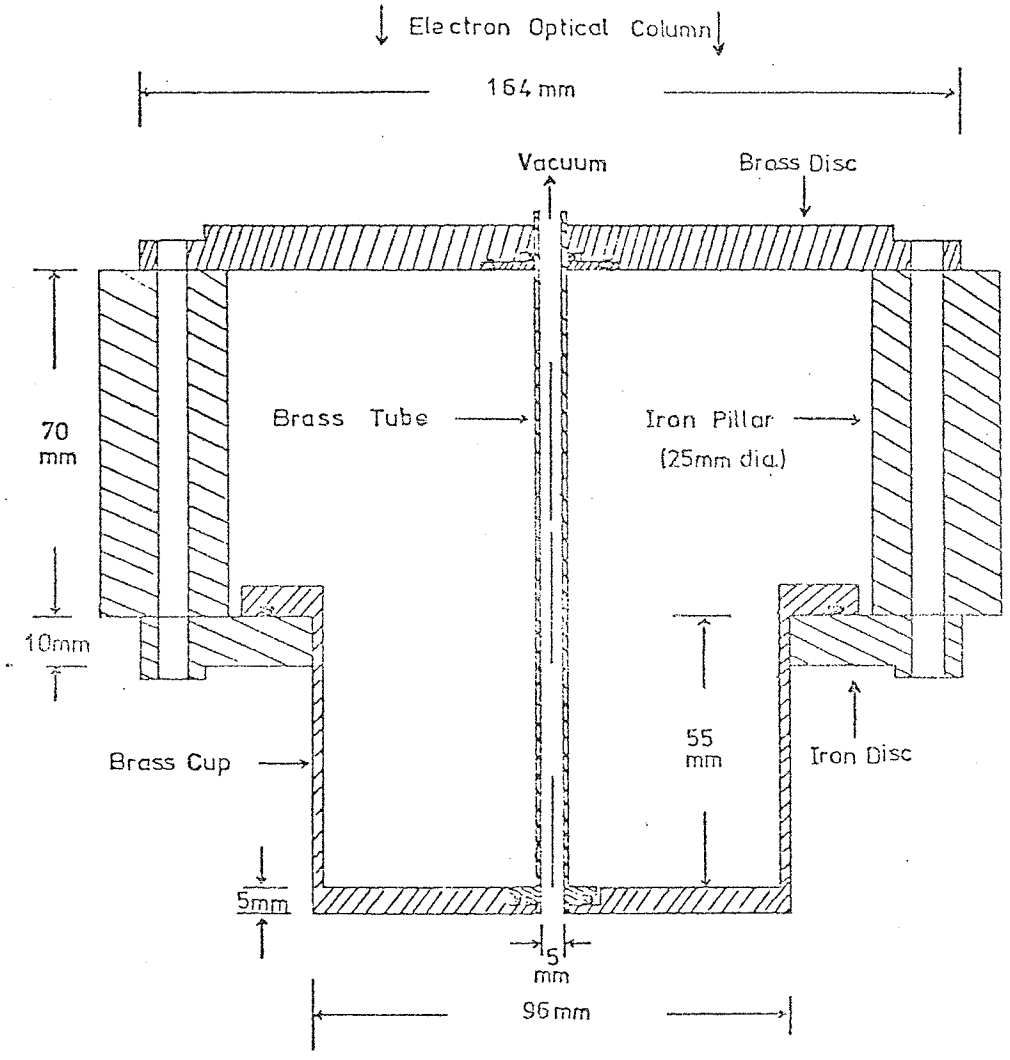

Fig. 6.4.1 Cross-section of the miniature projection stage which fits onto the flange of the EM6 viewing chamber.

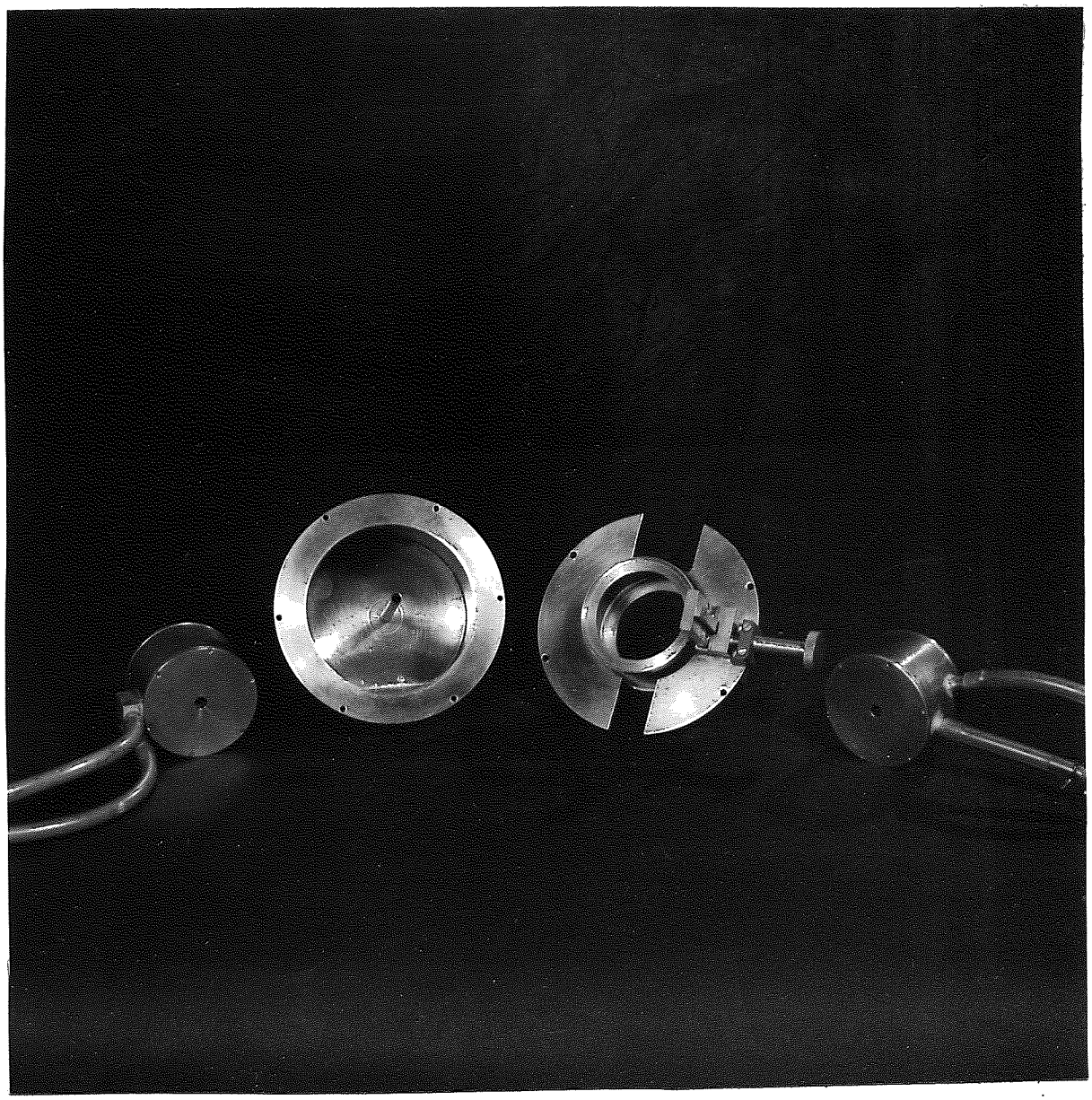

Fig. 6.4.2 Components of the miniature rotation-free projection system. From left to right, final projector doublet P_2, brass cup for P_2 with the brass vacuum tube, brass holder for P_1, the intermediate projector doublet P_1.

diameter = 6.4mm and inner diameter = 5mm) and the final projector lens rests on the base of the brass cup. The brass cup was inserted through the iron disc inside the viewing chamber with a projection distance of the final projector doublet of 300mm, as calculated in Section 6.3. The intermediate lens was mounted on a special brass holder which allowed the intermediate lens to be moved in a vertical direction with respect to the final projector. Figure 6.4.2 shows a photograph of the two lenses, the brass cup and the intermediate lens holder. This holder was fixed to the brass cup as shown in Figure 6.4.3. It should be mentioned that the pumping of the projector system took place through the brass tube whose two ends were inserted through two "O" rings, one in the upper brass disc and the other in the base of the brass cup. Thus the two lenses are outside the vacuum. They are water-cooled by the same cooling system of the original projector lenses without modification. All the attachments of the miniature projection stage were made of a non-magnetic material (brass) in order that the magnetic field of the snorkel lens should not be distorted.

This projection stage reduced the length of the whole optical column by a distance equal to the height of the intermediate lens (96mm), equivalent to a 13% reduction. This modification was carried out in such a way that the microscope could be restored immediately to its original form if necessary. For instance, (a) the pumping tube in the back of the electron optical column was shortened by 96mm but it could be restored to its original height by inserting the flange shown in Figure 6.4.4, (b) the two control rods of the specimen-shift control whose original lengths were 364mm each were replaced by two brass rods of length 268mm, i.e. 96mm or 26% shorter.

A cross-section of the imaging system and a general view of the modified EM6 electron microscope are shown in Figures 6.4.5 and 6.4.6. Two external current supplies capable of delivering up to 25 amperes

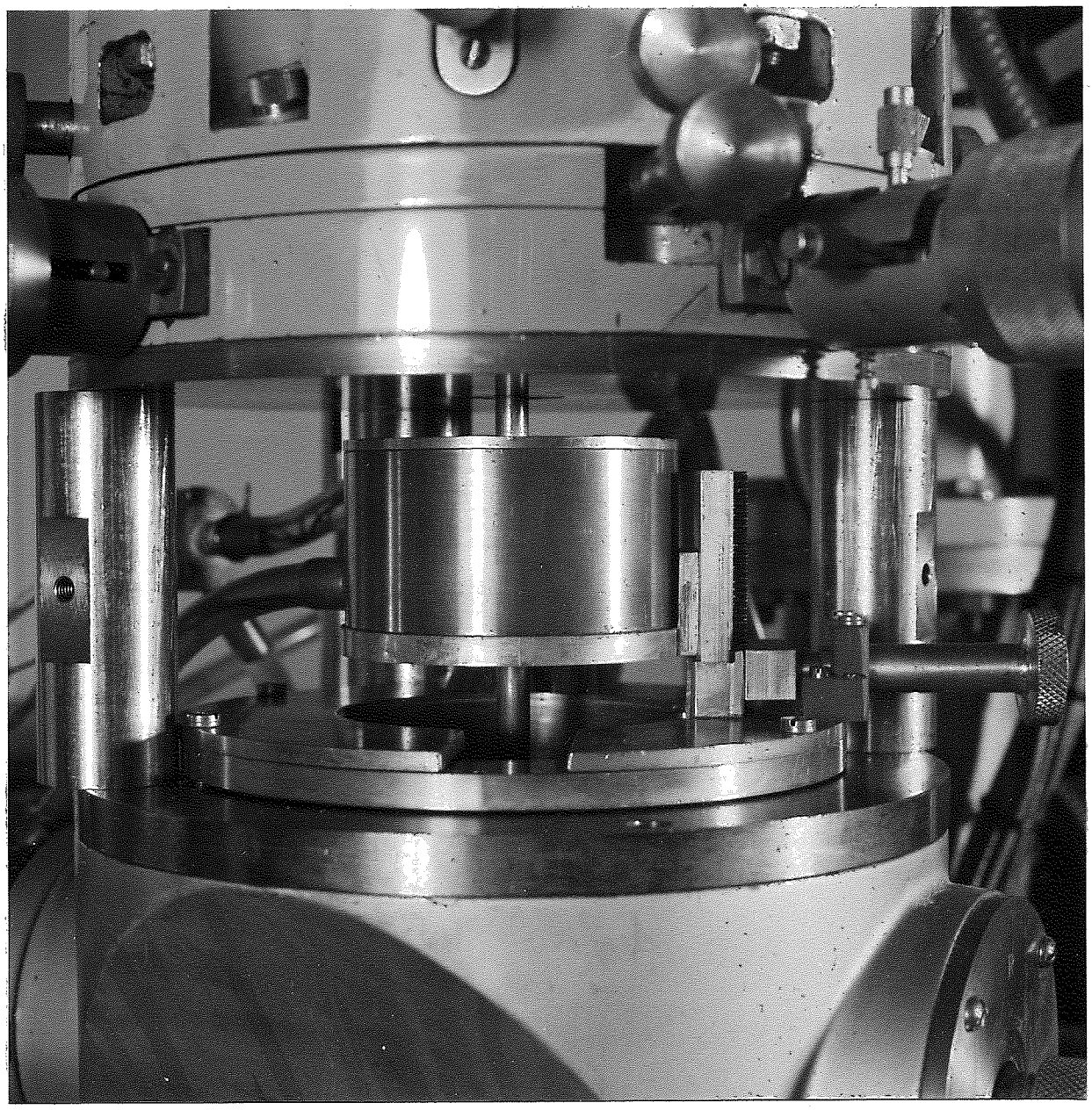

Fig. 6.4.3 Rotation-free intermediate projector lens in the miniature projection stage. The final rotation-free projector lens is hidden by the viewing chamber (see Figure 6.4.5).

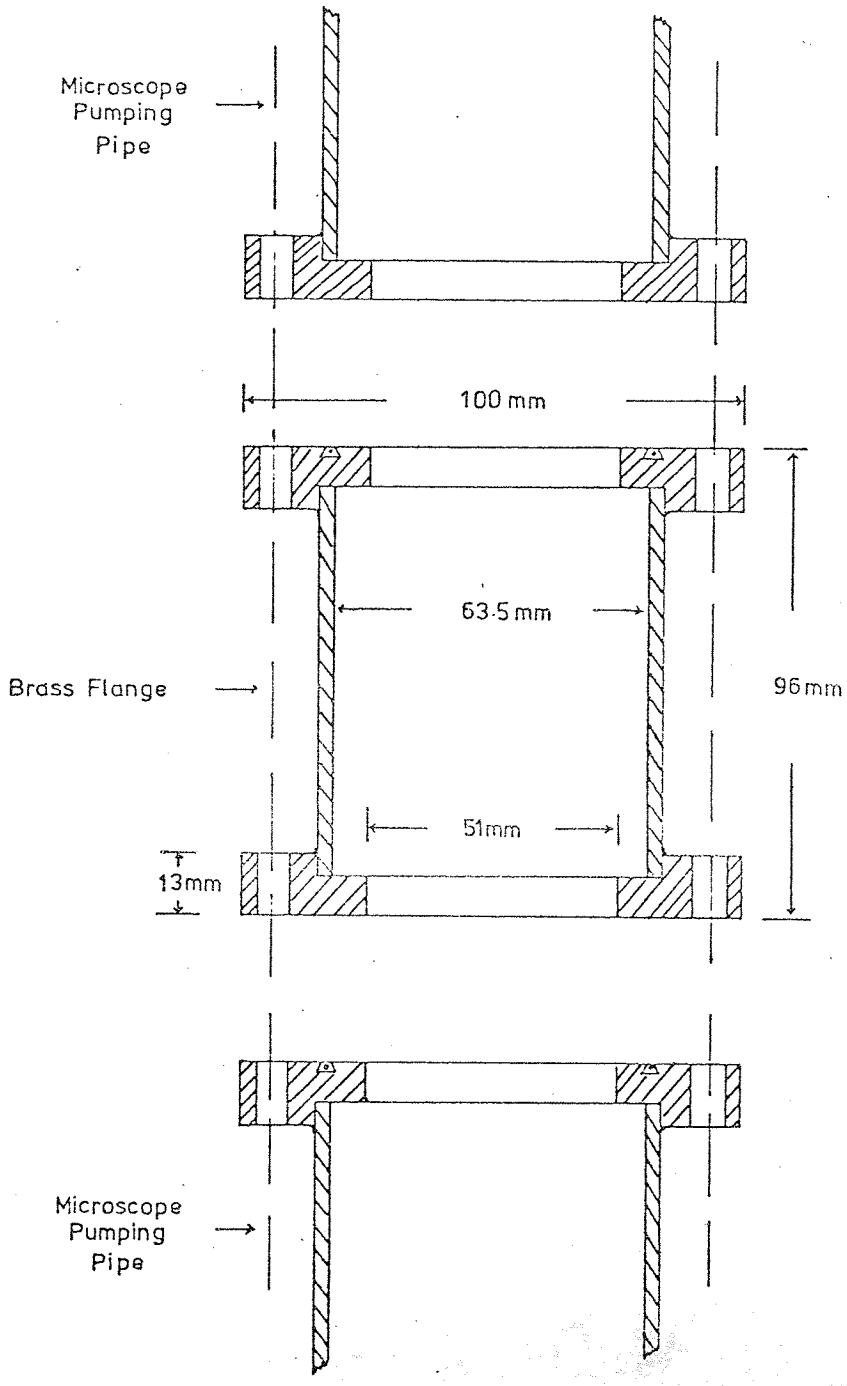

Fig. 6.4.4 Cross-section of the removable flange in the pumping pipe for shortening the electron optical column of the EM6 electron microscope.

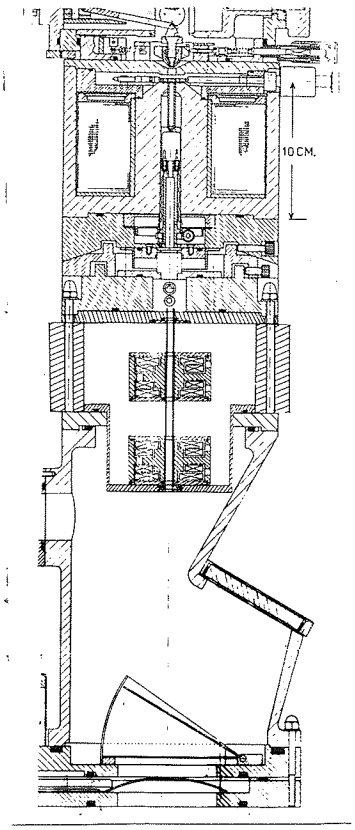

Fig. 6.4.5 Cross-section of the imaging system of the EM6 microscope with the miniature projection system.

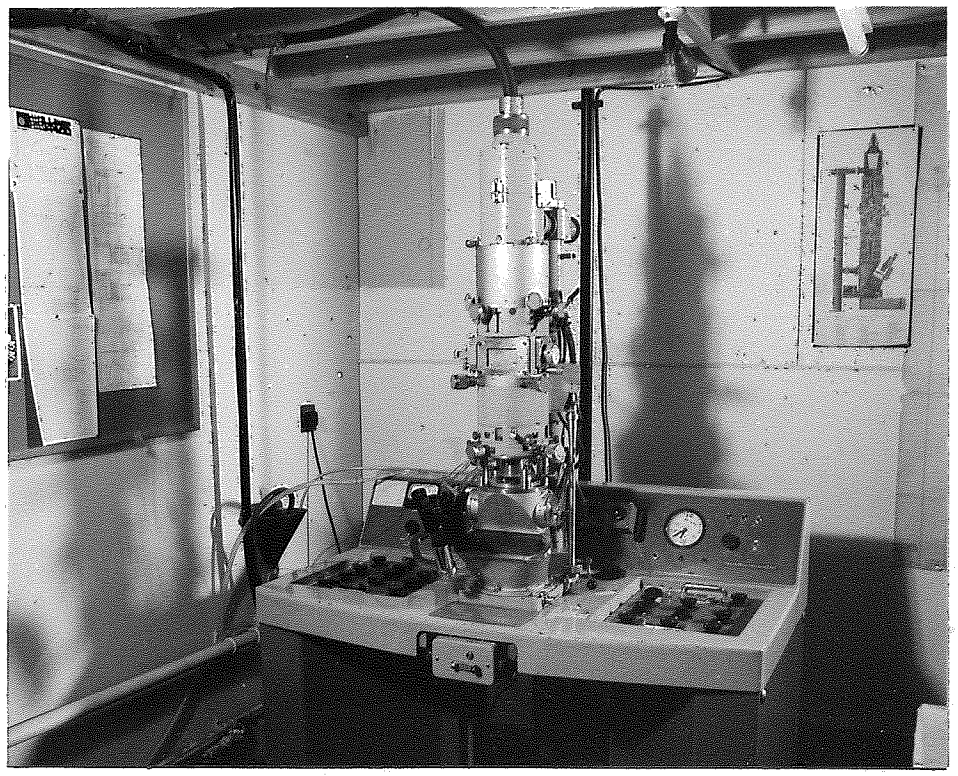

Fig. 6.4.6 The EM6 electron microscope with the miniature projection system. Notice the size of the projection system compared with the other components of the microscope.

were provided to energize the windings of the two projector doublets.

6.5 Properties of the imaging system

The microscope shown in Figure 6.4.5 has an imaging system whose components have different properties from those found in commercial microscopes.

Field of view of the objective lens

When the two projector lenses in the original EM6 microscope were switched off, the limiting aperture for the image formed by the objective lens alone was the 1.5mm diameter bore of the final projector lens P_2; this bore was situated half way between the objective lens and the photographic plate. In the imaging system shown in Figure 6.4.5, where the original objective lens was used, the limiting aperture for the image formed by the objective lens alone was the end of the 5mm diameter brass tube, which was also situated half-way between the objective lens and the photographic plate. The field of view of the two systems can be compared by considering Figure 6.5.1. In the original EM6 electron microscope, Figure 6.5.1a, the maximum diameter, X_a of a specimen which can contribute rays to the image with the objective lens alone on the photographic plate via the 1.5mm diameter bore of the final projector is given by

$$X_a = 3f_o/700 = 0.0043f_o \qquad \ldots\ldots 6.5.1$$

where f_o is the objective focal length. With the miniature projection stage, Figure 6.5.1b, the corresponding maximum diameter X_b of a specimen which can contribute rays to the image on the photographic plate formed by the objective lens alone via the 5mm diameter of the brass tube is given by

$$X_b = 10f_o/600 = 0.017f_o \qquad \ldots\ldots 6.5.2$$

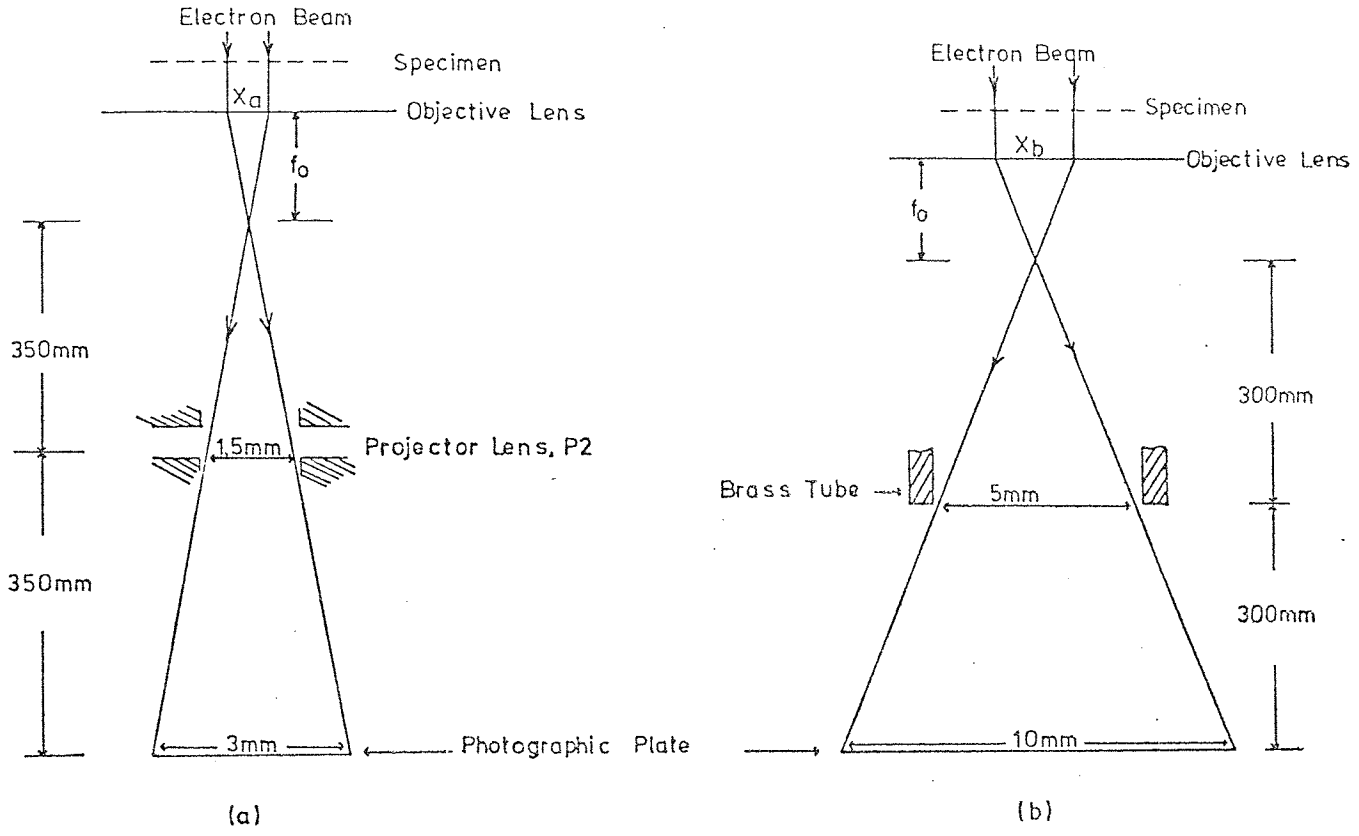

Fig. 6.5.1 Field of view in EM6 electron microscope, (a) original microscope, (b) with the miniature projection stage. For $f_o = 4$mm, the field of view in (a) is 17μm and 68μm in (b).

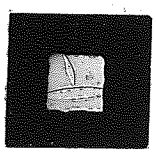

Fig. 6.5.2 Electron micrograph of an aluminium specimen on a 60μm pitch copper grid taken with the original objective lens of the EM6 microscope showing the large field of view with the miniature projection stage.

Equations 6.5.1 and 6.5.2 show that the ratio of the two fields of view $X_b/X_a=4$. The maximum value of X_a is 150 μm when f_o = 35mm at $NI/V_r^{\frac{1}{2}}$ = 3.2 and its minimum value is 17 um when f_o = 4mm at $NI/V_r^{\frac{1}{2}}$ = 12.5. Therefore, the minimum value of X_b is about 67μm; this is shown clearly in Figure 6.5.2 where an image of a specimen of an area more than 60μm in diameter is formed by the objective lens alone, magnified 150 X. The maximum magnification of the objective lens on the photographic plate was reduced from 175 X in the original EM6 microscope to 150 X with the miniature projection stage, i.e 14% reduction; on the other hand, the field of view was increased by a factor of four to values not usually obtained in commercial microscopes.

Properties of the 8mm bore single snorkel lens

The projector focal length of a single snorkel lens was measured by exciting only one lens of the doublet shown in Figure 6.4.5. Measurements were taken for the electron beam entering the lens field with the snout either facing away from the screen or towards it; the results were similar. Figure 6.5.3 shows the projector focal length, f_p which was computed from the field distribution is in good agreement with the experimental results, as a function of the excitation parameter $NI/V_r^{\frac{1}{2}}$. The measured minimum projector focal length of the single lens was 8mm at $NI_o/V_r^{\frac{1}{2}}$ = 14.5, equal in value to the bore diameter. This measured focal length is 4% less than the computed value. The curve of relative projector focal length $f_p/(f_p)_{min}$ of this single-pole lens as a function of the relative excitation NI/NI_o conforms approximately to the "universal" curve calculated for double-polepiece lenses, and is similar to that obtained for the 30kV single-pole lens shown in Figure 4.4.4. The focal length of the 100kV single-pole lens is just less than twice that of the 30kV (Figure 4.4.3) lens because of slight differences in the design which are mainly in the outer diameter of the lenses and the geometry of the snouts.

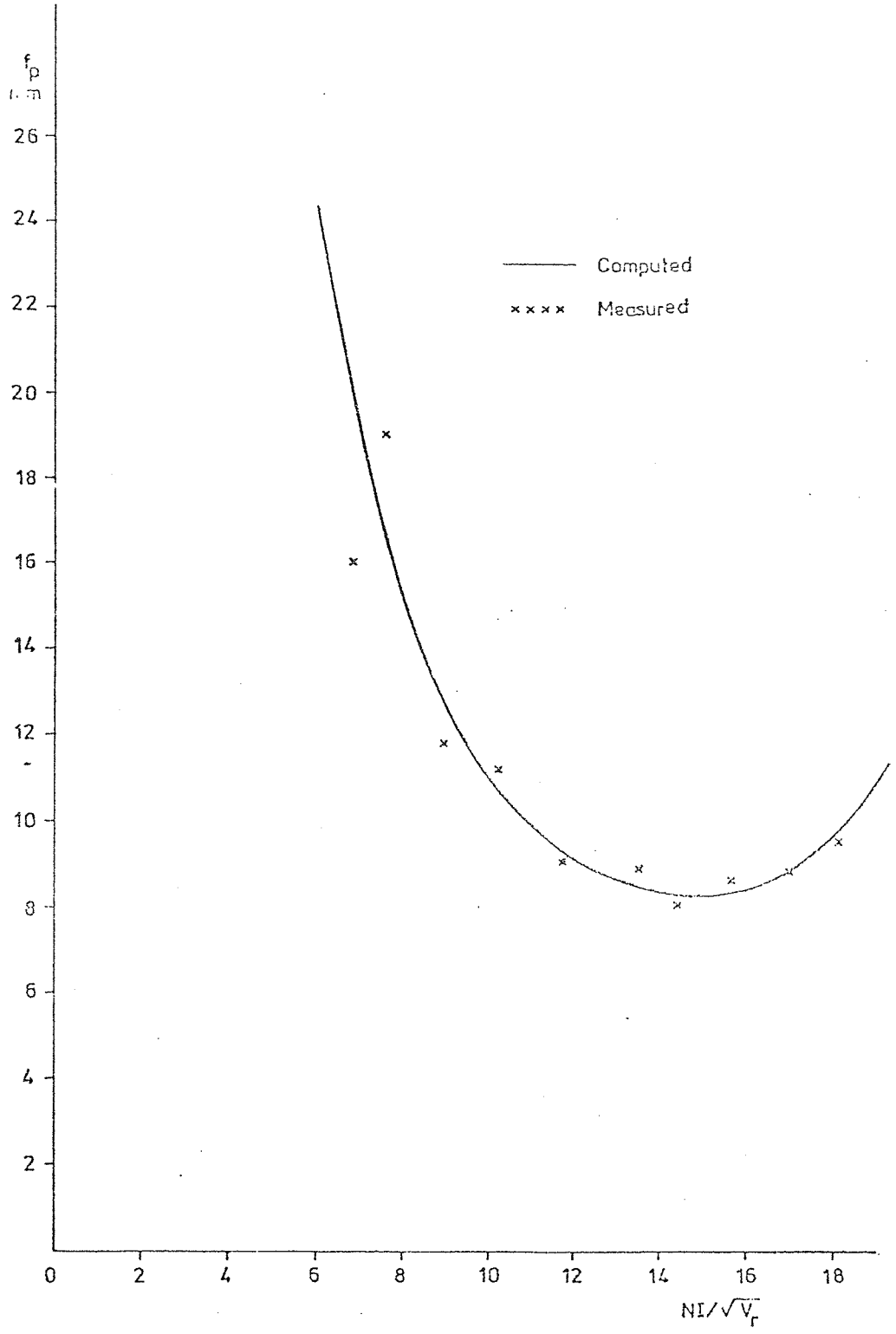

Fig. 6.5.3 Variation of projector focal length, f_p of the 8mm bore single-snorkel lens with excitation parameter $NI/V_r^{\frac{1}{2}}$.

The minimum focal length of this lens occurs at $NI/V_r^{\frac{1}{2}} = 14.5$; the computed coefficient of spiral distortion C_{sp_o} at this excitation, is 0.32 as shown in Figure 6.3.1. Experimentally, it was found that C_{sp} is 0.3, which agrees within the limits of experimental error. Therefore, at maximum magnification (minimum focal length), the 100kV single-pole lens produces 3% spiral distortion on photographic plate of radius 50mm placed at a distance of 300mm from the lens.

Properties of the 100kV double snorkel lens

The projector focal length of the 100kV rotation-free lens was measured experimentally. Figure 6.5.4 shows the measured focal length, F_p as a function of the excitation parameter $NI/V_r^{\frac{1}{2}}$. The first minimum focal length is 34mm at $NI/V_r^{\frac{1}{2}}$. As determined from the 30kV single-pole lens, this first minimum focal length is of the order of the axial distance between the faces of the snouts. In practice, the first minimum focal length is always slightly larger than this separation and shorter than the separation of the peaks. At this focal length an image can be obtained where the distortion is completely corrected. At this excitation, the computed focal length of each of the two single lenses are also 34mm i.e. the double and single lenses have equal focal lengths.

The effective focal length of this double lens is 2mm at $NI/V_r^{\frac{1}{2}} = 14.5$. At this focal length, the final rotation-free projector lens can magnify 150 X in this projection system. A projector focal length of 2mm is of the same order of magnitude as that commonly used in the final projector lenses in commercial electron microscopes, but such lenses usually have very small bores, e.g. the original projector lens P_2 of the EM6 microscope has a focal length of 1.7mm but its bore is only 1.5mm in diameter. The ratio of the volume of the original projector lens to that of the miniature rotation-free doublet one is 15:1. The ratio of the power consumed in the miniature lens doublet

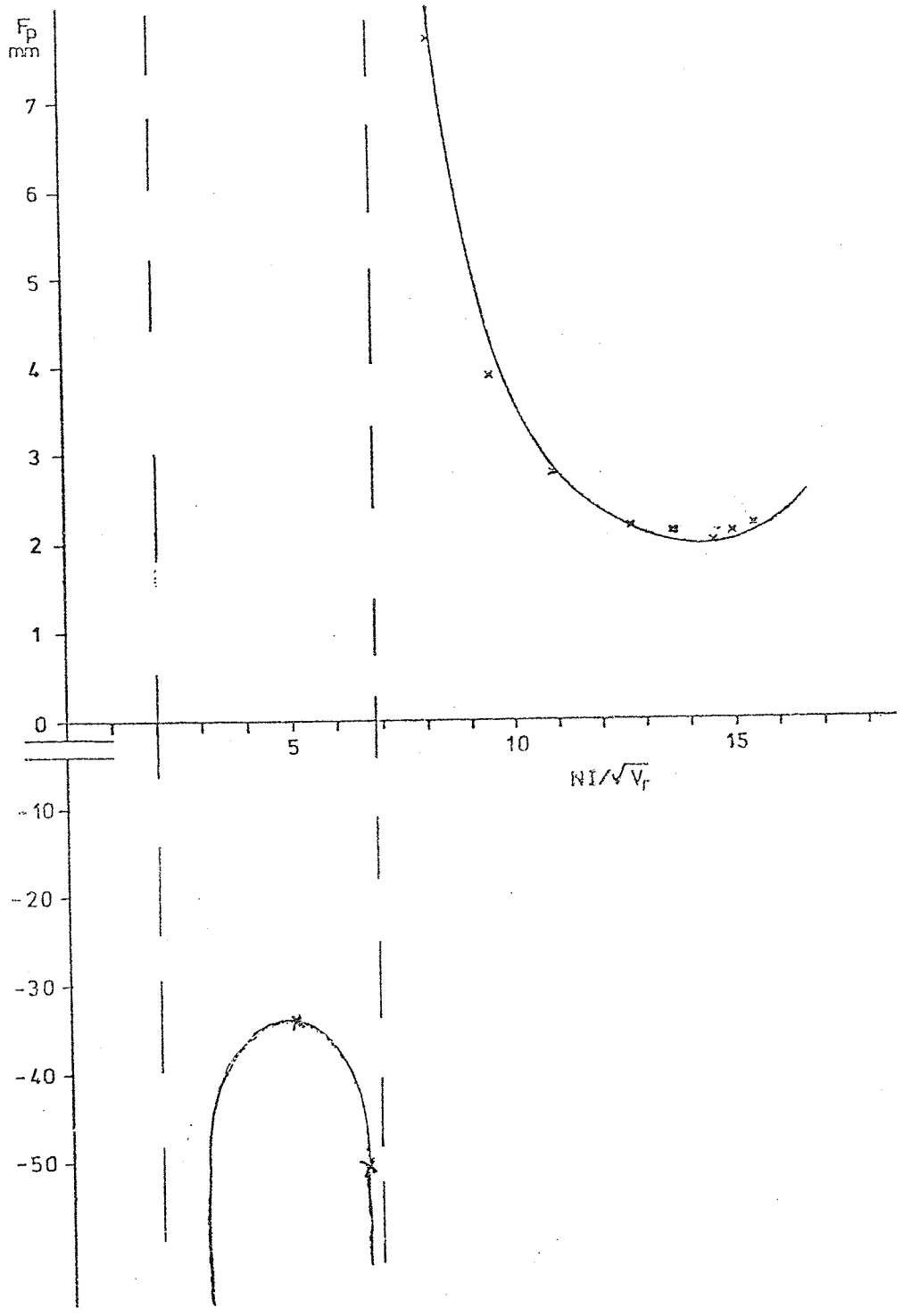

Fig.6.5.4 Variation of the projector focal length, F_p of the 8mm bore double snorkel lens with the excitation parameter $NI/V_r^{\frac{1}{2}}$.

to that in the original projector lens is about 20:1. The significance of this reduced volume is its usefulness in high voltage electron microscopy.

Figure 6.5.5 shows a series of rotation-free images of a copper grid placed in the intermediate aperture projected by the intermediate lens only. These images which are limited by the bore of the brass tube are superimposed on that of the objective lens. The doublet is rotation-free at all excitations.

6.6 Conclusion

A miniature rotation-free projection system, with two identical 100kV double snorkel lenses of short focal length, low distortion and large bore, was successfully constructed and tested. This projection system reduced the height of the EM6 electron microscope and greatly increased its field of view. The miniature projection system should be useful in high vacuum electron-optical columns and high voltage electron microscopes.

$NI/V_r^{\frac{1}{2}} = 9$

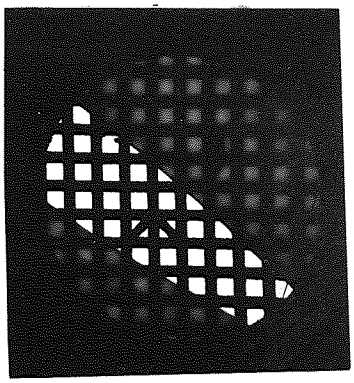

$NI/V_r^{\frac{1}{2}} = 10$

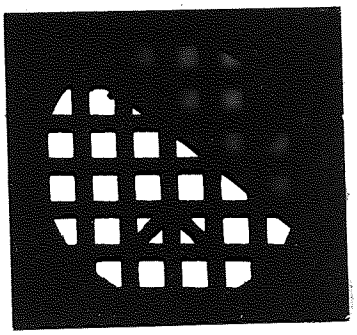

$NI/V_r^{\frac{1}{2}} = 11$

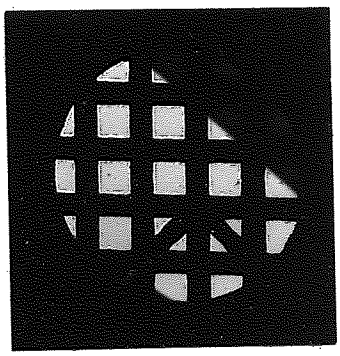

$NI/V_r^{\frac{1}{2}} = 12$

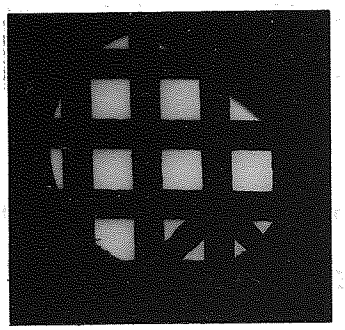

Fig. 6.5.5 Electron micrographs of a copper grid projected by the double intermediate lens at 75kV showing no image rotation at different excitations. Notice the large field of view and very low distortion.

7. THE MINIATURE OBJECTIVE LENS

The size and the position of the original objective lens of the EM6 electron microscope imposed restrictions on the miniature projection system described in Chapter Six. When the rotation-free intermediate projector lens focused the diffraction pattern form in the back focal plane of the objective lens, because the distance between the back focal plane of the objective lens and the intermediate projector doublet is larger than that between the latter and the final projector doublet (Figure 6.4.5), the diffraction pattern was demagnified about four times by the intermediate lens. The maximum magnification of the final rotation-free projector lens was 150 X on the photographic plate. The maximum magnification of the diffraction pattern was thus less than 40 times on the photographic plate. The size of this diffraction pattern was more than 4 times smaller than that obtained from the original lenses of the EM6 electron microscope. Moreover, the presence of the iron stage for the intermediate aperture, situated between the objective lens and the intermediate projector doublet (Figures 6.4.3 and 6.4.5), distorted the leakage flux of the upper lens of the doublet. All these difficulties suggested the need for a miniature objective lens to replace the conventional original lens.

A miniature objective lens was therefore designed and constructed. Besides the considerable advantage its small size, the lens could be used either as a single or as a double-pole objective lens. The double-pole lens had the ratio of S/D = 1 since it is known (Liebmann, 1951; Brookes et al, 1968) that such a lens has a low spherical and chromatic aberration.

7.1 Design of the experimental objective lens

The cross-section of the miniature objective lens is shown in Figure 7.1.1. It has an outer diameter of 110mm and a height of 20mm. The angle of the upper truncated conical polepiece taper was chosen to be 55° since high flux densities were required, (Mulvey, 1953). The lens bore diameter and the geometry of the upper surface around the bore were designed to house the normal EM6 specimen holder which enters the lens field by means of a top entry specimen chamber.

The lid of the lens is interchangeable. When made of iron, the lens becomes a double-pole objective lens with a gap width, S of 6mm and a 6mm bore diameter D, (S/D = 1). If the iron lid is replaced by a non-magnetic material (e.g. brass), the lens becomes a single-pole objective lens. Figure 7.1.2 shows a photograph of the lens with its two wire coils and the interchangeable lids. The lens lid and the upper polepiece are separated by a vacuum-tight brass cylinder of height slightly less than 6mm with a bore of 6mm diameter along its axis.

The iron lid has a round polepiece extending 1mm from its inner surface with a 12mm outer diameter. The 6mm bore diameter of this polepiece has sharp corners of good mechanical precision in order to avoid astigmatism. The outer diameter of this polepiece is equal to that of the flat surface of the upper conical polepiece.

The lens was excited by two coils. The coils were designed to produce 5500A-t from an external current supply capable of delivering up to 25 Amps at 60 volts. The appropriate wire size chosen to match the output of the power supply was 20 S.W.G. (about 1mm diameter) insulated copper wire. The two coils had the same outer diameter (86mm) the 4mm thickness containing four wire layers. The upper coil, (Figure 7.1.1) of I.D. = 26mm to suit the geometry of the conical polepiece, had 126 turns and a resistance of 0.65 ohm at 20°C. The

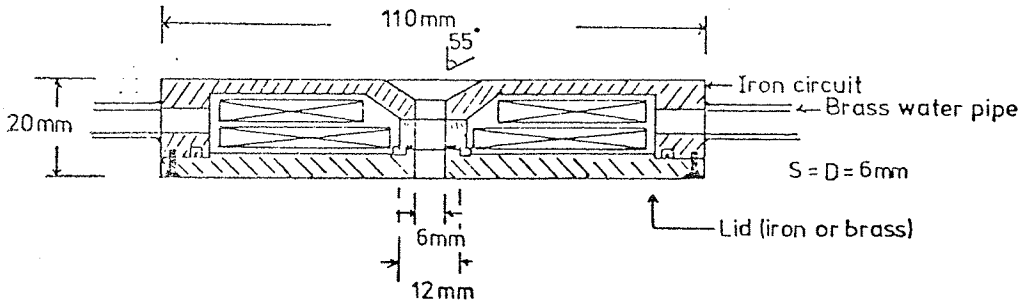

Fig. 7.1.1 Cross-section of the miniature objective lens.

Fig. 7.1.2 Components of the experimental miniature objective lens with its interchangable brass and iron lids.

lower coil of I.D. 16mm had 135 turns and a resistance of 0.67 ohm at 20°C. The total number of turns of the two coils was thus 261 with a resistance of 1.32 ohms at 20°C.

The energised coils were cooled by flowing water, entering and leaving the lens through two brass pipes. The cooling water passed through the channels around the coils which are shown in Figure 7.1.1. Due to the large surface area of the coils and the small number of layers along its width, the heat-transfer was very efficient so that the temperature rise of the coils was very low even at low water flow. For example, at a water flow of 1 litre/minute at 10°C, the temperature rise in the coils was only 25°C at 5500A-t.

7.2 Magnetic properties of the lens

The magnetic properties of the lens were tested magnetically as a single and double-pole objective lens by means of Hall-probe gaussmeter. The saturation curve is shown in Figure 7.2.1, where the maximum magnetic flux density, B_m, along the axis of the lens, is plotted as a function of the excitation, NI. In the case of the double-pole objective lens, B_m is the flux density at the centre of the lens, i.e. 3mm away from each pole; while in the single-pole (snorkel) objective lens, B_m is the flux density at a distance of 2.5mm from the flat surface of the truncated conical pole.

The double-pole lens showed some signs of saturation at excitations higher than 4000A-t, as shown by deviations from linearity in Figure 7.2.1. To investigate the saturated objective lens, its magnetic field distribution along its axis was measured at 5220A-t and compared with the unsaturated lens at half the above excitation as shown in Figure 7.2.2. It can be seen that the saturation takes place in the area around the bore, which is tapered to house the specimen holder, due to the small amount of iron. When a thin iron disc was

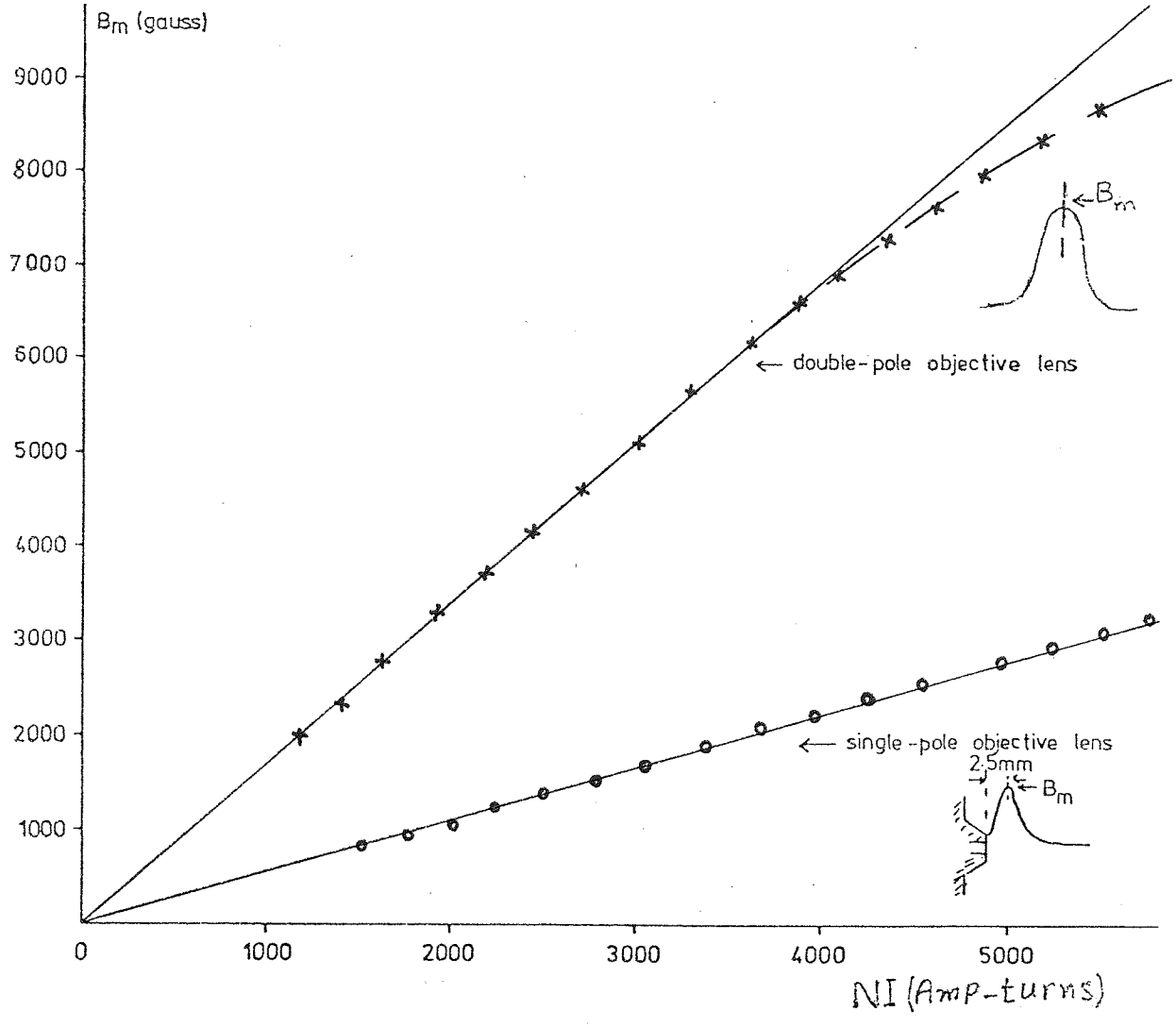

Fig. 7.2.1 Variation of the maximum flux density with the ampere-turns of the single and double-pole objective lens.

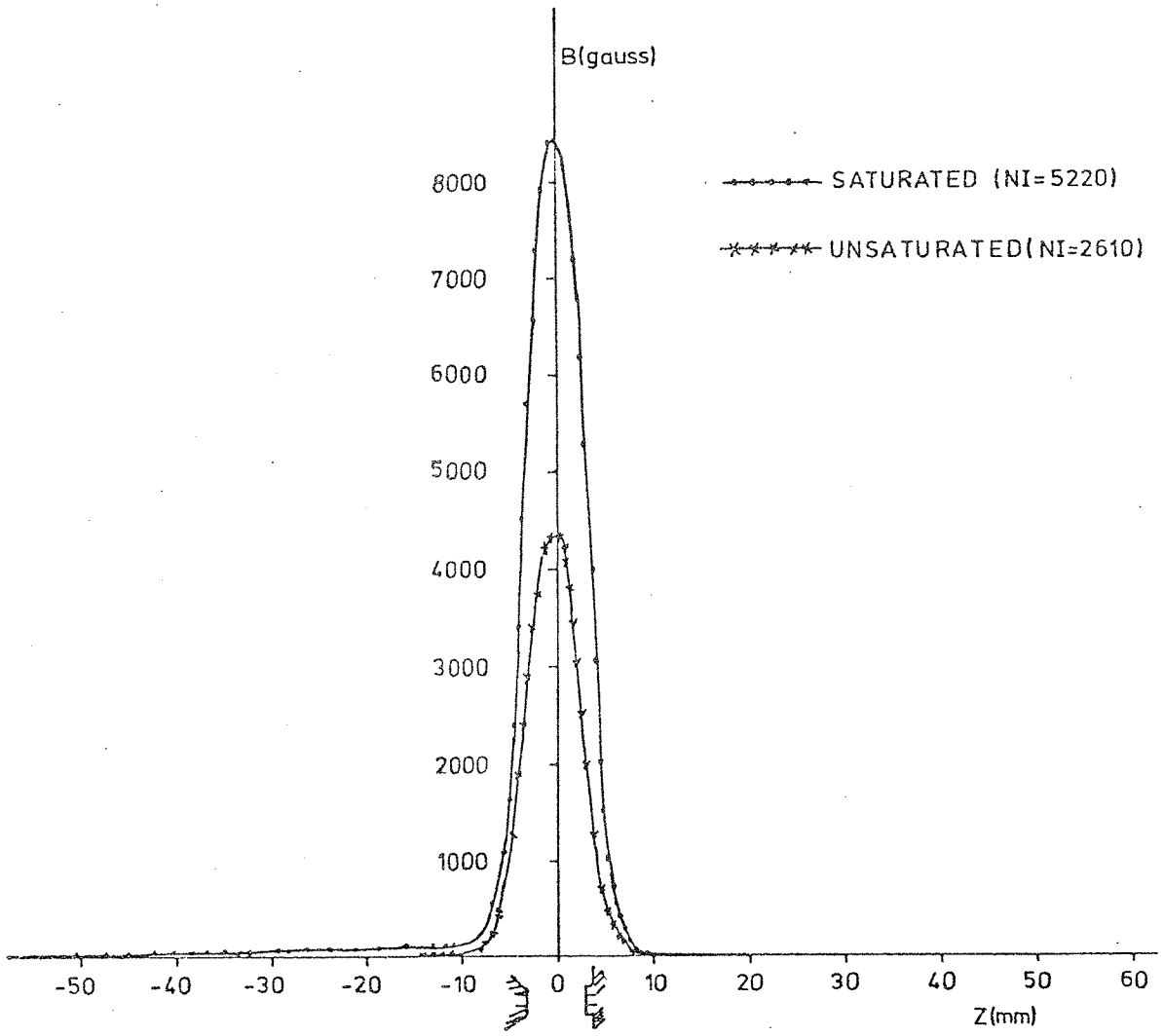

Fig. 7.2.2 Field distribution of the miniature double-pole objective lens.

placed on the top surface of the lens the saturation peak disappeared. Hence this lens needs an upper surface of at least 1mm thicker for linear operation at high excitations. However, this saturation peak is very small compared with the maximum flux density at the centre of the lens and its presence (Figure 7.2.2) reduced the maximum flux density at the centre of the lens by only 7%.

The field distribution of the unsaturated objective lens is shown in Figures 7.2.2 and 7.2.3. It can be seen that there is practically no magnetic field outside from the lens surfaces, i.e. the boundaries of the magnetic field distribution are confined within the lens structure along its 20mm long axis. The accuracy of the measurements was checked by measuring the area under the curve; the agreement was within 2% with that calculated from $\int Bdz = \mu_o NI$. Liebmann and Grad (1951) have shown that for a lens of S/D = 1, the ratio of the maximum flux density B_m along the lens axis and the magnetic flux density, B_p in parallel part of air gap, S of the lens (Figure 1.2.5) is 0.834;

$$\text{i.e.} \qquad \frac{B_m}{B_p} = 0.834$$

$$\text{where} \qquad B_p = \frac{4\pi NI}{10S} \quad \text{(gauss)}$$

S is in centimetres. At 2610A-t, the calculated value of B_p is 5481 gauss; therefore the calculated value of B_m is 4571 gauss. Experimentally, the value of B_m was found to be 4500 gauss which is only 2% less than that calculated. For a lens of S/D = 1, the ratio of the half-width, a of the field distribution and the radius R of the lens bore (Figure 1.2.6) is 1.15; i.e.

$$\frac{a}{R} = 1.15$$

where R = 3mm; thus the calculated a = 3.45mm and 2α = 6.9mm which

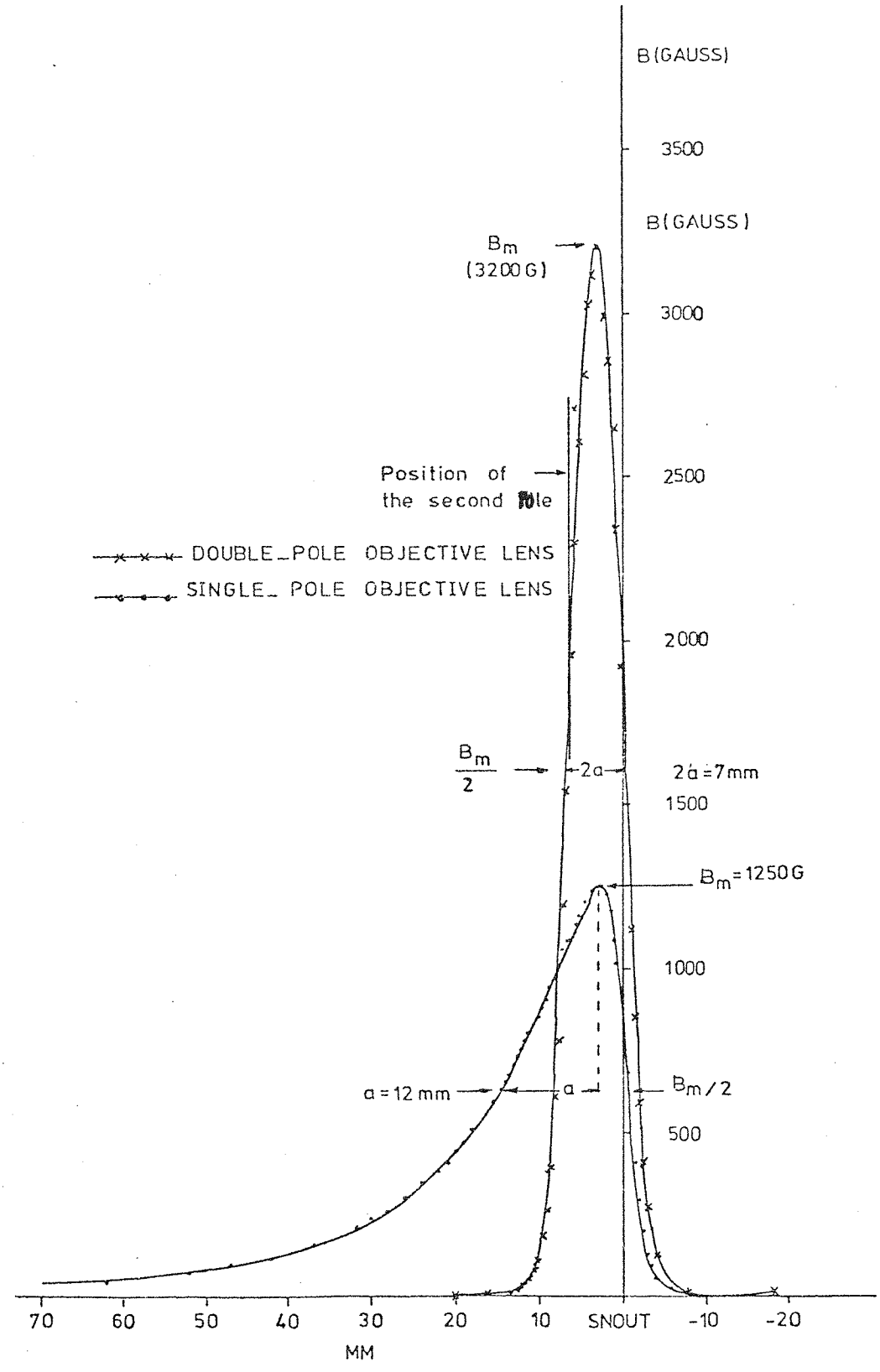

Fig. 7.2.3 Field distribution of single and double-pole miniature objective lens.

is the distance between the points where the field decreases to $0.5B_m$. Experimentally, it was found that 2a = 7mm which is again of 2% accuracy. It should also be mentioned that Durandeau and Fert (1957) have shown that $2a = 0.97\sqrt{S^2 + 0.45D^2}$ when the excitation $NI \leqslant 1000S$ where S is in millimetres. The calculated value of 2a from the above equation is 7mm for the lens whose S = D = 6mm which agrees with the experimental value. Therefore, there is a very good agreement between the calculated and the experimentally measured parameters of the magnetic field distribution.

The maximum magnetic flux density of the single-pole objective lens increases linearly with the excitation with no sign of saturation as shown in Figure 7.2.1. The maximum magnetic flux density of the single-pole objective lens is three times smaller than that of the double-pole lens; thus the focal length of the single-pole lens will be longer than that of the double-pole lens. However, the absence of saturation fields and the small amount of iron used in the lens iron circuit are two useful advantages. The magnetic field distribution of the single-pole objective lens is shown in Figure 7.2.3 compared with that of the double-pole lens; the areas under both curves are nearly equal as expected. The field distribution curve of the single-pole objective lens reaches its peak at a point 2.5mm from the pole. It exhibits a sudden drop on the right-hand-side of the peak i.e. near and inside the pole structure and a gentle descent on the left-hand-side of the peak. Since this lens is to be used with its snout facing the screen, the field on right-hand-side of the peak i.e. on the source side might have an important effect in reducing the source image on the specimen. The half-width of the field of the single-pole lens measured from the peak of the experimental field is 12mm as shown in Figure 7.2.3, which is of the order of magnitude of the minimum projector focal length, $(f_p)_{min}$.

7.3 Computed electron optical properties of the miniature objective lens

The data of the two field distribution curves shown in Figure 7.2.3 were used to compute the focal properties of the double and single-pole objective lens. The objective lens aberrations of greatest importance in well-centred electron optical systems of perfect rotational symmetry are spherical aberration and chromatic aberration. These two aberrations were computed for the miniature objective lens both as a double and single-pole lens from the data of the magnetic field distribution.

Double-pole objective lens

The properties of symmetrical double-pole lenses are well known. The miniature objective lens has its S/D ratio equal to unity, hence the comparison between the computed and those well-known properties is a good check for the computer program.

Figure 7.3.1 shows the variation of computed objective focal length, f_o and the projector focal length, f_p of the miniature lens with the excitation parameter $NI/V_r^{\frac{1}{2}}$. It can be seen that there is a good agreement between the computed results and those given by Liebmann and Grad (1951) and Kamminga et al (1968/9) for S/D = 1 where D = 6mm.

Liebmann and Grad (1951) have shown that the shortest focal length which can be obtained by any symmetrical lens when used as a projector lens is $(f_p)_{min} = 0.59D$. Therefore, for the miniature objective lens, its minimum projector focal length is 3.54mm at $NI/V_r^{\frac{1}{2}} = 13.6$. This value of f_p is 2% less than that calculated from equation $(f_p)_{min} = 0.5(S^2 + 0.45D^2)^{\frac{1}{2}}$. The projector focal length goes to infinity at about $NI/V_r^{\frac{1}{2}} = 22$ and there is a succession of similar loops for higher excitations.

For weak and moderately strong excitations, the projector

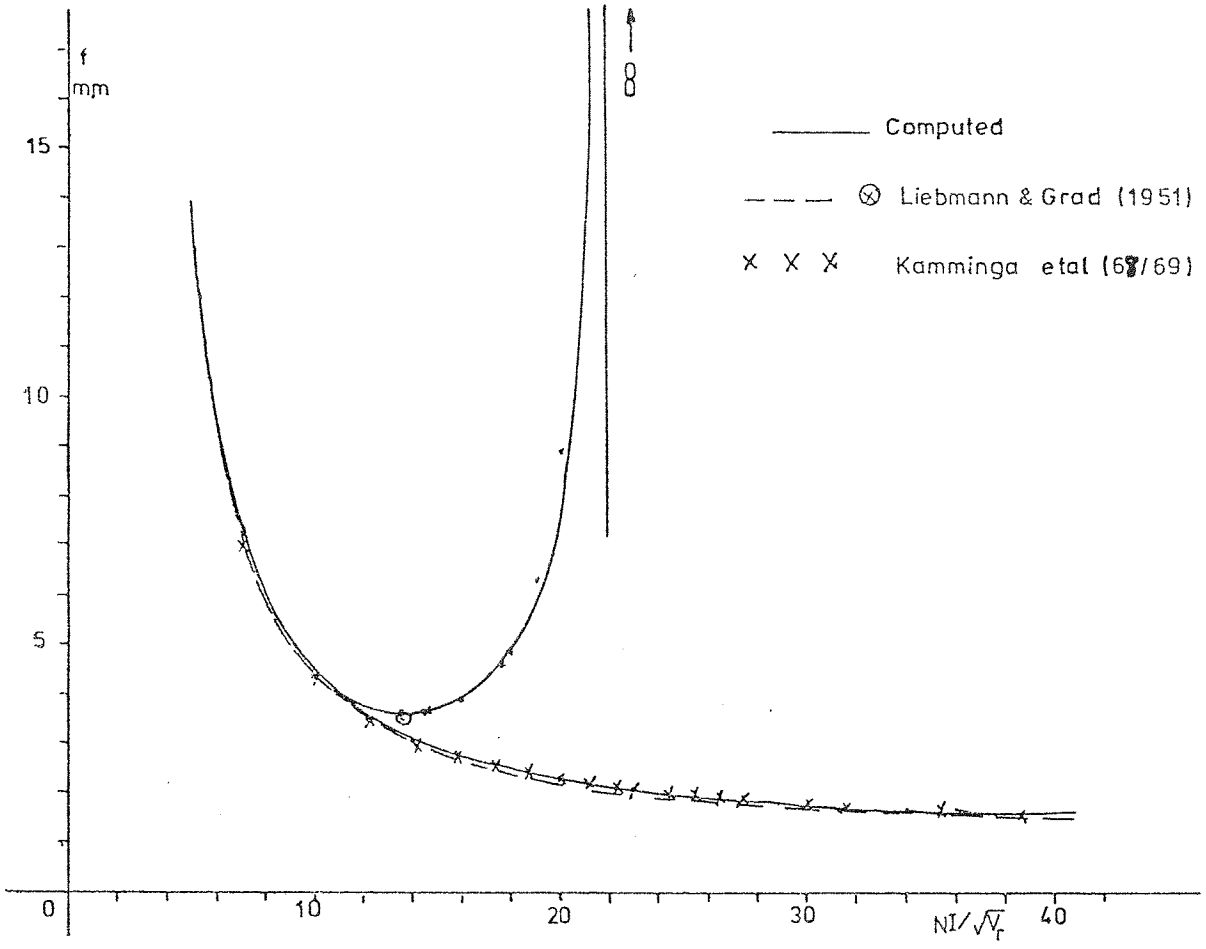

Fig. 7.3.1 Variation of the projector and objective focal length of the double-pole lens with the excitation parameter $NI/V_r^{\frac{1}{2}}$.

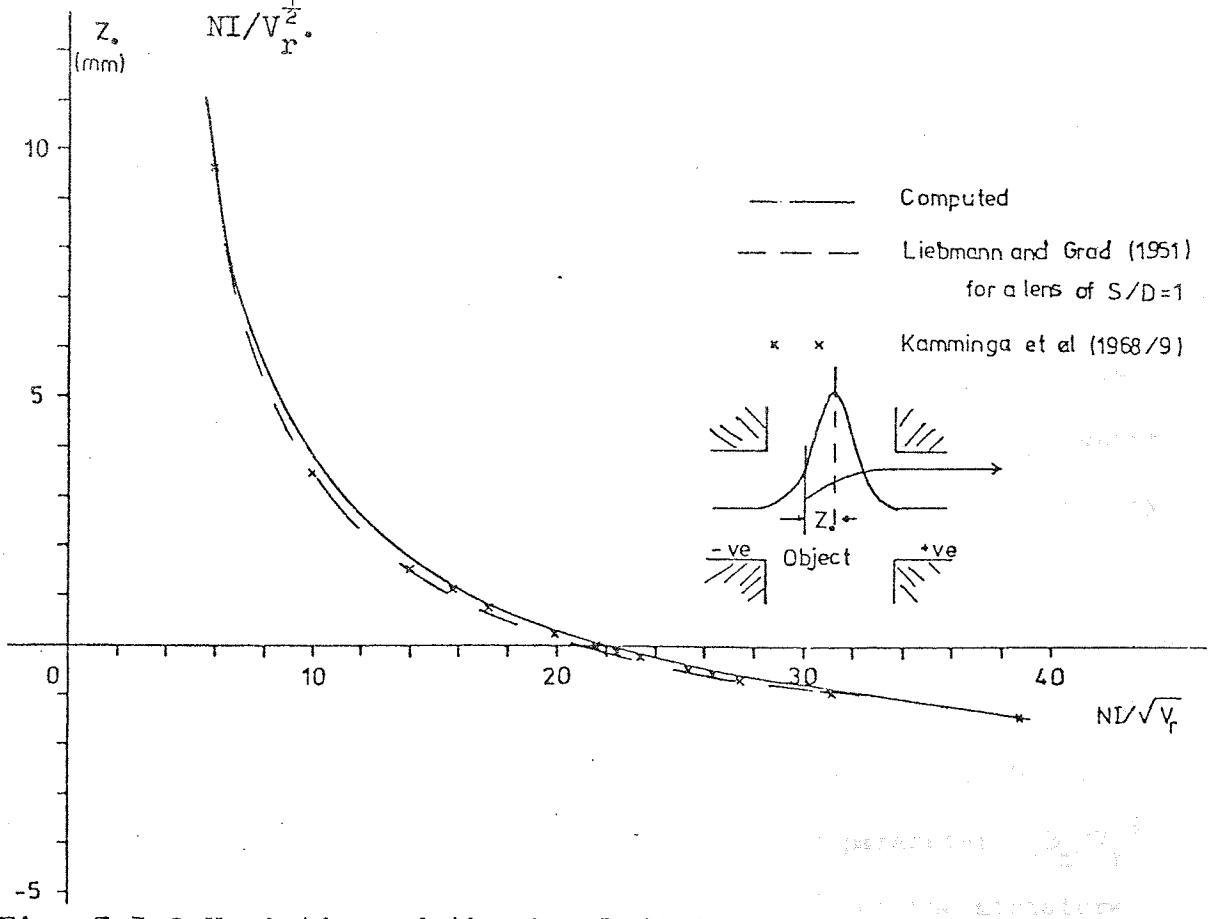

Fig. 7.3.2 Variation of the focal distance Z_o of the double-pole objective lens with the excitation parameter $NI/V_r^{\frac{1}{2}}$.

focal length, f_p and the objective focal length, f_o are identical as shown in Figure 7.3.1. A lens is considered weak when the focal length is inversely proportional to the excitation parameter $NI/V_r^{\frac{1}{2}}$. This occurs for $NI/V_r^{\frac{1}{2}} \ll 6$. Initially, the objective focal length, decreases steeply and then at a slower rate with increasing excitation. At high excitations, where $NI/V_r \gg 30$, f_o is nearly constant (1.6mm), i.e. independent of excitation.

Figure 7.3.2 shows the objective focal distance, Z_o of the double-pole objective lens as a function of the excitation parameter $NI/V_r^{\frac{1}{2}}$. In symmetrical double-pole lenses, Z_o represents the distance between the centre of the lens at S/2 and the object from which the electrons are scattered. The computed results of Z_o are in very good agreement with those determined by Liebmann and Grad (1951) and Kamminga et al (1968/9) for this specific lens geometry. The focal distance Z_o decreases with an increase in $NI/V_r^{\frac{1}{2}}$ but at an increasingly slower rate the higher $NI/V_r^{\frac{1}{2}}$ as shown in Figure 7.3.2. When $NI/V_r^{\frac{1}{2}}$ is about 22, Z_o passes through the origin i.e. the parallel electron beam crosses the centre of the lens.

The variation of the spherical aberration coefficient, C_s and the chromatic aberration coefficient, C_c of the double-pole objective lens with the excitation parameter $NI/V_r^{\frac{1}{2}}$ are shown in Figure 7.3.3. It can be seen that C_s falls steeply from quite high values at low excitations to a value as low as 0.7mm at $NI/V_r^{\frac{1}{2}} = 40$. The C_c curve shows that $C_c \backsimeq 0.7f$. The computed results of C_s and C_c are in very good agreement with those determined by Liebmann and Grad (1951) and Kamminga et al (1968/9). It should be mentioned, however, that it is not possible to design a lens having the minimum possible values of both spherical and chromatic aberrations, (Brookes, et al 1968).

Figure 7.3.4 shows the spherical aberration parameter $C_s B_m / V_r^{\frac{1}{2}}$ as a function of the excitation parameter $NI/V_r^{\frac{1}{2}}$ for the miniature

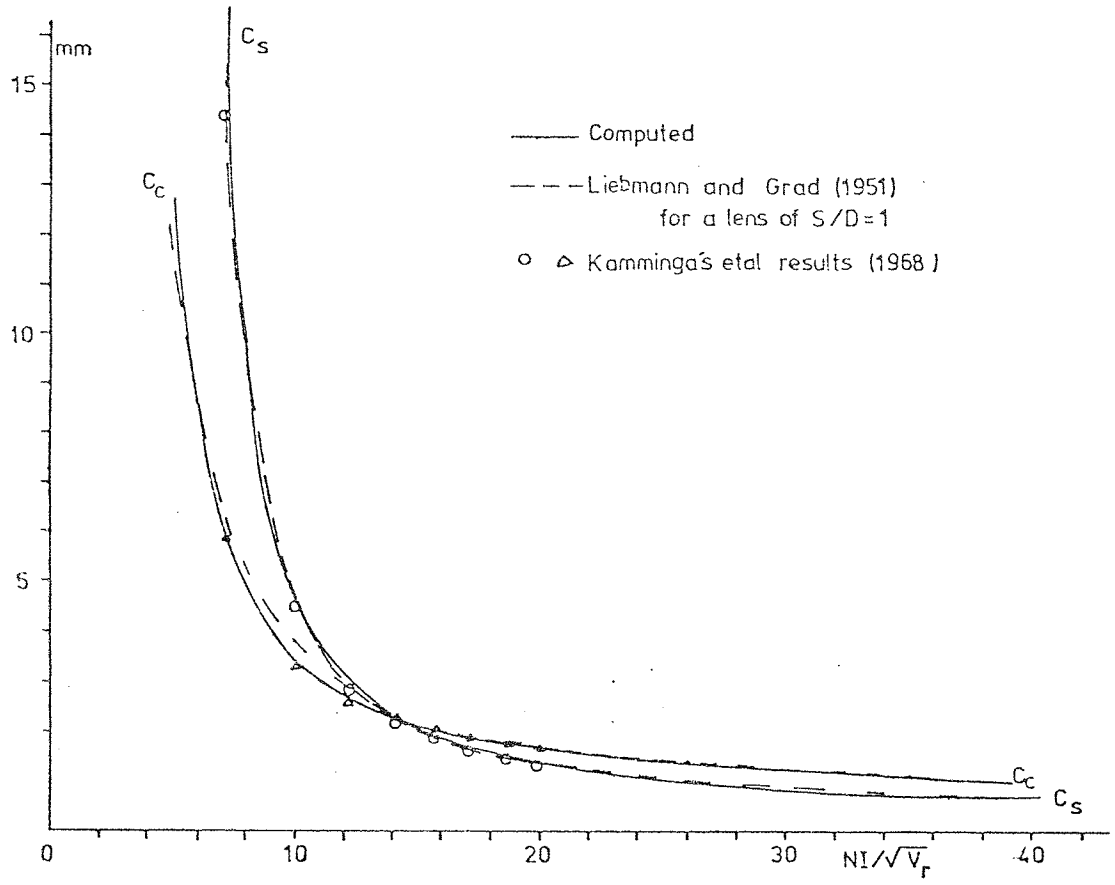

Fig. 7.3.3 Variation of the spherical and chromatic aberration coefficients of the double-pole objective lens with the excitation parameter $NI/V_r^{\frac{1}{2}}$.

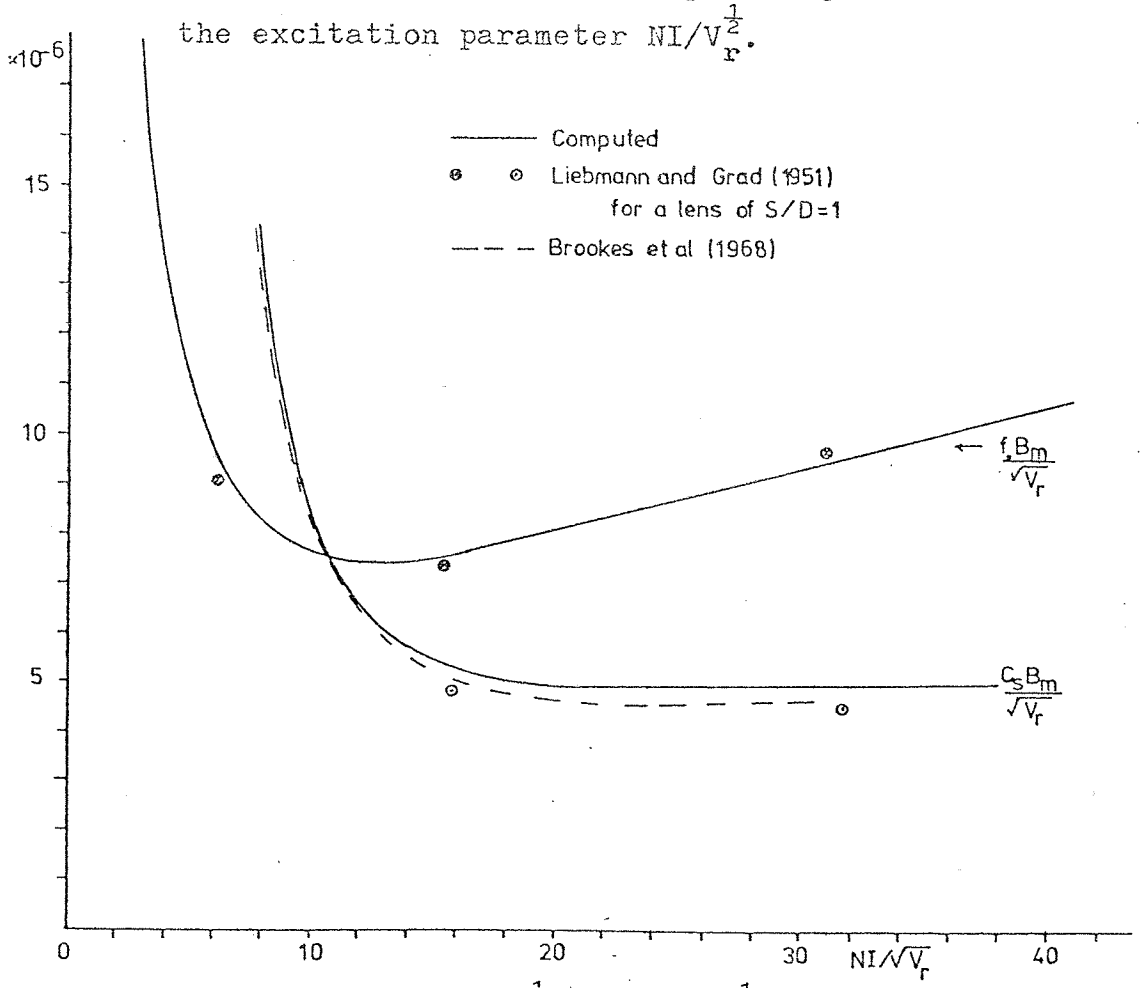

Fig. 7.3.4 Variation of $C_s B_m / V_r^{\frac{1}{2}}$ and $f_o B_m / V_r^{\frac{1}{2}}$ of the double-pole objective lens with the excitation parameter $NI/V_r^{\frac{1}{2}}$

objective lens. The computed results agree within about 5% with those given by Liebmann and Grad (1951) and Brookes et al (1968) for the lens of S/D = 1. The spherical aberration parameter $C_s B_m / V_r^{\frac{1}{2}}$ has a minimum value of 4.9×10^{-6} mTV$^{-\frac{1}{2}}$ at $NI/V_r^{\frac{1}{2}} = 24$. However, at the excitation interval $40 \gtrsim NI/V_r^{\frac{1}{2}} \gtrsim 20$, the parameter $C_s B_m / V_r^{\frac{1}{2}}$ changes very slightly that it can be considered constant and equal to about 5×10^{-6} mTV$^{-\frac{1}{2}}$. For this miniature objective lens it is therefore possible to write $(C_s)_{min} \simeq 5 \times 10^{-6} V_r^{\frac{1}{2}} / B_m$ m, where B_m is the maximum flux density on the lens axis in Tesla and V_r is the relativistically corrected accelerating voltage. Since the electron wavelength, $\lambda = 12.25 \times 10^{-10} / V_r^{\frac{1}{2}}$m, the corresponding best resolving power, obtained by substituting in the well known expression for resolving power, $d = 0.43\, C_s^{\frac{1}{4}} \lambda^{\frac{3}{4}}$, as limited by spherical aberration and diffraction, is given by

$$d_{min} \simeq 4.2 \times 10^{-9} / (V_r B_m)^{\frac{1}{4}} \text{ m} \qquad \ldots\ldots 7.3.1$$

Equation 7.3.1 is useful in determining the resolving power of the double-pole objective lens.

Figure 7.3.4 shows also the variation of the objective focal length parameter $f_o B_m / V_r^{\frac{1}{2}}$ with the excitation parameter $NI/V_r^{\frac{1}{2}}$. It can be seen that the computed results are in good agreement with those of Liebmann and Grad (1951) for the lens of S/D = 1. At low excitations, the parameter $f_o B_m / V_r^{\frac{1}{2}}$ decreases steeply with the increase of excitation and reaches a minimum of 7.4×10^{-6} mTV$^{-\frac{1}{2}}$ at $NI/V_r^{\frac{1}{2}} = 12$. The condition for minimum $f_o B_m / V_r^{\frac{1}{2}}$ corresponds roughly to minimum chromatic aberration parameter $C_c B_m / V_r^{\frac{1}{2}}$ but not to minimum spherical aberration parameter $C_s B_m / V_r^{\frac{1}{2}}$ (Mulvey and Wallington, 1969). In fact, the minimum value of $C_c B_m / V_r^{\frac{1}{2}}$ for the miniature objective lens is 5.6×10^{-6} mTV$^{-\frac{1}{2}}$ at $NI/V_r^{\frac{1}{2}} = 14$.

It can thus be concluded from the Figures 7.3.1 to 7.3.4 that

the agreement between the computed electron optical properties and those well known for the lens of S/D equal to unity, justifies the use of this computer program in determining the properties of any magnetic lens from its magnetic field distribution.

Single-pole objective lens

The data of the magnetic field distribution curve of the single-pole objective lens shown in Figure 7.2.3 were used to study the electron optical properties of this lens by means of the same computer program. Due to the asymmetric nature of the field, the electron optical properties of this lens were studied for the electron beam entering the lens in the two possible directions i.e. when the polepiece (snout) surface was facing the source side and also when the lens was inverted with the pole surface facing the image side.

The projector and the objective focal lengths of the single-pole objective lens are shown in Figure 7.3.5 as a function of the excitation parameter $NI/V_r^{\frac{1}{2}}$. The projector focal length, f_p is the same for both directions of the electron beam since it depends on the slope of the emerging beam after traversing the whole field. f_p has a minimum value of 13mm at about $NI/V_r^{\frac{1}{2}} = 13$. When the pole face is on the image side, the objective focal length, f_o passes through a minimum of 13mm at $NI/V_r^{\frac{1}{2}} = 14$, which is a high value for an objective lens. When the snout faces the source side, the objective focal length decreases steeply to low excitations and steadily at high excitations where it decreases from 5mm at $NI/V_r^{\frac{1}{2}} = 22$ to 3mm at $NI/V_r^{\frac{1}{2}} = 38$. It can be seen in Figure 7.3.5 that when the snout faces the source side, the objective focal length of the lens is always shorter than that when the snout faces the image side at all excitations. Therefore, to obtain a single-pole objective lens of short focal length, it is important to use this lens with its snout facing the source side.

The variation of the focal distance, Z_o of the single-pole

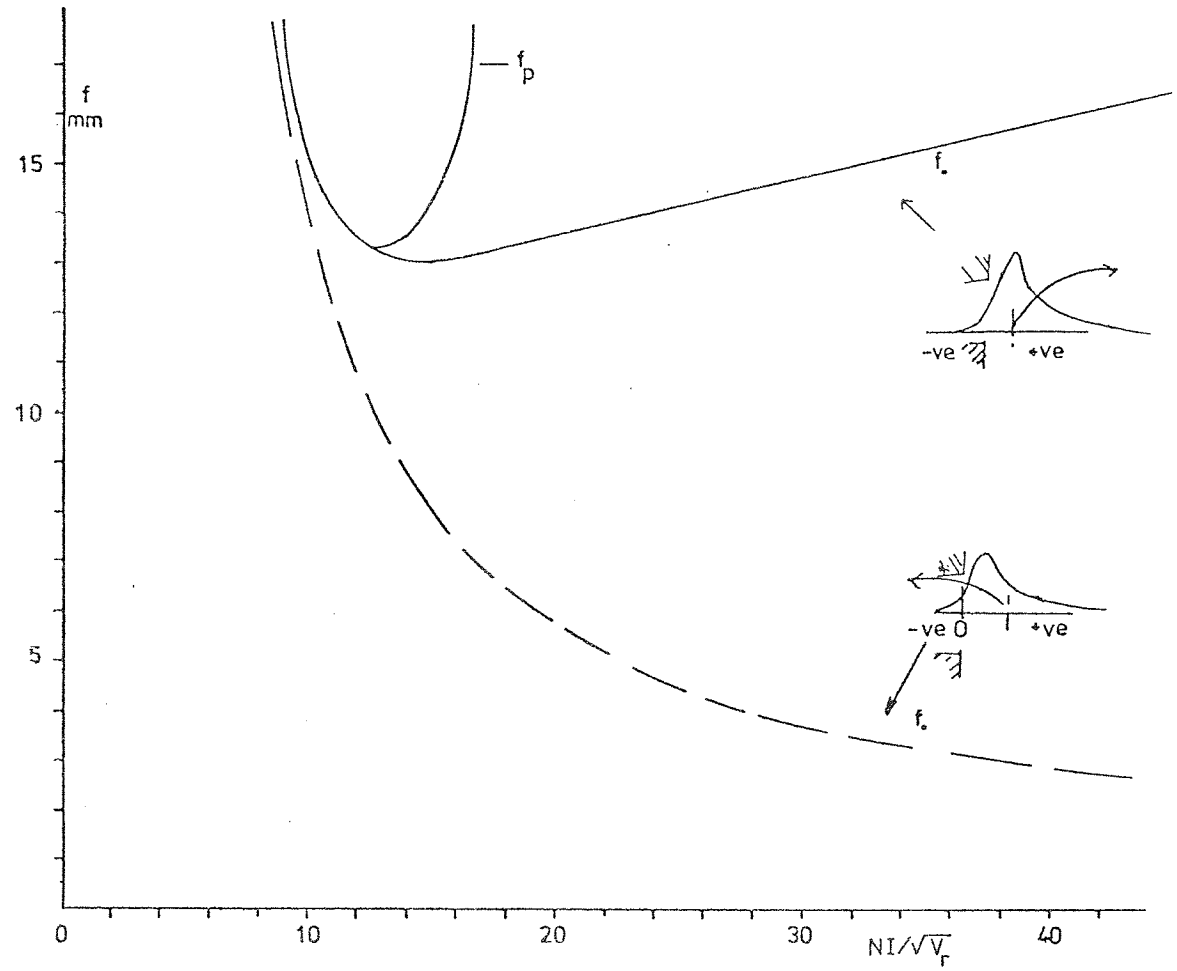

Fig. 7.3.5 Variation of the projector and objective focal length of the single-pole objective lens with the excitation parameter $NI/V_r^{\frac{1}{2}}$.

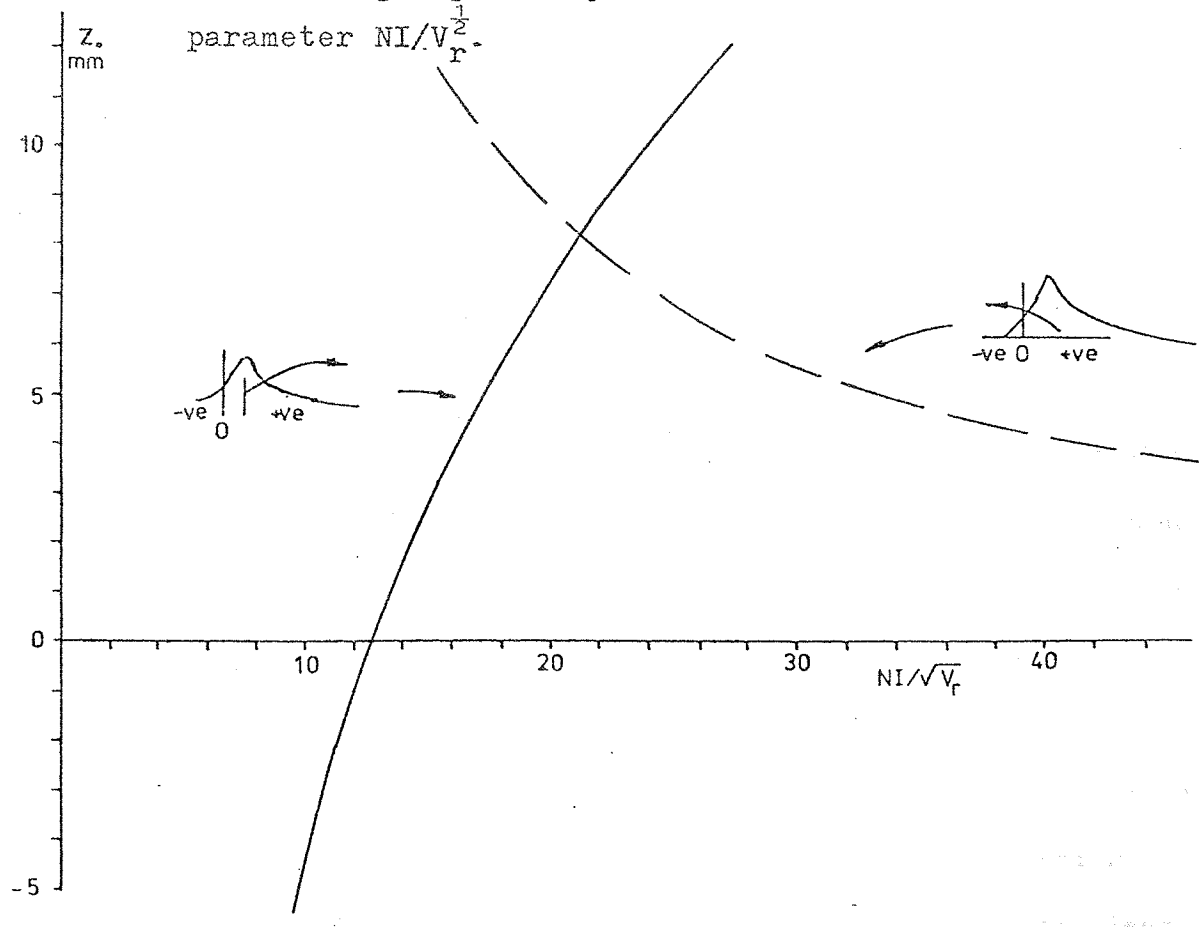

Fig. 7.3.6 Variation of the focal distance Z_o of the single-pole objective lens with the excitation parameter $NI/V_r^{\frac{1}{2}}$.

objective lens with the excitation parameter $NI/V_r^{\frac{1}{2}}$ is shown in Figure 7.3.6. The focal distance Z_o, is the distance between the snout's surface (taken as the origin) and the specimen position. It can be seen that when the snout is on the source side, Z_o is always positive even at high excitations. When the snout is on the image side, Z_o increases from negative values at low excitations i.e. the objective focal point is inside the lens bore and then passes through the origin (i.e. the specimen on the surface of the snout) at about $NI/V_r^{\frac{1}{2}} = 13$ where f_p is also minimum (Figure 7.3.5). At about $NI/V_r^{\frac{1}{2}} = 21$ the two curves meet where Z_o is about 8mm. Figure 7.3.6 shows that the rate of increase of Z_o with excitation when the snout faces the image side is higher than its rate of decrease when the snout faces the source side. Thus when the snout faces the image side, the lens provides plenty of space for specimen manipulation and incorporation of various attachments.

Figure 7.3.7 shows the spherical aberration coefficient, C_s of the single-pole objective lens as a function of the excitation parameter $NI/V_r^{\frac{1}{2}}$ for the two modes of operation. At low excitations, both curves decrease very steeply with increasing excitation and meet, at $NI/V_r^{\frac{1}{2}} = 28$ where C_s is about 4mm. Before the two curves meet, the value of C_s of the objective lens whose snout is on the image side is much lower than that when the snout is on the source side. At excitations higher than that of the meeting point, the value of C_s when the snout is on image side becomes slightly higher than that when the snout is on the source side. When the snout is on the source side the value of C_s decreases continuously with the increase of excitation. In the case of the snout being on the image side, C_s goes through a minimum of 3.7mm at $NI/V_r^{\frac{1}{2}} = 20$; however, Figure 7.3.7 shows that C_s can be considered constant at the excitation interval from about 14 to about 40 where C_s is about 4mm which is remarkably low considering the long focal length. At $NI/V_r^{\frac{1}{2}} = 20$, the value of C_s with the lens

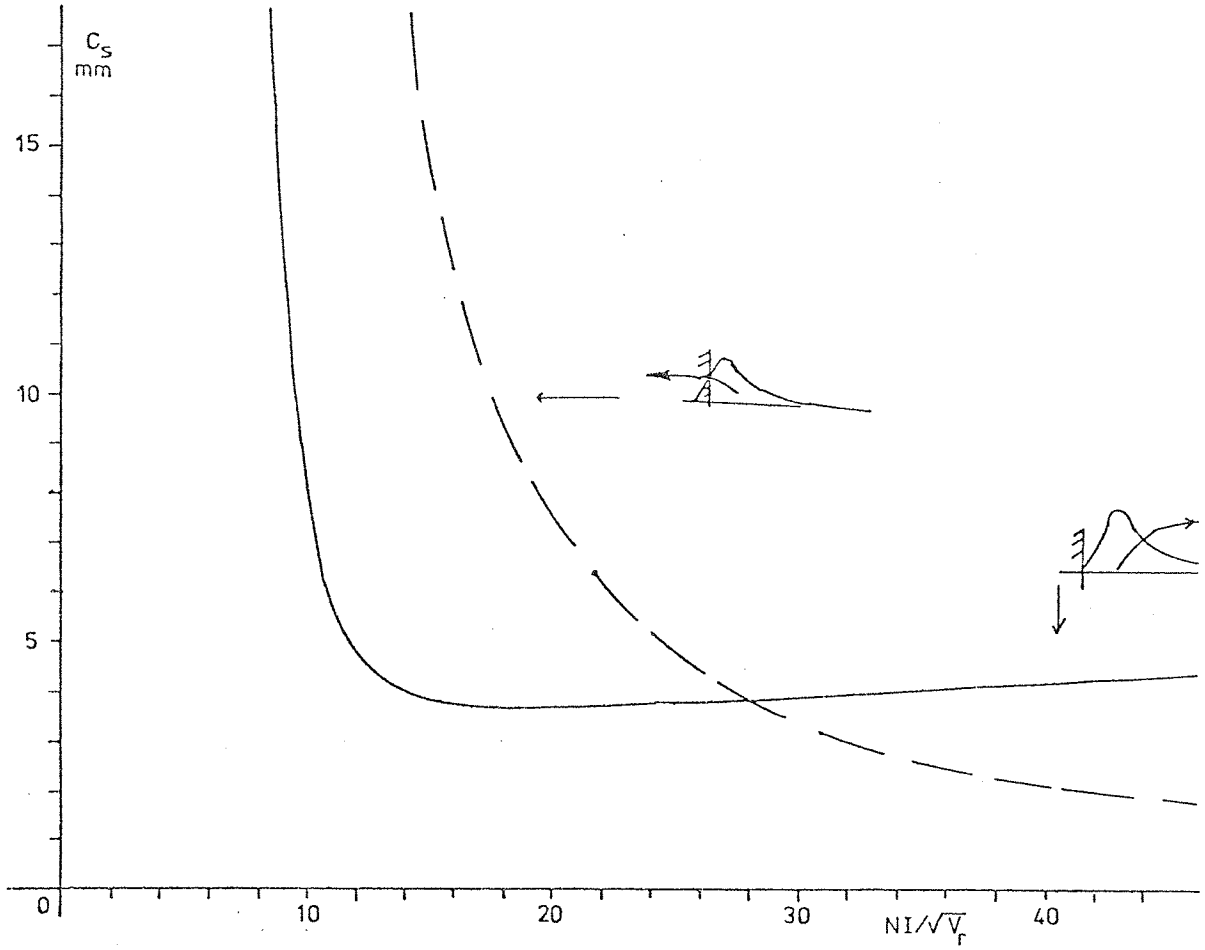

Fig. 7.3.7 Variation of the spherical aberration coefficient of the single-pole objective lens with the excitation parameter $NI/V_r^{\frac{1}{2}}$.

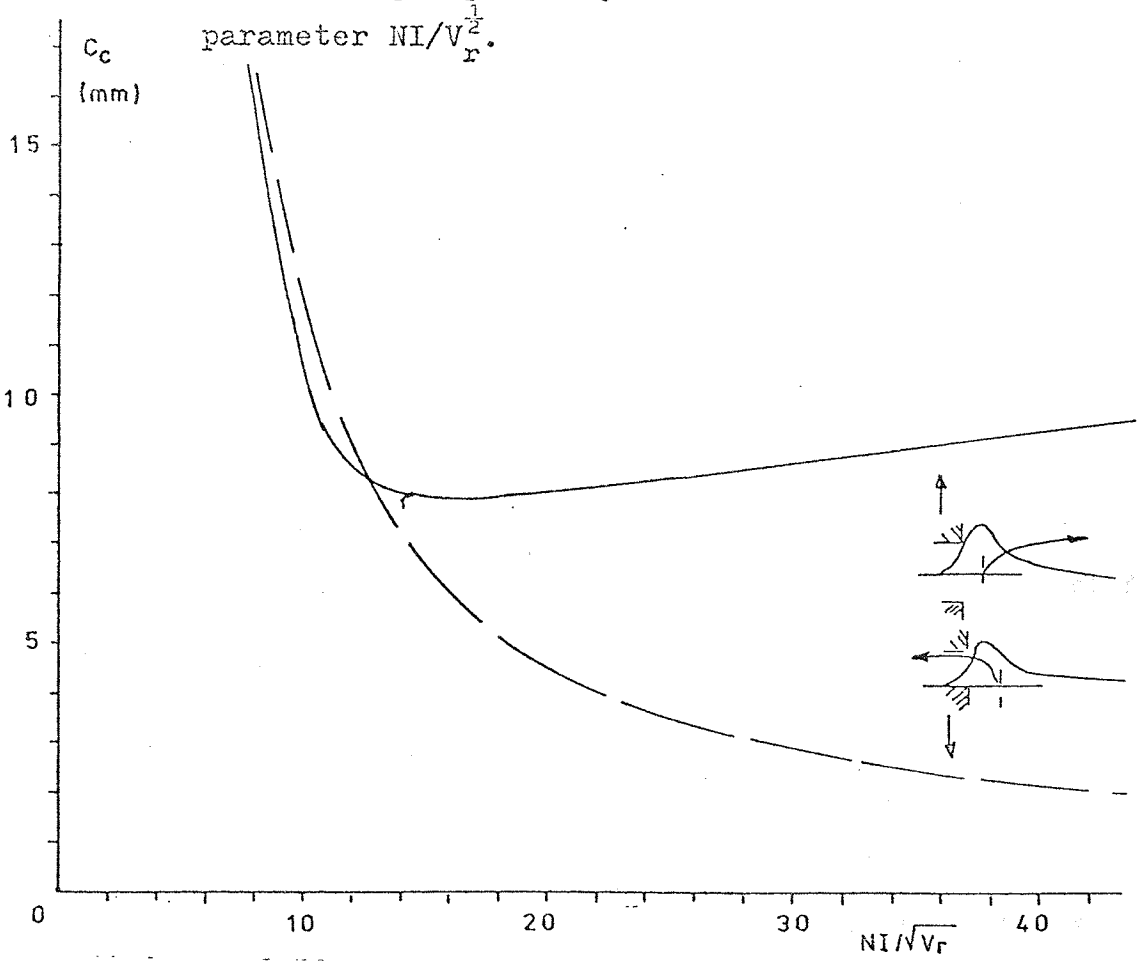

Fig. 7.3.8 Variation of the chromatic aberration coefficient of the single-pole objective lens with the excitation

snout on the image side is half that when the snout is on the source side which is an advantage in operating the lens in this mode. At high excitations such as $NI/V_r^{\frac{1}{2}} = 40$, the value of C_s with the snout on the image side is double that when the snout is on the source side which is not very useful since more power will be consumed and also the lens iron will saturate.

For the two modes of operation of the single-pole objective lens, the chromatic aberration coefficient C_c is shown in Figure 7.3.8 as a function of the excitation parameter $NI/V_r^{\frac{1}{2}}$. At low excitations the two curves decrease steeply and meet at about $NI/V_r^{\frac{1}{2}} = 13$ where C_c is about 8mm. When the snout is on the image side, C_c goes through a minimum of 7.9mm at $NI/V_r^{\frac{1}{2}} = 16$; however, the change in C_c from excitation 14 to 20 is negligible which is very useful since the lens is usually operated in this range of excitation. When the snout is on the source side, C_c decreases continuously with excitation, but it is initially higher than that for the snout on the image side until the two curves meet after which C_c becomes much lower and goes down to about 2mm at $NI/V_r^{\frac{1}{2}} = 40$ which means again that more power is required and the lens iron will saturate.

Therefore, when the single-pole objective lens has its snout facing the source side, the curves of f_o, C_s and C_c show that in this mode of operation the lens behaves like a conventional symmetrical lens since the tail of the field distribution curve is not used in imaging but as a pre-field condenser. In this case the values of f_o, C_s and C_c are low only at very high excitations which is a disadvantage. On the other hand, when the pole surface faces the image side, the exponential segment of the field distribution is the imaging part of the curve. This mode of operation has the advantage that f_o, C_s and C_c have approximately their lowest values at nearly the same low excitation parameter $NI/V_r^{\frac{1}{2}}$ of about 16.

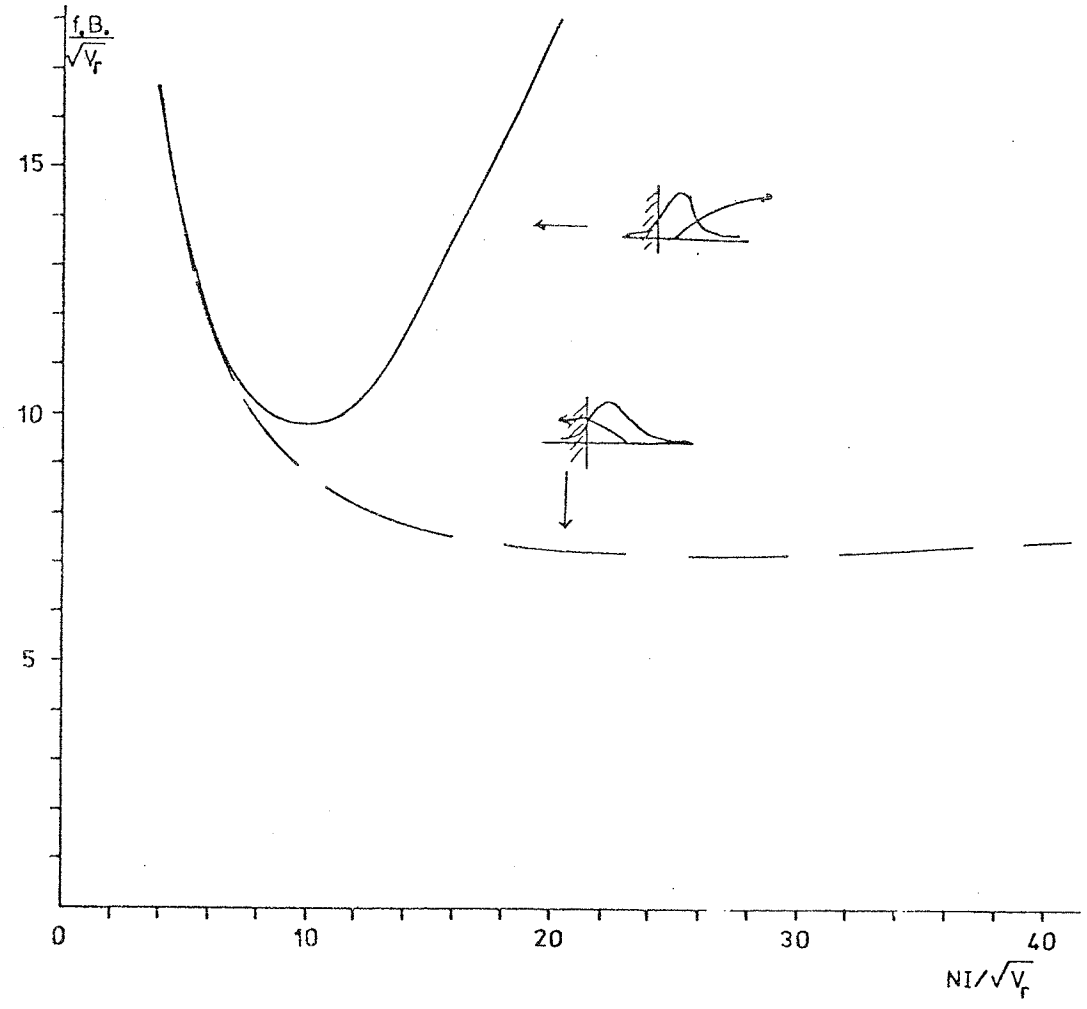

Fig. 7.3.9 Variation of the objective focal length parameter of the single-pole lens with the excitation parameter $NI/V_r^{\frac{1}{2}}$.

Although the objective lens with its snout surface facing the image side has a relatively large focal length parameter (Figure 7.3.9) but its spherical aberration parameter $C_s B_m / V_r^{\frac{1}{2}}$ shown in Figure 7.3.10 is lower than that of the best double-pole objective lens. The minimum value of $C_s B_m / V_r^{\frac{1}{2}}$ is 3.4×10^{-6} $mTV_r^{\frac{1}{2}}$. Thus $(C_s)_{min} = 3.4 \times 10^{-6}$ $V_r^{\frac{1}{2}}/B_m$ m, where B_m is the maximum value of the field distribution curve in Tesla. The corresponding best resolving power, obtained by substituting in the well known expression for resolving power, $d = 0.43\, C_s^{\frac{1}{4}} \lambda^{\frac{3}{4}}$, is given by

$$d_{min} \simeq 3.8 \times 10^{-9}/(V_r B_m)^{\frac{1}{4}} \quad m \qquad \ldots\ldots 7.3.2$$

This equation determines the resolution of the single-pole objective lens with its snout surface facing the image side.

7.4 Radial and spiral distortion coefficients of the experimental objective lens

Liebmann (1952) calculated the radial, C_d and spiral, C_{sp} distortion coefficients of symmetrical double-pole lenses with different S/D ratios. In order to check the accuracy of the computer program (Marai, 1975), the data of the magnetic field of the double-pole objective lens were used to compute C_d and C_{sp} for comparison with Liebmann's results. Figure 7.4.1 shows that for the spiral distortion coefficient, C_{sp} there is a very good agreement between the computed and Liebmann's results. The results on the radial distortion coefficient, C_d show some discrepancy mainly around the maximum at moderate excitations of about $NI/V_r^{\frac{1}{2}} = 10$. However, at high excitations, where lenses are usually operated, the agreement between the computed C_d and that of Liebmann is very good. It has been shown by Liebmann (1952) that, at low excitations, the radial distortion coefficient C_d is related to the spherical aberration coefficient C_s by the expression

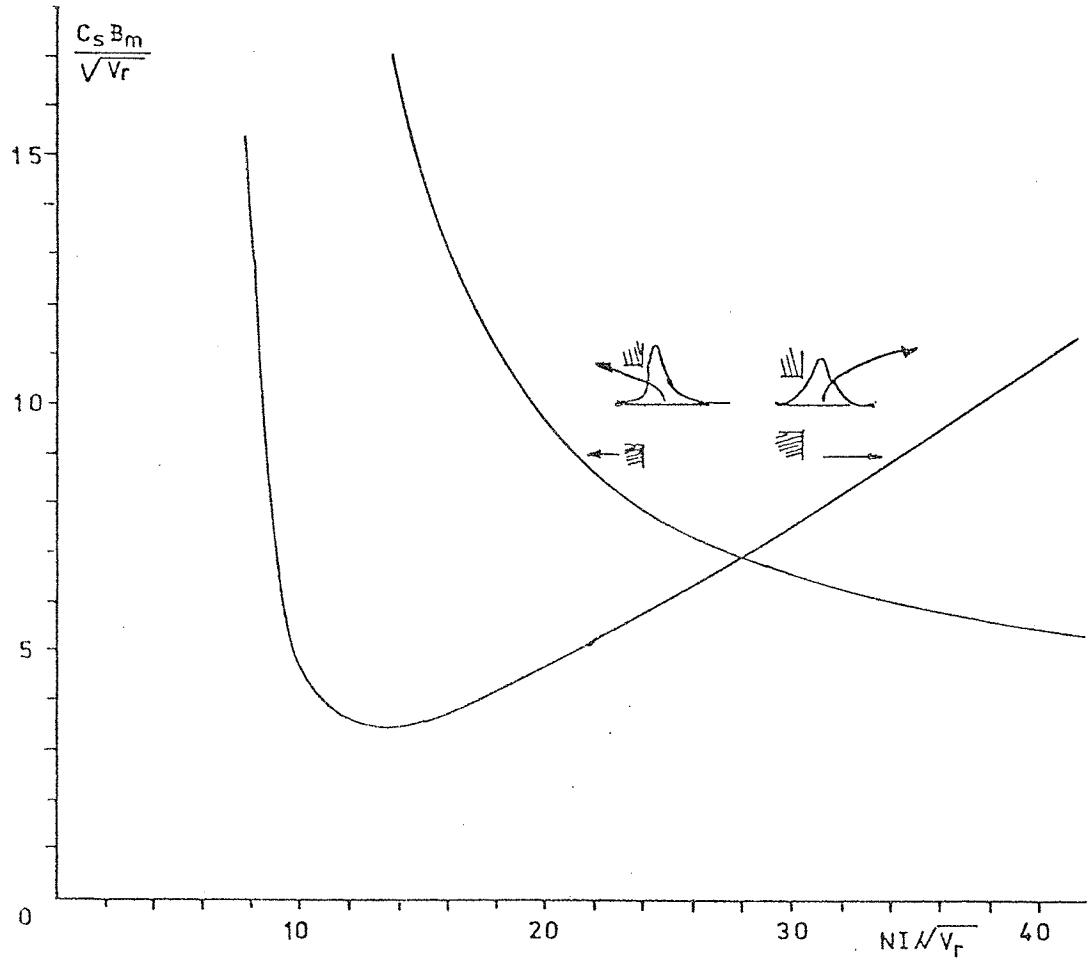

Fig. 7.3.10 Variation of the spherical aberration parameter $C_s B_m / V_r^{\frac{1}{2}}$ of the single-pole objective lens with the excitation parameter $NI/V_r^{\frac{1}{2}}$.

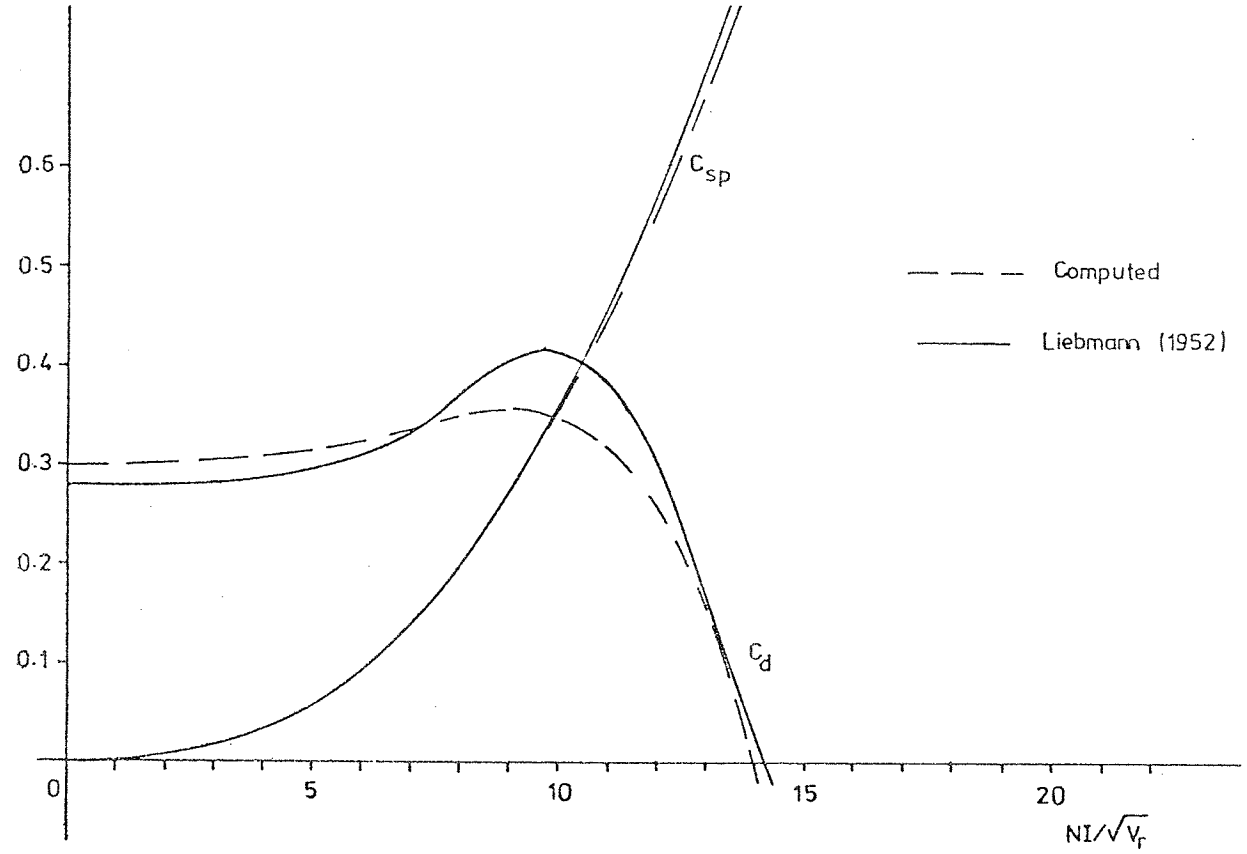

Fig. 7.4.1 Radial and spiral distortion coefficients of the double-pole objective lens as a function of the excitation parameter $NI/V_r^{\frac{1}{2}}$.

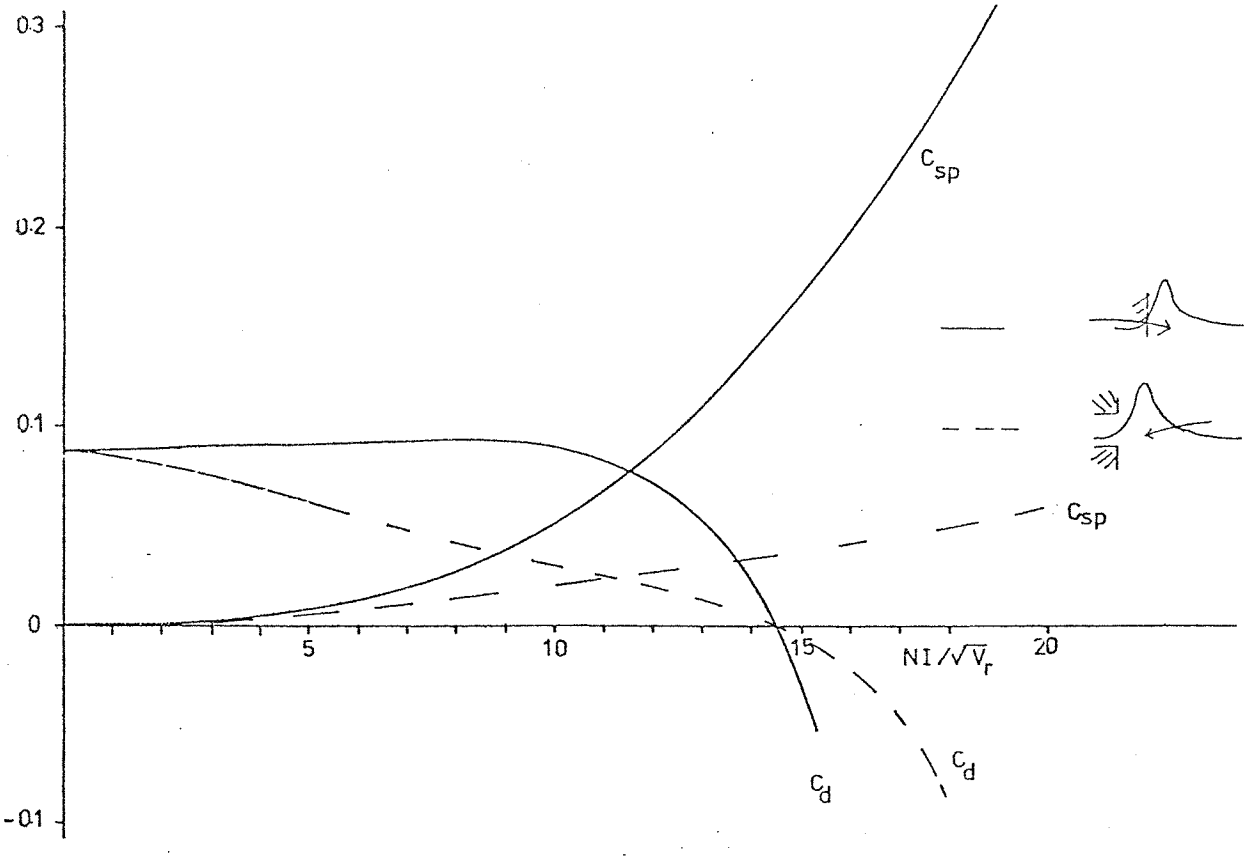

Fig. 7.4.2 Variation of the radial and spiral distortion coefficients of the single-pole objective lens with the excitation parameter $NI/V_r^{\frac{1}{2}}$.

$$C_d = R^2 C_s / f^3 \qquad \ldots\ldots 7.4.1$$

where R is the radius of the lens bore. It was found that by substituting the computed values of C_s and f (at low excitations $f_p = f_o$) of the double-pole lens (Figures 7.3.1 and 7.3.3), there was very good agreement with the computed C_d. The computed values of C_d and C_{sp} have been also verified experimentally in Chapter Four. Therefore, it can be concluded from the theoretical and experimental evidence that the computed results of C_d and C_{sp} of any magnetic lens from the data of its field distribution are of very good accuracy.

The field distribution data of the single-pole lens were also used to compute its radial and spiral distortion coefficients. Figure 7.4.2 shows the variation of C_d and C_{sp} with excitation for both modes of operation. It can be seen that for both modes of operation $C_d = 0$ at the same excitation parameter, $NI/V_r^{\frac{1}{2}} = 14.5$ which is lower than that for the double-pole lens. Hoever, Figure 7.4.2 shows the important result that by converting the double-pole lens into a snorkel lens, the radial and spiral distortion coefficients have fallen remarkably. For instance, C_{d_o} in the double-pole lens is about 0.3 and in the snorkel lens it is 0.075 which is four times smaller. With the surface of the snout of the snorkel lens facing the image plane, the maximum value of C_d is only 0.085 which is of the order of magnitude of C_{d_o}, while in the double-pole lens the maximum C_d value is about 0.4. The same argument applies to C_{sp} which, at $C_d = 0$, it is 0.85 for the double-pole lens and 0.15 for the single-pole lens whose snout is facing the image, i.e. more than five times smaller; it is also 0.07 for the snout facing the source which remarkably small. By substituting the computed values of C_s and f of the snorkel lens (Figures 7.3.5 and 7.3.7) for both modes of operation at low excitation in Equation 7.4.1, it was found that the calculated results of C_d were in very good

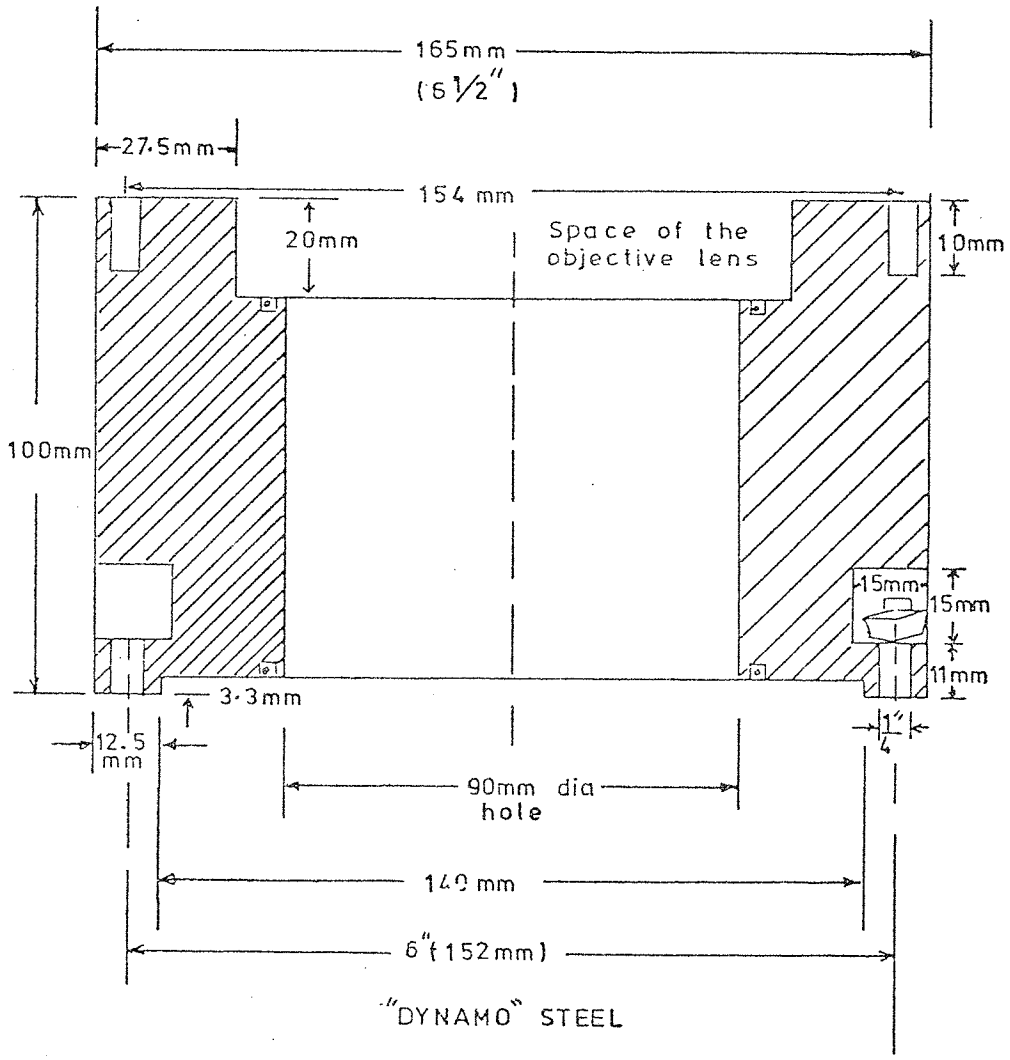

Fig. 7.5.1 Cross-section of the iron cylindrical stage for the miniature objective lens.

agreement with the two computed curves.

7.5 Design of the objective stage

In order to operate the miniature objective lens in the microscope, a special stage was constructed, replacing the original objective lens and the alignment stage of the EM6 microscope. Figure 7.5.1 shows a cross-section of the iron cylinder stage whose outer diameter was limited by the outer diameter of the EM6 column. Its height was chosen such that the total magnification of the miniature double-pole objective lens and the two projector doublets will be comparable to that of the original EM6 imaging system. The original objective aperture holder was mounted on this stage to the nearest possible distance from the bottom surface of the objective lens, Figure 7.5.2, together with the original specimen-shift controls. However, each of the two brass rods of the specimen-shift control was further shortened by 80mm to become 190mm long which is 50% shorter than the original rod of the EM6 microscope. Also the height of the pumping tube in the back of the electron optical column was shortened by a further 80mm by the same procedure shown in Figure 6.4.4; this enables one to restore the microscope to its original height without difficulty. The objective stage was firmly fastened to the miniature projection stage. With the objective lens mounted in its cylindrical stage (Figure 7.5.3), the height of the miniature imaging system, measured from the top surface of the objective lens to the screen, was about 440mm, which is equivalent to 30% reduction in the original height of the EM6 microscope.

7.6 Performance of single and double-pole miniature objective lens

The miniature objective lens was tested alone in the electron microscope at 75kV both as a double and single-pole lens. The snout of the single-pole objective lens was set facing the image side since

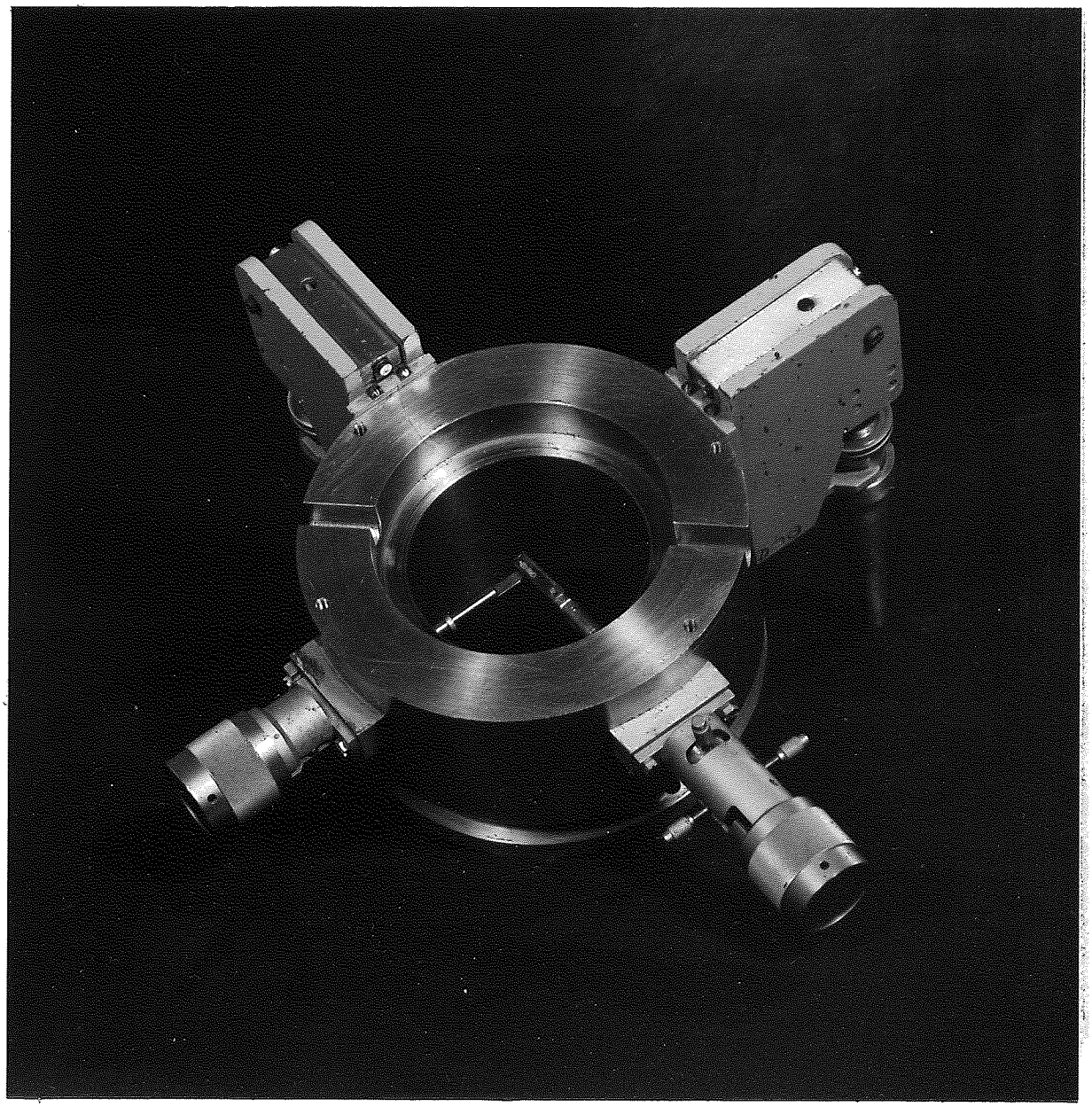

Fig.7.5.2 The objective stage with the two specimen-shift controls and the aperture holder mounted on it.

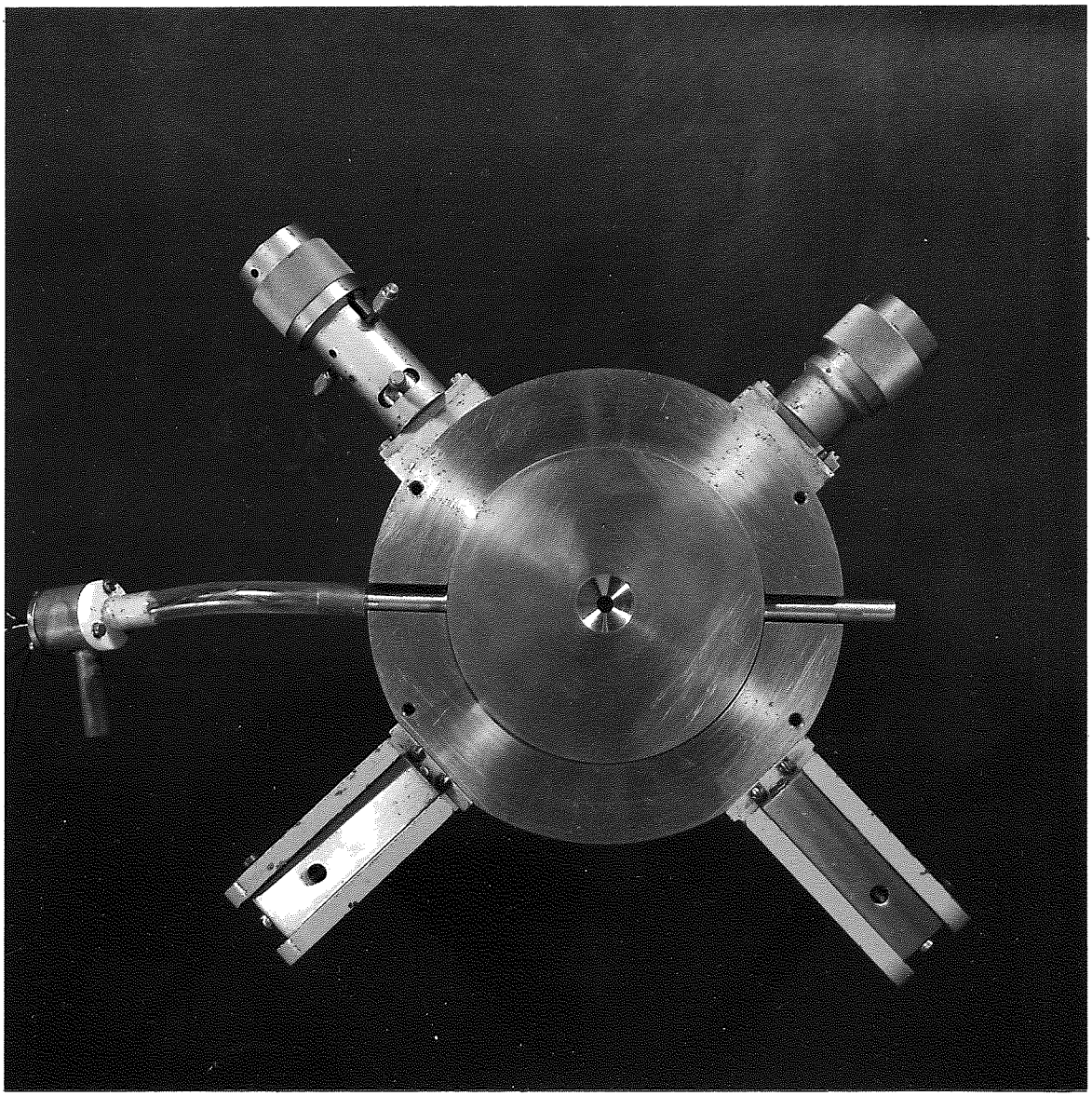

Fig.7.5.3 The miniature objective lens mounted on the iron cylindrical stage.

in this way the spherical aberration of the lens is very small.

With the distances below the objective lens in the microscope shown in Figure 7.6.1, the calculated field of view (X_o) of the image formed by the objective lens on the photographic plate is given by

$$X_o = 0.023\ f_o \qquad \ldots\ldots 7.6.1$$

where X_o is the maximum diameter of a specimen which contribute rays to the image and f_o is the objective focal length. The limiting aperture for the image is the bottom end of the 5mm inner diameter of the brass tube in the projection system. Figure 7.6.2 shows focused images of copper grids formed by the objective lens alone when used as a double and a single-pole lens for two different specimen positions, Z_o measured from the centre of the gap for the double-pole lens and from the surface of the snout for the single-pole lens. It can be seen that there is good agreement between the measured and the calculated field of view. It should be mentioned that the field of view of the image formed by the double-pole objective lens alone in this sytem is about four times greater than that of the EM6 microscope. This field of view is an advantage which is not met in commercial microscopes. with the snorkel objective the field of view is even larger.

The single and the double-pole lenses were capable of operating at 75kV where NI = 4500A-t for the former and 5200A-t for the latter. Under these imaging conditions, the resolving powers of the lenses, calculated from Equations 7.3.1 and 7.3.2 are 0.26nm for the double-pole objective and 0.32nm for the single-pole lens. This means that the resolution of the double-pole lens is only 20% better than that of the snorkel lens, although the latter is not a purpose-built snorkel objective lens. Therefore, high resolution can be obtained from a snorkel lens of good design. The maximum power consumed by the

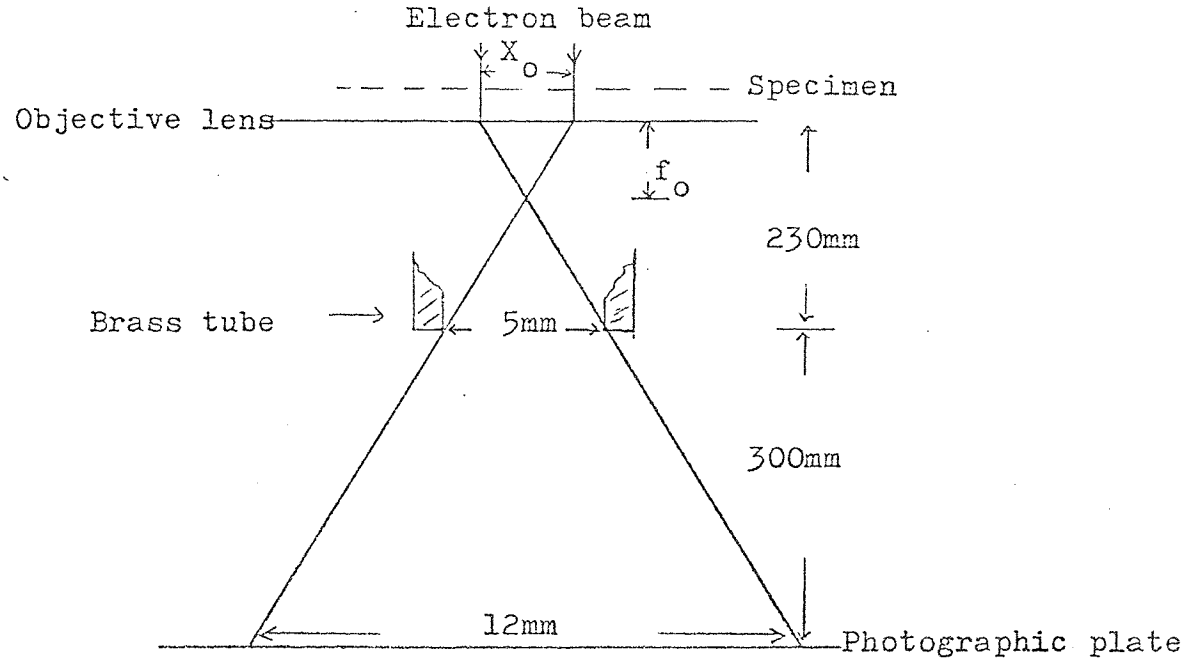

Fig. 7.6.1 The imaging of the miniature objective lens alone mounted in the miniature system.

Field of view
360μm measured (368μm calc.)

Field of view
290μm measured (288μm calc.)

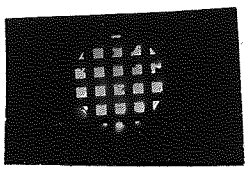

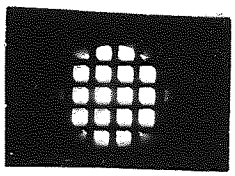

$NI/V_r^{\frac{1}{2}} = 11$, $Z_o = -2mm$
$f_o = 16mm$, $M = 33X$

$NI/V_r^{\frac{1}{2}} = 16$, $Z_o = 2.5mm$
$f_o = 12.5mm$, $M = 42X$

(a) Single-pole objective

Field of view
171μm measured (161μm calc.)

Field of view
60μm measured (64μm calc.)

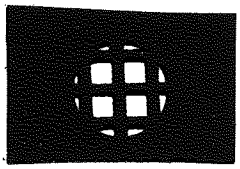

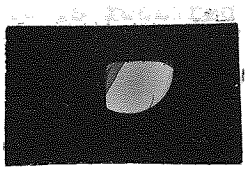

$NI/V_r^{\frac{1}{2}} = 7.7$, $Z_o = 5mm$
$f_o = 7mm$, $M = 70X$

$NI/V_r^{\frac{1}{2}} = 18.3$, $Z_o = 0.5mm$
$f_o = 2.8mm$, $M = 180X$

(b) double-pole objective

Fig. 7.6.2 Focused images formed by (a) the single-pole and (b) the double-pole objective lens.

objective lens was about 0.5kW which is ten times the power consumed by the original objective of the EM6 microscope but its volume is thirteen times smaller.

The focal properties of the double-pole objective lens as a function of the excitation parameter $NI/V_r^{\frac{1}{2}}$ are shown in Figure 7.6.3. It can be seen that there is a good agreement between the computed and the experimentally measured focal length and specimen position. However, Figure 7.6.4 shows that there is slight descrepancy between the computed and the measured values of f_o and Z_o; this could be caused by any experimental error in the measurement of the field distribution. At a distance Z_o = 2.5mm from the surface of the snout of the single-pole lens, the specimen was situated in the vicinity of the magnetic field and that the exponential segment of the field distribution was forming the image. For this same distance relative to the conical polepiece of the double-pole objective (i.e. Z_o = 0.5mm from the lens centre) most of the first half of the field acted as a pre-field condenser. Although the single-pole objective is not a purpose-built objective lens it gives a better performance than the double-pole one for a specific focal length. For instance, at a distance of 6mm below the surface of the polepiece ($NI/V_r^{\frac{1}{2}}$ = 18), the single-pole objective has f_o = 13mm, C_c = 8mm and C_s = 3.7mm. For the same focal length, the double-pole lens has C_c = 12mm and C_s = 77mm at $NI/V_r^{\frac{1}{2}}$ = 5. These figures indicate that the single-pole configuration is advantageous where it is required to have a large specimen or great freedom of movement.

In the imaging procedure of the whole microscope the miniature objective lens forms an image at the top end of the brass projection tube (5mm inner diameter) to be magnified by the intermediate projector doublet. In this distance (100mm) the magnification of the objective lens is $100/f_o$ which is also equal to $5/2r$, where r is the

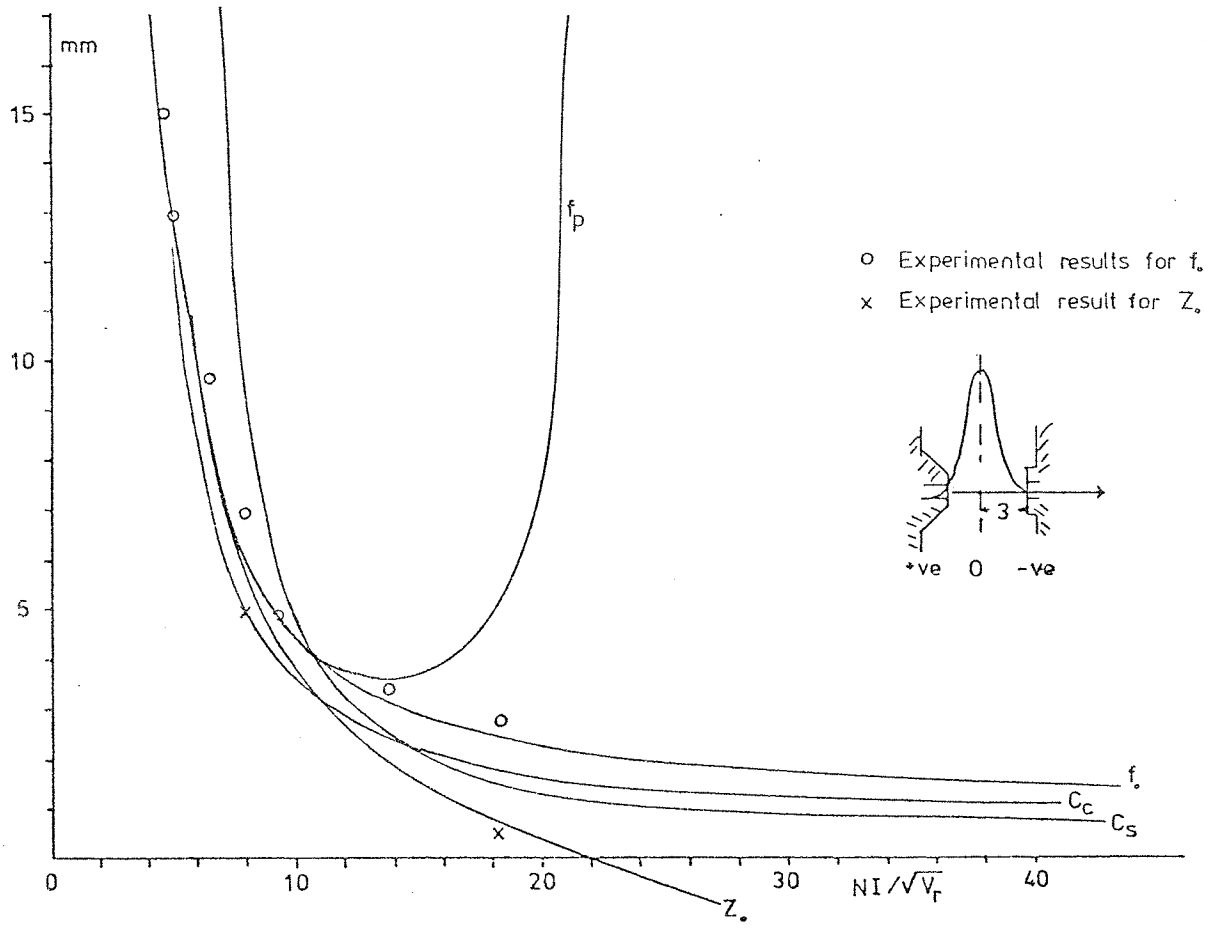

Fig. 7.6.3 Focal properties of the double-pole objective lens.

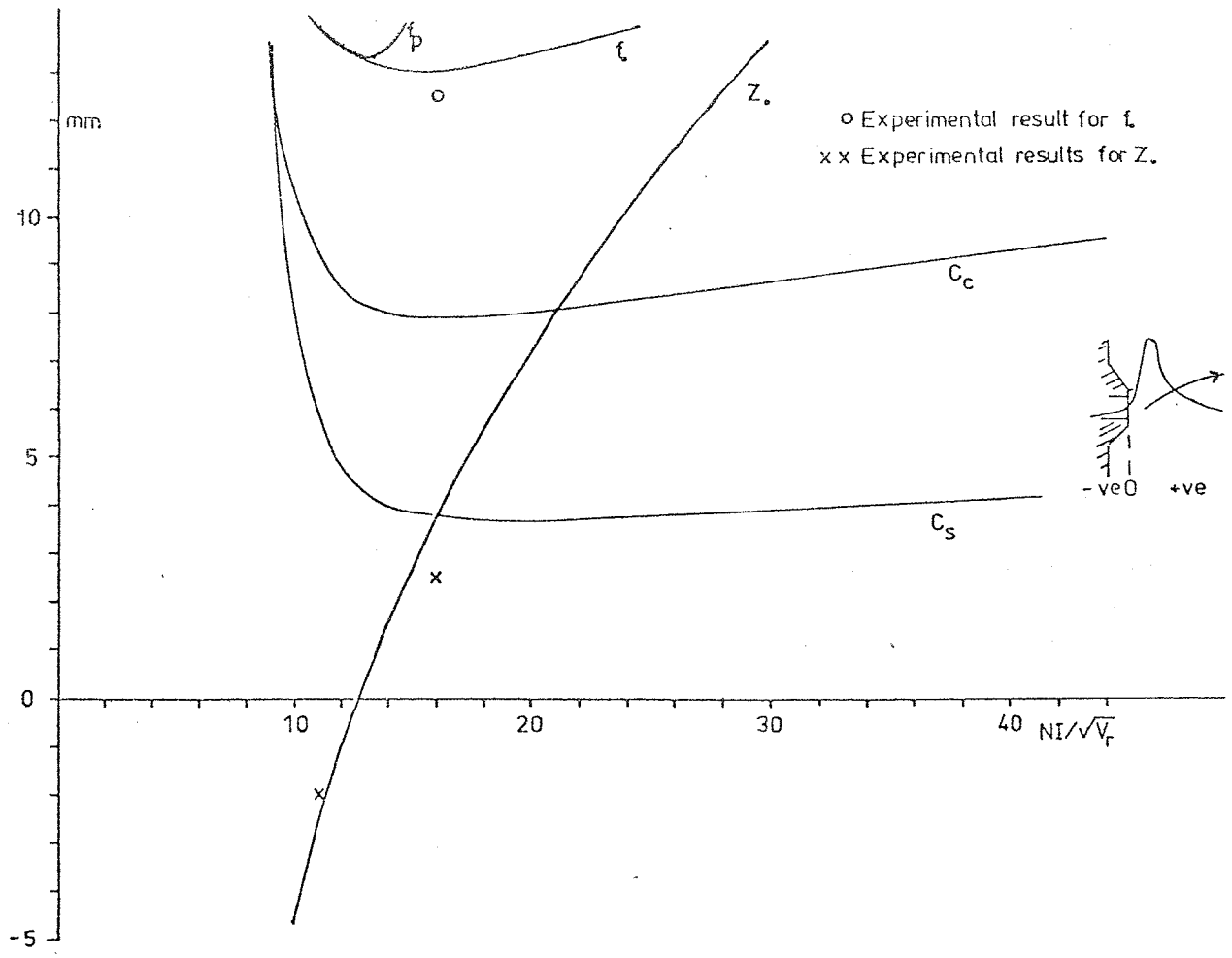

Fig. 7.6.4 Focal properties of the single-pole objective lens

radial displacement of the electron beam from the axis of the objective lens as the beam enters its magnetic field. Therefore, the radial and spiral distortions (Equations 1.5.4 and 1.5.6) in the intermediate image formed by the objective lens whose bore radius is 3mm are given by

$$\left(\frac{\Delta\rho}{\rho}\right)_{rad} = 7 \times 10^{-5} C_d f_o^2 \qquad \ldots\ldots 7.6.2A$$

$$\left(\frac{\Delta\rho}{\rho}\right)_{sp} = 7 \times 10^{-5} C_{sp} f_o^2 \qquad \ldots\ldots 7.6.2B$$

where f_o is in millimeters. Equations 7.6.2A and 7.6.2B show that the radial and spiral distortions of the objective lens are very small; e.g. when the focal length of the snorkel objective, f_o = 16mm at $NI/V_r^{\frac{1}{2}} = 11$, Figure 7.4.2 shows that $C_d = 0.08$ and $C_{sp} = 0.07$, hence

$$\left(\frac{\Delta\rho}{\rho}\right)_{rad} = 0.14\% \text{ and and } \left(\frac{\Delta\rho}{\rho}\right)_{sp} = 0.12\%$$

Similar remarkable low results are obtained for the double-pole objective lens. Hence, the radial and spiral distortions of the objective lens are negligible.

7.7 Conclusion

The miniature objective lens proved to be very successful. It is convertible to a double or a single-pole lens. To the author's knowledge, this experimental miniature objective lens is the first of its kind to be used in a microscope under practical conditions.

8. A MINIATURE ROTATION-FREE IMAGING SYSTEM

The assembly of the miniature objective lens, described in Chapter Seven, with the two miniature rotation-free lenses, described in Chapter Six, forms an entirely new rotation-free imaging system for a transmission electron microscope.

8.1 The miniature imaging system

The imaging system of the AEI EM6 electron microscope was replaced by the miniature rotation-free imaging system in order to evaluate the system under practical conditions of microscopy. Figure 8.1.1 shows the practical realization of the design. Figure 8.1.1a shows, for reference, the original imaging system consisting of objective lens, alignment section, intermediate and projector lens, viewing chamber, screen and camera. Figure 8.1.1b shows the projection system replaced by two identical 100kV single-pole rotation-free doublets each with an effective focal length of 2mm, mounted outside the vacuum system by means of a brass tube passing through the 8mm diameter lens bore. The objective lens and alignment section are supported on four iron pillars, allowing access to the projector doublets for alignment purposes. Because of the favourable distortion coefficients and magnification of the new lenses the column height was reduced by 13%. Figure 8.1.1c shows the complete column with miniaturized objective lens. The objective alignment section is not needed as both projector lenses can be aligned independently onto the axis of the objective. The objective lens is supported on a thick iron cylinder which provides magnetic screening and mechanical stability. The reduction in column height, measured from specimen to fluorescent screen, is about 30% with the magnification of the miniature imaging system being

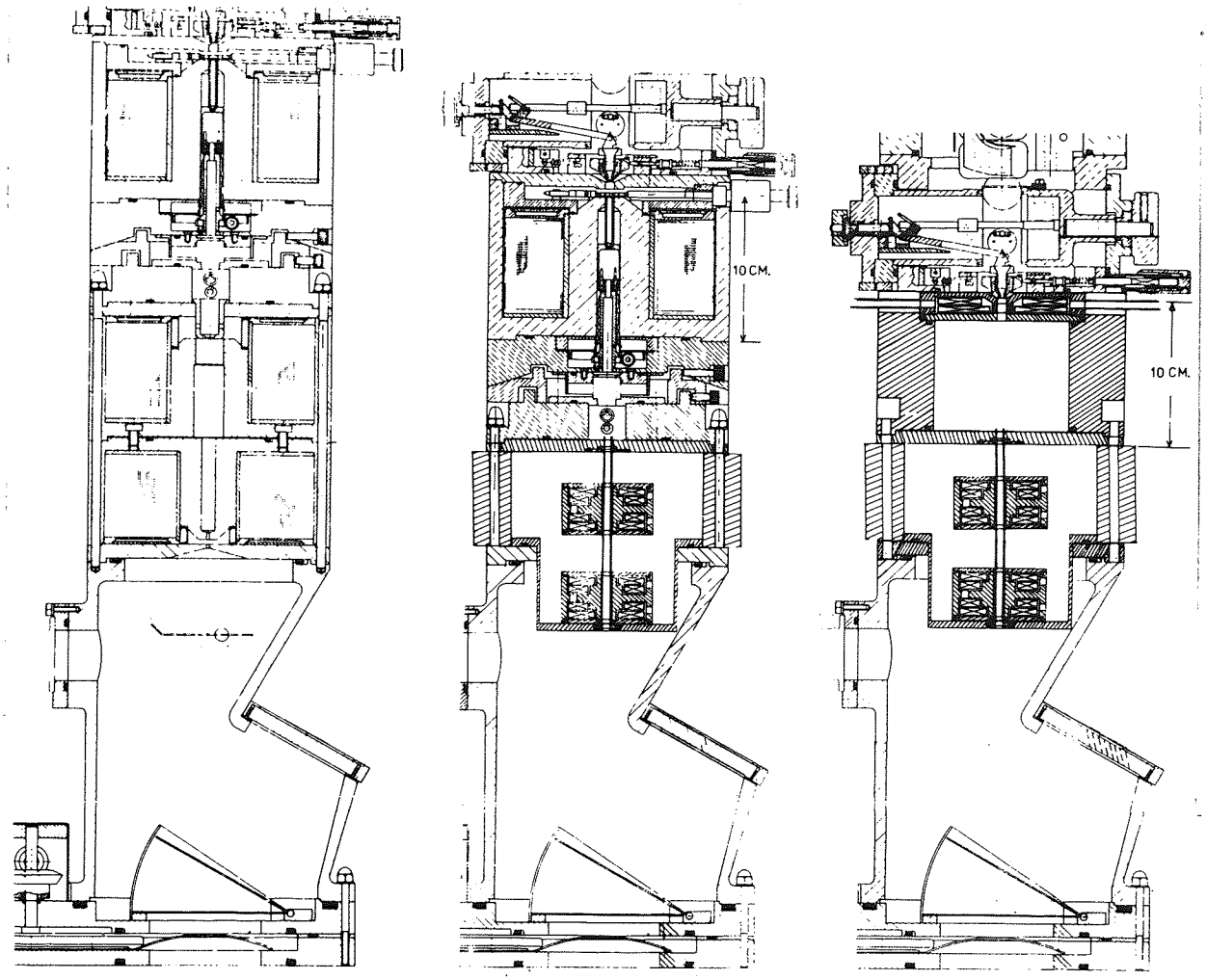

(a) Original imaging system of AEI EM6 electron microscope

(b) Miniature rotation-free projectors fitted

(c) Complete miniature imaging system

Fig. 8.1.1 Stages of development in the miniaturized imaging system of the EM6 electron microscope.

kept comparable to that of the original instrument (120,000 X). The importance of this reduction in the height of the electron optical column lies in the fact that the sensitivity of the column to stray magnetic fields falls with the square of the reduction in its height and that mechanical rigidity improves as the ratio of column-height to diameter is reduced; these two factors are especially relevant to high voltage microscopy. In fact, the reduction in column height if measured from specimen to the top of the viewing chamber is 50% where the two rods of the specimen shift control were reduced in length from 37cm to 19cm, Figures 8.1.2 and 8.1.3.

A close-up view of the miniature imaging system is shown in Figure 8.1.2. It shows the top entry specimen chamber placed on top of the objective lens which is hidden inside the thick iron cylinder. The second projector doublet is not shown because it is mounted on the brass cup which is placed inside the viewing chamber. The objective aperture was not placed in its correct position with respect to the miniature double-pole objective lens because it is impossible to insert it inside the structure of the water-cooled lens; but in spite of that it proved to be useful in improving the image contrast. The nearest distance that the aperture can be placed was 8mm below the bottom surface of the objective lens. However, this aperture position proved to be more useful in improving the contrast when the lens was converted into a single-pole objective lens of long focal length. Also the aperture holder can be used as a simple side entry specimen stage for a purpose-built single-pole objective lens.

A general view of the electron microscope with the miniature imaging system is shown in Figure 8.1.3. It is interesting to notice the reduction in size of the projector doublet when compared with the conventional double-condenser lens. The miniature objective lens and the two projector doublets were cooled by the original water-cooling

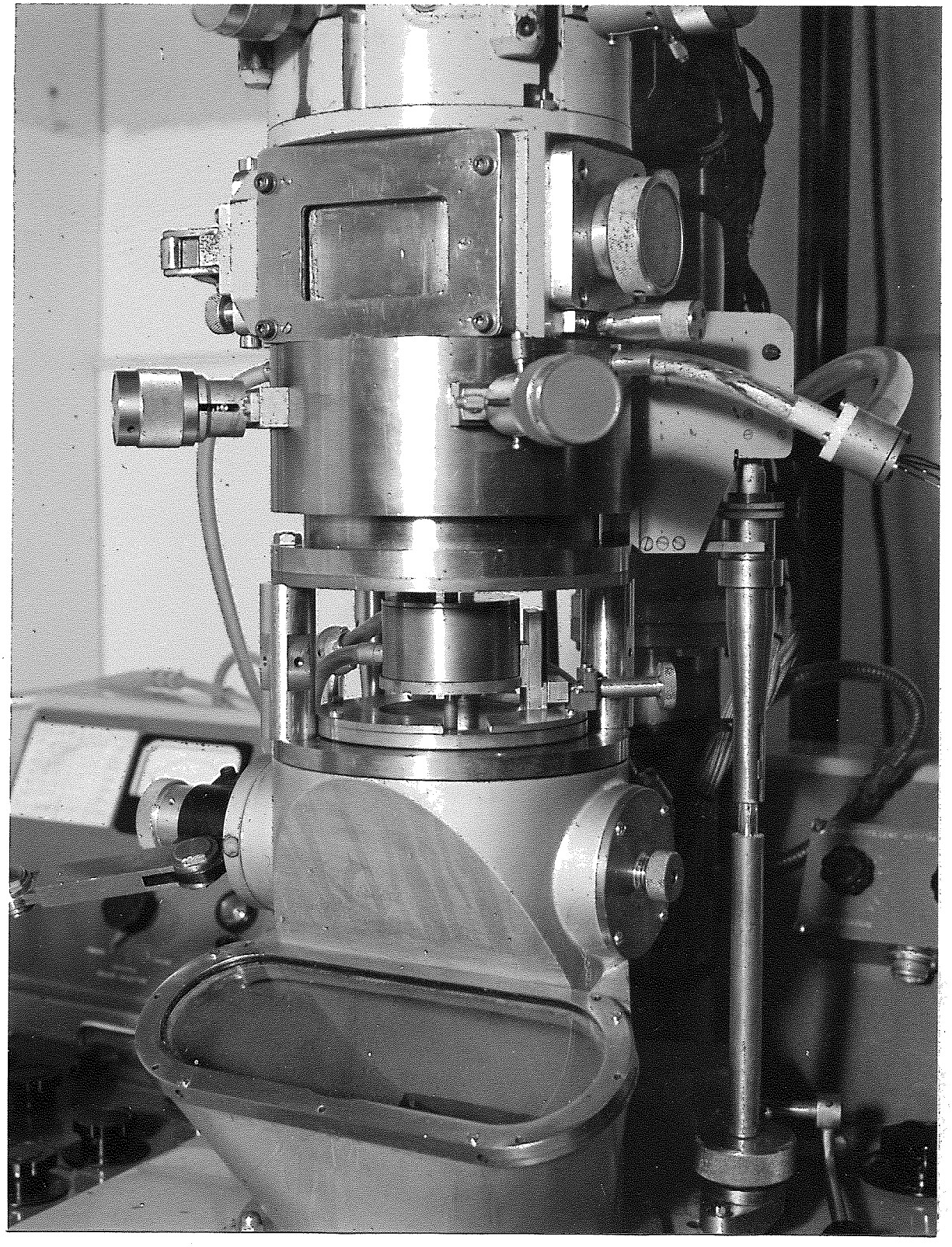

Fig.8.1.2 The miniature rotation-free imaging system. The final projector doublet is hidden by the viewing chamber (see Figure 8.1.1.C).

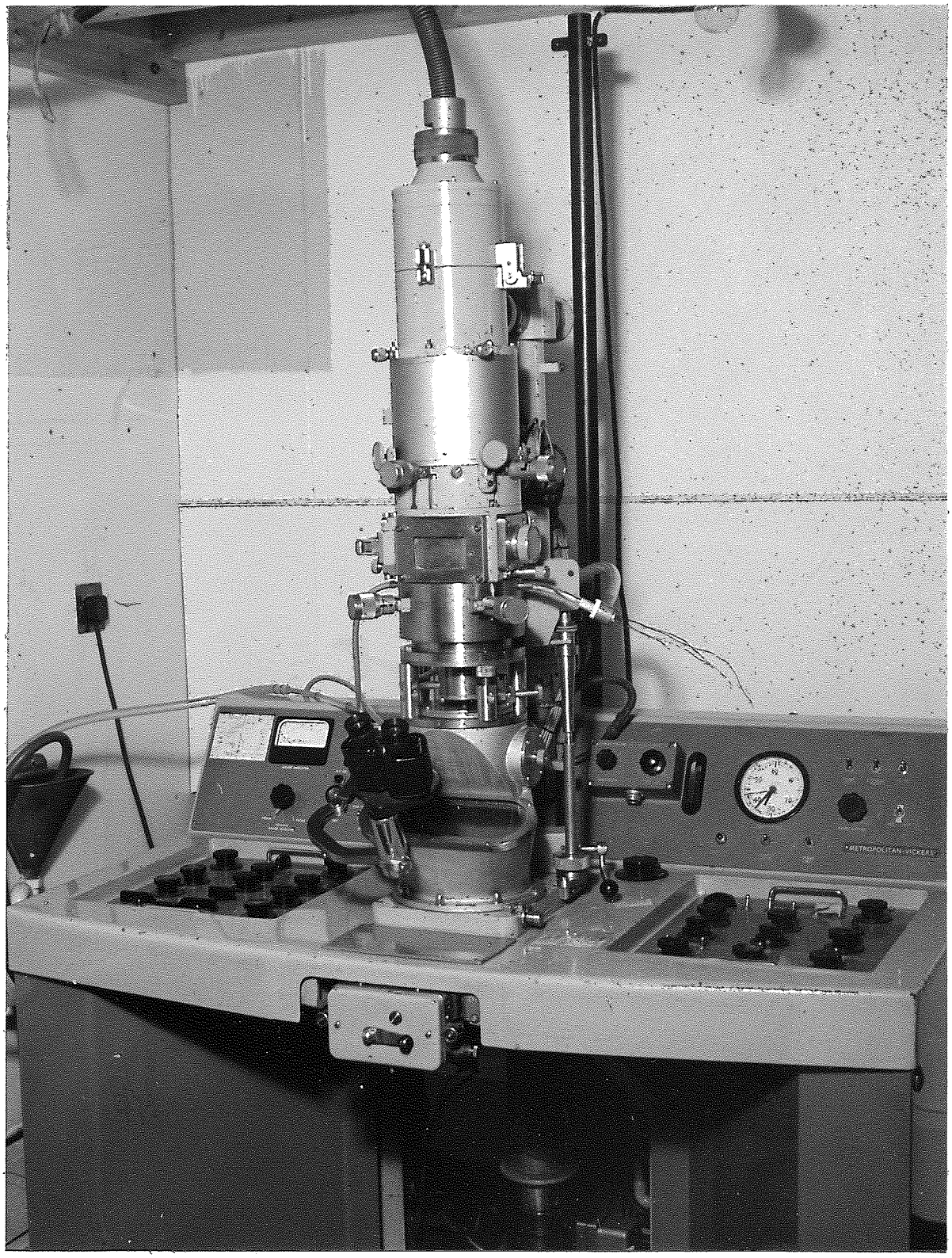

Fig.8.1.3 The experimental electron microscope with a miniature rotation-free imaging system.

system of the conventional objective, intermediate and projector lenses. The water-flow rate of slightly more than 1 litre/minute in each lens did not cause any mechanical vibration of the column and was completely adequate to extract the heat from the energised coils. The replacement of the original imaging system with the miniature one was carried out in such a way that the original microscope could aways be re-assembled easily.

The shape of the viewing chamber was designed by the manufacturers to suit the original performance of the microscope; it was found however that this shape distorted the magnetic flux of the bottom miniature lens of the second projector doublet which was deeply immersed in the viewing chamber. It was therefore found necessary to screen the bottom lens from the iron of the viewing chamber. Figure 8.1.4 shows a cross-section of the screening iron cylinder that was attached to the bottom of the brass cup where the second projector doublet was placed. The inner diameter of the cylinder did not limit the field of view on the photographic plate. The effect of this iron cylinder on the 8mm focal length of bottom single-pole lens was that it reduced it by 6% to 7.5mm as measured experimentally, due to the presence of the iron disc (76.2mm diameter) on the top end of the cylinder in front of the lens structure. This reduction in the focal length caused also an equivalent reduction in the effective focal length of the doublet; i.e. F_p = 1.88mm instead of 2mm. Hence the maximum magnification of the final projector doublet became 160X on the photographic plate.

Ideally, the projection system should also be screened from external fields; this is not usually done in commercial instruments. The shorter projection distance needed with the new lenses makes the column less sensitive to stray a.c. fields.

The miniature imaging system has the great merit of simplicity

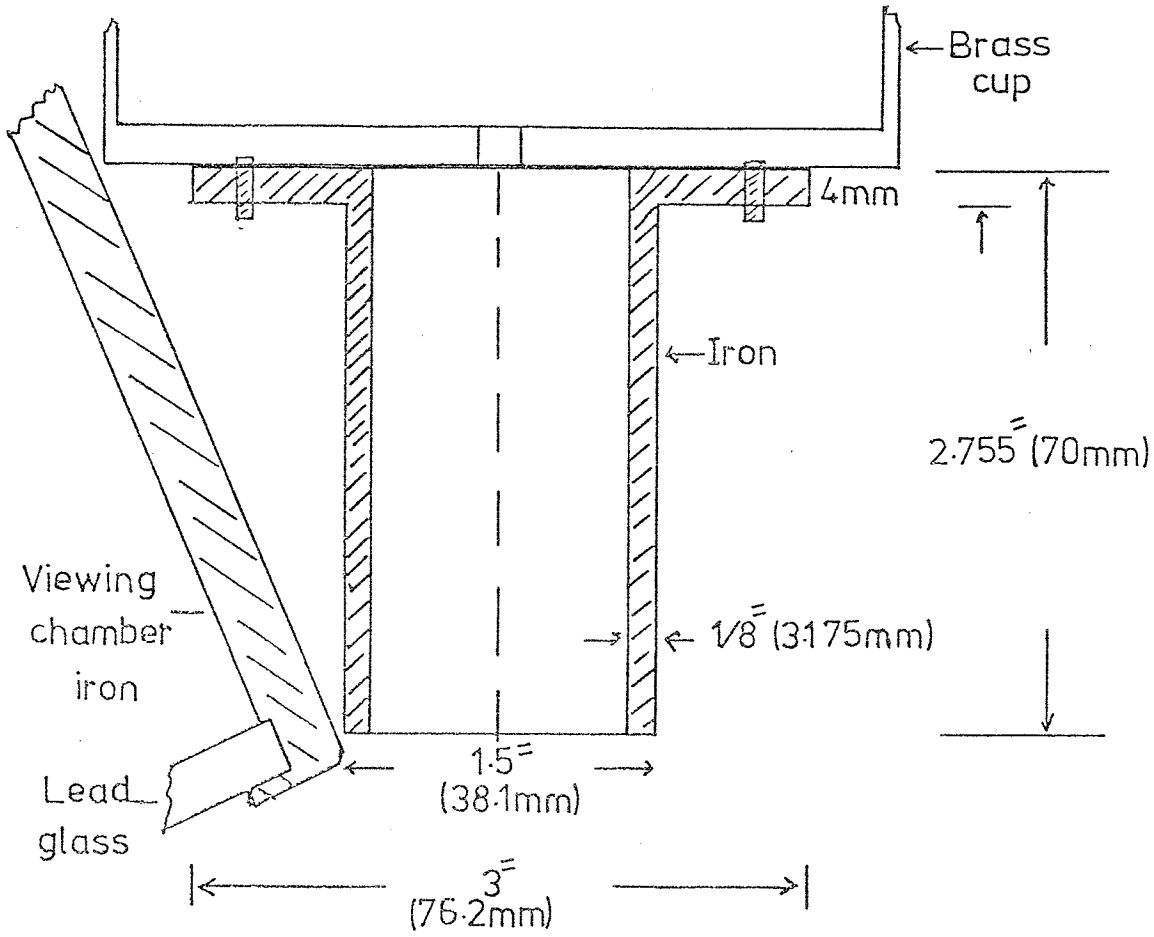

Fig. 8.1.4 Cross-section of the iron screening cylinder mounted on the bottom of the brass cup inside the viewing chamber.

of operation compared with a four lens conventional projector system since each doublet requires only one current supply. Since the projector doublets are under atmospheric pressure, they were easy to align. For most experiments with the imaging system the electron microscope was operated without the condenser lenses; a 20 μm aperture in the condenser aperture holder through which a parallel beam of electrons from the filament was passed was used where necessary to restrict the area of specimen illuminated.

8.2 Electron-optical properties of a two-stage rotation-free imaging system

An objective lens and one projector doublet are considered to constitute a two-stage, rotation-free imaging system. The two single lenses of the projector doublet are assumed thin and identical with equal projector focal lengths, f_p and separated by the distance between their magnetic flux peaks, Figure 8.2.1. The magnification and diffraction in such an imaging system are considered theoretically and experimentally where the derived mathematical equations are applicable to both single-pole and double-pole lenses.

Magnification of a two-stage rotation-free imaging system

Considering the imaging ray path through the objective lens of focal length, f_o and the projector doublet, Figure 8.2.1, it has been shown in Appendix IXA that the magnification, M of this system is given by

$$M = \frac{1}{f_o}\left\{(L_1+L_2+L_3) - \frac{1}{f_p}(L_1L_2+2L_1L_3+L_2L_3) + \frac{L_1L_2L_3}{f_p^2}\right\} \quad \ldots\ldots 8.2.1$$

Equation 8.2.1 shows that:

(a) when the projector doublet is not energised ($I_p=0$) i.e. f_p is infinite, the magnification of the system is simply that of the objective lens only given by $(L_1+L_2+L_3)/f_o$;

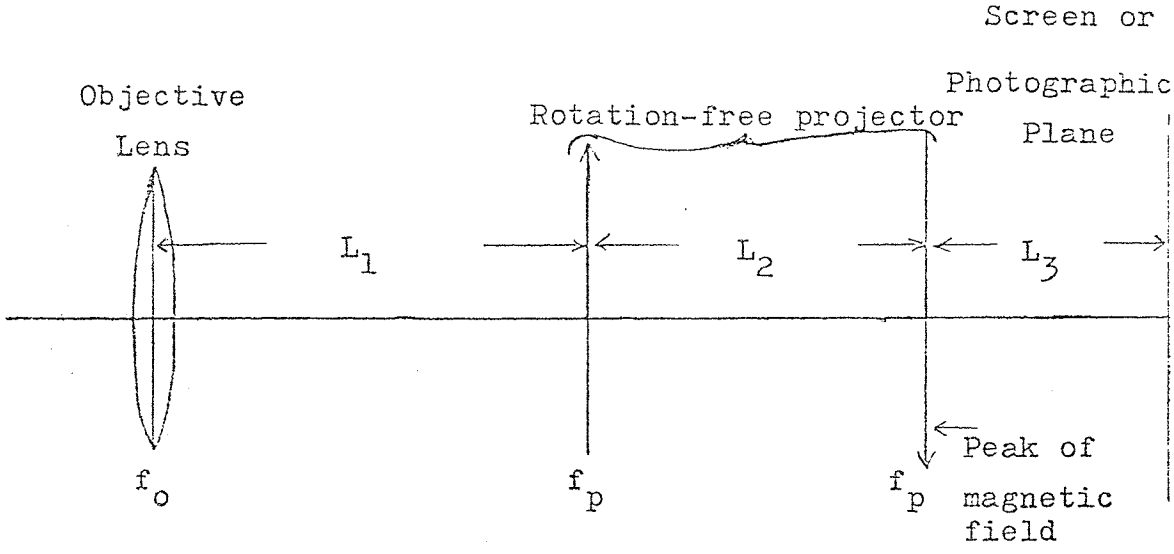

Fig. 8.2.1 Illustration of a two-stage rotation-free imaging system.

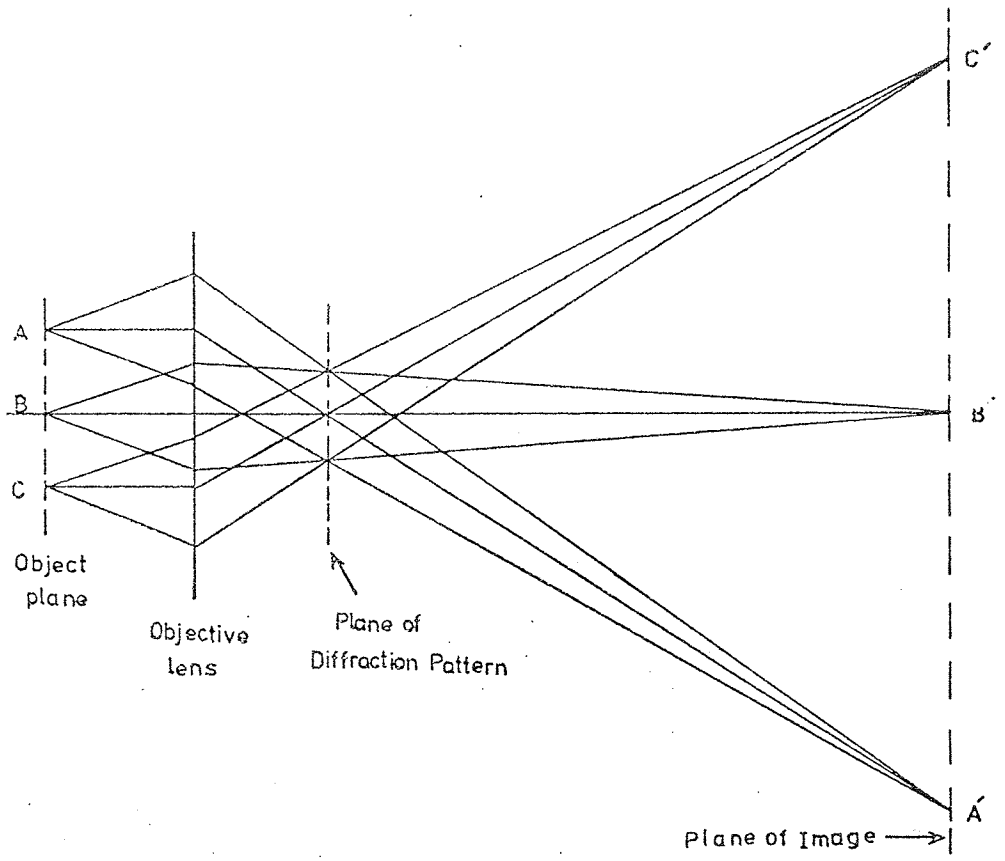

Fig. 8.2.2 Formation of image and diffraction pattern by the objective lens.

(b) when the magnification of the whole system is maximum, i.e. when f_p has a small minimum value, the result of the term

$$\left\{ \frac{(L_1+L_2+L_3)}{f_o} - \frac{1}{f_p f_o} (L_1L_2+2L_1L_3+L_2L_3) \right\}^2$$ is very small compared with the term $L_1L_2L_3/f_o f_p^{\,2}$; thus the maximum magnification of the system will be

$$(M)_{max\ 2} \simeq \frac{L_1L_2L_3}{f_o\, f_p^{\,2}} \qquad \ldots\ldots 8.2.2$$

which is simply the product of the maximum magnifications of the three single lenses;

(c) if the magnification M is differentiated with respect to f_p for maximum and minimum, there will be a value for f_p given by

$$f_p = 2L_1L_2L_3/(L_1L_2+L_2L_3+2L_1L_3) \qquad \ldots\ldots 8.2.3$$

at which the magnification will be maximum; i.e.

$$(M)_{max\ 1} = \frac{1}{f_o} \left\{ (L_1+L_2+L_3) - \frac{(L_1L_2+2L_1L_3+L_2L_3)^2}{4L_1L_2L_3} \right\} \qquad \ldots\ldots 8.2.4A$$

when f_p in Equation 8.2.3 is substituted in Equation 8.2.1. Usually L_2 is very small compared with L_1 and L_3. Therefore, the products L_1L_2 and L_2L_3 are small compared with $2L_1L_3$ in Equation 8.2.3. Hence the projector focal length f_p of each lens of the doublet is approximately L_2 when the system is at its first maximum magnification. In fact, f_p is slightly smaller than L_2; however, this means that f_p is independent of L_1 and L_3. In Equation 8.2.4A, the term $(L_1L_2+2L_1L_3+L_2L_3)^2/4L_1L_2L_3$ is always greater than $(L_1+L_2+L_3)$; therefore, the value of $(M)_{max\ 1}$ is always negative which means that the image is inverted. To a good approximation, the first maximum magnification of a two-stage rotation-free imaging system can be

written as,

$$(M)_{max\ 1} \simeq \frac{1}{f_o}\left(\frac{L_1 L_3}{L_2}\right) \qquad \ldots\ldots 8.2.4B$$

Equation 8.2.4B is simply the product of the magnifications of the objective lens (L_1/f_o) and first lens of the doublet (L_3/L_2) since $f_p \simeq L_2$ in this case. The second lens of the doublet does not contribute to the magnification of the system but it corrects the distortion of the first lens, since under this condition of focal length it is situated in the back focal plane of the first. Thus the first magnification will be distortion-free.

Diffraction in a two-stage rotation-free imaging system

The diffraction pattern from a crystalline specimen is formed at the back focal plane of the objective lens when the illumination on the object is parallel. Figure 8.2.2 shows the formation of the first image and the diffraction pattern by the objective lens, neglecting rotation due to the objective which acts equally on both image and diffraction pattern since they both experience the same field in the objective lens. The image formed by the objective lens is inverted relative to the object but the diffraction pattern in the back focal plane of the objective lens is erect with respect to the object. Subsequent lenses of the microscope produce equal numbers of inversions of the first image and the diffraction pattern.

In a two-stage rotation-free imaging system, it can be shown (Appendix IX B), that the projector doublet can project the diffraction pattern in the back focal plane of the objective at two different excitations. At diffraction, the two focal lengths of each lens of the doublet are given by

$$(f_p)_{diff} = \frac{(L_1L_2+2L_1L_3+L_2L_3) \pm \sqrt{(L_1L_2+2L_1L_3+L_2L_3)^2 - 4L_1L_2L_3(L_1+L_2+L_3)}}{2\,(L_1+L_2+L_3)}$$

..... 8.2.5

The first diffraction pattern is obtained at a weak excitation where $(f_p)_{diff}$ is long i.e. the two terms in the numerator of Equation 8.2.5 are added, and the second diffraction pattern is projected when $(f_p)_{diff}$ is short at a higher excitation where the numerator will be the difference between the two terms. Equation 8.2.5 shows that $(f_p)_{diff}$ depends on the projection distance L_3 which will have an effect on the focusing of the diffraction pattern. However this same equation can also be derived from Equation 8.2.1 when the magnification, M = 0 at diffraction.

It can also be shown (Appendix IX B) that a diffraction spot in the back focal plane of the objective lens will be magnified on the screen (or photographic plate) by an amount given by

$$(M)_{diff} = 1 - \frac{(L_2+2L_3)}{(f_p)_{diff}} + \frac{L_2L_3}{(f_p)^2_{diff}} \qquad \text{..... 8.2.6}$$

Since there are two different values for $(f_p)_{diff}$ given by Equation 8.2.5, the two diffraction patterns will be of different magnifications as shown in Equation 8.2.6. It can be seen that Equation 8.2.6 is independent of the objective focal length; hence the magnification of the diffraction pattern is independent of the specimen position. This means that at the same current in the projector doublet, diffraction patterns will be obtained with different specimen holders. When the projector doublet is weakly excited, f_p will be long; thus, the term L_2L_3/f_p^2 in Equation 8.2.6 will be very small, and the term $(L_2+2L_3)/f_p$ will be the dominant one which gives a negative value for the magnification. This negative value means that the first projected

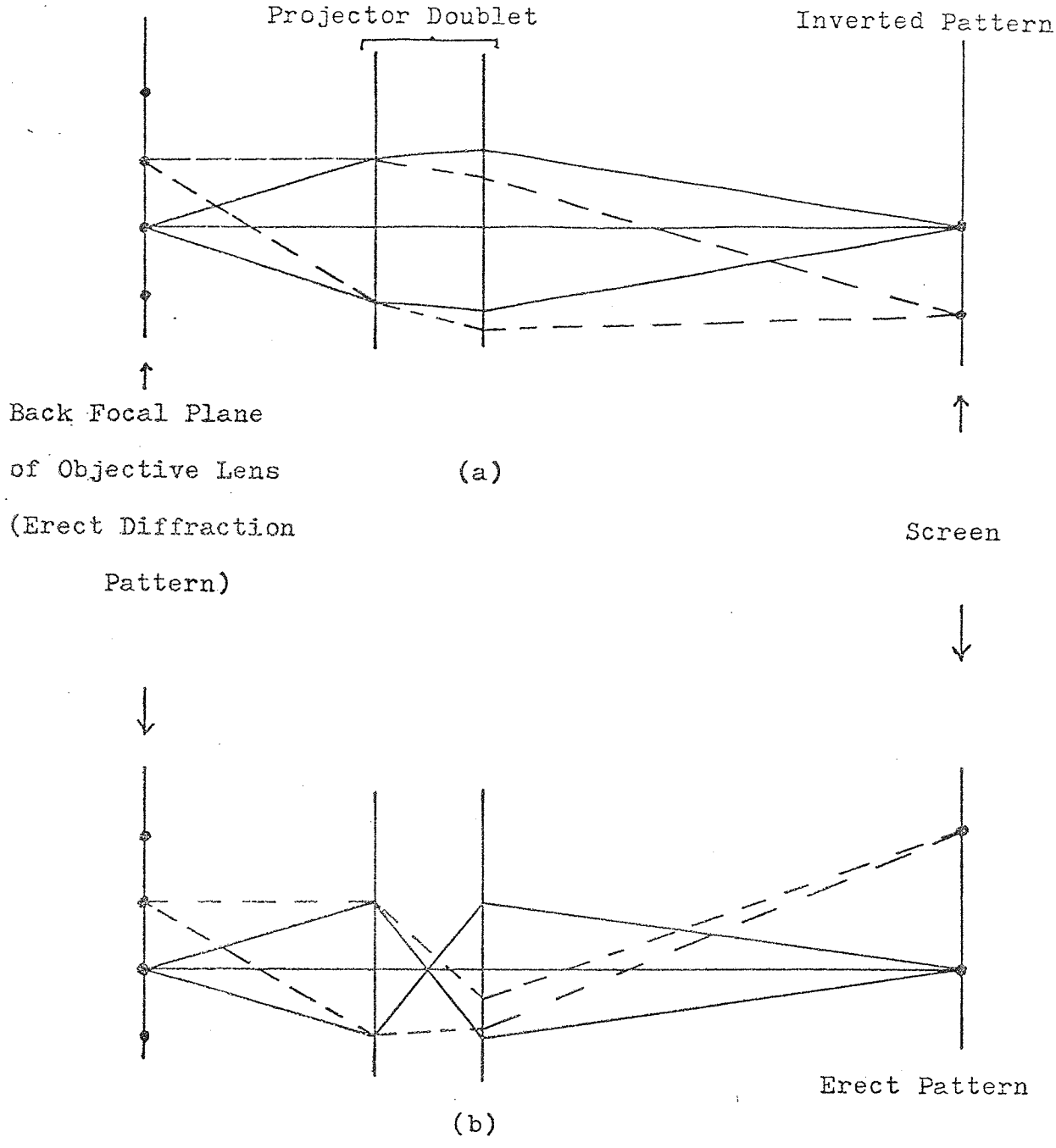

Fig. 8.2.3 Projection of the diffraction pattern formed at the back focal plane of the objective lens in a two-stage rotation-free imaging system,

(a) inverted first diffraction at weak projector doublet and

(b) erect second diffraction at strong projector doublet. The magnification in (b) is higher than that in (a).

diffraction pattern is inverted as shown by the ray diagram in Figure 8.2.3a. The second diffraction pattern will be projected when the lens is stronger and of shorter focal length, where in this case the term L_2L_3/f_p^2 will be the dominant one and hence the value of the diffraction magnification will be positive. This means that the second projected diffraction pattern will be erect as shown by the ray diagram in Figure 8.2.3b.

Performance of a two-stage rotation-free imaging system

Consider the objective lens and the first projector doublet (Figures 8.1.1c, 8.1.2). These two lenses constitute a rotation-free imaging system with the parameters L_1. L_1 and L_3 shown in Figure 8.2.1 are 100mm, 37mm and 400mm respectively; i.e. the height of this imaging system is 537mm measured from the specimen to the photographic plate. With the double-pole objective lens, the imaging system had the magnification characteristics for two different objective focal lengths, (i.e. two different specimen positions) as shown in Figure 8.2.4 when the excitation of the projector doublet was varied from zero to $NI/V_r^{\frac{1}{2}} = 16$ at 75kV.

The experiment has verified the theoretically predicted results on diffraction. As the excitation of the projector doublet was increased from zero, two diffraction pattern are obtained at $NI/V_r^{\frac{1}{2}} = 3$ and 7.5 for both objective focal lengths, showing that the diffraction excitation is independent of the objective focal length. The first diffraction, Figure 8.2.5a, was inverted and the second was erect; this was verified by imaging a copper grid with an arrow, placed in the objective aperture. The projector focal lengths of each lens of the doublet at diffraction as calculated from Equation 8.2.5 are 167mm for a weak lens and 16.5mm for a strong lens. These two values are in very good agreement with the experimentally measured focal lengths at $NI/V_r^{\frac{1}{2}} = 3$ and 7.5 shown in Figure 6.5.3. It can be

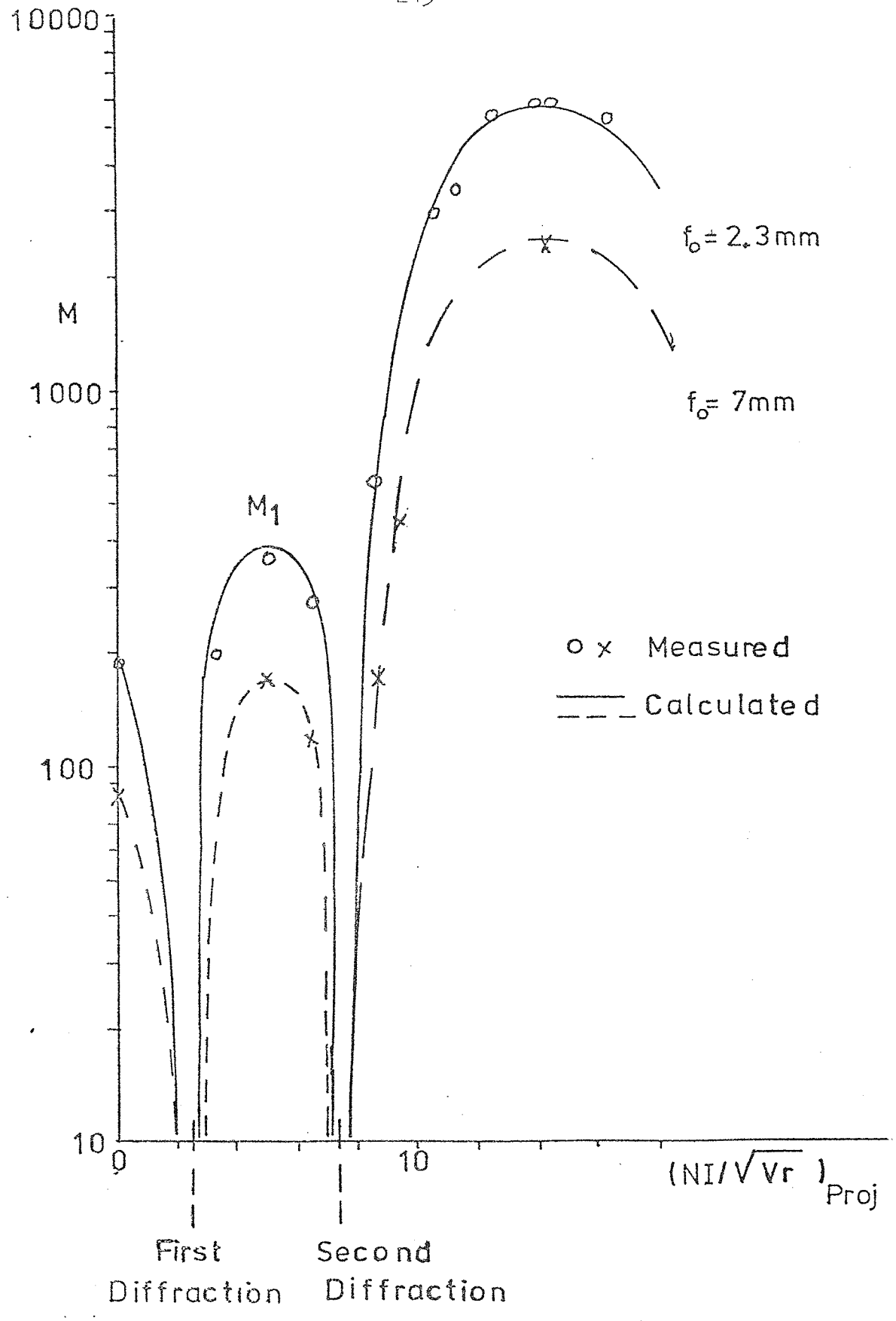

Fig 8.2.4 Magnification characteristics of the two-stage rotation-free imaging system for two objective focal lengths.

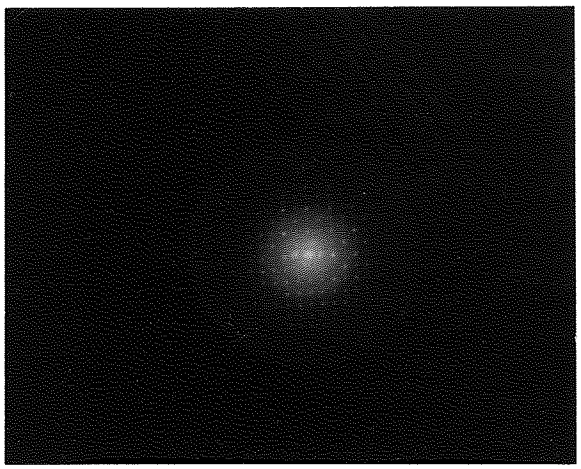

(a) $NI/V_r^{\frac{1}{2}}$ 3

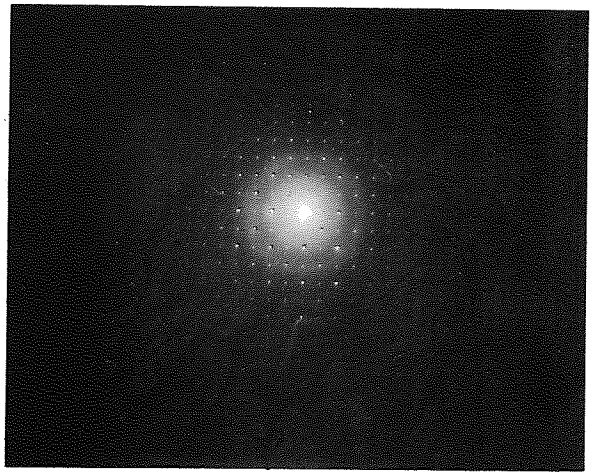

(b) $NI/V_r^{\frac{1}{2}}$ 7.5

Fig. 8.2.5 Two enlarged diffraction patterns of a molybdenum trioxide crystal, in a two-stage rotation-free imaging system.

Fig. 8.2.6

Enlarged first maximum magnification in a two-stage rotation-free imaging system. $f_o = 7mm$, $(NI/V_r^{\frac{1}{2}})_{proj} = 5$, M = 170X, field of view = 150μm.

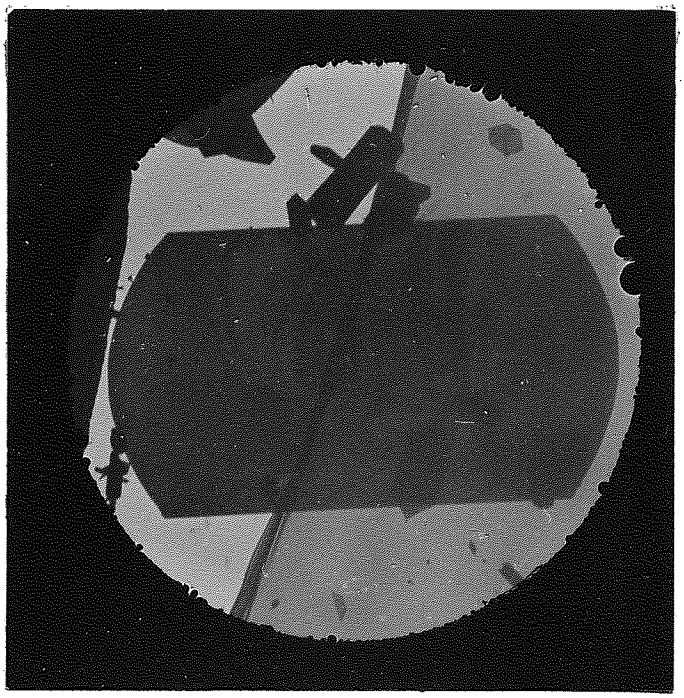

Fig. 8.2.7

Enlarged second maximum magnification in a two-stage rotation-free imaging system. $f_o = 7mm$, $(NI/V_r^{\frac{1}{2}})_{proj} = 14.5$, M = 2500X, field of view = 10μm.

seen that the first diffraction focal length is ten times higher than that of the second. As a weak doublet, its effective focal length at diffraction is 92mm as calculated from the equations $\frac{1}{F_p} = \frac{1}{u} + \frac{1}{v}$ and $\frac{1}{F_p} = \frac{2}{f_p} - \frac{L_2}{f_p^2}$. As a strong doublet, its effective focal length at diffraction is 68mm. The magnification of the first and second diffraction patterns as calculated from Equation 8.2.6 are 4 X and 5.7X respectively, i.e. the ratio of the second to that of the first is 1.43. Experimentally, the ratio of the second magnification to that of the first is 1.5, Figure 8.2.5, which agrees within 5% accuracy with theory. A similar ratio of magnifications at the same excitations was obtained when the double-pole objective lens was converted to a single-pole one of 16mm focal length showing that this ratio is independent of the objective focal length. The diffraction pattern is focused when it is free from any distortion where the barrel distortion of one lens is corrected by the pin-cushion distortion of the other.

Figure 8.2.4 shows two magnification loops which are in good agreement with that calculated from Equation 8.2.1 for two objective focal lengths. It can be seen that the projector doublet excitations at which the two maximum magnifications occur are independent of the objective focal length. The projector focal length of each unit of the doublet at which the first maximum magnification occurs is 32mm as calculated from Equation 8.2.3 and verified experimentally. This value of focal length is of the order of magnitude of the separation (31mm) of the snouts and that of the peaks (37mm). The image at the first maximum magnification is distortion-free and of large field of view (Figure 8.2.6) although limited by the projection brass tube, it is also inverted with respect to the image formed by the objective lens and since the objective image is itself inverted with respect to the object plane, the image at first magnification is erect with respect

to the object plane. The second maximum magnification is shown in Figure 8.2.7 where the highly magnified image is inverted relative to the object plane and with a small field of view. The ratio of the two maximum magnifications is 15:1 at different objective focal lengths which gives a wide range of magnifications of images with very low distortion. It should be mentioned that the projector-doublet forms images with barrel distortion in the range of excitations between zero and that near the first diffraction pattern. Between the first diffraction pattern and the first maximum magnification, the images suffer from pin-cushion distortion which then changes to barrel distortion for excitations between the first maximum and second diffraction pattern. From the second diffraction pattern to the second maximum magnification there was pin-cushion distortion which decreased with increase of excitation. The distortion of the doublet can therefore be corrected by an opposing distortion from another doublet as will be shown later.

The results shown in Figure 8.2.4 verify the theory on the magnification and diffraction in a two-stage rotation-free imaging system. Therefore, the projector doublet and the objective lens form a microscope of three single lenses which produces rotation-free images and diffraction patterns.

When the objective lens and the second projector doublet, Figure 8.1.1c, were used to form a two-stage rotation-free imaging system, the second maximum magnification was about 7000X at a 2.8mm focal length of the objective lens. However, because the projector doublet was nearly halfway between the objective lens and the photographic plate (L_1=270mm and L_3=300mm), the calculated magnification of the first and second diffraction patterns are 1.14X and 1.18X respectively, which were difficult to photograph in practice. At diffraction, the calculated projector focal lengths of

each unit of the doublet are 284mm at weak excitations and 17.4mm at higher excitations. The two maximum magnifications and the two diffraction patterns ocurred at the same excitations as those shown in Figure 8.2.4.

8.3 Electron-optical properties of a three-stage rotation-free imaging system

A three-stage rotation-free imaging system consists of an objective lens and two projector doublets (Figure 8.3.1). It can be shown (Appendix X) that the total image magnification of this system is given by

$$M = \frac{1}{f_o}\Big\{(L_1+L_2+L_3+L_4+L_5) - \frac{1}{f_{p_1}}\Big[2L_1(L_3+L_4+L_5) + L_1(L_2+L_3+L_4+L_5)\Big] +$$

$$\frac{1}{f_{p_1}^2}\Big[L_1L_2(L_3+L_4+L_5)\Big] - \frac{1}{f_{p_2}}\Big[2L_5(L_1+L_2+L_3+L_4) + L_4(L_1+L_2+L_3)\Big] +$$

$$\frac{1}{f_{p_2}^2}\Big[L_4L_5(L_1+L_2+L_3)\Big] + \frac{1}{f_{p_1}f_{p_2}}\Big[2L_1L_3L_4 + 2L_1L_2L_5 + 2L_1L_4L_5 + 4L_1L_3L_5 +$$

$$2L_2L_3L_5 + L_2L_3L_4 + L_1L_2L_4 + L_2L_4L_5\Big] - \frac{1}{f_{p_1}f_{p_2}}\Big[\frac{(L_1L_2L_3L_4 + 2L_1L_2L_3L_5 + L_1L_2L_4L_5)}{f_{p_1}} +$$

$$\frac{(L_1L_2L_4L_5 + 2L_1L_3L_4L_5 + L_2L_3L_4L_5)}{f_{p_2}}\Big] + \frac{L_1L_2L_3L_4L_5}{f_{p_1}^2 f_{p_2}^2}\Big\} \qquad \ldots\ldots 8.3.1$$

This expression for the magnification is applicable to all kinds of magnetic lenses which constitute a three-stage rotation-free imaging system. Equation 8.3.1 shows that when the projector doublets are not excited, the magnification of the system will be simply that of the objective lens only, given by $(L_1+L_2+L_3+L_4+L_5)/f_o$. When the projector doublets are at their minimum focal lengths the maximum magnification of the system is approximately given by

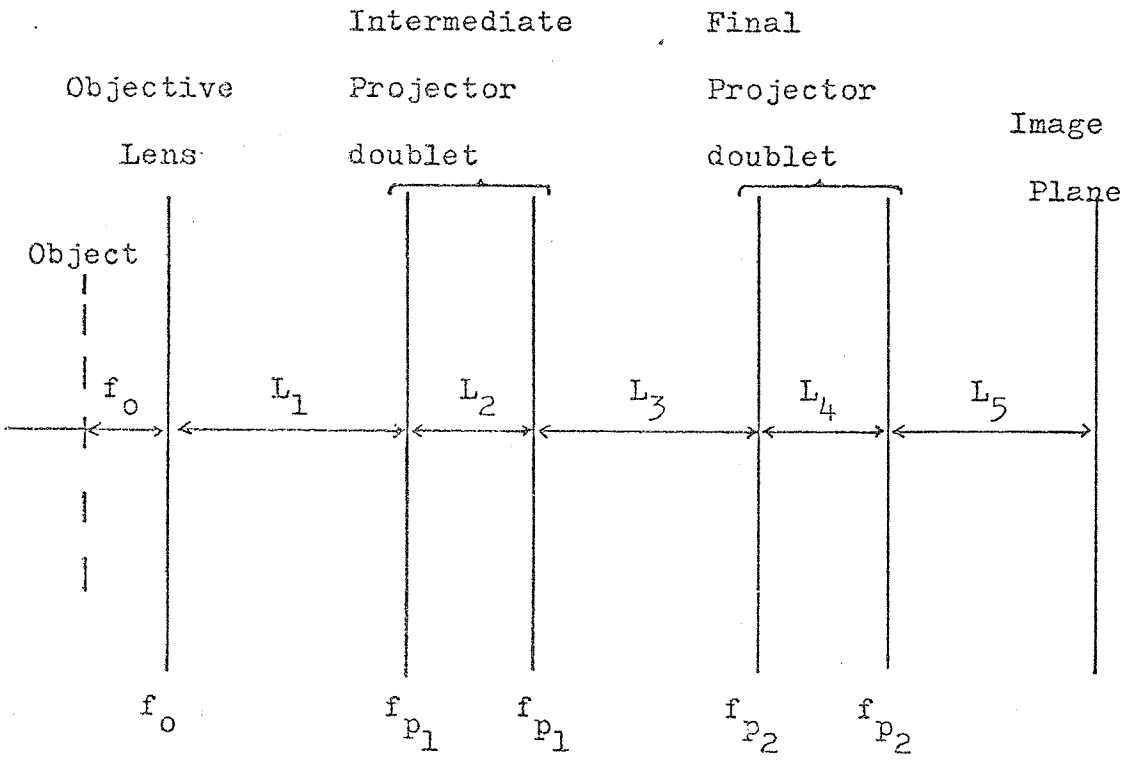

Fig. 8.3.1 Principal planes of the elements of a three-stage rotation-free imaging system.

$$(M)_{max} \simeq \frac{L_1 L_2 L_3 L_4 L_5}{f_o f_{p_1}^2 f_{p_2}^2}$$

which is the product of the magnifications of all units.

In the rotation-free imaging system shown in Figures 8.1.1c and 8.1.2, the two projector doublets are identical, hence, $L_2 = L_4 = \ell$ and $(f_{p_1})_{min} = (f_{p_2})_{min}$. Therefore, the maximum magnification of this system is approximately $L_1 L_3 L_5 \ell^2 / f_o (f_p)^4_{min}$. In the usual operation of the microscope, the objective lens and the final projector doublet were excited to give maximum magnification of a two stage system. The magnification of the whole three-stage system was varied by varying the excitation of the intermediate doublet. Figure 8.3.2 shows the magnification characteristics of the three-stage rotation-free imaging system for a 2.8mm focal length of the double-pole objective lens. It can be seen that the second maximum magnification (115000X) is comparable to that of the original imaging system of the EM6 microscope and it is in a very good agreement with that calculated from Equation 8.3.1. The ratio of the two maximum magnifications is 24:1 where the first maximum distortion-free image has a useful low value of magnification of about 5000X. The system has shown rotation-free images at all excitations (Figure 8.3.3) with good alignment (Figure 8.3.4).

Similar to the two-stage system, the three-stage rotation-free imaging system produced two diffraction patterns at different excitations of the intermediate doublet. The first and second diffraction pattern occurred when the excitation parameter $NI/V_r^{\frac{1}{2}}$ of the intermediate doublet was equal to 3 and 7.8 respectively, Figure 8.3.2, the final projector doublet being at its maximum magnification. These two diffraction excitations are higher than those in a two-stage system; however. The first inverted

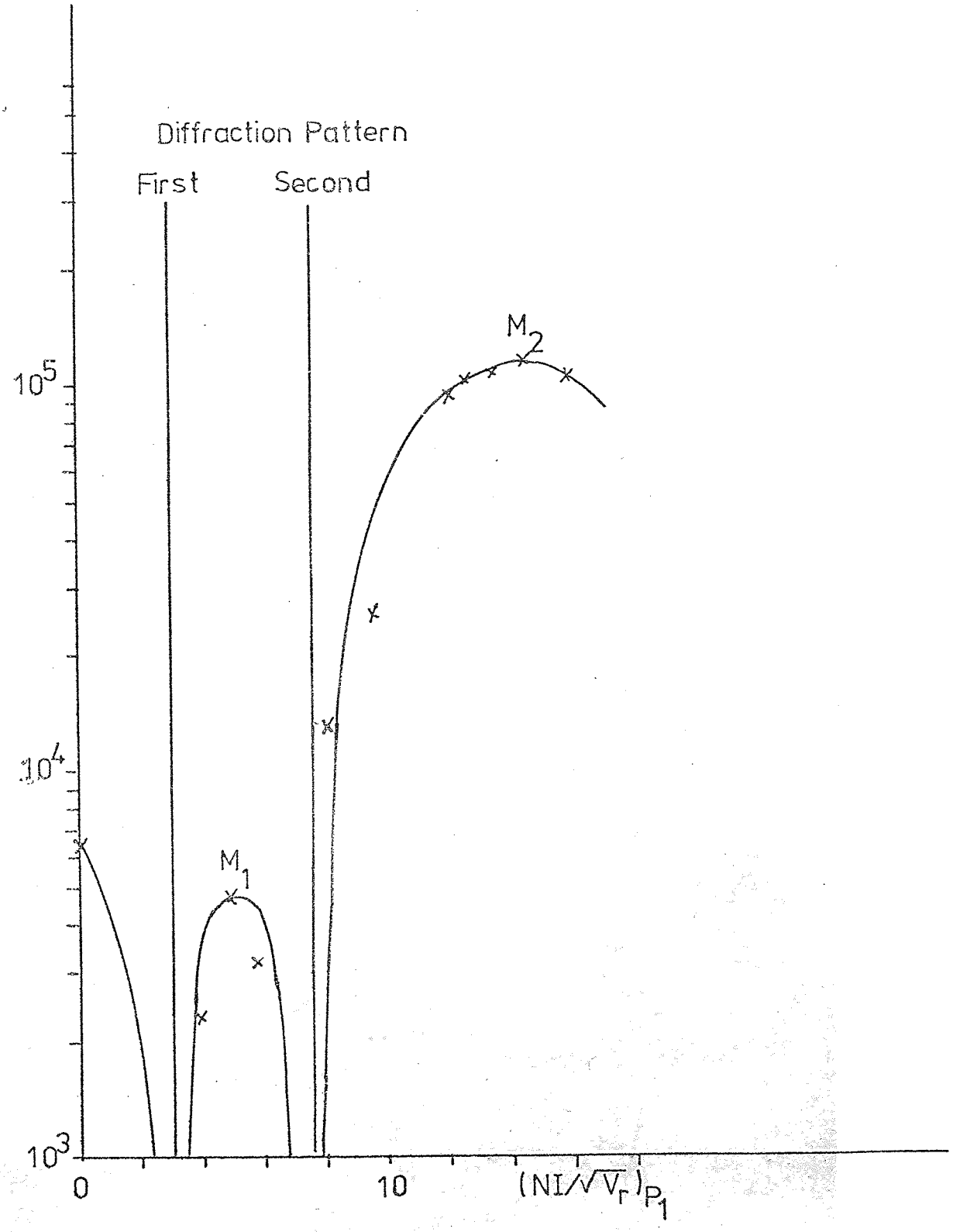

Fig. 8.3.2 Variation of the magnification of the three-stage rotation-free system with the excitation of the first projector doublet. The second projector doublet is held at its maximum magnification ($f_o = 2.8$mm).

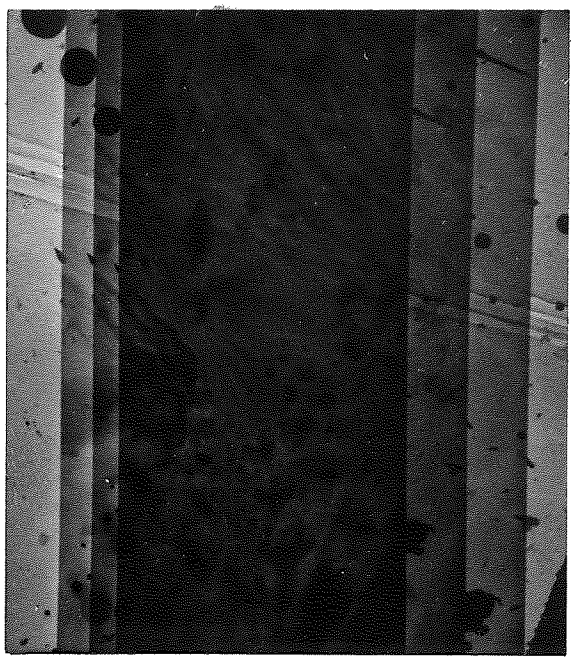

Fig. 8.3.3 Superimposed "zoom" rotation-free images of molybdenum trioxide crystal.

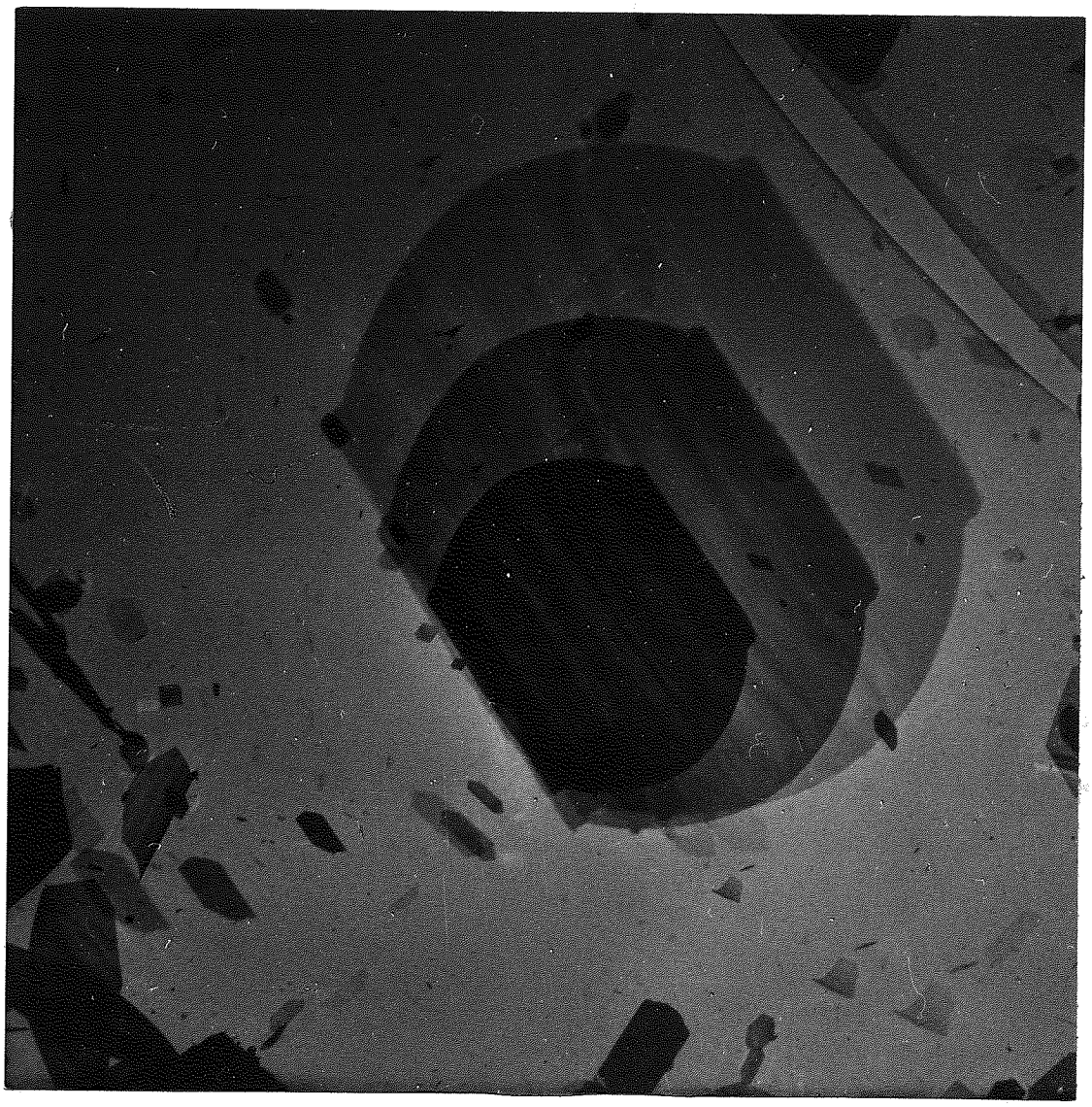

Fig. 8.3.4 Superimposed images of a molybdenum trioxide crystal showing the good alignment of the imaging system.

diffraction pattern is of higher magnification than the second erect pattern, Figure 8.3.5, which is in contrast to that of a two-stage system. The sense of direction of the two diffraction patterns was verified experimentally by imaging a copper grid incorporating an arrow pattern and mounted in the objective aperture. The final projector doublet produces an erect image of 160X magnification when it is operated at its minimum focal length. At the first diffraction pattern, the projector focal length of each lens of the intermediate doublet is 68mm and the effective focal length of the doublet is 45mm. Therefore, the intermediate projector doublet demagnifies the diffraction pattern in the back focal plane of the objective lens by about 0.6X. Therefore, the total magnification of the first diffraction pattern by this imaging system is about 100X. At the second diffraction pattern, the focal length of each lens of the intermediate doublet is 14mm and the effective focal length of the whole doublet is 25mm. Hence the second diffraction pattern is demagnified by the intermediate doublet by about 0.3X and the maximum magnification of the second diffraction by the whole system is about 50X. It can be concluded therefore, that at a constant excitation of the final projector doublet, the first diffraction pattern produced by this imaging system is always twice the size of the second diffraction pattern; this is shown clearly in Figure 8.3.5. The ray diagram of the imaging of the two diffraction patterns is illustrated in Figure 8.3.6, showing the magnification and the sense of direction relative to the back focal plane of the objective lens.

Consider the imaging procedure of the three-stage rotation-free system. The objective lens image is always inverted relative to the object plane. At maximum magnification of the whole system, the intermediate projector doublet produces a magnified image of the objective lens image with its sense of direction being kept the same,

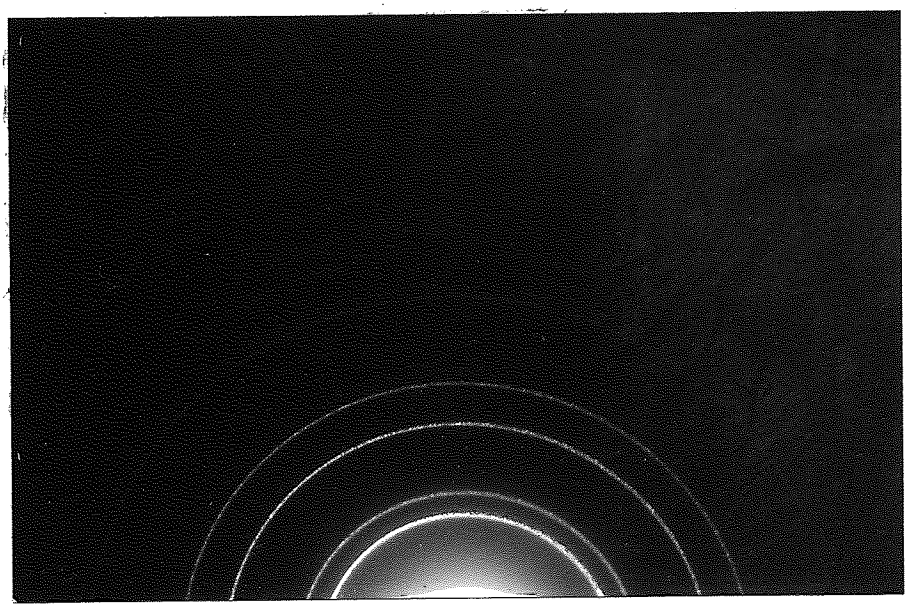

(a)

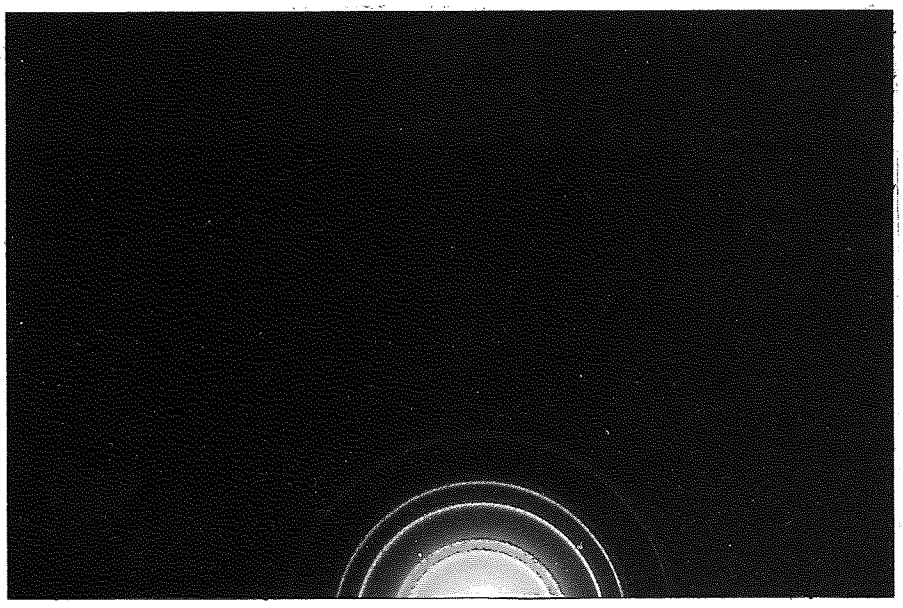

(b)

Fig. 8.3.5 The two high resolution diffraction patterns in a three-stage rotation-free imaging system; (a) first diffraction pattern (inverted) for weak excitation of the intermediate doublet, (b) second diffraction pattern (erect) for strong excitation of the intermediate doublet.

(a) Weak intermediate projector doublet

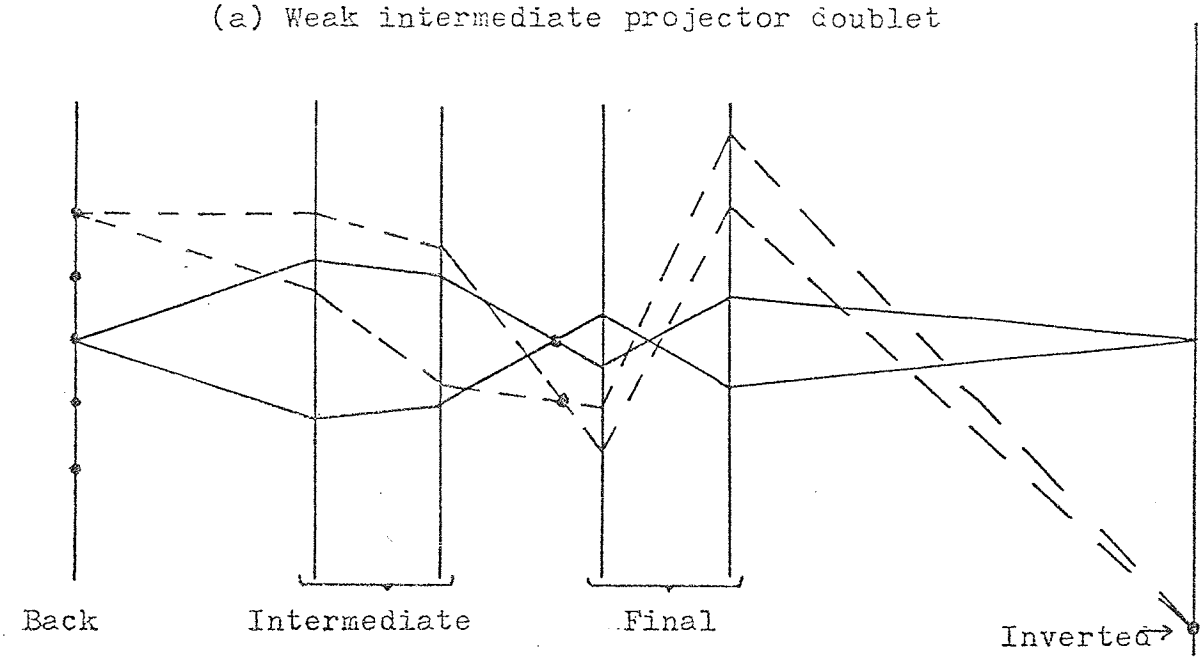

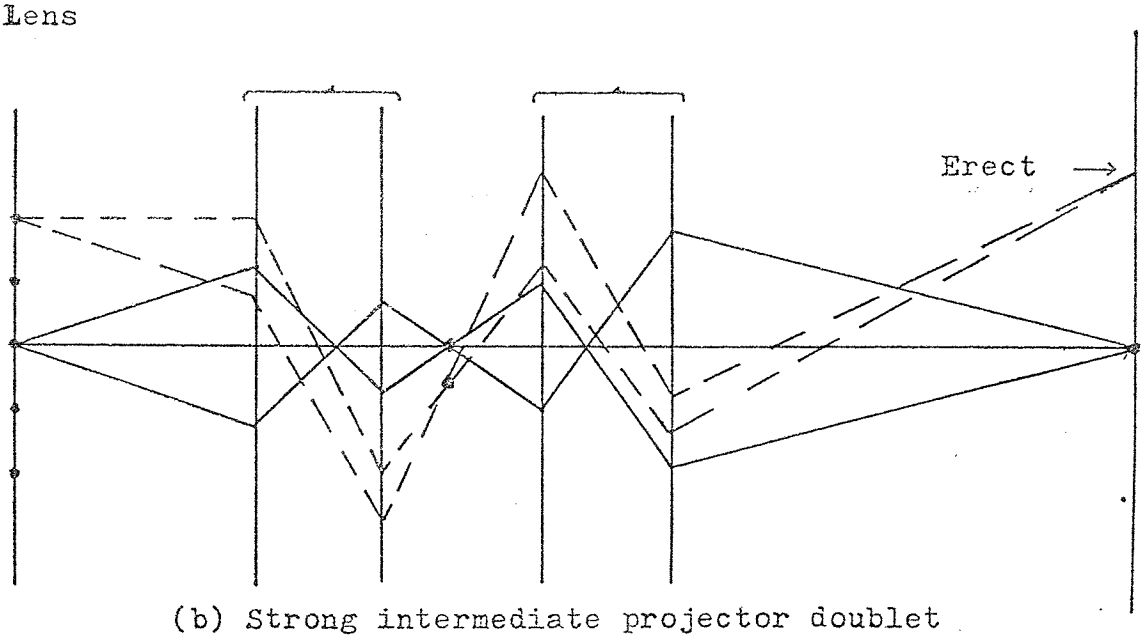

(b) Strong intermediate projector doublet

Fig. 8.3.6 Ray diagram in the diffraction mode in a three-stage rotation-free imaging system. The magnification of the inverted diffraction pattern in (a) is higher than the erect pattern in (b).

i.e. inverted relative to the object plane, and the final projector doublet does the same to the image of the intermediate projector doublet. Therefore, the final image is always inverted relative to the plane of the object when the projector doublets are operated in the second loop of their magnification curves. Hence, to relate an object to the correct orientation of its crystallographic planes, the first inverted diffraction pattern should be superimposed on the image of the specimen. However, the second diffraction pattern will give the correct orientations of the crystallographic planes although they are inverted. In commercial microscopes without exception, this procedure cannot be carried out, without careful calibration of the image rotation (Figure 8.3.7). If the excitations of the two lenses of the intermediate projector doublet are in the cooperation mode i.e. $(NI)_1 = + (NI)_2$ as shown in the diffraction pattern of Figure 8.3.8 an image rotation of about 3° occurs as expected theoretically. Figure 8.3.9 shows the first selected area micrograph of its kind, as far as the author is aware, in which in a magnetic lens system the rotation-free diffraction pattern of a molybdenum trioxide crystal is superimposed on its image in the correct orientation of the crystallographic planes of the object. This imaging system has the advantage of directly relating points in the image plane with their counterparts in the object plane, irrespective of the magnification.

Since each of the two projector doublets can be operated in two loops with two different kinds of radial distortions, a distortion in one doublet can be corrected by an opposing distortion in the other. In addition, each doublet produces a distortion-free image at its first maximum magnification, Figure 8.3.10. Therefore, a wide range of distortion-free images at low magnification and large field of view can be obtained by varying the excitations of both doublets. An

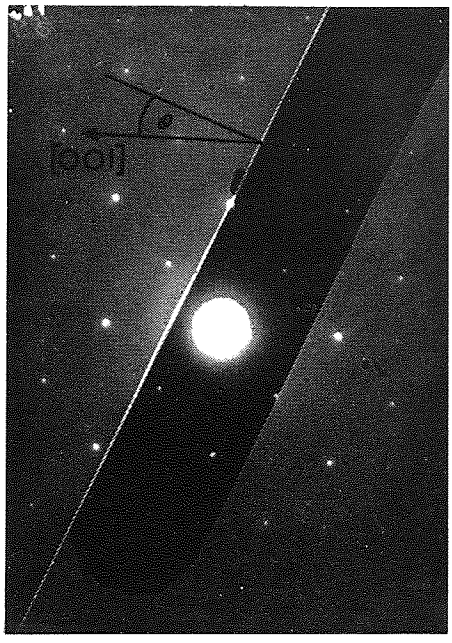

Fig. 8.3.7 Typical micrograph produced by a commercial electron microscope of a MoO_3 crystal diffraction pattern superimposed on the image of the crystal, (Hirsch et al 1965).

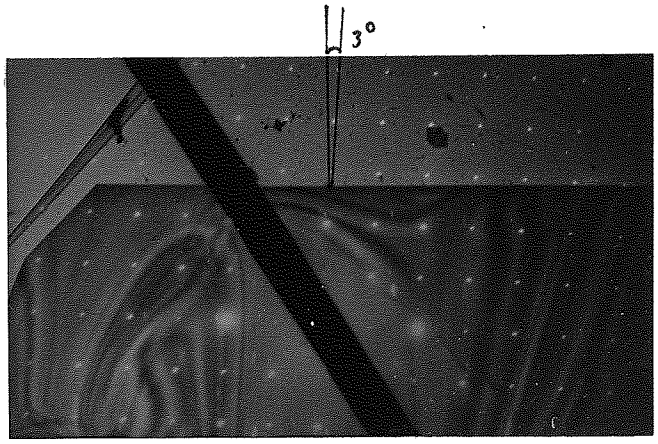

Fig. 8.3.8 Diffraction pattern of a MoO_3 crystal superimposed on the imge of the crystal when the excitations of the two lenses of the intermediate doublet are in cooperation, $(NI)_1 = +(NI)_2$, at diffraction.

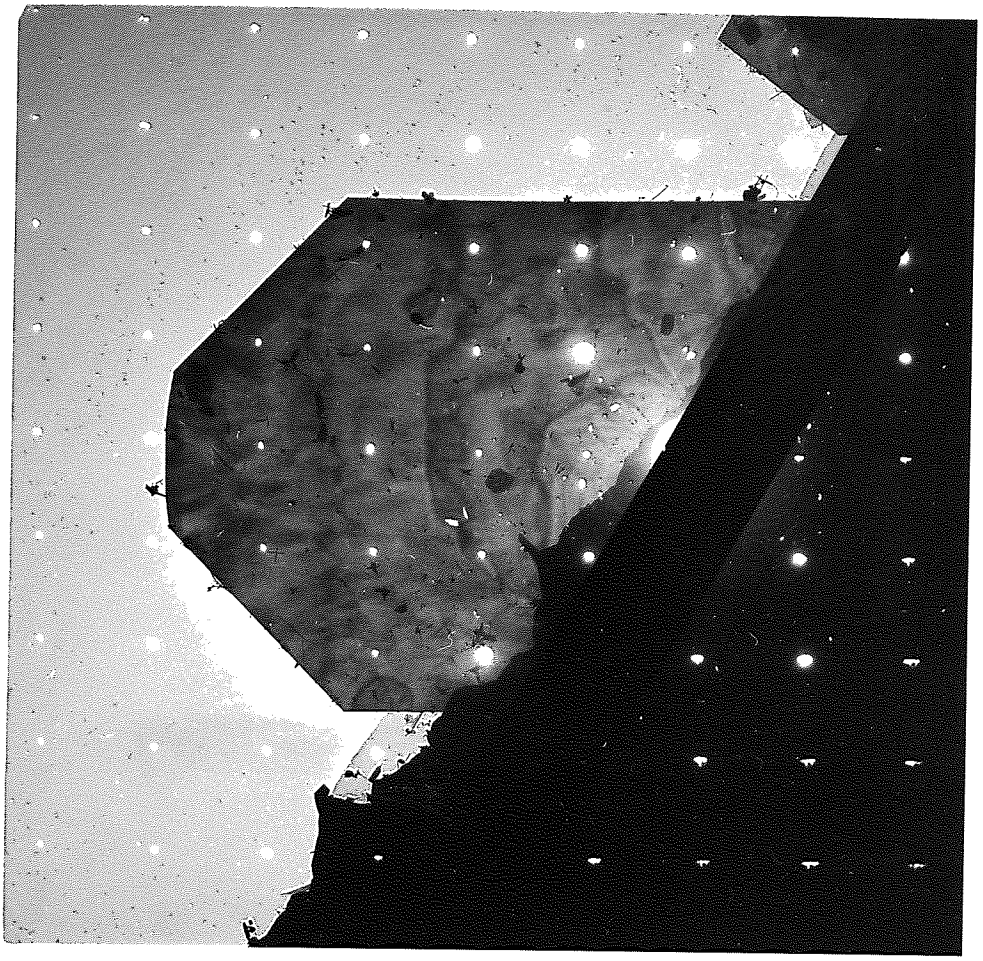

Fig.3.3.9 Rotation-free single crystal diffraction pattern of a molybdenum trioxide crystal (5 μm wide) superimposed on the image of the crystal with the correct orientation of the crystallographic planes.

(a) Two-stage rotation-free imaging system with the intermediate projector doublet at its first maximum magnification. M = 310X, field of view = 84μm.

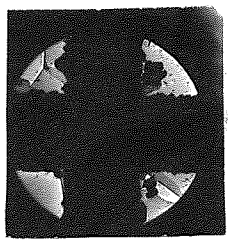

(b) Two-stage rotation-free imaging system with the final projector doublet at its first maximum magnification. M = 430X, field of view = 90μm.

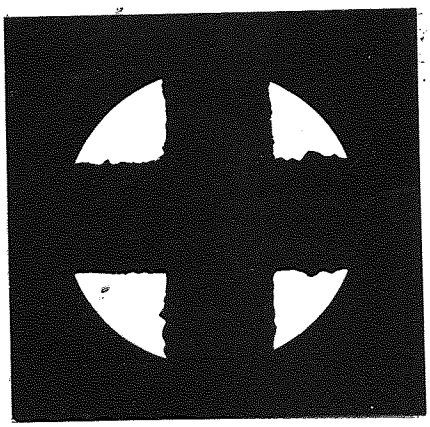

(c) Three-stage rotation-free imaging system with the two projector doublets at their first maximum magnifications. M = 333X, field of view = 120μm.

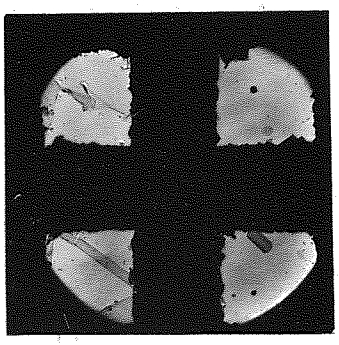

Fig. 8.3.10 Distortion-free micrographs by the projector doublets at their first maximum magnification for a constant objective focal length; f_o = 2.8mm.

example of this is shown in Figure 8.3.11. The magnification of the distortion-free images is in the range obtained from light microscopes which is a great advantage for the operator.

8.4 Non-conventional three-stage rotation-free imaging system

If the iron lid of the objective lens is replaced by a non-ferromagnetic material, the lens is converted to a single-pole objective lens. The single-pole objective lens and the two single-pole rotation-free projectors constitute an entirely non-conventional imaging system. The overall magnification of the imaging system is lower due to the long focal length of the single-pole objective lens but this can be compensated for in the projector system. The change in the overall magnification is equal to the ratio of the two different focal lengths of the double and single-pole objective lenses. For example, for the same specimen holder where $\mathcal{Z}_o$ = 2.5mm for the single-pole objective and 0.5mm for the double-pole objective lens, f_o is 12.5mm for the former and 2.8mm for the latter (Figure 7.6.2). Therefore, the ratio of the magnification with the double-pole objective lens to that with the single-pole one is 4.4; i.e. the magnification of the non-conventional system for this specimen position is 26,000X which has been verified experimentally.

An imaging system consisting of single-pole lenses is the first of its kind to be tested under practical conditions. Figure 8.4.1 shows electron micrographs obtained from this imaging system at 75kV showing the high performance of such lenses. Although the objective was not a purpose-built single-pole objective lens it does, however, indicate the practical advantages in using such lens.

A wide range of distortion-free images at low magnification and large field of view can be obtained from this system. Figure 8.4.2 shows a series of micrographs when the lenses are at distortion-free positions. Other distortion-free images can be obtained when the two

(a) $(NI/V_r^{\frac{1}{2}})_{P_2} = 2.4$ (pin-cushion)

$(NI/V_r^{\frac{1}{2}})_{P_1} = 3.9$ (barrel)

$f_o = 2.8$mm, M = 150X

field of view = 130μm

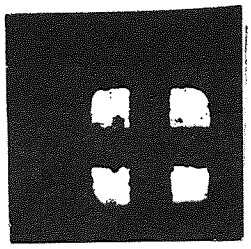

(b) $(NI/V_r^{\frac{1}{2}})_{P_2} = 6.6$ (barrel)

$(NI/V_r^{\frac{1}{2}})_{P_1} = 5$ (pin-cushion)

$f_o = 2.8$mm, M = 333X

field of view = 125μm

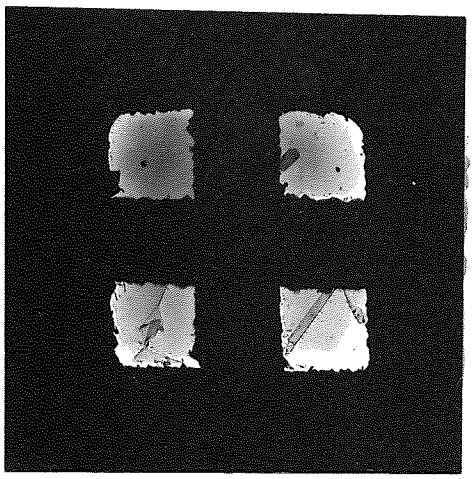

(c) $(NI/V_r^{\frac{1}{2}})_{P_2} = 8.1$ (pin-cushion)

$(NI/V_r^{\frac{1}{2}})_{P_1} = 3.8$ (barrel)

$f_o = 2.8$mm, M = 400X

field of view = 125μm

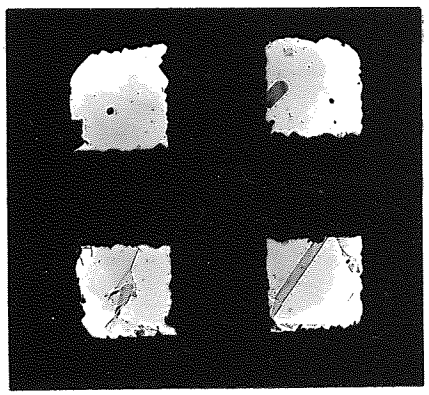

(d) Same excitation as (c)

$f_o = 7$mm, M = 114X

field of view = 450μm

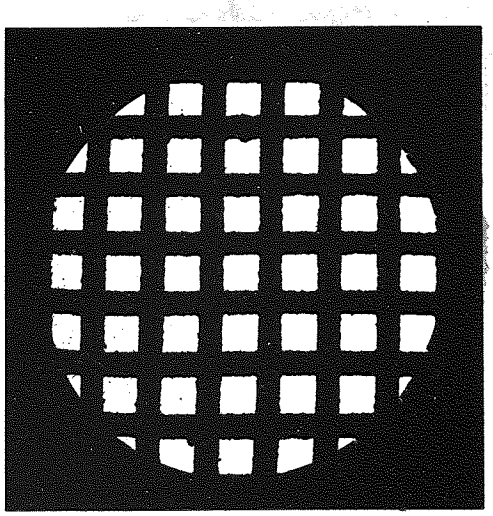

Fig. 8.3.11 Correction of distortion in the three-stage rotation-free imaging system.

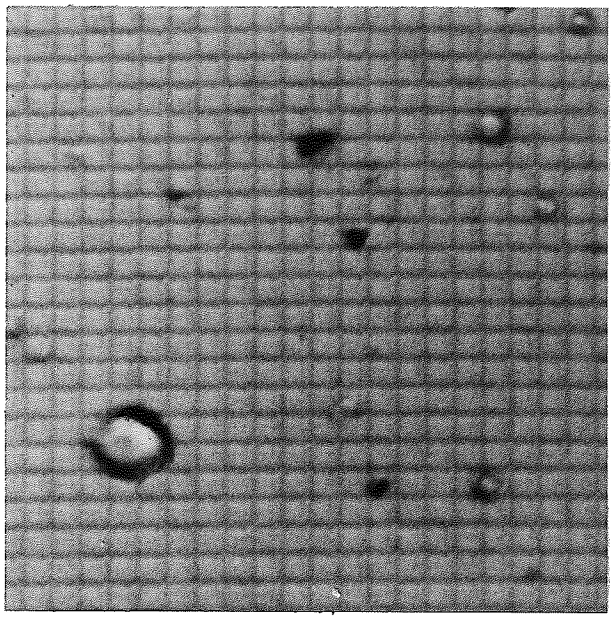

(a)

Micrograph of crossed grating at 7500X magnification.

(b)

Molybdenum trioxide crystal of 10μm width on a carbon film.

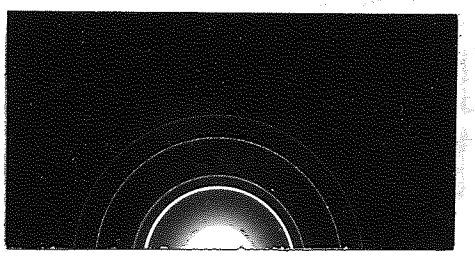

(c)

High resolution diffraction pattern of an aluminium specimen.

(d)

Selected-area diffraction of the crystal in (b) where the spots are normal to the crystal edges.

Fig. 8.4.1 Micrographs showing the performance of a three-stage non-conventional rotation-free imaging system.

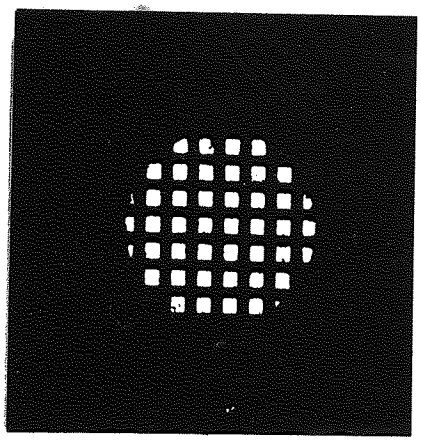

(a) Two-stage non-conventional rotation-free imaging system with the intermediate doublet at its first maximum magnification. M = 52X, field of view = 480μm.

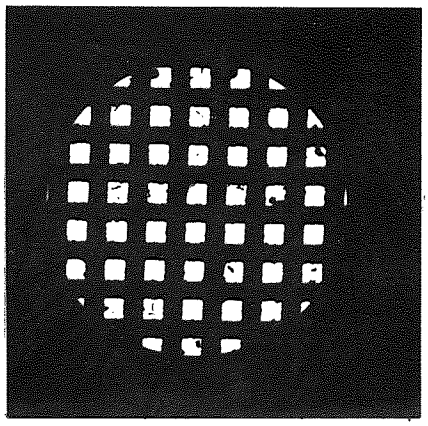

(b) Two-stage non-conventional rotation-free imaging system with the final projector doublet at its first maximum magnification. M = 78X, field of view = 500μm.

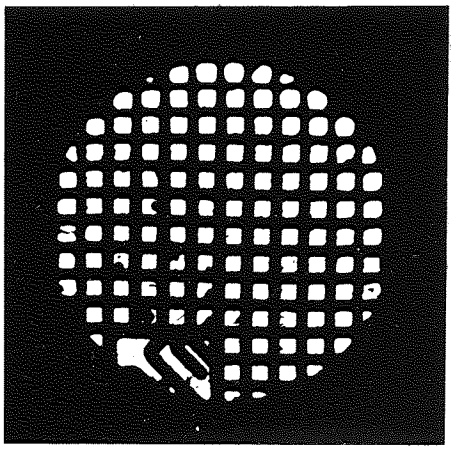

(c) Three-stage non-conventional rotation-free imaging system with the two projector doublets at their first maximum magnification. M = 55Xm field of view = 800μm.

Fig. 8.4.2 Distortion-free micrographs formed by non-conventional imaging system with the doublets are at their first maximum magnification, f_o = 16mm.

projector doublets correct the distortion of each other and when the snorkel objective has a different focal length, similar to those shown in Figure 8.3.11.

8.5 Camera-length of the three-stage rotation-free imaging system

The camera-length of an electron microscope in imaging a selected area diffraction pattern is equivalent to the physical distance through which the diffraction pattern would have to fall in field-free space to achieve the same magnification. In the analysis of the diffraction patterns the camera-length, L is given by the following basic diffraction formula

$$L = Rd/\lambda \qquad \ldots\ldots 8.5.1$$

where,

R = the distance between the central undiffracted spot and the appropriate diffraction spot or ring,

d = the lattice spacing,

λ = the electron wavelength.

To determine an experimental value for the camera-length of the three-stage rotation-free imaging system, the non-conventional system was used with an objective focal length of 17mm. Figure 8.5.1 shows the first diffraction pattern at maximum magnification of an aluminium specimen. The radius of the first ring is 41mm for the (111) plane with a d-spacing of 2.338×10^{-7}mm and an electron wavelength of 0.056×10^{-7}mm. Hence from Equation 8.5.1,

$$L = 1700\text{mm}$$

To verify this result by another method, the camera-length of the electron microscope is given by

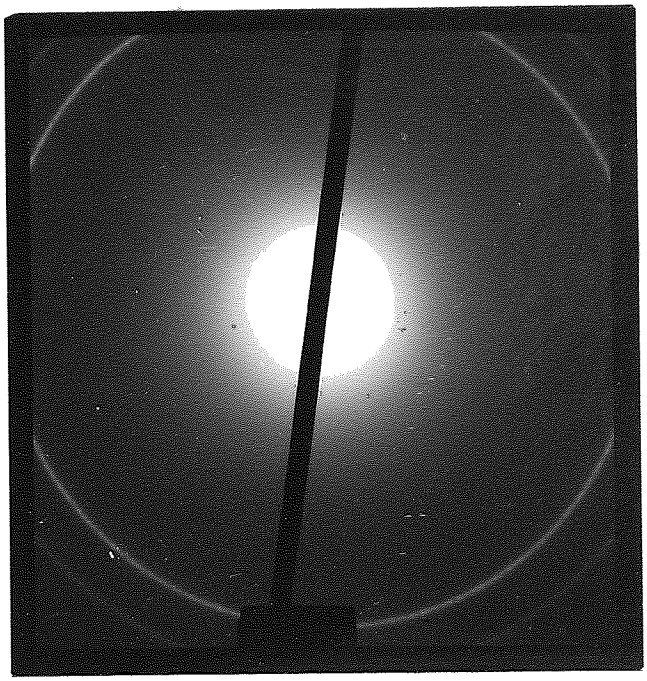

Fig. 8.5.1 Selected-area diffraction pattern of aluminium at maximum magnification in a non-conventional three-stage rotation-free imaging system.

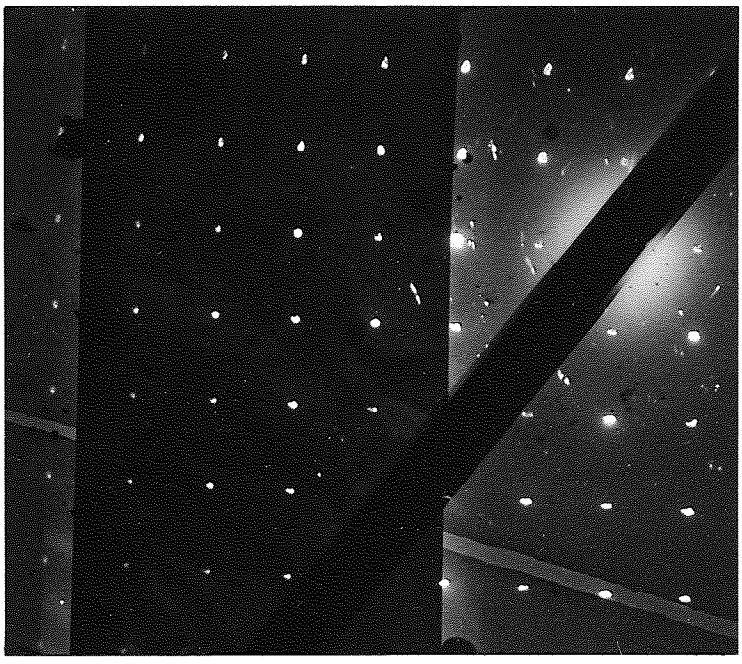

Fig. 8.5.2 Selected-area diffraction pattern of MoO_3 crystal superimposed on the image of the crystal. The excitation parameter of the final projector doublet is $NI/V_r^{\frac{1}{2}} = 10.8$ in imaging the crystal and 12.3 in imaging the pattern to obtain variable camera-length at diffraction. Notice the absence of the pattern relative to the crystal.

$$L = f_o M_p \qquad \ldots\ldots 8.5.2$$

where,

f_o = focal length of the objective lens,

M_p = the total magnification of the projection system of the electron microscope at any one particular setting.

At diffraction, it was shown that $M_p \simeq 100X$ for this miniature system; hence, for a 16mm objective focal length,

$$L \simeq 1600mm$$

which agrees with the previous result within 6% accuracy.

Therefore, the camera-length of the three-stage rotation-free imaging system can be written as

$$L = f_o M_{p_1} M_{p_2} \qquad \ldots\ldots 8.5.3$$

where M_{p_1} and M_{p_2} are the magnifications of the intermediate projector and final projector doublets respectively. Since, in this system, there are two magnifications at which the image can be viewed for selected area diffraction, therefore its two camera-lengths are $100f_o$ at weak excitation and $50f_o$ at strong excitation of the intermediate projector doublet. Therefore, for a particular setting of the objective lens and the final projector doublet, this miniature imaging system has two camera-lengths of ratio 2:1. The two camera lengths are particularly useful if a side entry specimen chamber is used with the snorkel objective because in this case the objective lens will only have one focal length unlike those with a top entry specimen chamber. In commercial microscopes the values of the camera-length vary between 250mm and 2500mm depending upon the instrument being used. However, keeping the projector doublet at a constant maximum magnification this miniature imaging system has a range of camera-lengths from 140mm for a 2.8mm focal length of the

double-pole objective lens at second diffraction to 1700mm with the snorkel objective without changing the basics of the instrument. This range of camera-lengths covers the camera-lengths of a large number of commercial microscopes. In many commercial electron microscopes, the camera-length is varied by varying the excitation of the final projector lens. If this procedure is followed in the miniature system, a very wide range of camera-lengths will be obtained (Figure 8.5.2) with the advantage of the absence of diffraction rotation.

8.6 Conclusion

The miniature three-stage rotation-free imaging system for a transmission electron microscope has been successfully operated with double and single-pole objective lenses. This experimental system has shown several desirable properties which are not yet available in commercial electron microscopes.

9. CONCLUSIONS

An entirely new type of imaging system has been developed and tried out in a 100 kV transmission electron microscope by replacing the conventional imaging system while retaining a comparable magnification to that of the original instrument (120,000X).

This imaging system consisted of miniature lenses with single rather than double polepieces. A miniature objective lens has been devised which can be used both as a double-pole or a single-pole objective lens. The low spherical aberration of the single-pole objective in spite of its comparatively long focal length indicate that the single-pole configuration could be advantageous where it is required to have a large specimen and great freedom of movement, together with good resolving power. A purpose-built single-pole objective lens can have a much shorter focal length and aberrations than that of the experimental lens described here.

The projection system consisted of two identical miniature rotation-free projector lenses with an 8mm bore diameter. Each projector doublet consisted of two single-pole lenses mounted back to back, an extremely simple construction; with no magnetic joints. Because of the wide bore, the projector doublets were mounted outside the vacuum system. The large bore has the following advantages:

(i) It provides a large field of view, making alignment easier, especially as the lenses are mounted outside the vacuum.

(ii) It is easy to clean if it contaminates.

(iii) It improves the pumping system.

(iv) It can easily be baked for ultra high vacuum work.

(v) Mechanical stability is improved since the lenses do not have to support the weight of the column above.

The miniature lenses of the new imaging system were cooled by the same water-cooling system of the original microscope. The lenses were reduced in size by miniaturising the energised coils. The investigation into these coils showed that current densities in the superconducting region can be obtained. The coils themselves should contain an even number of wire layers across their (small) width, with a large surface area. Vibration of the lenses due to the flowing water will not take place if quasi laminar flow rates of cooling water are used; this is quite sufficient to remove the heat.

The new rotation-free imaging system with single-pole lenses is an innovation with the following advantages:

(a) Rotation-free images are available at all excitations and magnifications, thus an orientation in the image can be related to its counterpart in the object.

(b) At two different camera lengths it produced rotation-free selected-area diffraction patterns which can be superimposed on the image to give the correct orientation of the crystallographic planes of the crystal.

(c) It is very simple in design and operation.

(d) Very large magnification can be produced in a comparatively short electron-optical column. The reduction in the height of the electron-optical column has the advantage of improving the screening of the column from external fields and also reducing the effect of mechanical vibrations.

(e) Single-pole projector lenses can have lower radial distortion than double-pole lenses, and single-pole objective lenses can have lower spherical aberration.

(f) A side-entry specimen holder can be used with the snorkel objective lens in the space available underneath it where cooling, heating and tilting of the specimen can be carried out without disturbing the system. The specimen can be immersed in the field away from the lens bore so that troublesome effects caused by inhomogenities in the iron polepiece will be reduced.

(g) The single-pole rotation-free projector lenses can be designed to have large bores (of the order of 1cm) with an effective focal length of one or two millimetres.

(h) Single-pole rotation-free projector lenses have larger mechanical tolerances. Alignment defects such as tilt are not so important as in conventional lenses since they are not very sensitive to this error.

(i) This type of system can be scaled up for operation at a million volts. The resulting size of the imaging column will be similar to that of a present day 100 kV commercial microscope.

APPENDIX I

Materials suitable for the electron lenses

The ideal lens material would be very soft ferromagnetic metal having a very large specific magnetic moment. The former would ensure good low excitation properties while the latter would allow very high flux densities to be reached before saturation set in. These two requirements are in general incompatible. Mumetal has a maximum permeability of 80,000 but a saturation flux density of about 0.8T. Cobalt iron has a saturation flux density of 2.4T, but a maximum permeability of only 8,000.

Commercial soft iron was used for the experimental lenses. Two kinds of material were available with specifications as shown below.

APPENDICES

	[illegible] Steel	Perm-Magnetic Iron
	Imperial Steel Corp.	Armco
	[illegible]	[illegible]
	Sheffield	

Iron	99.25%	99.85%
Silicon	0.47%	0.10%
Manganese	0.16%	-
Sulphur	0.03%	0.01%
Phosphorus	0.01%	0.005%
Chrome	0.05%	0.005%
Nickel	-	0.005%
Copper	-	0.01%
Tin	-	0.001%

APPENDIX I

The magnetic material for the electron lenses

The ideal lens material would be very soft ferromagnetic metal having a very large specific magnetic moment. The former would ensure good low excitation properties while the latter would allow very high flux densities to be reached before saturation set in. These two requirements are in general incompatible. Mumetal has a maximum permeability of 80,000 but a saturation flux density of about 0.8T. Cobalt iron has a saturation flux density of 2.4T, but a maximum permeability of only 8,000.

Commercial soft iron was used for the experimental lenses. Two kinds of material were available with specifications as shown below.

	"O" Quality Dynamo Steel Imperial Steel Works P.O. Box 38 Sheffield 9.	Remco Non-Magnetic Iron 39 Lombard St. London EC3V 9BU
Iron	99.266%	99.834%
Silicon	0.47%	0.10%
Manganese	0.16%	-
Sulphur	0.003%	0.01%
Phosphurus	0.011%	0.005%
Chrome	0.03%	0.005%
Nickel	-	0.005%
Copper	-	0.01%
Tin	-	0.001%

APPENDIX II

A paper published in the proceeding of the

Eighth International Congress on Electron Microscopy

"Electron Microscopy 1974"

Sanders and Goodchild, Eds.

Volume 1

Australian Academy of Science

Canberra

Aston University

Content has been removed for copyright reasons

Aston University

Content has been removed for copyright reasons

APPENDIX III

Wire diameter and insulation thickness

Figures (A) and (B) show the variation of the thickness of the insulating material with the wire diameter for all commercial wire gauges covered with normal insulator. These curves also represent the Lewmex wire of medium covering. To a good approximation the curve in Figure (A) can be represented by a parabola;

$$(2b)^2 = \text{Constant } (a)$$

The constant is 4.3×10^{-4} when (2b) and (a) are in centimetres. Hence from the above equation

$$2b = m\, a^{1/2}$$

where

$m = 2.07 \times 10^{-2}$ when (2b) and (a) are in centimetres.

A useful information in coil's design is shown in Figure (C). It shows the variation of wire gauge with the number of layers per centimetre of the coil's width obtainable from wires of normal (medium) covering.

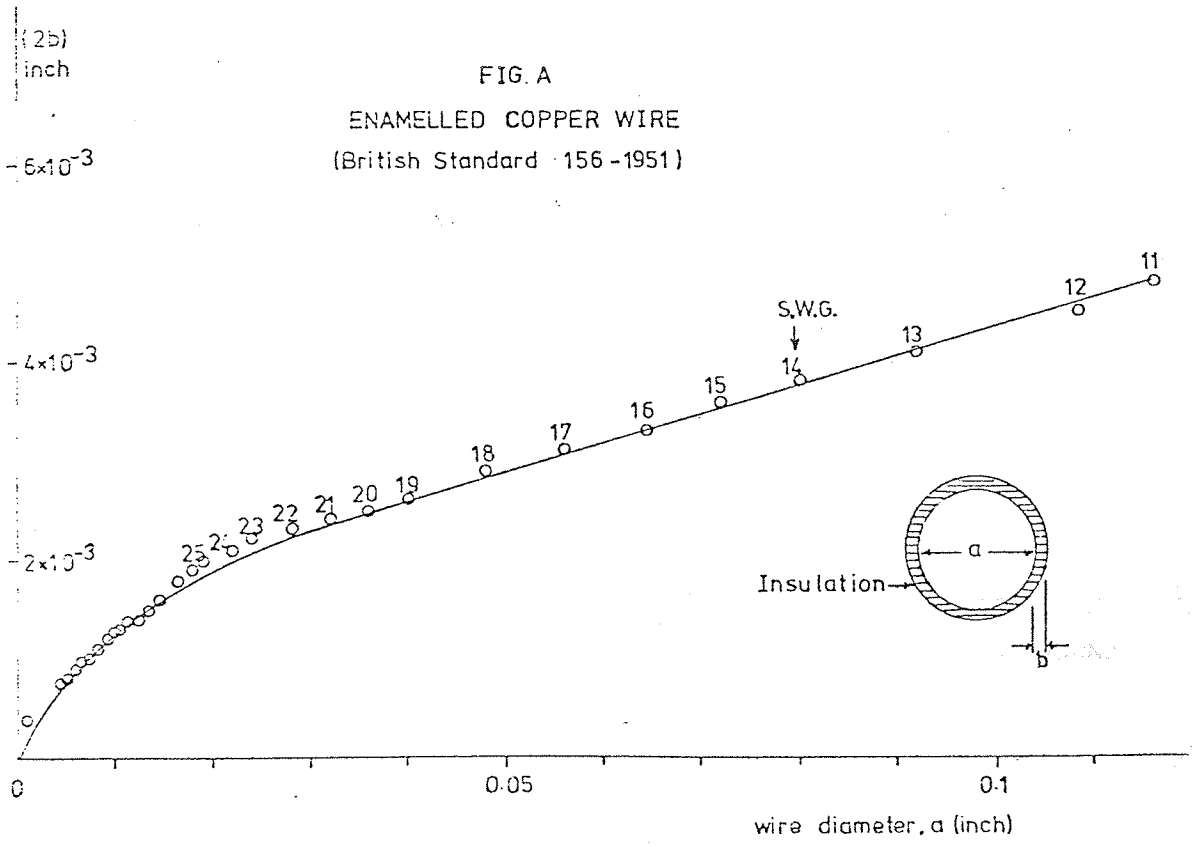

Aston University

Content has been removed for copyright reasons

APPENDIX IV

Temperature distribution along the width of the water-cooled coils

Due to the power dissipation and the cooling of the surfaces of the coil, the temperatures is different at different points across the width. In order to determine the temperature distribution along the width of all kinds of coils (i.e. tapes and wire), there are several simplifying assumptions to be made. Firstly, that the coil is homogeneous with a particular fixed thermal conductivity. Secondly, that the heat flow is in one direction towards a cooled surface of the coil. Thirdly, that the resistivity or power density ($H = \rho / \sigma^2$) is independent of temperature. In practice, the third assumption is only valid if the temperature difference between the centre of the coil and its cooling surface is small. But in any case the value of ρ can be chosen as that at the average temperature.

Consider a cross-section of a coil of width w, and thermal conductivity coefficient k_{coil}. Let T_s be the temperature of the cooled surface, T_c be the maximum temperature at the centre of the coil, T be the temperature at a distance x from the centre. At the steady state T_c and T_s are constants. The differential equation which applies to the steady-state temperature distribution in a coil winding is Poisson's equation:

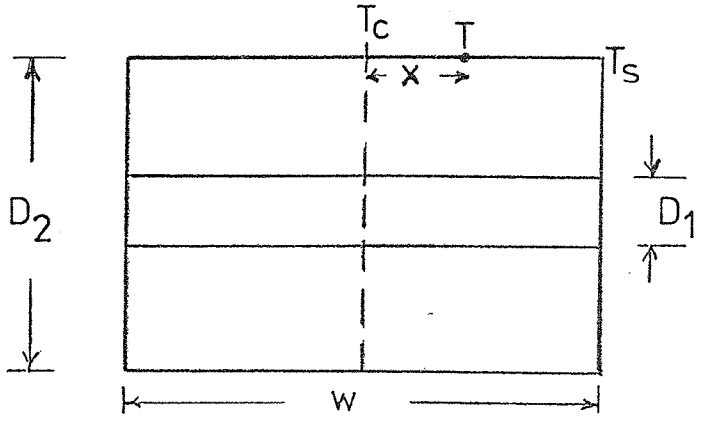

$$\nabla^2 T = - H/k_{coil} \quad \ldots\ldots\ldots 1$$

where T is the temperature at any point in the winding, H is the rate with which heat is generated per unit volume per unit time, and k_{coil} is the heat conducted per unit area per unit time per unit temperature gradient. The symbol ∇^2 denotes the Laplacian differential operator. In cartesian co-ordinates, Equation 1 would read

$$\frac{\partial^2 T}{\partial x^2} + \frac{\partial^2 T}{\partial y^2} + \frac{\partial^2 T}{\partial z^2} = - \frac{H}{k_{coil}} \quad \ldots\ldots\ldots 2$$

Since the heat flow is only in one direction, thus

$$\frac{\partial^2 T}{\partial x^2} = - \frac{H}{k_{coil}} \quad \ldots\ldots\ldots 3$$

Integrating this equation,

$$\int_{T_c}^{T} d\left(\frac{dT}{dx}\right) = - \int_{0}^{x} \frac{H}{k_{coil}} dx \quad , \text{ i.e.}$$

$$\frac{dT}{dx} = - \frac{Hx}{k_{coil}} \quad (\text{since } T_c = \text{constant}).$$

Integrating this last equation

$$\int_{T_c}^{T} dT = - \int_{0}^{x} \frac{Hx}{k_{coil}} dx$$

i.e.

$$T - T_c = - \frac{Hx^2}{2k_{coil}}$$

Therefore,

$$T = T_c - \frac{Hx^2}{2k_{coil}} \quad \ldots\ldots\ldots 4$$

The average temperature T_{av} is found from

$$T_{av} = \frac{1}{(\frac{w}{2})} \int_{0}^{(w/2)} T \, dx$$

i.e.

$$(T_{av} - T_s) = \frac{2}{3} (T_c - T_s) \quad \ldots\ldots\ldots 5$$

It was shown that the power per unit area q is given by

$$q = H \frac{w}{2}$$

Also $q = h (T_s - T_w)$

Therefore

$$H = 2h (T_s - T_w)/w \quad \ldots\ldots\ldots 6$$

when $x = w/2$, it can be seen from Equation 4 that

$$T_s = T_c - \frac{Hw^2}{8k_{coil}} \quad \ldots\ldots\ldots 7$$

i.e.

$$H = 8k_{coil} (T_c - T_s)/w^2 \quad \ldots\ldots\ldots 7a$$

Hence from Equations 5, 6 and 7

$$T_{av} = \frac{2T_c}{3} \left(\frac{wh + 6k_{coil}}{wh + 4k_{coil}}\right) - \frac{T}{3} \left(\frac{wh}{wh + 4k_{coil}}\right) \quad \ldots\ldots\ldots 8$$

which is independent of the cooled surface temperature.

From Equation 5 it can be deduced that

$$T_{av} = \frac{2}{3} (T_c - T_s) + T_s$$

Since

$$T_c - T_s = qw/4k_{coil}$$

and

$$T_s = \frac{q}{h} + T_w$$

therefore

$$T_{av} = \frac{qw}{6k_{coil}} + \frac{q}{h} + T_w$$

i.e.

$$T_{av} - T_w = q \left[\frac{w}{6k_{coil}} + \frac{1}{h}\right] \quad \ldots\ldots\ldots 9$$

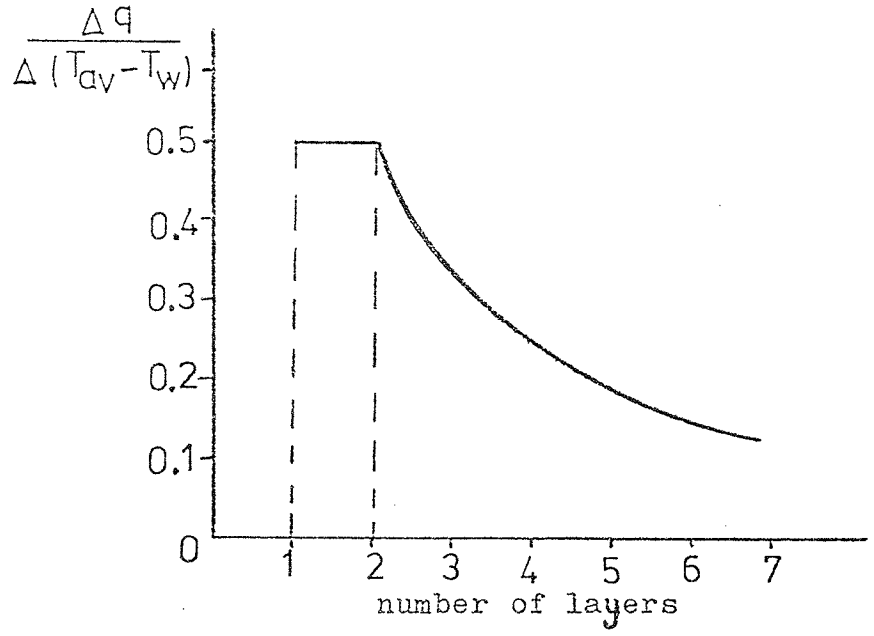

The terms in the square bracket are constants for a certain coil; hence the rise of the average temperature of any coil above that of water is directly proportional to the input power.

It can also be deduced from Equation 9 that the amount of power per unit area per average rise in the coil's temperature varies with the number of layers as shown in the above figure.

Since it is known that

$$w = 2NA/(D_2 - D_1)\lambda$$

and

$$H = \rho_T \lambda \sigma^2$$

therefore, Equation 7 becomes

$$T_c - T_s = \left(\frac{NI}{D_2 - D_1}\right)^2 \frac{\rho_T}{2 \lambda k_{coil}} \qquad \ldots\ldots\ldots 10$$

Equation 10 is independent of the width w; and it shows that the maximum temperature highly depends on the coil's diameter. The maximum temperature decreases with the increase of the value $(D_2 - D_1)$. Thus $(D_2 - D_1)$ should be large in order to reduce the maximum temperature at the centre of the width of the coil for the same ampere-turns.

APPENDIX V

Thermal conductivity of a wire coil

It was shown in Appendix IV that

$$T_c - T_s = Hw^2/8k_{coil}$$

where

$$H = 2q/w$$

therefore

$$T_c - T_s = qw/4k_{coil} \quad \ldots\ldots 1$$

For a wire coil of an even number of layers,

$$T_c - T_s = q\ (2b)\ (n_e - 2)/4k_{in} \quad \ldots\ldots 2$$

and for that of an odd number of layers

$$T_c - T_s = q\ (2b)\ (n_o - 1)^2/4n_o k_{in} \quad \ldots\ldots 3$$

where k_{in} is the coefficient of thermal conductivity of the insulating material. Hence, from Equations 1, 2 and 3,

$$(k_{coil})_{even} = k_{in}\left[w/2b(n_e - 2)\right] \quad \ldots\ldots 4$$

and

$$(k_{coil})_{odd} = k_{in}\left[n_o w/2b(n_o - 1)^2\right] \ldots\ldots 5$$

It was shown in Appendix III that $2b = m\ a^{1/2}$ where m is a constant and (a) is the wire diameter, therefore,

$$(k_{coil})_{even} = k_{in}\left[w/ma^{1/2}(n_e - 2)\right] \quad \ldots\ldots 6$$

and

$$(k_{coil})_{odd} = k_{in}\left[n_o w/ma^{1/2}(n_o - 1)^2\right] \quad \ldots\ldots 7$$

From the disc model $\lambda = a/(a + 2b) = na/w$; therefore, substituting for w and 2b in Equations 4 and 5 and writing k_c for k_{coil} one obtains

$$(k_c)_{even} = k_{in}\left[n_e/(1-\lambda)\ (n_e - 2)\right] \ldots\ldots 8$$

and

$$(k_c)_{odd} = k_{in}\left[n_o^2/(1-\lambda)\ (n_o - 1)^2\right] \ldots\ldots 9$$

All these equations are only applicable to multi-layer wire coils, where $n \geqslant 3$.

APPENDIX VI

Magnification and focal length of a double-pole rotation-free projector lens

The paraxial ray equation $\frac{d^2r}{dz^2} + k^2 r = 0$ is a linear differential equation of the second order. The general solution of this equation is given by

$$r = A \cos kz + B \sin kz \quad \ldots\ldots\ldots 1$$

where

r = displacement of the ray from the optical axis

A and B = constants

$$k = \frac{\mu_0 NI}{L} \left(\frac{e}{8mV_r}\right)^{\frac{1}{2}}$$

The refractive power is given by the derivative of Equation 1

$$\frac{dr}{dz} = -Ak \sin kz + Bk \cos kz \quad \ldots\ldots\ldots 2$$

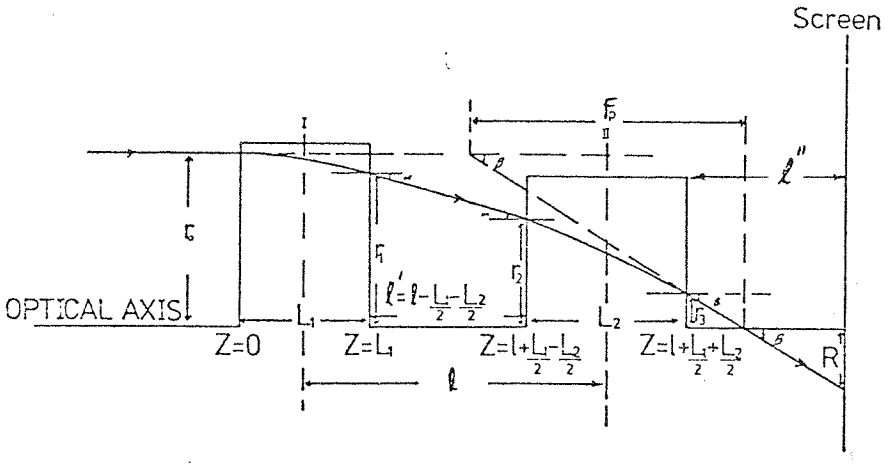

To determine the ray trajectory through two successive magnetic fields, consider the two different rectangular field distribution shown in the figure. If a parallel electron beam enters field I, the boundary conditions are

$$r = r_o \text{ and } \frac{dr}{dz} = 0 \text{ at } z = 0$$

By substituting these conditions in Equations 1 and 2 one gets

$$A_1 = r_o$$

$$B_1 = 0$$

Therefore the ray trajectory in field I is

$$r = r_o \text{ Cos } k_1 z \quad \ldots\ldots\ldots 3$$

and $$r' = -r_o k_1 \text{ Sin } k_1 z \quad \ldots\ldots\ldots 4$$

The ray emerges at $z = L_1$ where

$$r_1 = r_o \text{ Cos } k_1 L_1 \quad \ldots\ldots\ldots\ldots 5$$

$$r_1' = - r_o k_1 \text{ Sin } k_1 L_1 = |\tan \alpha| \quad \ldots\ldots\ldots 6$$

After emerging from the first field, the ray traverses a distance $\ell - \frac{1}{2}(L_1 + L_2)$ along the optical axis and then enters the second field. The boundary conditions in field II at $z = \ell + \left(\frac{L_1 - L_2}{2}\right)$ are

$$r = r_2 \text{ and } r' = r_2'$$

By substituting these conditions in Equationsl and 2 one gets

$$r_2 = A_2 \text{ Cos } k_2 \left[\ell + \frac{(L_1 - L_2)}{2}\right] + B_2 \text{ Sin } k_2 \left[\ell + \frac{(L_1 - L_2)}{2}\right] \ldots 7$$

and

$$r_2' = -A_2 k_2 \text{ Sin } k_2 \left[\ell + \frac{(L_1 - L_2)}{2}\right] + B_2 k_2 \text{ Cos } k_2 \left[\ell + \frac{(L_1 - L_2)}{2}\right] \ldots 8$$

The constants A_2 and B_2 are determined by solving Equations 7 and 8

i.e.

$$A_2 = r_2 \text{ Cos } k_2\left[\ell + \frac{(L_1 - L_2)}{2}\right] - \frac{r_2'}{k_2} \text{ Sin } k_2\left[\ell + \frac{(L_1 - L_2)}{2}\right] \quad \ldots\ldots 9$$

$$B_2 = \frac{r_2'}{k_2} \text{ Cos } k_2\left[\ell + \frac{(L_1 - L_2)}{2}\right] + r_2 \text{ Sin } k_2\left[\ell + \frac{(L_1 - L_2)}{2}\right] \quad \ldots.10$$

Therefore, the ray trajectory in field II is

$$r = r_2 \text{Cos } k_2\left[z - \ell - \frac{L_1}{2} + \frac{L_2}{2}\right] + \frac{r_2'}{k_2} \text{ Sin } k_2\left[z - \ell - \frac{L_1}{2} + \frac{L_2}{2}\right] \ldots 11$$

and

$$r' = r_2' \text{ Cos } k_2\left[z - \ell - \frac{L_1}{2} + \frac{L_2}{2}\right] - r_2 k_2 \text{ Sin } k_2\left[z - \ell - \frac{L_1}{2} + \frac{L_2}{2}\right] \ldots 12$$

It can be seen from the figure that

$$r_1' = r_2' = \left|\tan\alpha\right|$$

$$r_2' = - r_o k_1 \text{ Sin } k_1 L_1 \quad \ldots\ldots\ldots\ldots 13$$

$$\left|\tan\alpha\right| = (r_1 - r_2)/(\ell - \frac{L_1}{2} - \frac{L_2}{2})$$

i.e. $$r_2 = r_1 - (\ell - \frac{L_1}{2} - \frac{L_2}{2})\, r_o k_1 \text{ Sin } k_1 L_1 \quad \ldots\ldots\ldots 14$$

Substituting for r_1 in Equation 5 one gets

$$r_2 = r_o \text{ Cos } k_1 L_1 - (\ell - \frac{L_1}{2} - \frac{L_2}{2})\, r_o k_1 \text{ Sin } k_1 L_1 \ldots\ldots 15$$

At $z = \ell + \frac{L_1}{2} + \frac{L_2}{2}$, $r = r_3$; thus from Equations 11 and 12

$$r_3 = r_2 \text{ Cos } k_2 L_2 + \frac{r_2'}{k_2} \text{ Sin } k_2 L_2 \quad \ldots\ldots\ldots 16$$

and $$r_3' = r_2' \text{ Cos } k_2 L_2 - r_2 k_2 \text{ Sin } k_2 L_2 \quad \ldots\ldots\ldots 17$$

Substituting for r_2 and r_2' in Equations 16 and 17,

$$r_3 = r_o\left[\text{Cos } k_1 L_1 \text{ Cos } k_2 L_2 - (\ell - \frac{L_1}{2} - \frac{L_2}{2})\, k_1 \text{ Sin } k_1 L_1 \text{ Cos } k_2 L_2 - \frac{k_1}{k_2} \text{ Sin } k_1 L_1 \text{ Sin } k_2 L_2\right] \quad \ldots\ldots\ldots 18$$

$$r_3' = - r_o \left[k_1 \text{ Sin } k_1L_1 \text{ Cos } k_2L_2 + k_2 \text{ Cos } k_1L_1 \text{ Sin } k_2L_2 - k_1k_2 \left(\ell - \frac{L_1}{2} - \frac{L_2}{2} \right) \text{Sin } k_1L_1 \text{ Sin } k_2L_2 \right] \quad \ldots\ldots\ldots 19$$

If the image is projected on a screen at a distance ℓ'' from the point $z = \ell + \frac{L_1}{2} + \frac{L_2}{2}$, the beam will be on the screen at a radial displacement R from the optical axis. Hence

$$\tan \beta = |r_3'| = (-R \quad r_3)/\ell''$$

i.e. $$R = r_3 - |r_3'| \ell'' \quad \ldots\ldots\ldots 20$$

Substituting Equations 18 and 19 for r_3 and r_3' in Equation 20,

$$R = r_o \left\{ \text{Cos } k_1L_1 \text{ Cos } k_2L_2 - \left(\ell - \frac{L_1}{2} - \frac{L_2}{2} \right) k_1 \text{ Sin } k_1L_1 \text{ Cos } k_2L_2 - \frac{k_1}{k_2} \text{ Sin } k_1L_1 \text{ Sin } k_2L_2 - \ell'' \left[k_1 \text{ Sin } k_1L_1 \text{ Cos } k_2L_2 + k_2 \text{ Cos } k_1L_1 \text{ Sin } k_2L_2 - k_1k_2 \left(\ell - \frac{L_1}{2} - \frac{L_2}{2} \right) \text{Sin } k_1L_1 \text{ Sin } k_2L_2 \right] \right\}$$

$\ldots\ldots\ldots 21$

Since $kL = \mu_o NI \left(\frac{e}{8mV} \right)^{\frac{1}{2}} = \theta$, where θ the angle of rotation, the magnification $M = R/r_o$ and $\ell' = \ell - \frac{L_1}{2} - \frac{L_2}{2}$, therefore,

$$M = \text{Cos } \theta_1 \text{ Cos } \theta_2 - \ell' \frac{\theta_1}{L_1} \text{ Sin } \theta_1 \text{ Cos } \theta_2 - \frac{\theta_1 L_2}{\theta_2 L_1} \text{ Sin } \theta_1 \text{ Sin } \theta_2 - \ell'' \left[\frac{\theta_1}{L_1} \text{ Sin } \theta_1 \text{ Cos } \theta_2 + \frac{\theta_2}{L_2} \text{ Cos } \theta_1 \text{ Sin } \theta_2 - \frac{\theta_1\theta_2}{L_1L_2} \ell' \text{Sin } \theta_1 \text{ Sin } \theta_2 \right]$$

$\ldots\ldots\ldots 22$

The refractive power of the whole system is $r_3' = r_o/F_p$ where F_p is the projector focal length of the double lens system. Therefore, from Equation 19, F_p is given by

$$F_p = - \left[\frac{\theta_1}{L_1} \text{ Sin } \theta_1 \text{ Cos } \theta_2 + \frac{\theta_2}{L_2} \text{ Cos } \theta_1 \text{ Sin } \theta_2 - \frac{\theta_1\theta_2}{L_1L_2} \ell' \text{Sin } \theta_1 \text{ Sin } \theta_2 \right]^{-1}$$

$\ldots\ldots\ldots 23$

APPENDIX VII

Magnification and focal length of single and double projector lenses

(a) Single projector lens

Suppose an object of size p is illuminated by a source at a sistance S_o and its image is projected on the screen by a lens of focal length f_p. From the geometry of the above figure

$$\frac{x}{p} = \frac{u}{S_o}$$

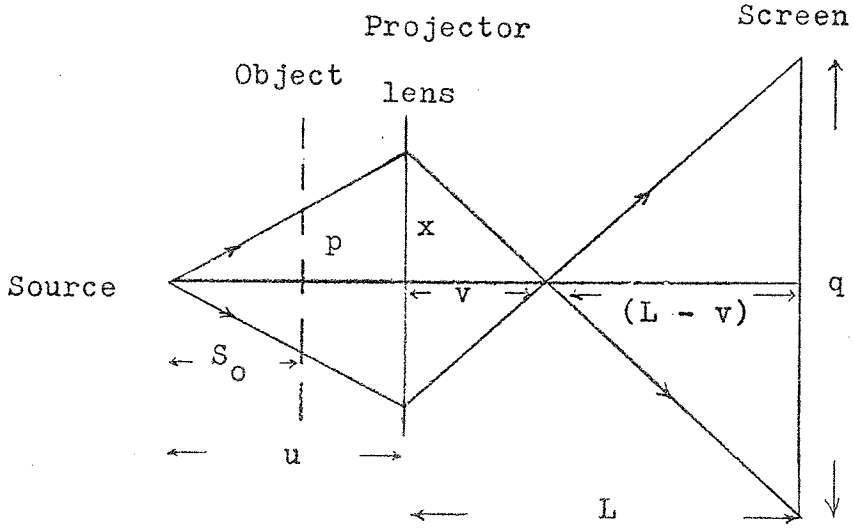

i.e. $$\frac{x/q}{p/q} = \frac{u}{S_o}$$

where q/x is the real magnification M of the projector lens and q/p is the apparent magnification M_{app}. Therefore,

$$M_{app}/M = u/S_o$$

or $$Mu = M_{app}\, S_o \qquad \ldots\ldots\ldots\ldots 1$$

From the lens equation $\frac{1}{u} + \frac{1}{v} = \frac{1}{f}$ where v will be

$$v = \frac{uf}{u - f}$$

The magnification M is given from the geometry by

$$M = \frac{L - v}{v};$$

thus $$v = \frac{L}{M + 1}$$

Therefore

$$\frac{uf}{u - f} = \frac{L}{M + 1}$$

hence

$$f = \frac{Lu}{Mu + u + L} \qquad \ldots\ldots\ldots\ldots 2$$

or

$$f = \frac{Lu}{M_{app}\, S_o + L + u} \qquad \ldots\ldots\ldots\ldots 3$$

(b) Double projector lens

Considering this figure,

$Z = x + y + r_3$

$r_r = Z - x - y$ .....(i)

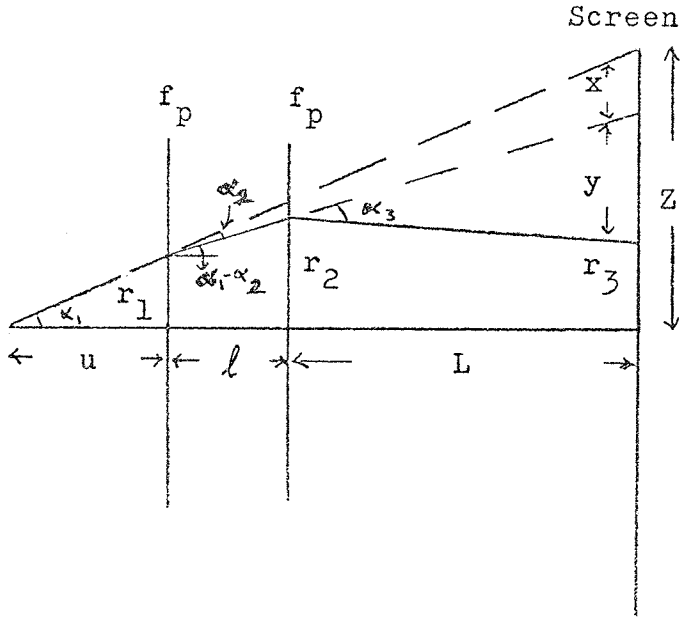

$\alpha_1 = Z/(u + \ell + L)$

i.e. $Z = \alpha_1(u + \ell + L)$ .....(ii)

Also $\alpha_1 = r_1/u$ .....(iii)

$x = \alpha_2(L + \ell)$ .....(iv)

$y = \alpha_3 L$ .....(v)

i.e.

$r_3 = \alpha_1(u + \ell + L) - \alpha_2(L + \ell) - \alpha_3 L$ .....(vi)

Since the magnification $M = r_3/r_1$, hence it is important to have α_1, α_2 and α_3 in terms of r_1.

$\alpha_2 = r_1/f_p$ .....(vii)

$\alpha_1 - \alpha_2 = (r_2 - r_1)/\ell$

i.e. $(r_1/u) - (r_1/f_p) = (r_2 - r_1)/\ell$

$$\frac{r_2}{\ell} = r_1 \left(\frac{1}{u} - \frac{1}{f_p} \frac{1}{\ell} \right)$$

$$r_2 = r_1 \left(\frac{\ell}{u} - \frac{\ell}{f_p} + 1 \right) \qquad \text{.....(viii)}$$

$$\alpha_3 = \frac{r_2}{f_p} = \frac{r_1}{f_p} \left[1 + \frac{\ell}{u} - \frac{\ell}{f_p} \right] \qquad \text{.....(ix)}$$

Substituting for α_1, α_2 and α_3 in Equations (iii), (vii) and (ix) in Equation (vi),

$$r_3 = \frac{r_1}{u} (u + \ell + L) - \frac{r_1}{f_p} (L + \ell) - \frac{r_1 L}{f_p} \left(1 + \frac{\ell}{u} - \frac{\ell}{f_p}\right)$$

i.e.

$$r_3 = r_1 \left\{ 1 + \frac{\ell}{u} + \frac{L}{u} - \frac{L}{f_p} - \frac{\ell}{f_p} - \frac{L}{f_p} - \frac{\ell L}{f_p u} \frac{\ell L}{f_p^2} \right\}$$

The magnification $M = r_3/r_1$; hence

$$M = 1 + \frac{\ell + L}{u} - \frac{1}{f_p} \left(\frac{\ell L}{u} + 2L + \ell \right) + \frac{\ell L}{f_p^2} \qquad \text{.....(x)}$$

M is the total magnification of the doublet.

APPENDIX VIII

Projection distance and distortion of the final projector lens in an electron microscope

Consider the projector lens of focal length f_p and radial and spiral distortion coefficient C_d and C_{sp} respectively. Let L be the distance between the photographic plate of radius R_p and the projector lens of bore radius R.

The radial distortion $\left(\frac{\Delta\rho}{\rho}\right)_{rad}$ is given by

Equation 1.5.5

$$\left(\frac{\Delta\rho}{\rho}\right)_{rad} = C_d \left(\frac{r}{R}\right)^2$$

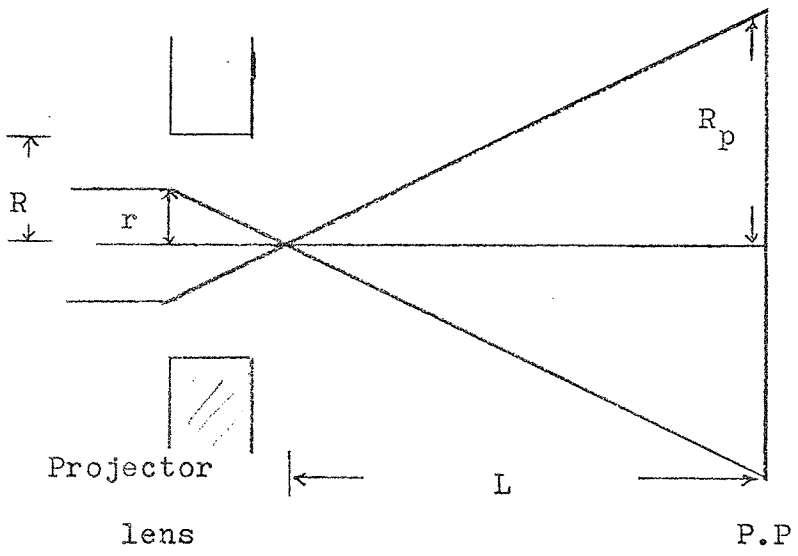

The radial displacement r of the electron beam from the lens axis is given by

$$r = \frac{R_p}{M} = \frac{R_p}{L/f_p}$$

where M is the magnification of the lens.

Therefore,

$$\left(\frac{\Delta\rho}{\rho}\right)_{rad} = \frac{C_d}{R^2} \left(\frac{R_p f_p}{L}\right)^2$$

or $$L^2 = \frac{C_d R_p^2 f_p^2}{R^2 \left(\frac{\Delta\rho}{\rho}\right)_{rad}}$$

i.e.

$$L = \left(R_p/R \right) \left(\frac{\Delta\rho}{\rho} \right)^{-\frac{1}{2}}_{rad} f_p \, C_d^{\frac{1}{2}}$$

Similarly, for spiral distortion

$$L = \left(R_p/R \right) \left(\frac{\Delta\rho}{\rho} \right)^{-\frac{1}{2}}_{sp} f_p \, C_{sp}^{\frac{1}{2}}$$

These two equations show that for a specific system, L is proportional to $f_p \, C_d^{\frac{1}{2}}$ and $f_p \, C_{sp}^{\frac{1}{2}}$.

APPENDIX IX

Magnification and diffraction in a two-stage rotation-free imaging system

(A) Magnification of objective and one rotation-free projector lens

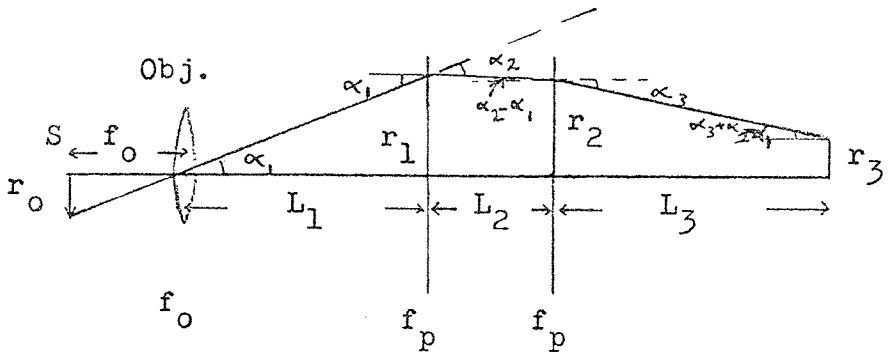

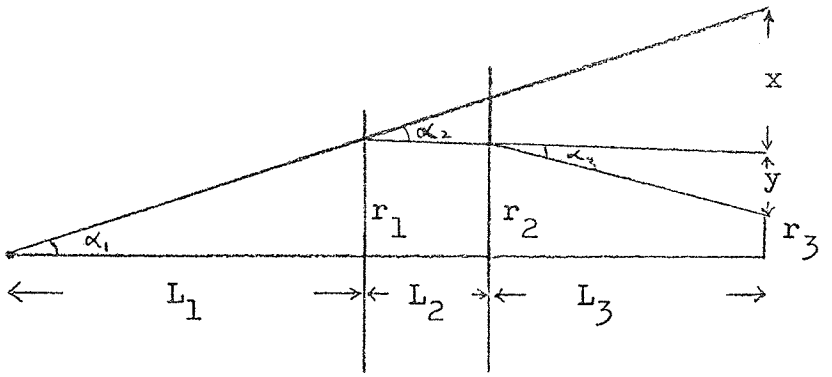

$$\alpha_1 = \frac{x + y + r_3}{L_1 + L_2 + L_3}$$

$$x = (L_2 + L_3)$$

$$y = \alpha_3 L_3$$

Hence $r_3 = \alpha_1(L_1 + L_2 + L_3) - \alpha_2(L_2 + L_3) - \alpha_3 L_3$ 1

$$\alpha_2 = r_1/f_p \qquad \text{.....2}$$

But $r_1 = \alpha_1 L_1$ .....

Hence $\alpha_2 = \frac{\alpha_1 L_1}{f_p}$ 3

$$\alpha_3 = \frac{r_2}{f_p} \qquad \ldots\ldots\ldots\ldots 4$$

$$\alpha_2 - \alpha_1 = \frac{r_1 - r_2}{L_2} \qquad \ldots\ldots\ldots 5$$

Substituting for α_2 and α_1 in Equation 5

$$\frac{r_1}{f_p} - \frac{r_1}{L_1} = \frac{r_1 - r_2}{L_2}$$

$$r_1 L_1 L_2 - r_1 f_p L_2 = r_1 f_p L_1 - r_2 f_p L_1$$

Hence

$$r_2 = \frac{r_1 (f_p L_1 + f_p L_2 - L_1 L_2)}{f_p L_1} \qquad \ldots\ldots\ldots 6$$

Substitute Equation 6 in Equation 4 and for $r_1 = \alpha_1 L_1$

$$\alpha_3 = \frac{\alpha_1 (f_p L_1 + f_p L_2 - L_1 L_2)}{f_p^2} \qquad \ldots\ldots\ldots 7$$

Substituting Equations 3 and 7 in 1

$$r_3 = \alpha_1 (L_1 + L_2 + L_3) - \frac{\alpha_1 L_1}{f_p} (L_2 + L_3) - \frac{\alpha_1 L_3 (f_p L_1 + f_p L_2 - L_1 L_2)}{f_p^2}$$

$$r_3 = \alpha_1 \left\{ (L_1 + L_2 + L_3) - \frac{1}{f_p} (L_1 L_2 + 2 L_1 L_3 + L_2 L_3) \frac{L_1 L_2 L_3}{f_p^2} \right\} \qquad \ldots\ldots\ldots 8$$

$\alpha_1 = r_o / f_o$ and the magnification, $M = r_3 / r_o$; hence from Equation 8 one obtains

$$M = \frac{1}{f_o} \left\{ (L_1 + L_2 + L_3) - \frac{1}{f_p} (L_1 L_2 + 2 L_1 L_3 + L_2 L_3) + \frac{L_1 L_2 L_3}{f_p^2} \right\} \qquad \ldots\ldots\ldots 9$$

(B) Diffraction pattern in a rotation-free microscope consisting of an objective lens and one rotation-free lens

On the photographic plate

$$r_3 = r_d + \Delta \qquad \ldots\ldots\ldots 1$$

$$\Delta = AD - BD \qquad \ldots\ldots\ldots\ldots 2$$

To find AD

$$\alpha_1 = \frac{AD}{L_1 + L_2 + L_3}$$

Hence

$$AD = (L_1 + L_2 + L_3)\,\alpha_1 \qquad \ldots\ldots\ldots 3$$

Back focal plane of objective lens

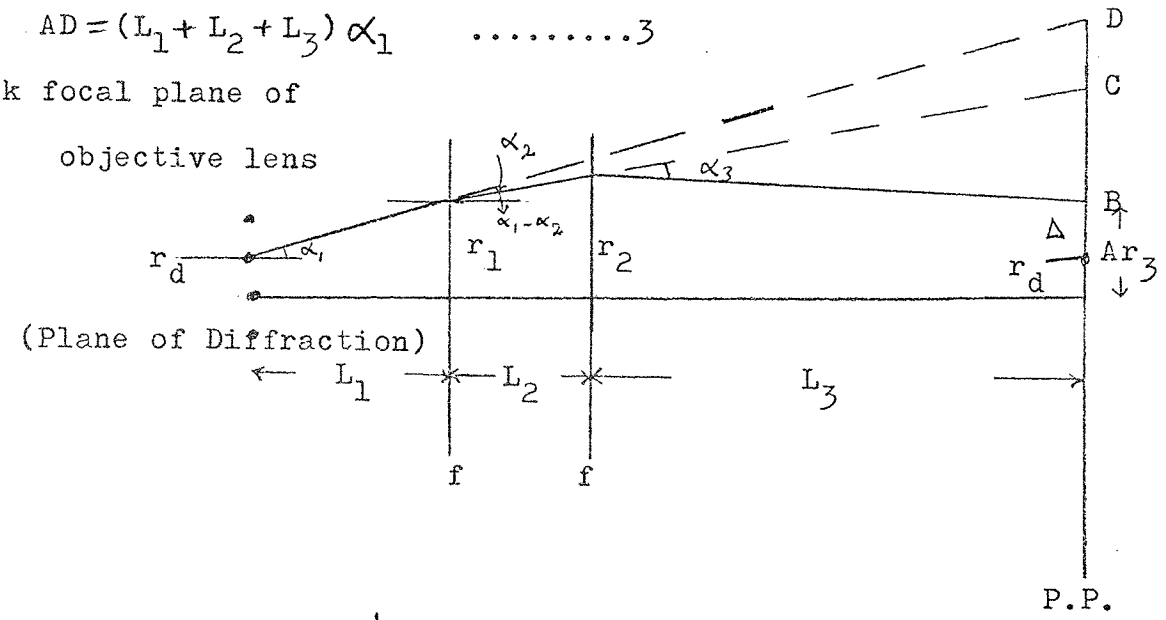

To find BD , $BC = \alpha_3 L_3$

$$BD = BC + CD$$

$$CD = \alpha_2 (L_2 + L_3)$$

Hence

$$BD = L_3 \alpha_3 + (L_2 + L_3)\alpha_2 \qquad \ldots\ldots\ldots 4$$

Substituting Equations 3 and 4 in 2

$$\Delta = (L_1 + L_2 + L_3)\alpha_1 - (L_2 + L_3)\alpha_2 - L_3 \alpha_3 \qquad \ldots\ldots\ldots 5$$

Substituting Equation 5 in Equation 1

$$r_3 = r_d + (L_1 + L_2 + L_3)\alpha_1 - (L_2 + L_3)\alpha_2 - L_3 \alpha_3 \qquad \ldots\ldots\ldots\ldots 6$$

To find α_2 and α_3 in terms of α_1

$$\alpha_2 = r_1/f = \frac{(r_d + L_1\alpha_1)}{f} \qquad \ldots\ldots\ldots 7$$

$$\alpha_3 = r_2/f = \frac{r_1 + (\alpha_1 - \alpha_2)L_2}{f}$$

$$= \frac{(r_d + L_1\alpha_1) + L_2\alpha_1 - \frac{(r_d + L_1\alpha_1)}{f} L_2}{f}$$

$$\alpha_3 = \frac{r_d + (L_1 + L_2)\alpha_1 - \frac{(r_d + L_1\alpha_1)}{f} L_2}{f} \qquad \ldots\ldots\ldots\ldots 8$$

Substituting Equations 7 and 8 in Equation 6 and simplifying

$$r_3 = r_d + (L_1 + L_2 + L_3)\alpha_1 - (L_2 + L_3)\frac{(r_d + L_1\alpha_1)}{f} -$$

$$L_3\left[\frac{r_d f + (L_1 + L_2) f\alpha_1 - r_d L_2 - L_1 L_2 \alpha_1}{f^2}\right]$$

$$= r_d - \frac{(L_2 + L_3)}{f} r_d - \frac{L_3 r_d}{f} + \frac{L_2 L_3}{f^2} r_d + (L_1 + L_2 + L_3)\alpha_1 -$$

$$\frac{L_1(L_2 + L_3)\alpha_1}{f} - \frac{(L_1 + L_2)L_3\alpha_1}{f} \frac{L_1 L_2 L_3}{f^2}\alpha_1$$

$$r_3 = r_d\left[1 - \frac{(L_2 + L_3)}{f} - \frac{L_3}{f} \frac{L_2 L_3}{f^2}\right] +$$

$$\alpha_1\left[(L_1 + L_2 + L_3) - \frac{L_1(L_2 + L_3)}{f} - \frac{L_3(L_1 + L_2)}{f} \frac{L_1 L_2 L_3}{f^2}\right]$$

$$\ldots\ldots\ldots 10$$

If $r_d = 0$ i.e. the central spot of the diffraction pattern,

hence $r_3 = 0$ if the term of α_1 in Equation 10 is zero; therefore,

$$(L_1 + L_2 + L_3) - \frac{1}{f}\left[L_3(L_1 + L_2) + L_1(L_2 + L_3)\right] + \frac{L_1 L_2 L_3}{f^2} = 0$$

or $$(L_1 + L_2 + L_3)f^2 - \left[(L_1 + L_2)L_3 + (L_2 + L_3)L_1\right] f + L_1 L_2 L_3 = 0$$

$$\ldots\ldots\ldots 11$$

Solving Equation 11 for f:

$$(f)_{diff} = \left\{(L_1 + L_2)L_3 + (L_2 + L_3)L_1 \pm \left[\left((L_1 + L_2)L_3 + (L_2 + L_3)L_1\right)^2 - 4(L_1 + L_2 + L_3)(L_1 L_2 L_3)\right]^{\frac{1}{2}}\right\} / 2(L_1 + L_2 + L_3)$$

$$(f)_{diff} = \left\{(L_1L_2 + 2L_1L_3 + L_2L_3) \pm \left[(L_1L_2 + 2L_1L_3 + L_2L_3)^2 - 4L_1L_2L_3(L_1 + L_2 + L_3)\right]^{1/2}\right\} / 2\,(L_1 + L_2 + L_3) \quad \ldots\ldots 12$$

When the condition in Equation 12 is fullfilled, a diffraction spot of raduis r_d will be magnified by an amount (r_3/r_d) given by

$$(M)_{diff} = r_3/r_d = \left\{1 - \frac{(L_2 + 2L_3)}{f_p} + \frac{L_2L_3}{f_p^2}\right\} \quad \ldots\ldots 13$$

APPENDIX X

Magnification in three-stage rotation-free imaging system of an electron microscope

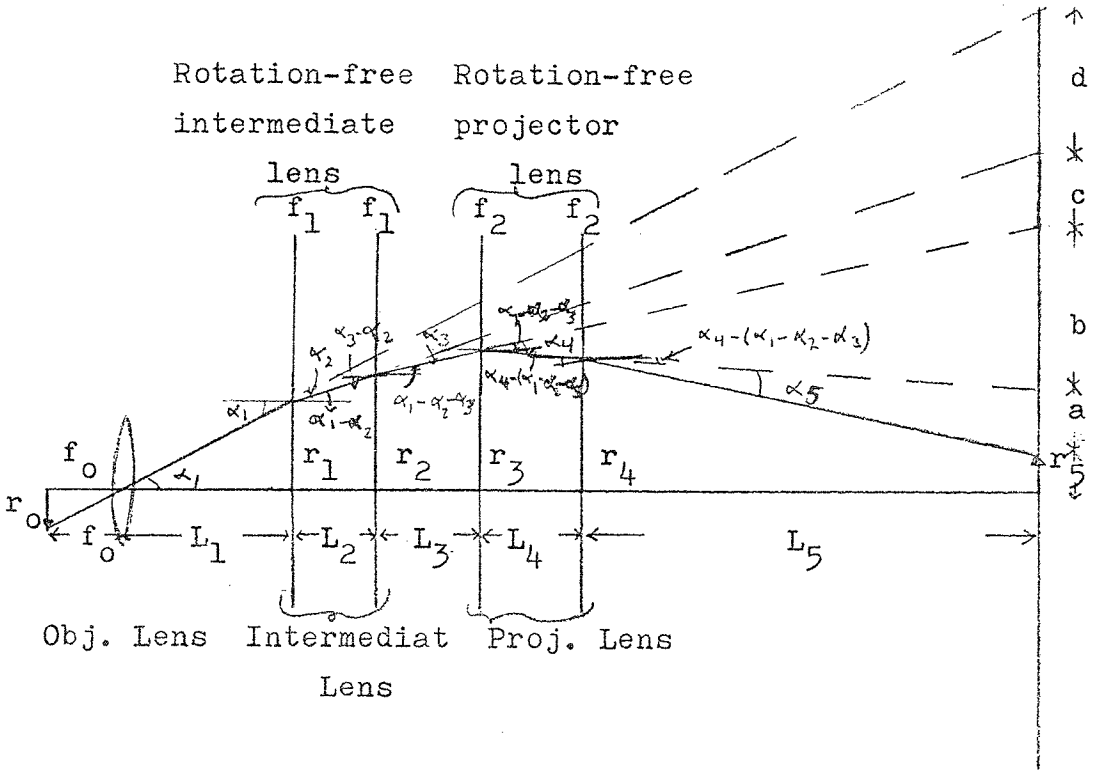

Considering the trajectory of an electron beam through the whole system,

$$\alpha_1 = \frac{d + c + b + a + r_5}{L_1 + L_2 + L_3 + L_4 + L_5} \qquad \ldots\ldots\ldots 1$$

$$= \frac{r_1}{L_1}$$

$$= \frac{r_o}{f_o}$$

From Equation 1

$$r_5 = \alpha_1(L_1 + L_2 + L_3 + L_4 + L_5) - d - c - b - a \qquad \ldots\ldots\ldots 2$$

$$\alpha_2 = \frac{d}{L_2 + L_3 + L_4 + L_5} = \frac{r_1}{-f_1} \qquad \ldots\ldots\ldots\ldots 3$$

$$\alpha_3 = \frac{c}{L_3 + L_4 + L_5} = \frac{r_2}{f_1} \qquad \ldots\ldots\ldots 4$$

$$\alpha_4 = \frac{b}{L_4 + L_5} = \frac{r_3}{f_2} \qquad \ldots\ldots\ldots\ldots 5$$

$$\alpha_5 = \frac{a}{L_5} = \frac{r_4}{f_2} \qquad \ldots\ldots\ldots\ldots 6$$

$$\alpha_1 - \alpha_2 = \frac{r_2 - r_1}{L_2}$$

$$\alpha_1 - \alpha_2 - \alpha_3 = \frac{r_3 - r_2}{L_3}$$

$$\alpha_4 - (\alpha_1 - \alpha_2 - \alpha_3) = \frac{r_3 - r_4}{L_4}$$

To find d:-

From Equation 1 $r_1 = L_1 \alpha_1$, hence Equation 3 becomes

$$\alpha_2 = \frac{L_1 \alpha_1}{f_1} = \frac{d}{L_2 + L_3 + L_4 + L_5}$$

i.e. $$d = \frac{L_1 \alpha_1}{f_1} (L_2 + L_3 + L_4 + L_5) \qquad \ldots\ldots\ldots 7$$

To find c:-

$$\alpha_1 - \alpha_2 = \frac{r_2 - r_1}{L_2}$$

i.e. $$\alpha_1 - \frac{L_1 \alpha_1}{f_1} = \frac{r_2}{L_2} - \frac{L_1 \alpha_1}{L_2}$$

or $$r_2 = \alpha_1 L_2 - \frac{L_1 \alpha_1 L_2}{f_1} + L_1 \alpha_1$$

$$r_2 = \alpha_1 \left(L_2 - \frac{L_1 L_2}{f_1} + L_1\right) \qquad \ldots\ldots\ldots\ldots 8$$

Substituting Equation 8 in Equation 4

$$\frac{c}{L_3 + L_4 + L_5} = \frac{\alpha_1}{f_1} \left(L_2 + L_1 - \frac{L_1 L_2}{f_1}\right.$$

$$c = \frac{\alpha_1}{f_1} \left(L_1 + L_2 - \frac{L_1 L_2}{f_1}\right)(L_3 + L_4 + L_5) \qquad \ldots\ldots\ldots 9$$

To find b:-

$$(\alpha_1 - \alpha_2 - \alpha_3)\, L_3 = r_3 - r_2$$

Substituting for α_2, α_3 in Equations 3 and 4 and for r_2 in Equation 8,

$$r_3 = \left[\alpha_1 - \frac{L_1\alpha_1}{f_1} - \frac{\alpha_1}{f_1}\left(L_1 + L_2 - \frac{L_1L_2}{f_1}\right)\right]L_3 + \alpha_1\left(L_1 + L_2 - \frac{L_1L_2}{f_1}\right)$$

i.e. $$r_3 = \alpha_1\left\{\left[1 - \frac{L_1}{f_1} - \frac{1}{f_1}\left(L_1 + L_2 - \frac{L_1L_2}{f_1}\right)\right]L_3 + L_1 + L_2 - \frac{L_1L_2}{f_1}\right\}$$

.....10

Hence $$\alpha_4 = \frac{\alpha_1}{f_2}\left\{\left[1 - \frac{L_1}{f_1} - \frac{1}{f_1}\left(L_1 + L_2 - \frac{L_1L_2}{f_1}\right)\right]L_3 + L_1 + L_2 - \frac{L_1L_2}{f_1}\right\}$$

.....11

From Equation 5

$$b = (L_4 + L_5)\alpha_4$$

i.e.

$$b = (L_4 + L_5)\frac{\alpha_1}{f_2}\left\{\left[1 - \frac{L_1}{f_1} - \frac{1}{f_1}\left(L_1 + L_2 - \frac{L_1L_2}{f_1}\right)\right]L_3 + L_1 + L_2 - \frac{L_1L_2}{f_1}\right\}$$

.....12

To find a:-

From Equation 6

$$a = L_5\alpha_5 = L_5\frac{r_4}{f_2}$$

r_4 must be found

$$\alpha_4 - (\alpha_1 - \alpha_2 - \alpha_3) = \frac{r_3 - r_4}{L_4}$$

$$\alpha_4L_4 - \alpha_1L_4 + \alpha_2L_4 + \alpha_3L_4 = r_3 - r_4$$

$$r_4 = r_3 - \alpha_4L_4 + \alpha_1L_4 - \alpha_2L_4 - \alpha_3L_4$$

Substituting for r_3 in Equation 10 and α_4 in Equation 11, α_3 in Equations 4 and 8, α_2 in Equation 3 then

$$r_4=\alpha_1\left\{\left[1-\frac{L_1}{f_1}-\frac{1}{f_1}(L_1+L_2-\frac{L_1L_2}{f_1})\right]L_3+L_1+L_2-\frac{L_1L_2}{f_1}\right\}-$$

$$\frac{\alpha_1L_4}{f_2}\left\{\left[1-\frac{L_1}{f_1}-\frac{1}{f_1}(L_1+L_2-\frac{L_1L_2}{f_1})\right]L_3+L_1+L_2-\frac{L_1L_2}{f_1}\right\}+$$

$$\alpha_1L_4-\frac{\alpha_1L_1L_4}{f_1}-\frac{\alpha_1L_4}{f_1}(L_1+L_2-\frac{L_1L_2}{f_1})$$

$$r_4=\alpha_1\left\{L_3-\frac{L_1L_3}{f_1}-\frac{L_1L_3}{f_1}-\frac{L_2L_3}{f_1}+\frac{L_1L_2L_3}{f_1^2}+L_1+L_2-\frac{L_1L_2}{f_1}-\frac{L_3L_4}{f_2}+\right.$$

$$\frac{L_1L_3L_4}{f_1f_2}+\frac{L_1L_3L_4}{f_1f_2}+\frac{L_2L_3L_4}{f_1f_2}-\frac{L_1L_2L_3L_4}{f_1^2f_2}-\frac{L_1L_4}{f_2}-\frac{L_2L_4}{f_2}+\frac{L_1L_2L_4}{f_1f_2}+$$

$$\left.L_4-\frac{L_1L_4}{f_1}-\frac{L_1L_4}{f_1}-\frac{L_2L_4}{f_1}+\frac{L_1L_2L_4}{f_1^2}\right\}$$

$$r_4=\alpha_1\left\{L_1+L_2+L_3+L_4-\frac{2L_1L_3}{f_1}-\frac{L_2L_3}{f_1}-\frac{L_1L_2}{f_1}-\frac{2L_1L_4}{f_1}-\frac{L_1L_4}{f_2}+\right.$$

$$\frac{2L_1L_3L_4}{f_1f_2}+\frac{L_1L_2L_4}{f_1f_2}+\frac{L_1L_2L_3}{f_1^2}+\frac{L_1L_2L_4}{f_1^2}-\frac{L_1L_2L_3L_4}{f_1^2f_2}-L_2L_4\left(\frac{1}{f_1}+\frac{1}{f_2}\right)$$

$$\left.-\frac{L_3L_4}{f_2}+\frac{L_2L_3L_4}{f_1f_2}\right\}$$

or $r_4=\alpha_1\{P\}$

Hence $a=\frac{L_5}{f_2}\alpha_1\{P\}$

$$r_5=\alpha_1(L_1+L_2+L_3+L_4+L_5)-d-c-b-a$$

$$=\alpha_1(L_1+L_2+L_3+L_4+L_5)-\frac{L_1\alpha_1}{f_1}(L_2+L_3+L_4+L_5)-$$

$$\alpha_1(\frac{L_1+L_2}{f_1}-\frac{L_1L_2}{f_1^2})(L_3+L_4+L_5)-$$

$$\alpha_1(\frac{L_4+L_5}{f_2})(L_3-\frac{2L_1L_3}{f_1}-\frac{L_2L_3}{f_1}+\frac{L_1L_2L_3}{f_1^2}+L_1+L_2-\frac{L_1L_2}{f_1})-\alpha_1\frac{L_5}{f_2}\{P\}$$

but $\alpha_1=\frac{r_o}{f_o}$

Total magnification $M_T=\frac{r_5}{r_o}$, hence

$$M_T = \frac{1}{f_o}\left[(L_1+L_2+L_3+L_4+L_5) - \frac{1}{f_1}(L_1L_2+2L_1L_3+2L_1L_5+2L_1L_4 \right.$$
$$+L_2L_3+L_2L_4+L_2L_5)+\frac{1}{f_1^2}(L_1L_2L_3+L_1L_2L_4+L_1L_2L_5) -$$
$$\frac{1}{f_2}(L_3L_4+L_1L_4+L_2L_4+2L_3L_5+2L_1L_5+2L_2L_5+L_4L_5)+$$
$$\frac{1}{f_2^2}(L_1L_4L_5+L_2L_4L_5+L_3L_4L_5)+\frac{1}{f_1f_2}(2L_1L_3L_4+L_2L_3L_4+L_1L_2L_4+$$
$$4L_1L_3L_5+2L_2L_3L_5+2L_1L_2L_5+2L_1L_4L_5 \quad L_2L_4L_5)$$
$$\frac{1}{f_1f_2}\left(\frac{L_1L_2L_3L_4+2L_1L_2L_3L_5+L_1L_2L_4L_5}{f_1}+\right.$$
$$\left.\left.\frac{L_1L_2L_4L_5+2L_1L_3L_4L_5+L_2L_3L_4L_5}{f_2}\right)+\frac{L_1L_2L_3L_4L_5}{f_1^2f_2^2}\right] \quad \ldots 13$$

REFERENCES

Bassett, R. and Mulvey, T. (1969). Zeits. für angew. Phys., 27, 142-145.

Becker, H. and Wallraff, A. (1940). Arch. Elektrotech. 34, 115-120.

Brookes, K.A., Mulvey, T. and Wallington, M.J. (1968). Proc. Itn. Conf. Elec. Micros. Vol. 1, (D.S. Bocciarelli, ed.), 165-166, Rome: Tipografia Poliglotta Vaticana.

Chapman, A.J. (1967). "Heat Transfer", 2nd Edition, Macmillan, New York.

Der-Schvarts, G.V. and Rachkov, V.P. (1965). R.E.E.P., 10, 783-789.

Durandeau, P. and Fert, C. (1957). Rev.Opt.Theor.Instrum. 36, 205-234.

Fert, C. and Durandeau, P. (1967). "Focusing of Charged Particles". Vol. 1, Ed. A. Septier, Academic Press.

Haine, M.E. (1961). "The Electron Microscope", Spon.

Haine, M.E. and Page, R.S. (1956). Proc. 5th Eur.Conf.Elect.Micros. (Stockholm), 32-34.

Herrmann, K.H., Ihmann, K. and Krahl, D. (1974). "Electron Microscopy 1974", (Sanders and Goodchild, eds.), Vol. 1, 132-133.

Hillier, J. (1946). J.Appl.Phys., 17, 411-419.

Hirsch, P.B., Howie, A., Nicholson, R.B., Pashley, D.W., Whelan, M.J. (1965). "Electron Microscopy of Thin Crystals", Butterworths.

Juma, S.M. (1972). M.Sc. Thesis, University of Aston in Birmingham, England.

Juma, S.M. and Mulvey, T. (1974). "Electron Microscopy 1974" (Sanders and Goodchild, eds) Vol. 1, 134-135, Australian Acad. Sci. Canberra.

Juma, S.M. and Mulvey, T. (1975). Proc. EMAG 75 Conf. Bristol, (In the Press).

Kamminga, W., Verster, J. and Francken, J.C. (1968/9). Optik, 28, 442-461.

Kanaya, K. (1958). Bull, Electrotech. Lab. (Tokyo). 22, 615-622.

Kanaya, K. and Ishikawa, A. (1958). Bull. Electrotech. Lab. (Tokyo), 22, 641-646.

Kroon, D.J. (1968). "Laboratory Magnets", Eindhoven, Netherlands: Phillips.

Kynaston, D. and Mulvey, T. (1963). Br.J.Appl.Phys., 14, 199-206.

Laverick, C. (1967). Adv.Electr.Elect.Phys., 23, 385.

Le Poole, J.B. (1964). Proc. 3rd Eur.Conf.Elec.Micros. Prague, Czech.Acad.Sci., Supplementary Pages.

Liebmann, G. (1951). Proc.Phys.Soc. B, 64, 972-977.

Liebmann, G. (1952). Proc.Phys.Soc. B, 65, 94-108.

Liebmann, G. (1955 A). Proc.Phys.Soc. B, 68, 679-685.

Liebmann, G. (1955 B). Proc.Phys.Soc. B, 68, 737-745.

Liebmann, G. and Grad, E.M. (1951). Proc.Phys.Soc. B, 64, 956-971.

Maclachlan, M.E.C. (1973). Ph.D. Thesis, Univ. of Cambridge.

Marai, F.Z. (1973). M.Sc. Thesis, University of Aston in Birmingham, England.

Marai, F.Z. (1974). Private Communication.

Marai, F.Z. (1975). Private Communication.

Marai, F.Z. and Mulvey, T. (1974). "Electron Microscopy 1974" (Sanders and Goodchild, eds), Vol. 1, 130-131, Australian Acad. Sci. Canberra.

Marai, F.Z. and Mulvey, T. (1975). Proc. EMAG 75 Conf. Bristol, (In the Press).

Montgomery, D.B. (1969). "Solenoid Magnet Design", Wiley-Interscience.

Mulvey, T. (1953). Proc.Phys.Soc. B, 66, 441-447.

Mulvey, T. (1967). "Focusing of Charged Particles", Vol. 1, Ed. A. Septier, Academic Press.

Mulvey, T. (1971). Proc. 25th Anniversary Meeting of EMAG (Cambridge), 78-83, Inst. Phys.

Mulvey, T. (1974). "Electron Microscopy 1974", (Sanders and Goodchild, eds) Vol. 1, 16-17, Australian Acad. Sci. Canberra.

Mulvey, T. and Newman, C.D. (1972). "Electron Microscopy 1972", 116-117, Inst. Phys.

Mulvey, T. and Newman, C.D. (1973 A). "Scanning electron microscopy: systems and applications 1973", (W.C. Nixon, ed), 16-21, Inst. Phys.

Mulvey, T. and Newman, C.D. (1973 B). "High voltage electron microscopy" (Swann et al, eds.), 98-102, Academic Press.

Mulvey, T. and Wallington, M.J. (1969). J.Phys. E: Sci. Instrum. 2, 466-472.

Ozasa, S., Katagiri, S., Kimura, H., Tadano, B. (1966). Proc. 6th Int.Cong.Elec.Micros., Kyoto, Japan, 149-150.

Prebus, A.F. (1942). Eng.Expt.Sta.News, 14, 6-32, Ohio State Univ.

Prior, A.C. (1967). Cryogenics, 7, 131-134.

Ruska, E. (1934). Z. s. f. Phys. 87, 580-602.

Stabenow, G. (1935). Zeits. Phys. 96, 634-642.

Yanaka, T. and Watanabe, M. (1966). Proc. 6th Int. Cong.Elec. Micros. Kyoto, Japan, 141-142.